Crystal Structure, Magnetic Structure and Magnetic Properties of (Nd, K)-Mn-O and (Nd, Na)-Mn-O based Manganites

A Thesis Submitted

By

Biswanath Samantaray

Roll No: 06612103

In Partial Fulfillment of the Requirements for the Award of the Degree of

Doctor of Philosophy in Physics

Department of Physics
Indian Institute of Technology Guwahati
Guwahati-781039, INDIA

September, 2011

Statement

The work contained in the thesis entitled **"Crystal Structure, Magnetic Structure and Magnetic Properties of (Nd, K)-Mn-O and (Nd, Na)-Mn-O based Manganites"** has been carried out by me under the supervision of Prof. S. Ravi, Department of Physics, Indian Institute of Technology Guwahati, Guwahati. This work has not been submitted elsewhere for the award of any degree.

2nd September, 2011

(Biswanath Samantaray)
Department of Physics
Indian Institute of Technology Guwahati
Guwahati – 781039, India

TH-1060_06612103

Certificate

It is certified that the work contained in the thesis entitled **"Crystal Structure, Magnetic Structure and Magnetic Properties of (Nd, K)-Mn-O and (Nd, Na)-Mn-O based Manganites"** by Mr. Biswanath Samantaray, a Ph. D. student of the Department of Physics, Indian Institute of Technology Guwahati, Guwahati for the award of the degree of *Doctor of Philosophy* has been carried out under my supervision. This work has not been submitted elsewhere for the award of any degree.

2nd September, 2011

(S. Ravi)
Professor, Department of Physics
Indian Institute of Technology Guwahati
Guwahati – 781 039, India

TH-1060_06612103

Dedicated

to

My Family

TH-1060_06612103

Acknowledgements

Looking back, I am surprised and at the same time very grateful for all I have received throughout these years. This is one of the rare occasions when I would like to express my gratitude to few people, who, over the years, have directly or indirectly been a part of my growth both as a researcher and a person.

First of all, I wish to give my sincere thanks to my research supervisor Prof. S. Ravi for his warmth encouragement and thoughtful guidance. It has been a great experience working with him. I will never forget his cool and down to earth behavior. He has enlightened me through his wide knowledge of physics and material science mainly experimental techniques, CMR materials, magnetism, etc., and numerous things in my personal life also. It was really incredible learning all these till the time of my thesis submission.

I would like to offer my thanks to the doctoral committee (DC) members, Prof. A. Srinivasan (Chairman), Dr. A. Perumal, and Dr. S. Kanagaraj for their constructive comments and suggestions that helped to improve the quality of my work.

I am very much grateful to my collaborators Dr. Amitabh Das from Bhabha Atomic research center, Mumbai for neutron powder diffraction measurements and Dr. Sandeep Srivastava from Nell Institute, France for high field magnetization measurements.

I will never fail to give my gratitude to my lab mates. They themselves have made the environment, interesting to work. So, in no particular order, I offer my thanks to former and present research group members for their assistance, advice and cooperation: Dr Manoranjan Kar, Dr Pramoda Kumar Nayak, Dr. Sandeep Kumar Srivastava, Sunita Mohanty, Tribedi Bora, Padam Rajendra, and Bipul Deka.

I am thankful to the Head of department Prof. S. Ravi for his help towards departmental facility. I would like to thanks Prof. Alika Khare (former HOD) for her cooperation in all regards. I am thankful to all other faculty members of this department. I feel privileged to be a member of department of physics. I am thankful to Dr. Sidananda Sarma for helping me to carry out different experiments and Mr. Basab Bijoy Purakayasthya for interfacing of instruments by Lab View Program. I am thankful to other staff members of my department.

TH-1060_06612103

I am thankful to Central Instrumental Facility (CIF), IIT-Guwahati, for enabling me to avail several sophisticated instruments to perform the experiments. I am also thankful to Prof. Arun Chattopadhyay former Head of the Center for Nanotechnology for extending X-ray diffractometer facility.

Department of Science and Technology for facilitating vibrating sample magnetometer and UGC-DAE CSR, Mumbai for facilitating the collaborative neutron diffraction studies are gratefully acknowledge.

I am thankful to Dr. Charudatt Kadolkar for the colorful and memorable times, we had together. I am benefited a lot from his amazing insights and fundamental tricks in physics during my research period.

My special thanks to batch mates Biswanath Dutta, Arpita, Aneesh, and Pravakar having very good friendship. I am thankful to Poloumi, Debabrata, Meera, Rahul, Supriya, Santosh Kumar, Ranjan, Akhilesh, Bhargab, Brahmananda, Batakrushna and all research scholars of my department for pleasant memories had with them.

Special mention must go to Prakash (from JNCASR) and Pratap (from IIT Kharagpur) for their continuous support and warmth in the back drop of this journey- my heartiest thanks to them. I would like to thanks my other friends Ramesh, Susanta, and Manas for very good friendship.

One of the most precious gifts of my life is my wife, Lipi. She is so supportive and understanding. I am indebted to her for the unconditional love and making my life so colorful. None of this would have been possible without her constant support, love, and encouragement.

Finally, my sincere gratitude must go to my family, specially my parents, my loving wife (Lipi), elder brother (Vivek), elder sister (Laxmi), my parents-in-law, my cousin uncle (Bhimasen) and aunty (Manjulata) for their continuous love and encouragement. I am thankful to my other family members for their encouragement.

Last but not the least, I am grateful to Indian Institute of Technology Guwahati for giving the financial support to carry out the present thesis work.

Biswanath Samantaray

IIT Guwahati, INDIA, 2nd September, 2011

TH-1060_06612103

Abstract

Colossal magnetoresistive oxides, one of the amazing classes of materials have been the subject of research for more than a decade, due to their fascinating electrical and magnetic properties and, their potential applications in spintronics devices and magnetic storage. The alkaline earth doped rare earth manganites based materials are mostly known to exhibit colossal magneto-resistivity (CMR), i.e. large negative magneto-resistivity in the vicinity of ferromagnetic (FM) transition temperature (T_C) due to the double exchange ferromagnetic interaction.

There are several reports on Nd based divalent alkaline earth doped manganites. The magnetic and transport properties of such materials are found to be quite interesting. In Ca doped Nd-Mn-O series, FM transition with T_C around 110 K, along with the presence of charge ordering and antiferromagnetism (AFM) has been observed without any metal-insulator transition. The application of magnetic field was found to induce semiconductor–metal and AFM-FM transitions in the composition range of $0.30 \leq x \leq 0.45$. The charge ordering and its destruction by the application of large magnetic field were reported in half doped, $Nd_{0.5}Ca_{0.5}MnO_3$ series. In $Nd_{0.7}Sr_{0.3}MnO_3$, FM and metal-insulator (M-I) transitions have been observed with T_C in the range of 230 K to 250 K because of its relatively large A site ionic size ($< r_A > =1.212$) compared to that of (Nd, Ca)-Mn-O series. However, in half-doped $Nd_{0.5}Sr_{0.5}MnO_3$ material, charge ordering transition has been reported at around 150 K from the detailed neutron diffraction, magnetization and electrical resistivity studies. In (Nd, Ba)-Mn-O series, even though the $< r_A >$ value is quite large, FM was observed only in a narrow composition range of x = 0.2 to 0.4 with relatively lower T_C 120 K.

In this research work, mainly monovalent (K and Na) doped Nd-based manganites have been taken up for study. The monovalent doping has the advantage of creation of optimum concentration of Mn^{3+}/Mn^{4+} ions with relatively small level of doping. Thus, the lattice distortion can be kept minimum in the monovalent doped materials. Crystal structure, magnetic structure and lattice distortion have been investigated using neutron and X-ray diffraction measurements. DC magnetization and ac susceptibility measurements have been carried out to investigate the nature of magnetic properties for different doping concentrations. Moreover, FM, spin glass like behavior, critical exponent behavior in the vicinity of FM transition, charge ordering, etc. were studied in detail in these materials. Suppression of charge-ordering in $Nd_{0.8}Na_{0.2}MnO_3$ compound by varying two parameters,

TH-1060_06612103

namely particle size down to nano-metric scale and magnetic field up to 10 T has been investigated.

The following three series of samples were prepared.

1. $Nd_{1-x}K_xMnO_3$ (x = 0.10 - 0.30)
2. $Nd_{1-x}Na_xMnO_3$ (x = 0 - 0.20)
3. Nanoparticle samples of $Nd_{0.8}Na_{0.2}MnO_3$

The above samples were characterized by using powder X-ray diffractometer (XRD), scanning electron microscope (SEM), field emission SEM, transmission electron microscope (TEM), energy-dispersive spectrometer (EDS), and chemical titration. To determine the crystal structure and magnetic structure of the above materials, neutron powder diffraction (NPD) patterns were recorded at selected temperatures down to 5 K by using multi-position sensitive detector based powder diffractometer (λ = 1.249 Å) at Dhruva reactor, BARC, Mumbai. To understand the magnetic properties and different magnetic interactions involved, the following measurements were carried out; (1) temperature and frequency variations of ac susceptibility by using home-made ac susceptometer, (2) dc magnetization as a function of temperature, field and time by using a Lakeshore make vibrating sample magnetometer of model no. 7410 and Quantum Design make SQUID based magnetic property system. To explore the electronic transport properties, temperature variations of electrical resistivity and magneto-resistivity measurements were carried out by using the standard linear four-probe technique.

The thesis contains six chapters, namely,

(1) Introduction (2) Experimental Techniques (3) (Nd, K)-Mn-O Series (4) (Nd, Na)-Mn-O Series (5) Charge Order Suppression in $Nd_{0.8}Na_{0.2}MnO_3$ and (6) Conclusions.

In chapter 1, the discovery of colossal magneto-resistivity in perovskite manganites is reviewed briefly. The role of crystal structure, crystal field effect, Jahn-teller distortion, electron-phonon coupling, etc. on the physical properties of rare earth manganites is then discussed. The reported magnetic properties and the proposed mechanism in various manganites and the different electrical conductivity mechanism are also presented. The introduction also contains the literature review on mixed valent Nd-based manganites, with special emphasis on their crystal structure, magnetic structure, electrical transport and magnetic properties

Chapter 2 is devoted to the detailed experimental techniques followed in the present thesis work. The method of material preparation and, the experimental techniques employed for various physical measurements, such as electrical resistivity, magneto-resistivity, ac

TH-1060_06612103

susceptibility, dc magnetization, etc. are presented. The working principles of various sophisticated instruments such as powder X-Ray diffractometer, neutron powder diffractometer, scanning electron microscope, transmission electron microscope, vibrating sample magnetometer, and SQUID based magnetic property measurement system are discussed.

Chapter 3 deals with $Nd_{1-x}K_xMnO_3$ series. Samples of this series were prepared in single phase form with *Pnma* space group, for x = 0.10 to 0.30. The crystal structure, magnetic structure and magnetic properties of two samples x = 0.15 and x = 0.20 were studied by recording neutron powder diffraction (NPD) patterns down to 22 K. The patterns at low temperatures could be refined by considering magnetic reflections corresponding to ferromagnetic structure. The refined magnetic moments of Mn ion were found to be ferromagnetically aligned along *ac*-plane with a typical value of 2.82 (3) μ_B per Mn ion at 22 K for x = 0.15 sample.

The magnetic properties were studied by measuring dc magnetization and ac susceptibility. They exhibit paramagnetic to ferromagnetic transition with T_C ranging from 116 K to 128 K. The magnetization data could be analyzed by using Brillouin function model and by taking into account the ferromagnetic interaction. The effective spin contribution towards the FM interaction was estimated and those values were found to increase with increase in doping concentration. Magnetocaloric effect (MCE) has been studied and the maximum change in entropy was found to be 1.76 J/kg K for 1 T field. Metal-Insulator transition and colossal magnetoresistance of the order of 60% for 1T field were observed for x = 0.20 sample.

The temperature and frequency variations of ac susceptibility in x = 0.15 sample were analyzed to study the spin glass behavior. The spin glass behavior was also studied by recording third harmonic ac susceptibility and thermo remanent magnetization. The origin of spin glass behavior was found to be due to the freezing of clusters rather than magnetic frustration at atomic scale.

Isothermal magnetization was measured as a function of field in the vicinity of FM transition on two samples. They were analyzed in terms of modified Arrott plot method and the estimated critical exponents, $\beta = 0.57\pm0.03$, $\gamma = 1.04\pm0.02$, and $\delta = 2.82\pm0.03$ were found to be close to the mean field model values. The role of ferromagnetic clusters on the scaling behavior was discussed. The critical exponent values were found to be consistent with the Widom scaling relation $\delta = (1+\gamma/\beta)$ and the universal scaling hypothesis.

TH-1060_06612103

Chapter 4 deals with (Nd, Na)-Mn-O series, where the detailed magnetic properties from the analysis of magnetization and neutron powder diffraction patterns are presented for samples upto 20 % of Na doping.

The $Nd_{1-x}Na_xMnO_3$ samples for $0.05 \leq x \leq 0.15$ exhibit PM to FM transition with a maximum T_C of 113 K for x = 0.15 sample. They also exhibit an anomaly at around 40 K due to the spin glass like behavior. The temperature variation of magnetization of x = 0.20 sample exhibits a charge-order transition at 180 K, followed by reentrant spin glass like transition at around 40 K. The saturation magnetization of x = 0.05, 0.10 & 0.15 samples after subtracting the linear contribution are found to be 4, 4.3 and 3.3 μ_B respectively at 5 K. The observed large magnetic moments could be explained in terms of contribution of spin canted 'Nd' moment at 5 K.

The magnetic dynamics of charge ordered $Nd_{0.8}Na_{0.2}MnO_3$ compound was studied by measuring the temperature variation of magnetization for different magnetic fields up to 7 T and, the field variation of magnetization at different temperatures down to 5 K. Suppression of charge-ordering (CO) and spin glass like transition and, increase in FM T_C were observed with an increase in magnetic field. However at 5 K, a distinct irreversible field induced first order phase transition from spin frozen state to FM state was observed above a characteristic field (H_S) and is discussed in detail. Electrical resistivity measurements show that the samples are insulators and their temperature variation could be explained by using adiabatic small Polaron model.

Neutron powder diffraction measurements were carried out on x = 0, 0.15 and 0.20 samples and a systematic study of crystal structure, magnetic structure and magnetic properties was carried out. A transition from A-type AFM structure for x = 0 to pseudo CE-type AFM phase for x = 0.20 through the spin canted FM phase for x = 0.15 was observed with change in doping concentration. The x = 0 sample exhibits canting of Mn moments away from *ac*-plane. Nd ions are found to couple ferrimagnetically with Mn ions. The values of Mn and Nd moments at 5 K are found to be 3.0 μ_B and 1.3 μ_B respectively. The x = 0.15 sample exhibits increase in intensity of (101) and (121) peaks with decrease in temperature below 80 K and it depicts the ferromagnetic nature of the sample. The magnetic structure of x = 0.20 sample for $T < 125$ K could be successfully explained in terms of pseudo CE-type AFM structure with $P2_1/m$ space group. Here the Mn^{3+} sublattice is associated with a propagation vector $k_1 = (0\ 0\ ½)$ and Mn^{4+} sublattice is associated with a propagation vector $k_2 = (½\ 0\ ½)$. The maximum refined magnetic moment values for Mn^{3+} and Mn^{4+} sublattices are found to be 3.20(5) μ_B and 3.00(2) μ_B respectively.

TH-1060_06612103

In chapter 5, the suppression of charge-ordering and the evolution of FM cluster glass phase by reducing the average particle size of the $Nd_{0.8}Na_{0.2}MnO_3$ compound to nano-metric scale are discussed. Single phase samples of charge ordered $Nd_{0.8}Na_{0.2}MnO_3$ were prepared with different particle sizes ranging from 700 nm to 30 nm. The effect of particle size and applied magnetic field on the magnetic properties of the CO phase was studied extensively by carrying out temperature and field variations of magnetization measurements and their analysis. The bulk samples, i.e. with particle size $D \geq 140$ nm, different magnetic ground states namely PM, CO, cluster glass FM and AFM/RSG were observed in different temperature regions. However, in nano-sized particles, with $D \leq 80$ nm suppression of CO and the enhancement of FM T_C were observed. *M~H* loops recorded at different temperatures show the field induced transition from CO-AFM to FM beyond a threshold field H_C. The threshold field is found to decrease with decrease in particle size at a given temperature. The phase boundary between CO-AFM and FM was found to shift towards higher temperature and lower field. The temperature and field variations of magnetization on nanoparticles of $Nd_{0.8}Na_{0.2}MnO_3$ samples could be explained in terms of the core-shell model.

In chapter 6, the summary of conclusions drawn from the analysis of experimental data on two monovalent hole doped series and particle size effect on charge-ordered $Nd_{0.8}Na_{0.2}MnO_3$ compound are presented. Thus, the double exchange ferromagnetic samples K-doped Nd-Mn-O series and, charge-ordered and ferromagnetic insulating of Na-doped sample were prepared in single phase form and their magnetic properties were studied. It is demonstrated that the observed charge ordering in $Nd_{0.8}Na_{0.2}MnO_3$ can be suppressed by tuning their particle size and applied magnetic field. The *T-H* phase diagram of $Nd_{0.8}Na_{0.2}MnO_3$ samples were constructed for different particle sizes.

TH-1060_06612103

List of Abbreviations used in this Thesis

AFM Antiferromagnet (ic)

CCR Close Cycle Refrigerator

CE Charge Exchange

CG Cluster Glass

CMR Colossal Magnetoresistivity

CO Charge-Ordered

COO Charge-Orbital-Ordered

DE Double Exchange

EDS Energy Dispersive Spectra

ES-VRH Efros-Shklovskii Variable Range Hopping

FC Field Cooled

FCC Field Cooled Cooling

FCW Field Cooled Warming

FE Field Emission

FE-SEM Field Emission Scanning Electron Microscope

FM Ferromagnet (ic)

FM-CG Ferromagnetic Cluster Glass

FMI Ferromagnetic Insulator

FMM Ferromagnetic Metal

FWH Full Width Half Maxima

GMR Giant Magneto Resistivity

JT Jahn-Teller

MAP Modified Arrot Plot

MCE Magnetocaloric Effect

MPMS Magnetic Property Measurement System

MR Magnetoresistance

NPD Neutron Powder Diffraction

NTC Negative Temperature Coefficient

PID Proportional–Integral–Derivative

PM Paramagnet (ic)

TH-1060_06612103

RF Radio Frequency

RSG Re-entrant Spin Glass

SE Superexchange

SEM Scanning Electron Micrograph

SG Spin glass

SPH Small Polaron Hopping

SQUID Superconducting Quantum Interference Device

TCM Temperature Controller Module

TEM Transmission Electron Microscope

TMO Transition Metal Oxide

TRM Thermoremanent Magnetization

VRH Variable Range Hopping

VSM Vibrating Sample Magnetometer

XRD X-ray Diffractometer

ZFC Zero-Field Cooled

TH-1060_06612103

Table of Contents

Content **Page No.**

TH-1060_06612103

TH-1060_06612103

TH-1060_06612103

List of Figures

Page No.

Chapter 1:

TH-1060_06612103

Chapter 2:

TH-1060_06612103

Chapter 3:

TH-1060_06612103

TH-1060_06612103

Chapter 4:

TH-1060_06612103

Chapter 5:

TH-1060_06612103

TH-1060_06612103

TH-1060_06612103

List of Tables

Page No.

Chapter 1:

Chapter 3:

Chapter 4:

TH-1060_06612103

TH-1060_06612103

Chapter 1

Introduction

TH-1060_06612103

Chapter 2

Experimental Techniques

TH-1060_06612103

Chapter 3

(Nd, K)-Mn-O Series

TH-1060_06612103

Chapter 4

(Nd, Na)-Mn-O Series

TH-1060_06612103

Chapter 5

Charge Order Suppression in $Nd_{0.8}Na_{0.2}MnO_3$

TH-1060_06612103

Chapter 6

Conclusions

TH-1060_06612103

Chapter 1: Introduction

The success of technological advancement in developing smart and nano magnetic materials in last two decades towards applications in memory device, data storage processing and probing has attracted much interest in magnetic materials. The transition metal oxide (TMO) based magnetoelectronics is fast emerging as future feasible technology. The transition metal oxide based materials with perovskite (ABO_3 type) structure are in the limelight of research pursued by physicists, materials scientists, etc., because of their interesting physical properties and technological applications [1]. They exhibit variety of rich phenomena such as, ferroelectricity in titanates (doped $BaTiO_3$) [2, 3], colossal magneto resistance in manganites [4-9], high temperature superconductivity in cuprates ($La_{2-x}Ba_xCuO_4$, etc.) [10-12], and multiferrocity [3, 13-15].

Colossal magnetoresistive oxides, one amazing class of materials are being the subject matter of a large number of studies for more than a decade, due to their fascinating electrical and magnetic properties and, potential applications in magnetic recording and spintronics devices [4-8]. The rare earth manganites with perovskite structure was found to exhibit colossal magneto-resistivity (CMR) because of their prototype correlated electron systems, where spin, charge, lattice and orbital degrees of freedom play a role simultaneously and give rise to tunable physical properties. The phenomenon of CMR can be described as a dramatic decrease of electrical resistance by the application of magnetic field, in perovskite manganites and it arises from the spin polarization of the conduction electrons. The discovery of large negative magneto-resistivity in the vicinity of ferromagnetic (FM) transition temperature (T_C) of alkaline earth doped $LaMnO_3$ has renewed the attention of researchers in perovskite manganites because of their potential applications in data storage and retrieval, electrically-readable magnetic-field sensor, magnetic refrigeration and magnetic switches [16]. These materials exhibit mixed valency of Mn ions.

The mixed valent manganites are described by the chemical formula $R_{1-x}A_xMnO_3$, where R (La, Nd, Pr, Sm, Eu, Tb, Gd, etc.) is a trivalent rare earth element and A (Sr, Ca, Ba, K, Na, etc) is a divalent alkaline earth element or a monovalent alkali element. The parent compounds $LaMnO_3$, $PrMnO_3$, $NdMnO_3$, etc. are electrical insulators and they exhibit antiferromagnetic (AFM) transition with Neel temperature, T_N in the range of 80-140 K for different samples. $LaMnO_3$ exhibits A-type AFM ordering with T_N in the range of 100-140 K, where spins of Mn^{3+} ions ($3d^4$: $t_{2g}^3\ e_g^1$) in each layer is aligned ferromagnetically with a net AFM interaction between the layers [17-19]. The electrical and magnetic properties are

TH-1060_06612103

closely related to the crystal structure and Jahn-Teller (JT) distortion around Mn^{3+} ions. The mixed valent oxides $(R^{3+}_{1-x}A^{1+}_{x})(Mn^{3+}_{1-2x}Mn^{4+}_{2x})O_3$ / $(R^{3+}_{1-x}A^{2+}_{x})(Mn^{3+}_{1-x}Mn^{4+}_{x})O_3$ can be obtained by the substitution of mono-valent/divalent elements in place of R or by doping at Mn site. One can also get mixed valent manganites by self doping in parent compounds, i.e., by creating vacancy in Mn or R site [4-8]. The doped perovskite manganites exhibit transition from paramagnetic (PM) insulator to ferromagnetic (FM) metallic state upon cooling along with CMR behavior. They are explained on the basis of Zener double exchange (DE) ferromagnetic (FM) interaction in Mn^{3+}-O^{2-}-Mn^{4+} networks [20]. The other factors such as mixed valency, ionic size mismatch, Mn-O bond length, $\angle Mn-O-Mn$ bond angle, strong electron-phonon interaction, etc. are known to play a considerable role on the CMR behavior [21, 22]. The coexistence of ferromagnetic metallic (FMM) and antiferromagnetic (AFM) charge or orbital ordered insulating phases due to magnetic phase separation plays a considerable role in colossal magnetoresistance phenomena. These properties also depend upon the hole doping level and average A-site ionic radius $<r_A>$, which in turn control the effective e_g electron band width.

In this chapter, the crystal structure, magnetic structure, magnetic and electrical transport properties of manganites are reviewed.

1.1. Crystal Structure

The crystal structure of perovskite manganites $RMnO_3$ (R = rare earth), originates from the ideal cubic perovskite structure of ABO_3 type as shown in figure 1.1. Here the A site R ions occupy the vertices of the cubic unit cell. MnO_6 octahedra is formed with Mn ion occupying the B site, i.e., the body centered position and with O ions occupying the six faces of the cube. The regular arrangement of MnO_6 octahedra with vertex sharing can be seen in figure 1.2. Here Mn-O-Mn bond angle is 180° and the unit cell dimensions are equivalent to Mn-Mn bond lengths. However, the actual crystal structure of both undoped and doped compounds of $RMnO_3$ series deviates from the ideal cubic structure due to lattice distortion: one possible origin of lattice distortion is the deformation of the MnO_6 octahedra due to the Jahn-Teller effect and it is inherent due to high-spin (S = 2) Mn^{3+} ion, with double degeneracy of e_g orbitals. Oxygen off-stoichiometry or cation vacancy also leads to the lattice distortion and reduced crystal symmetry in undoped $RMnO_3$. In doped $RMnO_3$, the lattice distortion arises mainly due to the ionic size mismatch at R site and it leads to the tilting of MnO_6 octahedra

TH-1060_06612103

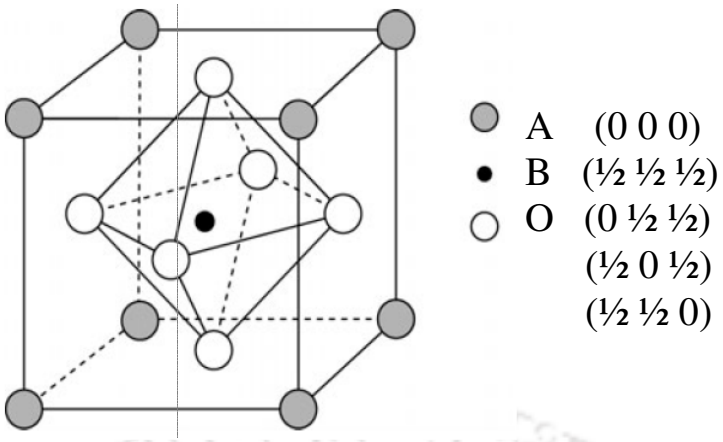

Figure 1.1: Crystal structure of cubic perovskite with chemical formula ABO_3.

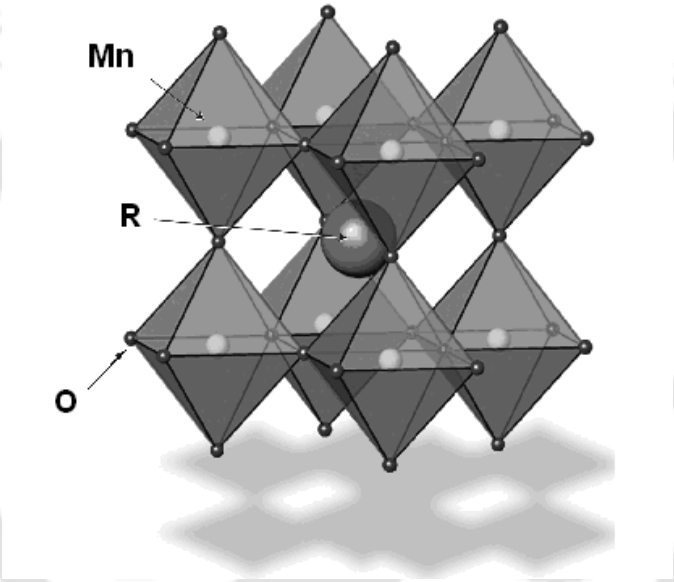

Figure 1.2: The ideal cubic crystal structure of $RMnO_3$.

towards or away from the R ion. The tilting of one MnO_6 octahedra leads to the tilting of other neighboring octahedra, and as a result there is a co-operative tilting of MnO_6 octahedra. The tilting gives rise to change in crystal symmetry and space group. Such a lattice distortion is governed by the Goldschmidt tolerance factor t [23], and defined as $\left[t = \frac{d_{R-O}}{\sqrt{2} d_{Mn-O}} = \frac{\langle r_R \rangle + r_O}{\sqrt{2}(\langle r_{Mn} \rangle + r_O)} \right]$. Here t is a measure of lattice distortion from the ideal cubic structure; $d_{R\text{-}O}$ is the distance between the R ion and the nearest neighbor oxygen ion and $d_{Mn\text{-}O}$ is the shortest Mn-O distance. Here r_R, r_{Mn} and r_O are the radii for the 12-coordinated R-site cations, 6-coordinated Mn cations and Oxygen anions respectively in $RMnO_3$ crystal structure. For the cubic symmetry, the Mn-O-Mn bond is quite straight, i.e., $d_{A\text{-}O} = \sqrt{2} d_{Mn\text{-}O}$,

TH-1060_06612103

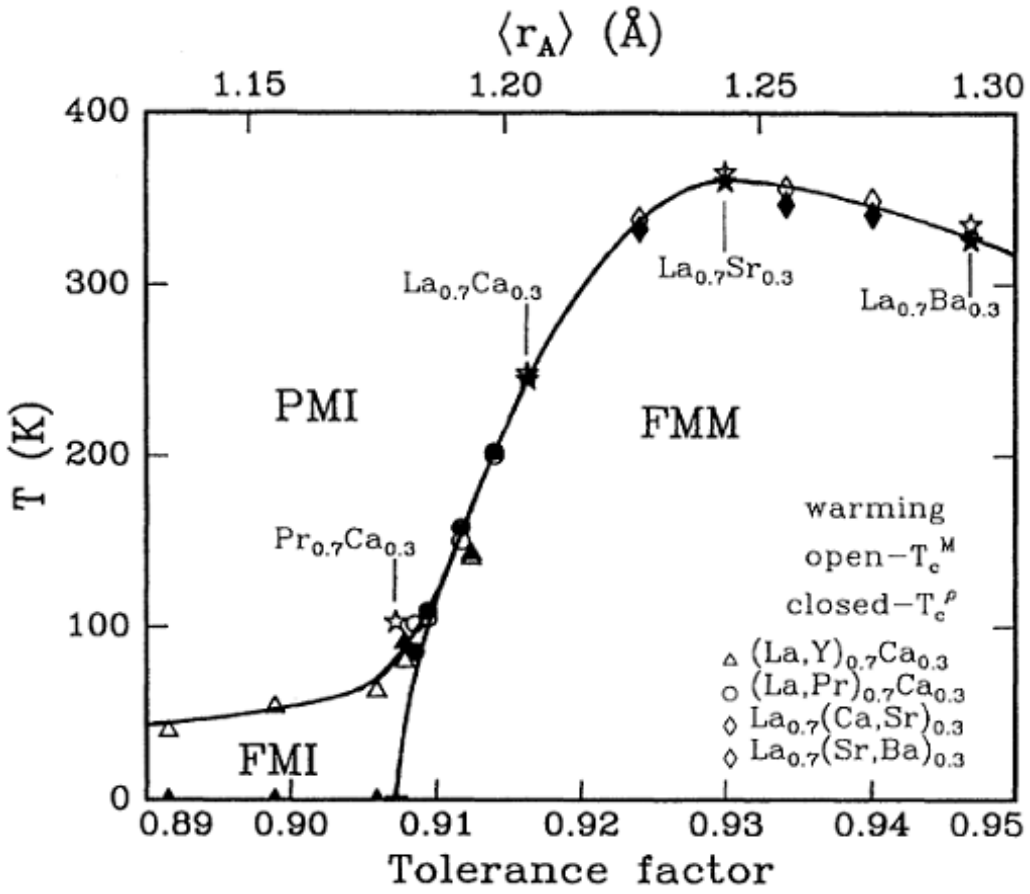

Figure 1.3: Phase diagram of $R_{0.7}A_{0.3}MnO_3$ (R = trivalent rare earth and A = divalent alkaline earth ion) in terms of tolerance factor. Open symbols denote the T_C (PM to FM transition temperature) measured at 100 Oe and closed circles denote T_{MI} (Insulator to metal transition temperature). (Reproduced from Hwang *et al.* [24])

and hence t = 1. However, in doped perovskite manganites, the average A-site ionic radius is reduced and to fill up the void, the MnO_6 octahedra tends to move towards the center and it causes the reduction in tolerance factor value. Stable perovskite structure is expected for $0.89 \leq t \leq 1.02$ [1]. Unit cell with orthorhombic symmetry due to the cooperative tilting of MnO_6 octahedra is expected for 't' values in between 0.75 and 0.9 [25]. Hwang *et al*. [24] have studied the correlation between the crystal structure and the electrical and magnetic properties of $R_{0.7}A_{0.3}MnO_3$ (A = divalent elements) compounds by selecting various 'R' and 'A' ions. They have mapped out the phase diagram by plotting the transition temperature as a function of tolerance factor for the above system as shown in figure 1.3. Three different regions such as paramagnetic insulating region, ferromagnetic metallic region and ferromagnetic insulating region are seen.

TH-1060_06612103

Manganites based on R ions having relatively large ionic radii such as La, Ce, Pr, Nd, Sm, Eu, Gd, Tb, Dy etc. are expected to form perovskite structure with rhombohedral or orthorhombic symmetries. Moreover, CMR materials are prepared by doping various alkaline earth, alkali ion elements, etc., in place of R ions. So the effective A site ionic radius, $<r_A>$ depends on both R and dopant elements. So, $<r_A>$ plays a major role in tuning the crystal structure of the materials [1]. Typical crystal structure of $(R_{1-x}A_x)MnO_3$ compounds with orthorhombic symmetry is shown in figure 1.4 (a), where we can see the reduced crystal

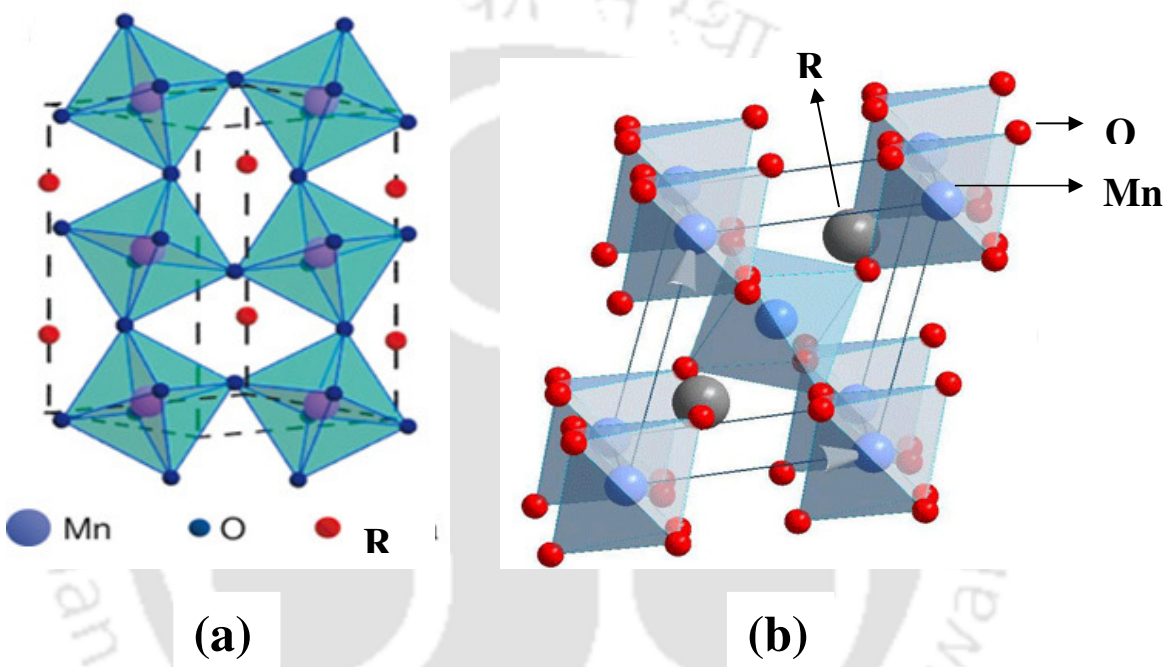

Figure 1.4: (a) Orthorhombic crystal structure of manganites (b) Rhombohedral crystal Structure of manganites.

Table 1.1: Atomic positions of $RMnO_3$ in *Pnma* space group.

Ion	Site	(x, y, z)
R	4c	(x, ¼, z) ≅ (0.03, ¼, 0.99)
Mn	4b	(0, 0, ½) ≅ (0, 0, ½)
O_1	4c	(x, ¼, z) ≅ (0.49, ¼, 0.07)
O_2	8d	(x, y, z) ≅ (0.28, 0.04, 0.72)

TH-1060_06612103

symmetry compared to the ideal cubic structure due to the tilting of MnO_6 octahedra. If a_p is the unit cell dimension of the cubic crystal structure, the lattice parameters of the above orthorhombic structure can be approximately written as, $a \cong c = \sqrt{2}\, a_p$ and $b = 2a_p$. It has *Pnma* space group symmetry. The general atomic positions are given in table 1.1. The crystal structure of CMR materials such as $(La_{1-x}Ca_x)MnO_3$ [26] and $(La_{1-x}Ba_x)MnO_3$ [27, 28] were found to form in *Pbnm* space group with typical lattice parameters, $a = 5.474$, $b = 5.460$ and c= 7.715 Å and Mn-O-Mn bond angle in the order of 155 to 160°. The number of formula units per unit cell, Z in the above orthorhombic cell is 4.

The typical rhombohedral crystal structure of $(R_{1-x}A_x)MnO_3$ compounds is shown in figure 1.4 (b). Here also, each Mn ion is octahedrally coordinated with O ions. The rotation of MnO_6 octahedra along the three fold rotational axis of the ideal cubic structure gives rise to rhombohedral symmetry. These structural parameters are generally referred in hexagonal co-ordinate system.

Table 1.2: Atomic positions of $RMnO_3$ in $R\bar{3}c$ space group given in hexagonal coordinate system.

Ion	Site	x,	y,	z
R	6 *a*	0	0	¼
Mn	6 b	0	0	0
O	18e	0.55 (x)	0	¼

Unlike the case of orthorhombic cell, there is no buckling of MnO_6 octahedra and hence the Mn-O bond lengths are identical in all the three directions. The Mn-O-Mn bond angle is found to be slightly larger than that of orthorhombic cell and is around 165°. The Z value is found to be 6.

Most of the mono-valent and alkali ion doped manganites with relatively large $\langle r_A \rangle$ exhibit such rhombohedral structure [28-34]. The typical lattice parameters of $La_{0.82}Na_{0.16}MnO_3$ compound with rhombohedral structure are reported to be $a = b = 5.490$ Å and c= 13.319 Å with typical Mn-O bond-length and Mn-O-Mn bond angle 1.951 Å and 165.2° respectively [29].

TH-1060_06612103

1.2. Crystal Field and Jahn-Teller Distortion

Atoms in a solid with a regular crystal structure are influenced by the electric field due to the neighboring atoms in the crystal. Such electric fields are called crystal field [35]. Crystal field depends upon the local environments, such as nature of atomic co-ordination, etc. The basic building block of perovskite manganite is MnO_6 octahedra. The hybridization and electrostatic interaction of outermost *3-d* orbital of Mn^{3+} ions with *2p* orbital of oxygen ions gives rise to a crystal field effect, in the cubic environment of MnO_6 octahedra. The d shell has five orbitals, namely d_{xy}, d_{yz}, d_{zx}, d_{z^2}, and $d_{x^2-y^2}$; out of them, the first three are called t_{2g} orbitals and last two are called e_g orbitals. The electronic distributions of *d* orbitals are shown in figure 1.5. In the absence of crystal field, all the five levels are degenerate. The t_{2g} orbitals point along in between x, y and z axes, but the e_g orbitals point along the direction of x, y and z axes. In MnO_6 octahedral environment, the electrons in the 3d shell of Mn ions are under the Coulomb interaction of electrons from the *2p* shell of O ions. Since the p_x, p_y, p_z orbitals of O point along x, y and z directions respectively, there will be a overlapping with e_g orbitals of Mn ions. So, the energy of e_g orbitals is raised compared to t_{2g} orbitals. Figure 1.6(a) shows a two dimensional diagram of typical overlapping of one of the e_g orbitals ($d_{x^2-y^2}$) with *p* orbitals of neighboring O ions. On the other hand, we can see no such overlapping with a t_{2g} orbital, as shown in figure 1.6 (b). In view of the above crystal field effect, the fivefold degeneracy of *d* orbitals are lifted by raising the energy of e_g orbitals with respect to t_{2g} orbitals as shown in figure 1.6 (c) for octahedral co-ordination [35].

The energy difference between t_{2g} and e_g orbitals due to the crystal field effect on $LaMnO_3$ is approximately 1.5 eV [22]. It may be noted that for tetrahedral co-ordination, the energy splitting will be in the opposite way, i.e., t_{2g} levels will be lifted compared to e_g level. So, the nature of atomic environment plays a very important role in crystal field. Because of the crystal field effect, the magnetic moment of transition metal ions does not follow the estimated theoretical moment based on total angular momentum, i.e., $\mu_{th} = g\mu_B\sqrt{J(J+1)}$ as stipulated by Hund's rules. The crystal field energy is mostly stronger than the spin-orbit coupling as per Hund's third rule and it leads to orbital quenching, i.e., L=0. It is rather close to magnetic moment due to spin only contribution, $\mu_{th} = g\mu_B\sqrt{S(S+1)}$. The observed degeneracy in crystal field splitting can be further broken by the lattice distortion. The oxygen ions are surrounded by Mn^{3+} ions, and the readjustment of their position can lead to

TH-1060_06612103

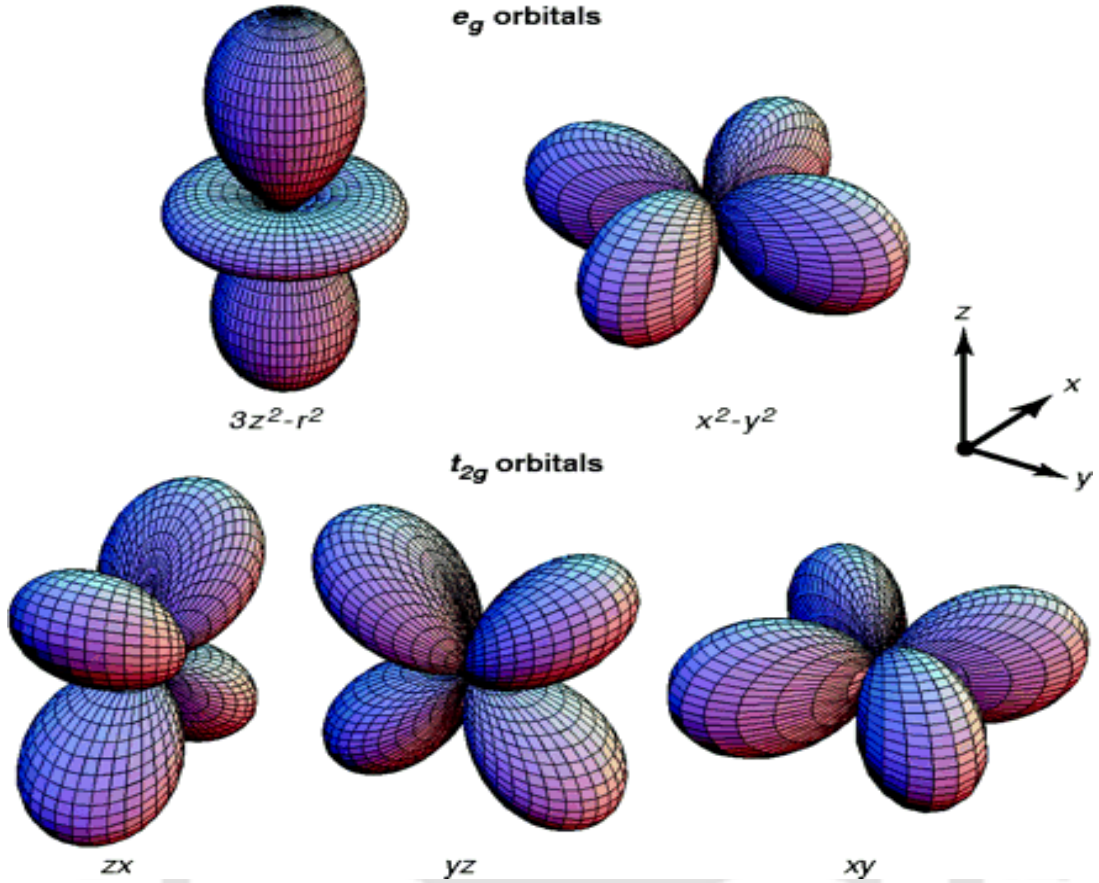

Figure 1.5: The electronic distribution of 3-*d* orbitals. In the cubic crystal field, this fivefold degeneracy is lifted to two e_g orbitals ((x^2-y^2) and ($3z^2 - r^2$)) and three t_2g orbitals ((*xy*), (*yz*) and (*zx*)). (Reproduced from Tokura *et al.* [36])

further asymmetry in MnO_6 octahedra. The above lattice asymmetry lifts the degeneracy of t_{2g} and e_g orbitals. The lifting of degeneracy due to orbital-lattice interaction is known as Jahn- Teller (JT) distortion. The Jahn-Teller distortion is significant for partially filled orbitals, where there is a net energy gain. This distortion leads to increase in elastic energy and decrease in electronic energy such that there is a net reduction in energy. Mn^{3+} ions are JT active, while Mn^{4+} ions are inactive for JT distortion in octahedral environment. Mn^{3+} ions have one e_g electron out of two orbitals namely, $d_{3z^2-r^2}$ and $d_{x^2-y^2}$. The elongation of MnO_6 octahedra along z-axis gives rise to reduction in $d_{3z^2-r^2}$ level compared to $d_{x^2-y^2}$.level. Since, there is only one e_g electron, which occupies the $d_{3z^2-r^2}$ level, there is a reduction in electronic energy. The splitting of e_g and t_{2g} orbits due to JT distortion is shown in figure 1.6 (c). On the other hand, Mn^{4+} ion does not have e_g electron, so reduction in electronic energy is not feasible and hence no JT distortion.

TH-1060_06612103

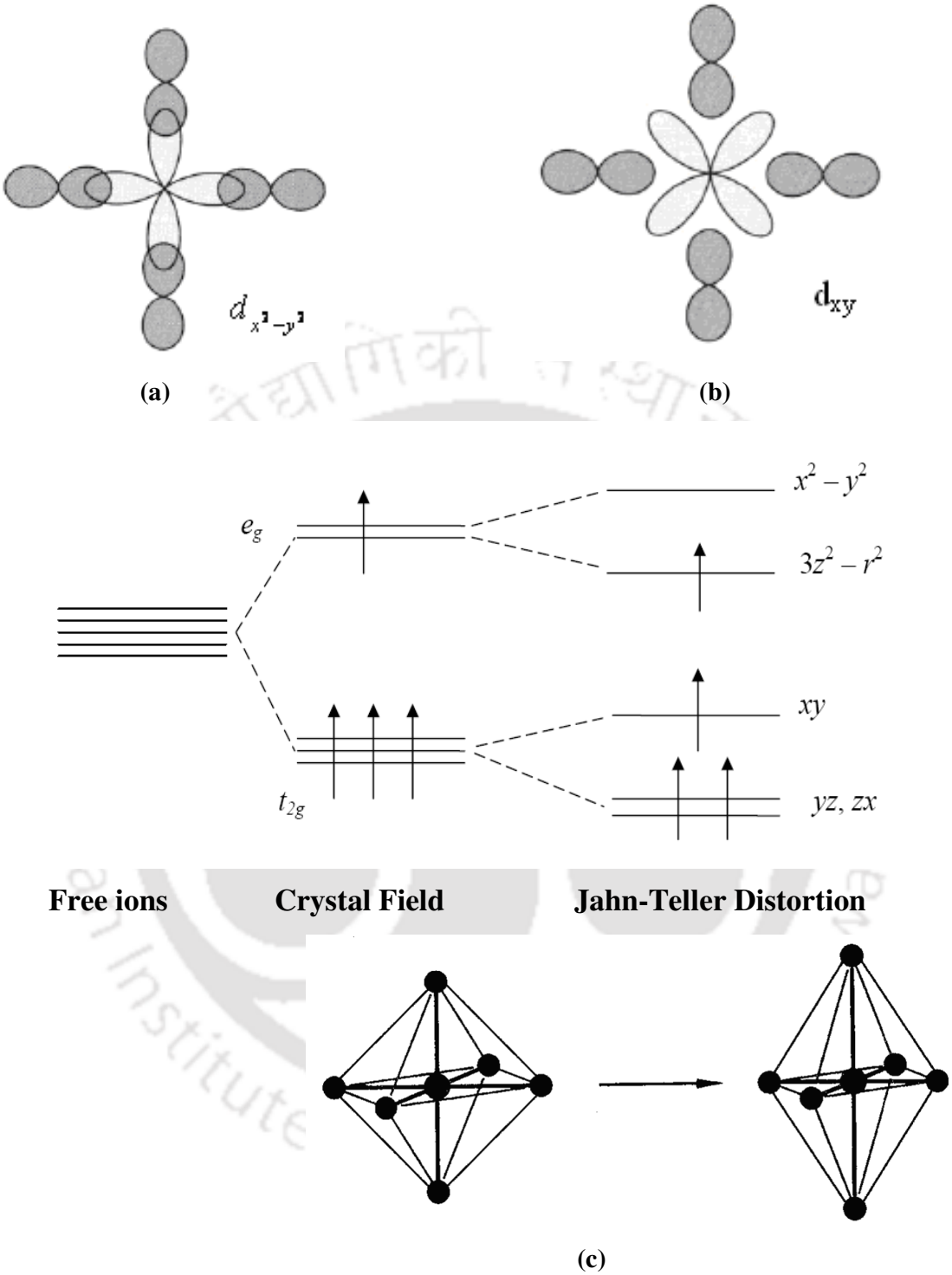

Figure 1.6: (a) Typical overlapping of one of the e_g orbitals ($d_{x^2-y^2}$) with p orbital of neighboring O in a two dimensional diagram (b) One of the t_{2g} orbitals with p orbital (c) The crystal field splitting of d shell in octahedral environment. The Jahn-Teller distortion leads to a further splitting of both the t_{2g} and e_g states.

TH-1060_06612103

The Mn-O bonds are primarily responsible for the electrical conduction through Mn-O-Mn networks and the long range ferromagnetic (FM) double exchange interaction. Two types of JT distortion are usually observed in manganites, namely Q_2 mode and Q_3 mode. In Q_2 mode, the effective distortion is in the basal plane of MnO_6 octahedra, where the diagonally opposite O pairs move outwards and the other pairs move inward. However, in Q_3 mode, there is contraction of four O atoms in basal plane and elongation of two O atoms away from basal plane in MnO_6 octahedra. Hence, the presence of JT distortion increases the Mn-O bond length along z-direction and reduces the overlap of electronic orbitals and which in turn gives rise to reduction in long range DE interaction.

1.3. Exchange Interactions

The lattice structure of MnO_6 octahedra in perovskite manganites plays a major role in magnetic exchange interaction. In parent compounds, with mostly Mn^{3+} ions, the e_g state electrons tend to localize leading to Mott insulative behavior. However, the e_g electrons become itinerant upon hole doping, i.e., in the presence of electron vacancies. Thus, the hole doping gives rise to oxidation of some of Mn^{3+} ions into Mn^{4+} state. Unlike e_g electrons, the t_{2g} electrons are less hybridized with O-*2p* orbitals and they are stabilized just by crystal field splitting. Thus, the t_{2g} electrons are localized with a local spin S = 3/2, even in the metallic state. There is a strong Hund's coupling between the e_g conduction electron spin (S = ½) and the t_{2g} localized electron spins (S = 3/2). The Hund's coupling energy J_H is as large as 2 to 3 eV for the manganites and exceeds the intersite hopping interaction t_{ij}^0 of the e_g electrons between the neighboring sites, *i* and *j*. According to Anderson-Hasegawa [37], in the case of a strong coupling limit, i.e., with $J_H/t_{ij} \rightarrow \infty$, the effective hopping interaction t_{ij} can be written as,

$$t_{ij} = t_{ij}^0[\cos(\theta_i/2)\cos(\theta_j/2) + \exp[i(\phi_i - \phi_j)]\sin(\theta_i/2)\sin(\theta_j/2)] \quad \text{---------- (1.1)}$$

where, the core spins are treated as purely classical object and described by unit vectors θ_i, ϕ_i and θ_j, ϕ_j at sites *i* and *j* respectively. Here θ and ϕ are polar and azimuthal angles. By neglecting the Berry phase term exp *{(i(ϕ_i - ϕ_j)}*, one can get,

$$t_{ij} = t_{ij}^0 \cos(\theta_{ij}/2) \quad \text{---------- (1.2)}$$

So, the absolute magnitude of the effective hopping depends upon the relative angle θ_{ij} between the neighboring spins. The ferromagnetic interaction through the exchange of

TH-1060_06612103

conduction electron, such that it exhibits on-site Hund's coupling with the spin of the local electrons is called double-exchange interaction and is discussed in detail in the next section. The ferromagnetic metallic state is stabilized by maximizing the kinetic energy of the conduction electrons ($\theta_{ij} = 0$). When temperature is raised to T_C, the configuration of the spin is dynamically disordered and accordingly the effective hopping interaction is also subjected to disorder and, the average hopping interaction is reduced. This leads to the enhancement of the resistivity in the vicinity of T_C. Therefore, large magnetoresistance (MR) can be expected around T_C, since the local spins can be aligned easily by application of an external magnetic field and it reduces the randomness of the e_g electrons. It was the initial explanation for CMR behavior. However, the physics of the CMR behavior is found to be more complex.

1.3.1. Double Exchange Interaction

Double exchange (DE) interaction is one kind of indirect magnetic exchange interaction between *3d* electrons of transition elements through a non-magnetic ion such as oxygen. This was described by Zener in 1951 and is known as Zener double exchange interaction [20, 38]. Here the hopping of itinerant electrons from the *3d* shell of one ion to another ion is possible only if their core *3d* electrons are aligned parallel to each other. Zener showed that the above ferromagnetic interactions are energetically favored only in the presence of conduction electrons. The exchange between Mn^{3+} and Mn^{4+} ions via an oxygen ion, as per Zener DE interaction, i.e., simultaneous transfer of an electron from Mn^{3+} to O^{2-} and from O^{2-} to Mn^{4+} ions is shown in figure 1.7. Two simultaneous electron transfers are involved in this process, and so it is called double exchange (DE) interaction. The hopping of electron can be shown as, $Mn^{3+}_{1\uparrow} O_{2\uparrow,3\downarrow} Mn^{4+} \rightarrow Mn^{4+} O_{1\uparrow,3\downarrow} Mn^{3+}_{2\uparrow}$, where the electron spins are labeled as 1, 2 and 3. Anderson and Hasegawa [37] presented the DE mechanism in detail by visualizing a second order process, in which, the electron transfer takes as follows $Mn^{3+}_{1\uparrow} O_{2\uparrow,3\downarrow} Mn^{4+} \rightarrow Mn^{3+}_{1\uparrow} O_{3\downarrow} Mn^{3+}_{2\uparrow} \rightarrow Mn^{4+} O_{1\uparrow,3\downarrow} Mn^{3+}_{2\uparrow}$. The effective hopping integral for the electron to move from one Mn site to another Mn site is proportional to the square of the hoping integral between p-oxygen and d-manganese orbitals. If the localized spins (t_{2g}, S = 3/2) are considered as classical objects and if they are canted with an angle θ between the nearest neighbor spins, the effective hopping integral would be proportional to $cos(\theta/2)$. The probability of transfer of electrons varies from 1 for $\theta = 0$ to zero for $\theta = 180°$. Later on, de Gennes [39] explained the DE interaction in the presence of antiferromagnetic background

TH-1060_06612103

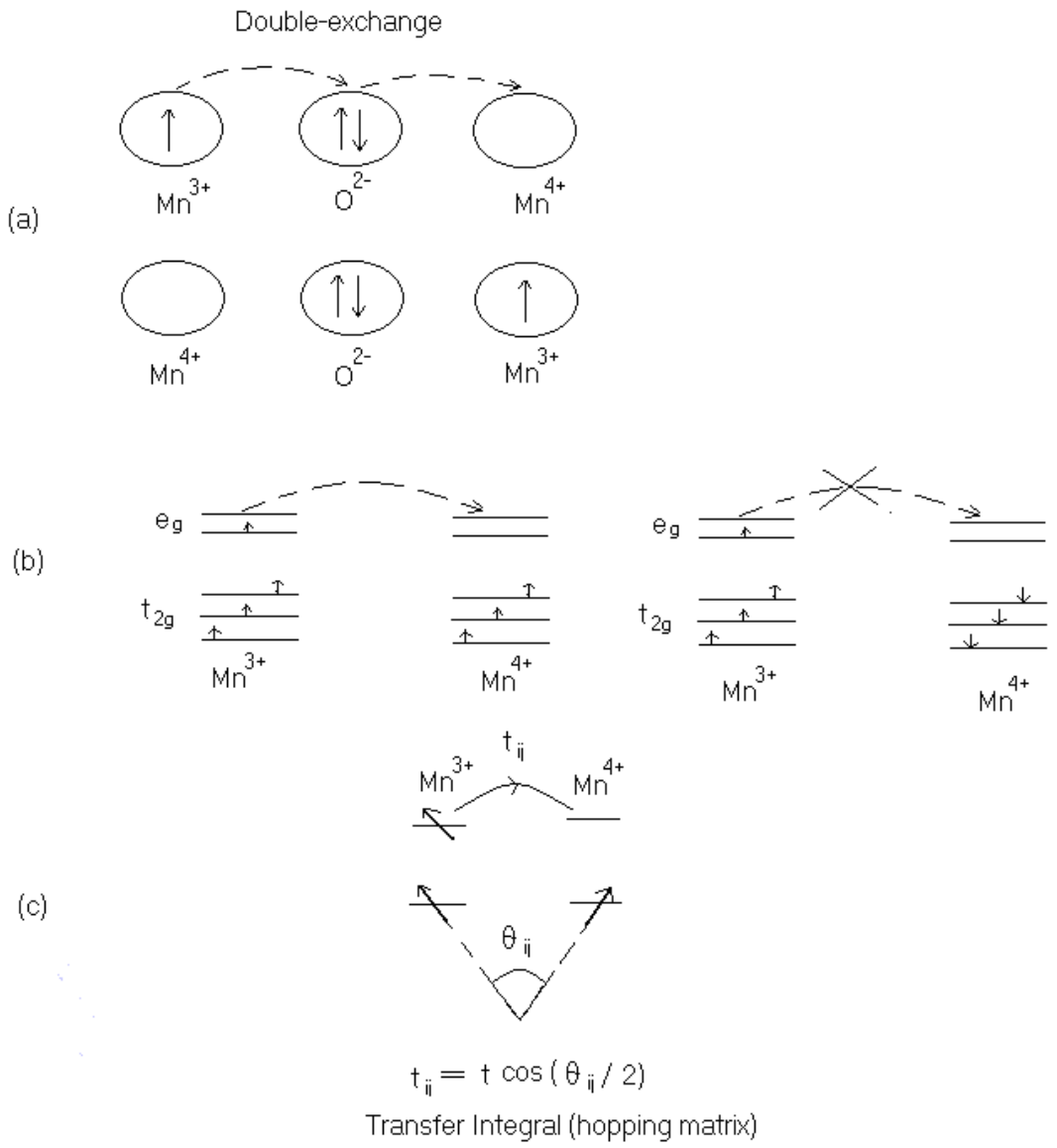

Figure 1.7: (a) Sketch of the double exchange mechanism which involves two Mn ions and one O ion. (b) The mobility of e_g electrons improves if the localized spins are polarized. The transfer integral is shown in the figure (c).

with the help of mean-field type description. He predicted that the manganites with low level of doping would be a mixture FM & AFM states leading to spin canted state. However, the recent studies have shown that the origin of spin canted state is due to the tendency of magnetic phase separation [6, 40-43]. In addition to the DE interaction, other interactions such as, the electron-lattice interaction, antiferromagnetic superexchange interaction between the t_{2g} local spins, inter-site Coulomb repulsion among e_g electrons, phase separation scenario etc. have to be taken into account.

TH-1060_06612103

1.3.2. Superexchange Interaction

Goodenough [21] and Kanamori [44] pointed out that ferromagnetic and anti-ferromagnetic interactions are possible by a mechanism called superexchange (SE) interactions. In this case, the two magnetic ions interact through an intermediate non-

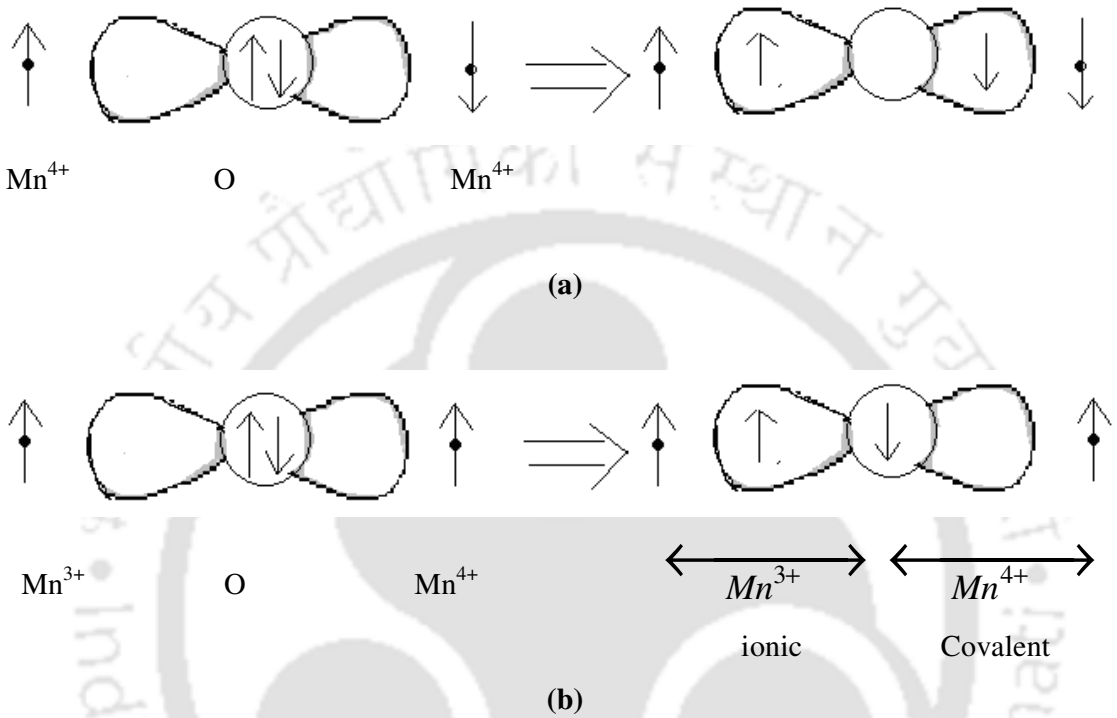

Figure 1.8: Schematic diagram showing the arrangement of spins and orbitals in (a) anti-ferromagnetic super-exchange interaction (b) Ferromagnetic super-exchange interaction.

magnetic ion. This is a common interaction in the insulating magnetic oxides, where the intermediate ion is O^{2-}. This interaction mechanism is explained as follows.

For example consider two Mn^{4+} ions with an intermediate O ion. Figure 1.8 (a) shows the situation, where the unoccupied *3d* orbitals of Mn^{4+} ions are pointing towards O-*2p* orbital. Due to this overlapping, the two spins of O-*2p* with opposite spins are likely to spend some time, on the unoccupied *3d*-orbitals and thus, there is a simultaneous bond formation of the anion (O) with the cations (Mn^{4+}) on both sides. If the spins of the cations are anti-parallel, the positive spin of O-*2p* orbital forms the partial bond with the cation having positive spins and the negative spin of O-*2p* orbital forms the bond with the other cation having negative spin. So, there is a FM coupling between the electron of the anion and the

TH-1060_06612103

cation and this process leads to net anti-ferromagnetic interaction between cations as shown in figure 1.8 (a). Similar superexchange interaction is possible between two Mn^{3+} ions separated by O [21]. The above type of bond formation cannot occur if the spins of the cations are parallel.

According to Goodenough [21], the SE interaction in Mn-O-Mn networks can be also ferromagnetic, if one of the Mn-O bonds is covalent, while the other Mn-O bond is ionic. Below the Curie temperature, the covalent bond becomes semi-covalence (bonding occurs between parallel spins) and the O^{2-} ion is left out with a single electron, since the other electron is associated with Mn ion in covalence bonding. There is a direct exchange interaction (AFM) between magnetic moment of anion (due to its isolate electron) and that of other Mn ion, which is ionically bound to it. Thus, two Mn ions are coupled FM as shown in figure 1.8 (b).

Thus, according to Goodenough, the SE interactions in Mn^{3+}-O^{2-}-Mn^{3+} and Mn^{4+}-O^{2-}-Mn^{4+} networks are AFM in nature, while the Mn^{3+}-O^{2-}-Mn^{4+} networks is FM. The above SE interaction mainly leads to electrically insulating behavior.

1.4. Electron-Phonon Coupling in Manganites

The DE interaction could not completely explain the transport properties of manganites. The limitations are mainly in explaining the, magnitude of CMR effect, underestimated values of resistivity in the PM region, existence of charge ordering, AFM and magnetic phase separation scenario. Millis *et al.* [22] presented that the strong electron-phonon coupling due to the dynamic Jahn-Teller distortion along with localization of charge carriers and Hund's coupling is responsible for the above limitations. In manganites, the Jahn-Teller active Mn^{3+} ions induce the local lattice distortion. It breaks the cubic symmetry of the crystal structure by distorting MnO_6 octahedra. The above distortion leads to the lifting of degeneracy of e_g orbitals. The lower lying e_g electron of Mn^{3+} ion moves through the crystal and polarizes the crystal. The lattice distortion follows the path of e_g carrier, thus one can speaks of a cloud of phonons accompanying the electron. The local lattice distortion creates a potential well, which hinders the movement of e_g carriers and thus decreasing its mobility. Therefore electron and the accompanying self consistent polarization field can move in the crystal as a whole entity and may be considered as a quasi-particle, called a lattice Polaron or Jahn-Teller Polaron. This transport of lattice and spin distortions is also called magnetic Polaron. Localization of charge carriers due to Jahn-Teller coupling have been observed around and

TH-1060_06612103

above T_C [45-50]. This leads to the observed activated behavior in the paramagnetic phase. Below T_C, the self trapping of e_g carriers disappears due to the enhanced double exchange interaction, which in turn leads to the relaxation of lattice and enhance the conductivity. The static coherent MnO_6 distortion from neutron diffraction measurements was reported by Radaelli *et al.* [51] in $R_{1-x}A_xMnO_3$ (R = La, Pr and A = Ca, Sr) series and it indicates the localization of e_g electrons above T_C and it leads to insulating behavior.

1.5. Magnetic Structure

The magnetic structure refers to the ordered arrangement of magnetic spins associated with each atom in a magnetic unit cell. The volume of magnetic unit cell can be different from that of crystal unit cell. The three dimensional magnetic structure, orientation of magnetic dipole with respect to crystallographic direction and its magnitude associated with each magnetic ion are best obtained from the measurement and analysis of neutron powder diffraction (NPD) patterns. The neutron beams in NPD experiment are not only scattered by the atoms present at the lattice site but also by the magnetic moment of each atom. So, distinct NPD peaks or increase in intensities of Bragg's reflections are seen especially below the magnetic ordering temperature. The magnetic structure of rare earth manganites falls into different categories depending on the nature and the level of A site (Rare earth site) doping [17].

A-type structure gives rise to a net AFM interaction, where magnetic spins are aligned parallel in each (001) plane but with spins in alternate planes aligned in opposite orientation. So, basically, there is an AFM interaction between the planes. The parent compound, $LaMnO_3$ exhibits A- type structure. In a three dimensional network of magnetic ions, each ion has six nearest neighboring magnetic ions and out of them four are ferromagnetically coupled and two are antiferromagnetically coupled as shown in figure 1.9 (a). B-type structure is a ferromagnetic one, where all the six nearest magnetic ions are coupled ferromagnetically and is shown in figure 1.9 (b). In C-type structure, the atoms in (101) and $(\bar{1}10)$ planes are ferromagnetically aligned. Each atom has two ferro and four antiferromagnetic nearest neighbours such that there is a net antiferromagnetic unit cell.

In G-type structure each ion is coupled antiferromagnetically to all six nearest neighbours. Hence the atoms of up and down spins are arranged periodically. Similarly, the other types of magnetic structures, D, E and F along with relative number of FM and AFM bonds are (2, 4), (2, 4) and (3, 3) respectively. Some of the materials follow a structure, which is a result of coupling of two types of magnetic structures. One such example is CE-

TH-1060_06612103

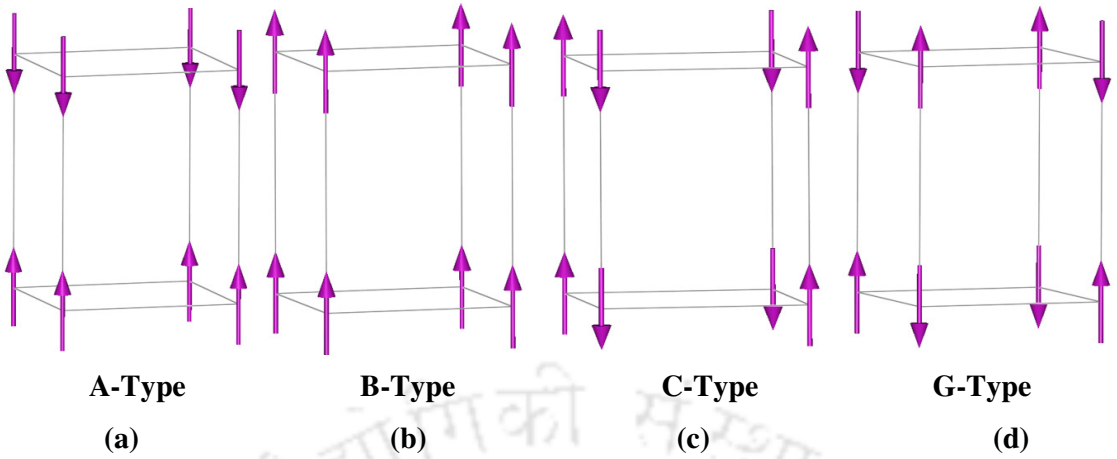

Figure 1.9: Magnetic structures and their arrangements.

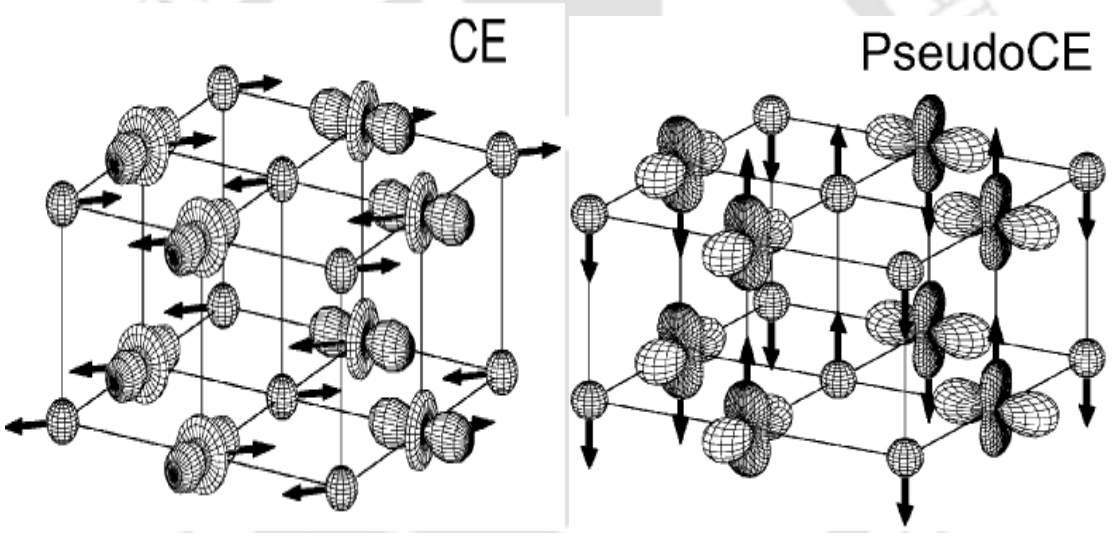

Figure 1.10: Charge and orbital ordering and magnetic spin arrangement in CE and Pseudo CE-type AFM phases. (Reproduced from Jirak *et al.* [52])

type, where there is a coherent stacking of octants of C and E type structures. The charge ordered (CO) manganites, for example $La_{0.5}Ca_{0.5}MnO_3$ [17] exhibits such CE type AFM structure as shown in figure 1.10. However, the other monovalent doped CO manganite, $Pr_{0.8}Na_{0.2}MnO_3$ [52] exhibits Pseudo-CE-type AFM structure. Despite the different orientation of spins, the AFM arrangement with in the plane is the same for both CE-type and Pseudo-CE-type phases. However, the coupling between the planes is AFM and FM respectively.

TH-1060_06612103

1.6. Charge and Orbital Ordering in Manganites

Charge ordering is a fascinating phenomenon and it is found to occur in transition metal oxides. Here the electrons become localized due to the ordering of cations on specific lattice sites depending upon their valence states. This phenomenon of charge ordering along with a resistivity anomaly is well known in Fe_3O_4, and is called Vervey transition [53]. The charge ordering in rare earth manganites was first discovered by Wollan and Koehler [17] and the qualitative theoretical work was presented by Goodenough [21]. Wollan and Koehler studied the magnetic structure of $La_{1-x}Ca_xMnO_3$ compounds for different x values by recording neutron diffraction patterns. They have found charge exchange (CE) type antiferromagnetic structure for x = 0.5 sample, where the magnetic spins of Mn^{3+} and Mn^{4+} ions in 1:1 ratio are ordered in a-b plane as shown in figure 1.11. The $Mn^{3+}$and Mn^{4+} ions are regularly arranged at alternative sites, such that they form a zigzag chain of Mn^{3+} and Mn^{4+} ions. The intra-chain magnetic moment of Mn^{3+} or Mn^{4+} ions are ordered ferromagnetically, while all the neighboring chains are ordered antiferromagnetically in *ab*-plane. The same is true along c-axis but, the inter planner coupling between the *ab*-plane is antiferromagnetic. The three dimensional charge, orbital, and spin ordering in CE-type AFM structure are shown in figure 1.10. Here Mn^{3+} sublattices are shown as e_g electron density distribution and Mn^{4+} sublattices are shown as spheres. This ordering is possible because of migration of e_g electrons from Mn^{3+} to Mn^{4+} at the CO transition temperature, T_{CO}. This ordering is also facilitated by lattice distortion to keep the net electro-static and elastic energy minimum and they dominate over the electronic energy.

In charge-ordered state, the charge carrier localization and ordering is particularly strong in half-doped manganites, due to the relatively enhanced electron/hole-lattice coupling. Eventually, the coulomb interaction wins over the kinetic energy of the electrons to form long range CO state. The energy scale of CO is around 0.5-1eV. This is comparable to the unscreened bare nearest neighbour coulomb repulsion. In addition to the CO, due to the orbital degree of freedom of the e_g electrons in Mn^{3+} ions, they undergo orbital ordering such that electronic energy is lowered.

The first evidence of charge ordering by electron diffraction was observed by Ramirez *et al.* [54] and Chen *et al.* [55] on (La, Ca)-Mn-O series. The electron-diffraction pattern of $La_{0.5}Ca_{0.5}MnO_3$ compound, was found to show a quasi-commensurate satellite reflections with a modulation wave vector q = $2\pi/a$ (½ - ε, 0, 0) below T_N as shown in figure 1.12. The CO behavior in $Pr_{1-x}Ca_xMnO_3$ system was studied by Jirak *et al.* [56] from neutron powder

TH-1060_06612103

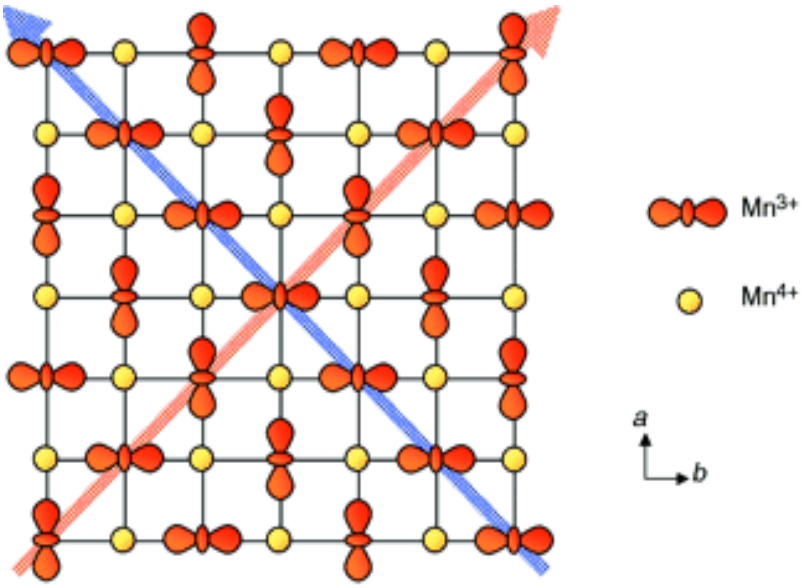

Figure 1.11: The charge and orbital ordering of Mn^{3+} and Mn^{4+} ions in the a-b plane.

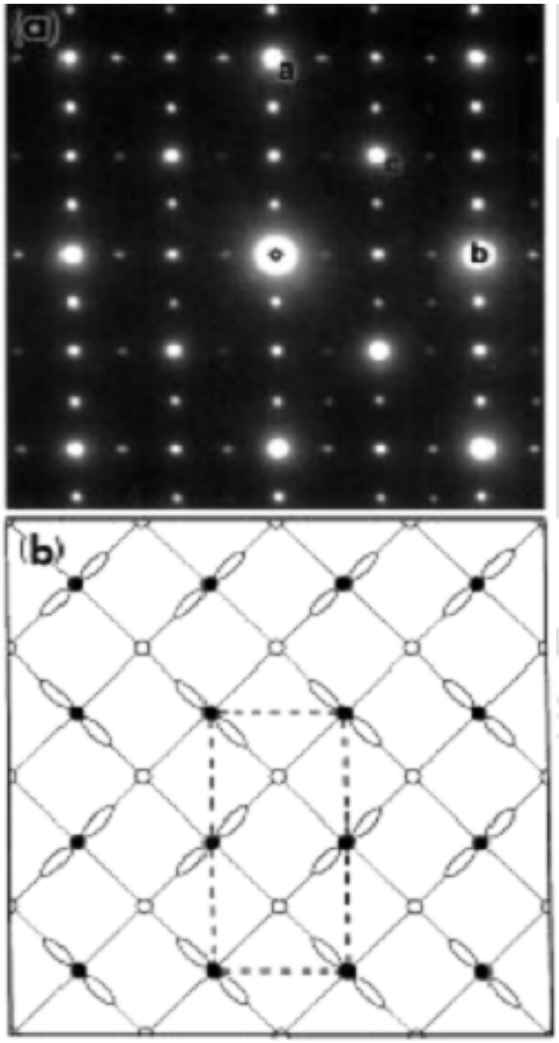

Figure 1.12: (a) [001] zone-axis electron diffraction pattern of $La_{0.5}Ca_{0.5}MnO_3$ at 95K. The fundamental Bragg peaks labeled *a*, *b* and *c* can be indexed as (200), (020) and (110), respectively. The presence of superlattice spots with modulation wave vector (1/2,0,0) or (0,1/2, 0) is evident. (b) Schematic charge ordering picture of Mn^{3+} and Mn^{4+} ions. Open and closed circles represent Mn^{4+} and Mn^{3+} ions, respectively. (Reproduced from Chen *et al.* [55])

TH-1060_06612103

diffraction measurements. They found a superstructure corresponding to double the orthorhombic unit cell along (0 1 0) direction for x = 0.5. Knizek *et al.* [57] reported that $Pr_{0.5}Sr_{0.5}MnO_3$ exhibits A-type antiferromagnetic insulating ground state below 160 K. However, the $Pr_{0.7}Ca_{0.3}MnO_3$ exhibits CE-type antiferromagnetic structure. It has been also reported that the 1:1 ratio of Mn^{3+} and Mn^{4+} ions were not required for CO. In $Nd_{0.5}Sr_{0.5}MnO_3$, Kawano *et al.* [58] reported CE-type AFM structure similar to the case of $La_{0.5}Ca_{0.5}MnO_3$ with T_{CO} = 160 K.

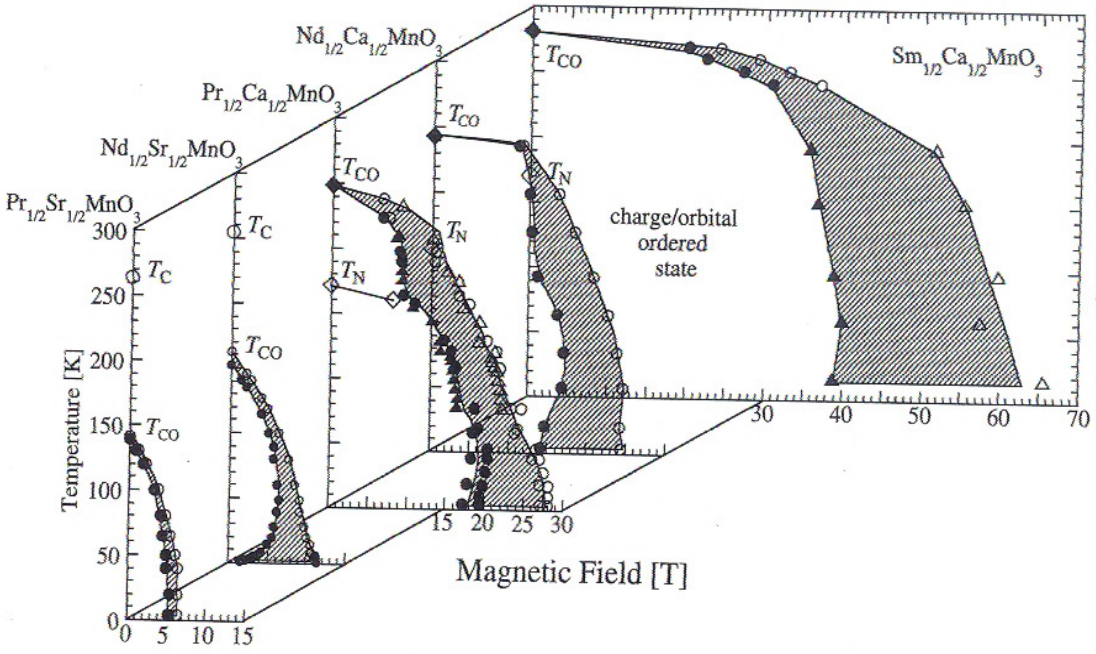

Figure 1.13: The charge/orbital ordered phase of various $R_{1/2}A_{1/2}MnO_3$ (R = rare earth Pr, Nd, Sm, and A = Alkaline earth Ca, Sr) compounds plotted in magnetic field-temperature plane. (Reproduced from Y. Tokura [5])

The CO state can be melted into a metallic ferromagnetic state, by the application of external magnetic field [59-62], pressure [63], exposure to x-ray photons [64], electric field [65] and laser pulses in visible-IR spectrum [66]. The transition from AFM insulating state in the absence of magnetic field, H to FM metallic state in the presence of H is nothing but a first order insulator to metal transition induced by the applied magnetic field [59, 67]. The above effect is generally accompanied by considerable hysteresis [54]. Rao *et al.* [68] studied the effect of $<r_A>$ value on CO properties and concluded that the T_{CO} increases with decrease

TH-1060_06612103

$\langle r_A \rangle$. The reductions of $\langle r_A \rangle$ in rare earth manganites, leads to decrease in one electron band width (W) and it stabilizes CO/OO. The H-T phase diagrams of various $R_{1/2}A_{1/2}MnO_3$ (R = rare earth Pr, Nd, Sm, and A = Alkaline earth Ca, Sr) compounds are reproduced in figure 1.13. The phase boundaries have been mostly determined from the ρ vs. H and M vs. H measurements at fixed temperatures [69]. The critical field required to suppress the CO in $Nd_{1/2}Sr_{1/2}MnO_3$ compound was reported to be 11 T at 4.2 K, while that of $Pr_{1/2}Ca_{1/2}MnO_3$ was found to be 27 T. In the case of $Sm_{1/2}Ca_{1/2}MnO_3$ compound, the CO is so robust such that, the required critical field is as high as about 50 T at 4.2 K. Tokunaga *et al.* [70] have mapped phase diagram of $Pr_{1-x}Ca_xMnO_3$ and $Nd_{1-x}Ca_xMnO_3$ compounds and reported the suppression of CO and the introduction of metallic behavior. The required threshold fields for such first order metamagnetic transition were found to increase with decrease in temperature. Thus, the CO plays a very important role in shaping the structural, electrical and magnetic properties of manganites.

1.7. Spin Glass and Magnetic Frustrations

A frustrated magnetic system due to competing magnetic interactions undergoes a transition from disordered spin state to metastable frozen disordered state below a spin glass transition temperature T_g [71-75]. The frozen disordered state is known as spin glass. Here each spin is under the competing magnetic interactions with the nearest or next nearest ions. The spins can not find a ground state by simultaneously minimizing their energy with each neighboring spins, so they are frozen in a metastable random direction to minimize the total energy. Unlike the other phase transitions, where a system undergoes transition from disordered to ordered state, here the system undergoes transition from one disordered state to another disordered state. The debate was, whether it is really a thermodynamic phase transition. More or less, it is agreed that spin glass is a phase transition because the high temperature disorder is due to random thermal fluctuations without any interaction between magnetic spins. On the other hand, the low temperature frozen disordered state is due to long range magnetic interaction of opposite signs. It is explained as following.

Conventional spin glass materials are basically the transition element doped metallic alloys known as diluted magnetic alloys, namely CuMn, AgMn, AuFe, etc. [71, 72] and references therein. Typical spin glass transition observed in CuMn alloy from ac susceptibility measurement is shown in figure 1.14, where one can see a sharp cusp. The interesting feature of the transition is its frequency dependence due to the relaxation

TH-1060_06612103

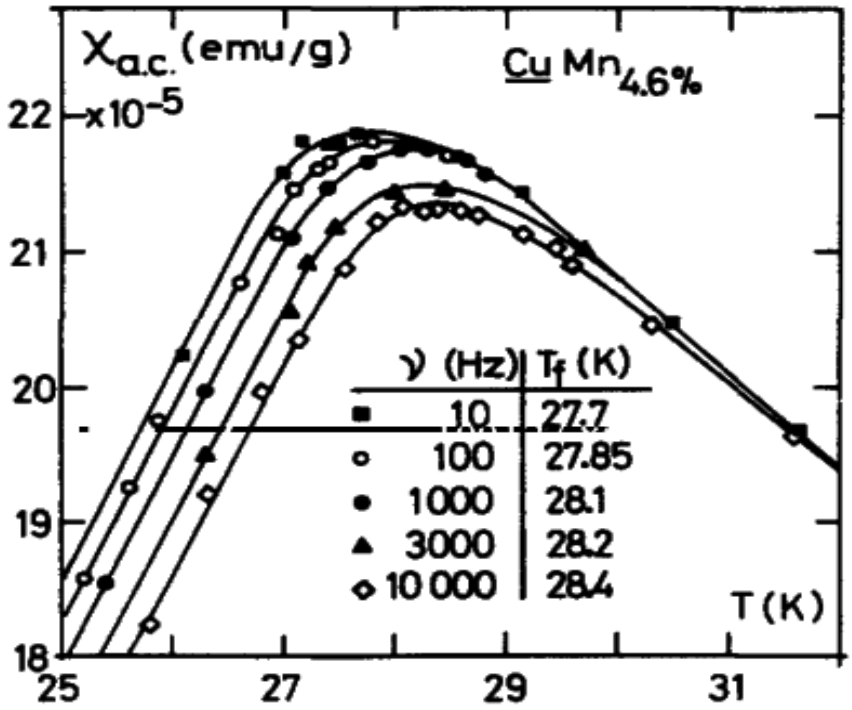

Figure 1.14: Spin glass transition observed in CuMn (with 4.6 at. % Mn) alloys from frequency variation of ac susceptibility measurement (Reproduced from Tholence *et al.* [76]).

behavior of frozen spins. The dc susceptibility of conventional spin glass materials exhibit bifurcation of zero field cooled (ZFC) and field cooled (FC) curves at T_f as reported by Nagata *et al.* [77]. The frequency dependence of T_f was analyzed in terms of various empirical relations [75, 78]**.** According to Arrhenius law, for thermal activation,

$$\tau = \tau_0 \exp\left(\frac{E_a}{kT}\right) \qquad \text{---------- (1.3)}$$

where, $\tau = \frac{1}{f}$ is the *relaxation* time corresponding to the driving frequency in ac susceptibility measurement. τ_0 is a characteristic time constant (the spin flipping time constant) and E_a is thermal activation energy. However the analysis using the above relation was found to yield unphysical values. Another relation used in the literature is Vogel-Fulcher law [72],

$$\tau = \tau_0 \exp\left[\frac{E_a}{k_B\left(T_f - T_0\right)}\right] \qquad \text{----------(1.4)}$$

where, T_0 is a characteristic temperature. Vogel-Fulcher model is found to explain the

TH-1060_06612103

frequency dependence of T_f for number of conventional spin glass system [72-74, 76, 79, 80]. However, the physical meaning of T_0 could not be understood.

The third approach originates from conventional scaling theory near phase transition, where the relaxation time τ is related to correlation length ξ as, $\tau \sim \xi^{z}$. The correlation length diverges with temperature as, $\xi \sim \left(\frac{T_f - T_g}{T_f}\right)^{-\upsilon}$, where T_g is the spin glass transition temperature. So we have the power law relation [81],

$$\tau = \tau_0 \left(\frac{T_f - T_g}{T_f}\right)^{-z\upsilon} \quad \text{---------- (1.5)}$$

The experimental data on several conventional spin glass materials were analyzed based on the above power law relation and the parameters τ_0, T_g, $z\upsilon$ were found to be reasonable [74].

Another important parameter in studying the spin glass transition is non-linear susceptibility χ_{nl}. The magnetization in spin glass system can be expressed in odd power of the magnetizing field, H,

i.e., $$M = \chi_1 H + \chi_3 H^3 + \chi_5 H^5 + \ldots \quad \text{---------- (1.6)}$$

Here, even powers of H are ignored because of inversion symmetry of magnetization of spin glass materials [72, 82]. If a phase transition occurs at T_g, the linear susceptibility term χ_1 is non-divergent, whereas higher order term diverges in the critical region. So the nonlinear susceptibility χ_{nl} diverges at the transition [82-84].

$$\chi_{nl} = \chi_1 - \frac{M}{H} \quad \text{---------- (1.7)}$$

Similarly ac susceptibility technique with ac field amplitude h at a frequency ω can be used for studying the non-linear susceptibility and the magnetization expression is given as follows,

$$M(\omega) = \sum_{k=odd} M_k' \cos k\omega t + M_k'' \sin k\omega t \quad \text{---------- (1.8)}$$

Where, $$M_1' = \chi_1' h + \frac{3}{4}\chi_3' h^3 + \frac{5}{8}\chi_5' h^5 + \ldots \quad \text{---------- (1.9)}$$

$$M_3' = \tfrac{1}{4}\chi_3' h^3 + \tfrac{5}{16}\chi_5' h^5 \quad \text{---------- (1.10)}$$

$$M_5' = \frac{1}{16}\chi_5' h^5 + \ldots \quad \text{---------- (1.11)}$$

Here the experimentally measured fundamental susceptibility is

TH-1060_06612103

$$\chi'_{1e} = \chi'_1 + \frac{3}{4}\chi'_3 h^2 + \frac{5}{8}\chi'_5 h^4 + \ldots \quad \text{---------- (1.12)}$$

Similarly the experimental higher harmonic susceptibility can be equated. For low applied field, the amplitude of third harmonic susceptibility χ_3' diverges as,

$$\chi'_3 \sim \left(\frac{T - T_g}{T_g}\right)^{-\gamma'} \quad \text{---------- (1.13)}$$

where, γ' is the critical exponent. In conventional spin glass system such as AgMn and PdMn, the values of γ' are reported to be 2.3 and 2.2 respectively [85, 86]. On the other hand, it is reported to be 3.2 ± 0.2 in $Ni_{77}Mn_{23}$ ferromagnetic spin glass system [87].

The aging behavior is the general characteristics of spin glass system and that could be analyzed from the decay of the thermoremanent magnetization (TRM) and the relaxation of zero field cooled magnetization measurements [88]. The aging phenomenon starts, when a magnetic frustrated system is cooled below its spin glass transition temperature (T_g). The system starts to age; from a completely random initial configuration to progressively spin rigidity network and generates a response function *S(t)*, which can be defined as [89],

$$S(t) = \frac{d\left[-M_{TRM}(t,t_w)/_H\right]}{d \ln t} \quad \text{---------- (1.14)}$$

where, M_{TRM} *(t,* t_w*)* is the thermoremanent magnetization at time *t* after cutting the magnetic field to zero and t_w is the waiting time before cutting down the field. Chu *et al.* [90] and Kenning *et al*. [91] have shown that in the spin frozen state, the application of magnetic field reduces the height of the barrier or the depth of the trap. This depth of the trap can be quantified by an amount E_Z, called Zeeman energy, which helps the spins to escape towards a region of more favorable magnetization [88]. The time corresponding to peak in *S(t)* function is defined as the effective time, t_{eff} and is given by $ln(t_{eff} / t_w) = - E_z / K_B T$ [92]. The Zeeman energy E_Z can be equated to $\sqrt{NH(m\mu_B)}$. Here *N* is the number of spins which are effectively blocked together and $m\mu_B$ is the effective moment of one spin entity. Joh *et al.* [89] proved experimentally and compared with the simulation results that the inside the barrier the spin correlation length (ξ) is equivalent to $N^{1/3}$.

So far, we discussed about conventional spin glass behavior, where a system undergoes transition from disordered paramagnetic spins to disordered metastable frozen state. On the other hand, in ferromagnets with weak random frustration, the Curie temperature decreases with increase in disorder up to a certain level, and beyond which the

TH-1060_06612103

system exhibits spin glass transition due to strong random frustration. So, the system exhibits paramagnetic to ferromagnetic transition followed by spin glass transition as the temperature is lowered. It is generally referred as re-entrant spin glass (RSG) state, because the system reenters into the disordered (spin glass) state after undergoing disordered (paramagnetic)-ordered (ferromagnetic) phase transition. The insulating Heisenberg ferromagnetic system, $Sr_{1-x}Eu_xS$ [93, 94] and several perovskite rare earth manganites fall under this category [95-100].

In certain level of doping, SG behavior with random canting of magnetic spins were observed in $La_{(2-x)/3}Ba_{(1+x)/3}Mn_{1-x}Cu_xO_3$ [95]. Here, as a result of competing interaction between FM ordering with AFM interactions, the spins are frozen in random direction below certain temperatures and it results in sharp fall in susceptibility or magnetization such that their values are quite low. Three dimensional X-Y spin glass was found in high quality single crystal of $Eu_{0.5}Sr_{1.5}MnO_4$, with a finite phase transition at T_g = 18 K [101]. Nair *et al.* [102] have determined the critical exponent and correlation length values of $Eu_{0.5}Ba_{0.5}MnO_3$ undergoing SG transition, from linear and non linear magnetic susceptibility measurements. The critical exponents were found to be comparable to Ising universality class.

The Mn site doped manganites were also found to exhibit spin-glass behavior [95, 99, 103]. The replacement of about 20% of the Mn in $(La_{0.67}Ca_{0.33})MnO_3$ compound with Cu, results in destruction of ferromagnetic metallic state and the evolution of re-entrant spin glass (RSG) behavior [96]. The RSG behavior has been reported by Dho *et al.* [98] in $(La_{0.46}Sr_{0.54})(Mn_{0.98}Cr_{0.02})O_3$ from the study of frequency variation of ac susceptibility and from the observed bifurcation of dc magnetization in zero field cooling (ZFC) and field cooling (FC) conditions. Several other groups have used frequency variation of ac susceptibility, ZFC and FC dc magnetization and, nonlinear ac susceptibility measurements to study the RSG state [98-100, 104, 105].

1.8. Critical Exponents in Magnetic Transition

The study of critical phenomena in the second order magnetic phase transition, i.e., close to FM T_C in amorphous and crystalline ferromagnets has been the field of interest for a long time to understand the type of magnetic interactions. The famous Landau theory for the second order magnetic phase transition assumed that the Gibb's free energy is a function of the order parameter and temperature dependent coefficients [106]. The Gibb's free energy G

TH-1060_06612103

was written in terms of powers of order parameters. The magnetization M is taken as the order parameter. The expression for G as per Landau theory is given as,

$$G(T,M) = G_0 - MH + aM^2 + bM^4 + \cdots \quad \text{----------(1.15)}$$

Here, the coefficients a and b are temperature dependent parameters. The condition for the minimum free energy in isothermal system, without any external influence can be written as ($\partial G/\partial M = 0$), and it gives rise,

$$\frac{H}{M} = 2a + 4bM^2 \quad \text{----------(1.16)}$$

According to eq. 1.16, a plot of M^2 versus H/M should be a straight line with a positive slope [107]. So, for a second order magnetic phase transition, the plot of M^2 versus H/M is expected to be a straight line, with a positive slope [108]. The spontaneous magnetization, $M_s(0, T)$, the inverse susceptibility, $\chi_0^{-1}(T)$ and the isothermal magnetization at the critical temperature $M(H, T=T_C)$ follow the power law behavior as given below [109],

$$M_S(T) \propto |\varepsilon|^{-\beta} \qquad \varepsilon < 0 \quad \text{----------(1.17)}$$

$$\chi_0^{-1}(T) \propto |\varepsilon|^{\gamma} \qquad \varepsilon > 0 \quad \text{----------(1.18)}$$

$$M(H, T = T_C) \propto H^{\frac{1}{\delta}} \qquad \varepsilon = 0 \quad \text{----------(1.19)}$$

Here β, γ and δ are critical exponents corresponding to M_S, χ_0 and isothermal magnetic magnetization at T_C and $\varepsilon = (T-T_C)/T_C$ is the reduced temperature. According to Arrott and Noakes [110], the mean-field relation (eq.1.16) can be modified for a more general case as given below,

$$\left(\frac{H}{M}\right)^{1/\gamma} = \frac{(T - T_C)}{T_1} + \left(\frac{M}{M_1}\right)^{1/\beta} \quad \text{----------(1.20)}$$

where, T_1 and M_1 are material dependent constants. For the critical exponent values corresponding to the mean-field model, i.e., $\beta = 0.5$ and $\gamma = 1$, eqn. (1.20) reduces to eqn. (1.16).

In the mean-field model (or molecular field model), the magnetic spins interact with one another through a molecular field proportional to the average magnetization. Here, the exchange interaction, J_{ij} between all the spins S_i and S_j is identical and independent of displacement. This model is appropriate, whenever the interaction is in long range. Chamberlin [111] has proposed the mean-field cluster model to explain the existence of long range interaction in different substances.

For high magnetic anisotropic materials, the critical exponents generally follow the Ising model. This model deals with only one component of the spins. In highly anisotropic

TH-1060_06612103

materials, a stronger magnetic coupling is seen in one of the components of spin compared to other two components. The γ value corresponding to three dimensional Ising model is 1.25.

Heisenberg model is an isotropic model, where all components of spins play a equal role in magnetic interactions. The magnetic interaction energy between spins S_i and S_j of atoms present at nearest neighboring positions i and j can be written as $U = -2 J S_i . S_j$, where, J is the exchange integral and is related to the overlap of the charge distributions of the atoms i, j. Such interaction takes place mostly with nearest neighbour magnetic ions and known as short range interaction.

The list of critical exponents γ, β and δ predicted by different theoretical models are given as follows.

3-D Heisenberg model	$\gamma = 1.336$,	$\beta = 0.365$	$\delta = 4.80$
3-D XY model	$\gamma = 1.30$,	$\beta = 0.34$	$\delta = 4.80$
3-D Ising model	$\gamma = 1.241$,	$\beta = 0.325$	$\delta = 4.82$
Mean-field model	$\gamma = 1.00$,	$\beta = 0.50$	$\delta = 3.0$
Tricritical mean-field	$\gamma = 1.00$,	$\beta = 0.25$	$\delta = 5.0$

The above critical exponents are related to each other by the Widom scaling relation [112],

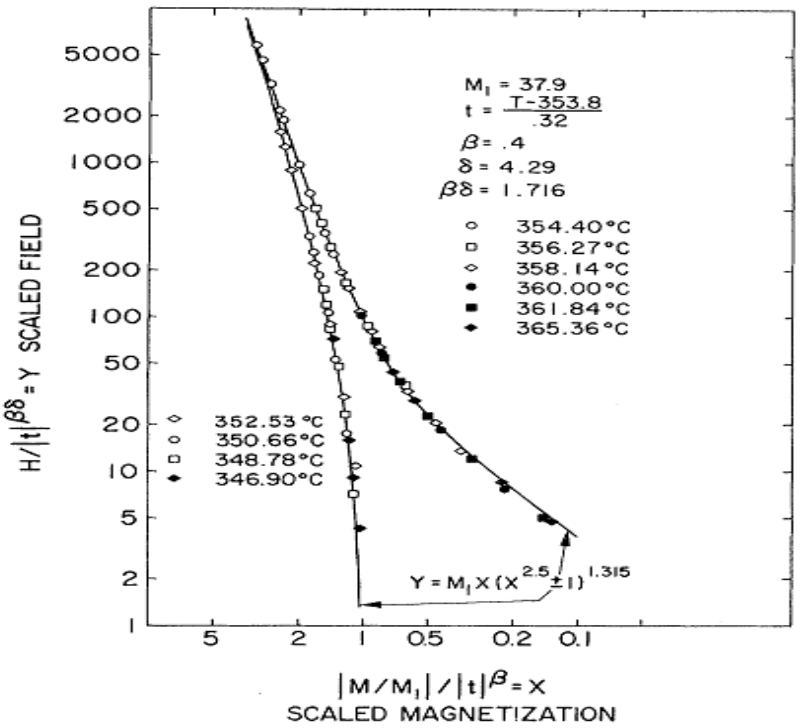

Figure 1.15: Scaling law for nickel sample using the data of Weiss and Forrer. The left side and right side curves correspond to $T < T_C$ and $T > T_C$ respectively. 't' denotes the reduced temperature $\varepsilon = (T - T_C)/T_C$ and M_1 is a constant. (Reproduced from Green *et al.* [113])

TH-1060_06612103

$\delta = 1 + \gamma/\beta$ and follow the static scaling hypothesis. The static scaling hypothesis predicts that $M(H, \varepsilon)$ is an universal function of ε and H as given below,

$$M(H,\varepsilon)|\varepsilon|^{-\beta} = f_{\pm}\left(H|\varepsilon|^{-(\beta+\gamma)}\right) \qquad \text{---------- (1.21)}$$

where, f_+ and f_- are regular analytical functions for $\varepsilon > 0$ and $\varepsilon < 0$, respectively. According to eqn. (1.21), plots of $M(H, \varepsilon)|\varepsilon|^{-\beta}$ versus $H|\varepsilon|^{-(\beta+\gamma)}$ would lead to universal curves, one for temperatures $T > T_C$ $(\varepsilon > 0)$ and the other for $T < T_C$ $(\varepsilon < 0)$. A typical scaling hypothesis plot for Ni sample reported by Green *et al.*[113] from the experimental data of Weiss and Forrer [114] is shown in figure 1.15. They used the exponent values of $\beta = 0.4$, $\gamma = 1.315$ with Curie temperature $T_C = 353.8$ °C.

The study of critical behavior of PM to FM transition in $R_{1-x}A_xMnO_3$ manganites provides important information about the nature of magnetic interaction and its influence on the electrical transport properties. Archibald *et al.* [115] proposed that the transition from the super-exchange FM coupling state with polaronic electron hopping to the DE FM coupling state with extended itinerant electrons behavior should be of first order in nature. It is demonstrated that $La_{0.7}Ca_{0.3}MnO_3$ exhibits such first order transition [116, 117]. On the other hand, a second order magnetic phase transition was observed in (La, Sr)MnO_3 [118-122] and (La,Ba)MnO_3 [123] systems. The reported values of critical exponent in the literature on various perovskite colossal magneto-resistance materials have been found to be disparate with values corresponding to both long range and short range FM interactions. Motome *et al.* [124] estimated the value of β from the Monte-Carlo simulation and predicted that the above class of materials follows three dimensional (3D) Heisenberg model. Lofland et al. [118] and a few other research groups [120, 125] have observed long range interactions in (La, Sr)MnO_3 system, with estimated critical exponent values following the mean-field model. On the other hand, FM transitions in Sr, Ba and Ag substituted La-Mn-O compounds have been shown to follow either 3D Heisenberg [122, 123, 126] or 3D Ising [127] model. Venkatesh *et al.* [128] extracted the critical exponents from magnetization, ac susceptibility, resistivity and specific heat measurements on $Nd_{0.5}Sr_{0.5}MnO_3$ single crystalline sample. They reported that, the exponent values were all between mean-field and 3d-Heisenberg models.

1.9. Electrical Resistivity and Magneto-resistivity

The parent compounds $RMnO_3$ and $AMnO_3$ (R-rare earth, A-alkaline earth) are electrical insulators, where the Mn is in Mn^{3+} and Mn^{4+} state respectively. A solid solution with the general chemical formula $R_{1-x}A_xMnO_3$ exhibits metal to insulator transition for

TH-1060_06612103

certain composition range depending upon the nature of R ion. These materials consist of Mn^{3+} and Mn^{4+} mixture.

The sharpness of the transition often depends on the sample quality. For samples with grain size of the order of 5μm or more, transition is relatively sharp. The temperature dependent resistivity curve can be divided into three regions, namely high temperature (insulating region), low temperature (metallic region) and critical (the intermediate region) regions. Critical behaviors are best described by thermodynamic measurements, which couple directly to the magnetic correlation length. High temperature electrical resistivity data have been explained by Variable Range Hopping model (VRH), Small Polaron Hopping (SPH) model or the simple thermal excitation model [129-133]. The electrical resistivity in the ferromagnetic region has been investigated by several groups. In the region just below T_C, ρ falls rapidly. For $T < 0.5T_C$, typically the variation is less rapid, but it is different from what is generally seen in a metallic ferromagnet. A few attempts have been made to understand the critical region by assuming the existence of both insulating and metallic behavior.

1.9.1. Magneto-Resistance (MR)

Magneto-Resistivity (MR) can be defined as the relative change in the electrical resistivity of a material on the application of an external magnetic field. MR is generally defined by the equation,

$$MR(T) = \frac{\rho(H,T) - \rho(0,T)}{\rho(0,T)} \qquad \text{---------- (1.22)}$$

Here, ρ(H, T) and ρ(0, T) are the electrical resistivity measured in the presence and absence of applied magnetic field.

MR can be a positive or a negative value depending upon increase or decrease in electrical resistivity, by the application of magnetic field. The electrical resistivity in magnetic materials depends on the direction of the applied magnetic field relative to the orientation of the crystal itself [134], a phenomenon known as anisotropic magneto-resistivity. On the other hand, the ordinary magneto-resistivity, which is related to the Hall effect, originates from the impact of the Lorentz-force on moving charge carriers. In absolute numbers, the magnitudes of anisotropic and ordinary magneto-resistivity are moderate and typically not more than a few percentage. All metals show a few percentage of MR and the MR values depend on the strength and the direction of the applied magnetic field [135]. Non-magnetic metals, such as Au, exhibit small MR, but the values in ferromagnetic metals such

TH-1060_06612103

as Fe and Co can be up to 15 %. The semimetal Bi also shows ~ 18% MR in a transverse field of 0.6 T [136]. Half-metallic ferromagnets such as CrO_2 etc. exhibit positive MR and it varies as B^2 (B = applied magnetic field) [137]. In late 1980's, a large negative MR close to about 50% was discovered in multi-layers of magnetic and nonmagnetic metallic materials [134], and it was called giant magneto-resistivity (GMR). Only about half a decade later, it was discovered that doped rare-earth manganese oxides by themselves could possess even higher MR (in some cases close to 100%) [1, 4, 16, 24, 138]. The MR values in manganites were found to be even higher than that of GMR and hence the term colossal [16, 139] was coined to describe the MR of manganites. In magnetic tunnel junctions, there was another type of magneto-resistivity, known as tunneling magneto-resistivity or junction magneto-resistivity [140-142]. The resistivity of a magnetic tunnel junction would be lower for a parallel configuration of magnetization of electrodes. The anisotropic, ordinary and colossal MR can be considered as intrinsic effects of the material, while giant and tunneling MR depend on extrinsic parameters. The MR in perovskite manganites is associated with a crossover from insulating to metallic state, and is accompanied by a magnetic phase transition. The large MR is essentially linked to the presence of an adequate amount of Mn^{4+} (around 33%) ions, which can be introduced by cation substitution or cation deficiency.

1.9.2. Electrical Resistivity in the Metallic Region

The electrical resistivity, ρ in the metallic region, i.e., below the metal-insulator (M-I) transition temperature, where $d\rho/dT > 0$, is analyzed in terms of various empirical relations corresponding to various charge carrier scattering mechanisms. The general empirical relation can be written as:

$$\rho(T) = \rho_0 + \rho_m T^m + \rho_n T^n \qquad \text{---------- (1.23)}$$

Where, ρ_0 is the temperature-independent residual resistivity due to the scattering by impurities, defects, grain boundaries, and domain walls, etc. Here m and n are exponents and their values are generally 2, 2.5, 3, 4.5 or 5 depending upon the nature of scattering mechanism.

In manganites, several groups analyzed and fitted, the resistivity data in the metallic region to the following empirical relation,

$$\rho(T) = \rho_0 + \rho_2 T^2 \qquad \text{---------- (1.24)}$$

The second term with the coefficient ρ_2 is ascribed to the electron–electron [143, 144] or single magnon [4, 5, 145, 146] scattering. Many researchers attributed the T^2 dependence to

TH-1060_06612103

the electron–electron scattering process [143, 144]**.** However, it was later emphasized that the T^2 dependence was due to the appearance of minority spin states that are accessible to thermally excited magnons [4, 5, 145, 146]. It is explained in terms of single-magnon scattering. Jaime *et al.* [145] argued that the T^2 dependence was due to single magnon scattering. They have extended the calculation of Mannari *et al.* [147] for the case, where the minority and majority spin sub-bands differ by a constant energy leading to the T^2 dependence.

The low temperature resistivity of manganites has been calculated separately by Wang and Zhang [148] and by Furukawa [149]. Their calculation of resistivity yields a temperature dependence of $T^{2.5}$ and $T^{1.5}$ above and below 60 K respectively. Schiffer *et al.* [144] could successfully fit the low temperature resistivity of $La_{1-x}Ca_xMnO_3$ (x = 0.20, 0.33 and 0.45) samples to the expression,

$$\rho(T) = \rho_0 + \rho_{2.5}T^{2.5} \qquad \text{---------- (1.25)}$$

The above model predicts a significant magneto-resistivity at low temperature; however Hwang *et al.* [150] have not observed any such magneto-resistance on single crystals and thin films of $La_{2/3}Sr_{1/3}MnO_3$.

Furukawa [149] considered the existence of minority spin states created as a result of spin fluctuations leading to a T^3 temperature dependence of ρ as,

$$\rho(T) = \rho_0 + \rho_3 T^3 \qquad \text{---------- (1.26)}$$

This model could be used to fit the low temperature resistivity of $La_{1-x}Sr_xMnO_3$ (x = 0.2, 0.3, 0.4) to a wider lower temperature range compared to that of T^2 fit.

A $T^{4.5}$ dependence was observed by Snyder *et al*. [151] and this was attributed to double magnon scattering mechanism as calculated by Kubo and Ohata [152]. However, the temperatures involved are too high, at which there would be a substantial density of states of minority spins at the Fermi level and hence single-magnon scattering cannot be ruled out. So, they proposed the expression for resistivity as,

$$\rho(T) = \rho_0 + \rho_2 T^2 + \rho_{4.5}T^{4.5} \qquad \text{---------- (1.27)}$$

Jaime *et al*. [145] have fitted the low temperature resistivity data to the expression,

$$\rho(T) = \rho_0 + \rho_2 T^2 + \rho_5 T^5 \qquad \text{---------- (1.28)}$$

where, the second term with the coefficient ρ_2 is ascribed to single magnon scattering and the third term with T^5 function is attributed to electron-phonon process.

TH-1060_06612103

The above eqn. 1.27 was used by Ravindranath *et al.* [153] to analyze the resistivity data in the metallic regime in $(La_{0.7-x}R_x)Ca_{0.3}MnO_3$, where R = Ho (magnetic) and Y (nonmagnetic).

1.9.3. Electrical Resistivity in the Semiconducting Region

According to Millis *et al.* [22], the existing models based upon DE interaction strongly underestimate the magnitude of resistance change during the M-I transition. The transition from metallic to insulating phase is described as localization of itinerant electrons as per Mott-transition. The charge transport still occurs in the insulating regime, but the carriers are more localized than that of metallic phase. Already de Gennes [39] demonstrated that for small values of x in $R_{1-x}A_xMnO_3$, local distortions of the AFM structure tends to trap the doped charge carriers. Localization of charge carriers will increase their interaction with the surrounding (magnetic) environment and hence a virtual effective mass is added to the hopping electrons. But charge hopping is also related to the lattice distortions as described by the Jahn-Teller effect. This transport of lattice and spin distortions is usually referred as magnetic polarons. Several studies have indicated the charge localization and the formation of small polarons in perovskite manganite materials above T_C [45-48]. If the range of association of charge carriers to crystalline distortion is less than the size of the unit cell, they are called small polarons. In this case, the charge carriers are always found at the lattice site. The temperature variation of resistivity above T_C is mostly found to follow the small polaron model [154], i.e.,

$$\rho = \rho_{sp} T^n \exp\left(\frac{E_{sp}}{k_B T}\right) \qquad \text{---------- (1.29)}$$

Here, E_{sp} is the hopping energy, T is the temperature and k_B is the Boltzmann constant. n = 1 corresponds to adiabatic small polaron hopping and n = 3/2 corresponds to non-adiabatic small polaron hopping. According to adiabatic small polaron hopping, the charge carriers hop more rapidly and each time the carrier hops, the configuration of vibrating atoms in the adjacent site coincides with that of occupied state. In non-adiabatic case the motion of small polaron is quite slow.

The variable-range-hopping (VRH) and non-adiabatic small polaron hopping models were found to explain the experimental data of polycrystalline, thin film an un-annealed sample with oxygen deficiency [129-131]. According to three dimensional Mott variable

TH-1060_06612103

range hopping (Mott-VRH) model, the expression for electrical resistivity can be written as, [132, 133],

$$\rho = \rho_{0m} \exp\left(\frac{T_{0m}}{T}\right)^{1/4} \quad \text{---------- (1.30)}$$

Here, ρ_{0m} is the Mott residual resistivity and T_{0m} is the Mott characteristic temperature. The density of states in the vicinity of Fermi level, $N(E_F)$ and, hopping distance $R_{hop}(T)$ and hopping energy, $E_{hop}(T)$ can be written as,

$$N(E_F) = \frac{18}{k_B T_{0m} a^3} \quad \text{---------- (1.31)}$$

$$R_{hop}(T) = \frac{3}{8} a \left(\frac{T_{0m}}{T}\right)^{1/4} \quad \text{---------- (1.32)}$$

$$E_{hop}(T) = \frac{1}{4} k_B T^{3/4} T_{0m}^{1/4} \quad \text{---------- (1.33)}$$

Here a is the localization length. According to VRH model, the charge carriers hop from one localized to another localized state having overlapping electron wave function. The energy required for such hopping is taken from phonon (lattice vibration). Efros and Skhlovskii (ES) [155] have modified the Mott-VRH model by taking into account the coulomb interaction between the charge carriers and the corresponding resistivity expression is,

$$\rho = \rho_{0s} \exp\left(\frac{T_{0s}}{T}\right)^{1/2} \quad \text{---------- (1.34)}$$

where, ρ_{0s} is the ES residual resistivity and T_{0s}, the ES characteristic temperature is defined as,

$$T_{0s} = \frac{\beta_1 e^2}{k_B a 4\pi\varepsilon_0\varepsilon_r} \quad \text{---------- (1.35)}$$

Here a is the localization length, ε_r is the dielectric constant and β_1 = 2.8 is a numerical constant.

1. 10. La-Mn-O Based Compounds

$La_{1-x}A_xMnO_3$ (A= Ca, Sr Ba and Pb) based colossal magneto-resistivity (CMR) materials are widely studied compared to other rare earth based CMR materials. They exhibit relatively large ferromagnetic (FM) T_C close to room temperature. The $La_{1-x}Ca_xMnO_3$ ($0 < x < 0.50$) series show paramagnetic to ferromagnetic transitions with T_C ranging from 160 to

TH-1060_06612103

272 K [144, 156, 157]. However, metal-insulator (M-I) transitions were observed for 0.20 < x < 0.50 with a maximum T_C for x ≈ 0.33 [158]. The maximum magnetoresistance (MR) was found to be around 80% at T_C ≈ 240K for an applied field of 6 T (60kOe) [159]. At x ≈ 0.50, this compound undergoes paramagnetic to ferromagnetic transition at around 225 K and then to a charge ordered antiferro-magnetic phase at T_{CO} ≈ 155 K [144]. In $La_{1-x}Sr_xMnO_3$ series, Urushibara *et al.* [160] carried out detailed study of electrical and magnetic properties for x = 0 to 0.60. According to them, for x ≥ 0.10, these materials exhibit PM to FM transition with T_C ranging from 145 K for x = 0.10 to 370 K for x = 0.3 and 0.4. They have observed M-I transitions in the vicinity of FM T_C for 0.175 ≤ x ≤ 0.40 with a maximum magneto-resistivity of 90% for 5 T field. In $La_{2/3}Ba_{1/3}MnO_3$, Von Helmolt *et al.* [16] reported M-I transition above room temperature on thin film sample with magneto-resistivity values as high as 60% at room temperature for a field of 5 T. Several authors reported M-I and FM transitions at around 340 to 350 K for the composition close to x = 0.30, in $La_{1-x}Ba_xMnO_3$ [95, 161, 162]. Other than alkaline earth elements, the Pb doped $La_{1-x}Pb_xMnO_3$ compounds are also found to exhibit M-I transition, PM-FM transition and CMR behavior in the vicinity of room temperature [163-167]. The T_{MI} values of polycrystalline $La_{1-x}Pb_xMnO_3$ (0 ≤ x ≤ 0.50) was found to vary from 230 to 275 K [168]. M-I transitions have been also reported in $La_{1-x}Ca_xMnO_3$ compound [169].

Other than the divalent doped materials, several authors have studied monovalent doped La-Mn-O series. Itoh *et al.* [30] were the first one to demonstrate M-I and FM transitions on mono-valent alkali ion doped, $La_{1-x}A_xMnO_3$ (here A= Na, K, Rb, etc.) compounds. According to them, the FM T_C of Na substituted samples varies from 219 to 336 K for 0.04 ≤ x ≤ 0.12. The maximum T_C value of K and Rb substituted compounds are found to be 330 and 234 K respectively. Similar studies have been carried out by many other groups [29, 170-172]. Similar to alkali ions, the Ag doping also falls into the category of mono-valent doping, where each doped element is expected to oxidize two Mn^{3+} ions into Mn^{4+} state. The Ag doping has been studied by a few groups and reported M-I and FM transition in the vicinity of room temperature [32, 34, 173]. The mechanism of electrical resistivity in the presence and absence of magnetic field was studied by Kar *et al.* [34] in the $(La_{1-x}Ag_x)MnO_3$ series. Kar and Ravi have reported that Cu substitution also plays the role of monovalent hole doping with FM and MI transitions [174, 175]. Metal–insulator transition temperature was found to vary from 43 to 92 K for x ≤ 0.10. Paramagnetic to ferromagnetic transitions with a signature of competing AFM interaction have been observed.

TH-1060_06612103

1. 11. Nd-Mn-O Based Compounds

The La-Mn-O series is found to have large e_g electron band width due to its large A site ionic size. On the other hand, Nd-Mn-O series falls in the category of medium size e_g band width and hence the ionic size of doped materials plays a very sensitive and crucial role in tuning the magnetic properties in this system.

$NdMnO_3$

Unlike $LaMnO_3$ series, $NdMnO_3$ exhibits complex behavior due to the presence of two magnetic sublattices, namely Mn and Nd. The perovskite structure of $NdMnO_3$ is orthorhombically distorted due to the tilting of MnO_6 octahedra and it follows *Pnma* space group [176]. In this distorted MnO_6 octahedra, the degeneracy of the e_g orbitals in the $t_{2g}^3 e_g^1$ electron configuration of Mn ions is destroyed due to the cooperative Jahn-Teller distortion**.** A-type AFM has been observed in the parent $NdMnO_3$ compound [177-179]. In $NdMnO_3$, the Mn sub-lattice atoms were found to undergo AFM ordering with Neel temperature $T_N \approx 78$ K and the Nd sub-lattice atoms exhibited a magnetic ordering at $T \approx 13$ K [177]. According to the neutron powder diffraction results of $NdMnO_3$, Wu. *et al.* [178] and Munoz *et al.* [177] reported that there was a spin canting with FM and AFM components. The negative magnetization observed in $NdMnO_{3+\delta}$ was explained in terms of phase separation by Bartolome *et al.* [180, 181] from the neutron powder diffraction (NPD) and x-ray magnetic circular dichroism measurements, and, it was comparable to the two phase model proposed by Troyanchuk *et al.*[182]. The frustration in A-type ordering and decrease in T_N value from 150 K for R = La ion to ~40 K for R = Eu ion was reported due to the decrease in average radius of R ion in $RMnO_3$ [183]. A systematic decrease in T_N value accompanied by a decrease in Mn-O-Mn bond angle has been observed with increase in 'Y' concentration in $Nd_{1-x}Y_xMnO_3$, as per the NPD analysis [184]. The decrease in average radius of the A-site cations ($\langle r_A \rangle$) due to the substitution of Nd^{3+} in $La_{1-x}Nd_xMnO_{3+\delta}$ was found to introduce a structural transition from rhombohedral structure (*R3-c*) for x = 0 to monoclinic phase ($P2_1/c$) for x = 1.0 through orthorhombic structure (*Pnma*) for $0.1 \geq x \leq 0.9$ [185]. The decrease in FM interaction with respect to AFM superexchange interaction for $x > 0.6$ and increase in spin canting angle with increase in Nd concentration at low temperature were reported.

(Nd, Ca)-Mn-O

Troyanchuk *et al.* [186] studied systematically the magnetic properties of $Nd_{1-x}Ca_xMnO_3$ compounds and observed FM transition with T_C around 110 K followed by a broad

TH-1060_06612103

peak at around 72 K. The maximum saturation magnetization was found to be 2.8 μ_B at 5 K for 1 T field. Large difference between zero field cooled (ZFC) and field cooled (FC) magnetization was observed with electrical resistivity following a semi-conducting behavior. Liu *et al.* [187] reported semiconducting behavior of $Nd_{1-x}Ca_xMnO_3$ compounds for x = 0 to 1 and found that they exhibited CO and AFM transition. However, the application of magnetic field was found to induce semiconductor–metal and AFM-FM transitions in the composition range $0.30 \leq x \leq 0.45$. From NPD measurements, a long-range AFM phase of CE-type ordering was observed in $Nd_{0.5}Ca_{0.5}MnO_3$ compound below T_N = 160 K [188]. The CO [189] and its destruction by the application of large magnetic field of around 25 T was reported by Tokunaga *et al.* [70] in $Nd_{0.5}Ca_{0.5}MnO_3$. Cao *et al.* [190] reported CO transition at T_{CO} ~ 240 K and AFM transition at T_N ~ 160 K followed by a low temperature RSG state at around 41 K in $Nd_{0.5}Ca_{0.5}MnO_3$. Troyanchuk *et al.*[182] studied the magnetic properties of $Nd_{1-x}Ca_xMnO_3$ compounds and explained the result in terms of two phase model, where, there is an exchange coupling between antiferromagnetic and ferromagnetic phases for the composition range x = 0.06 to 0.15. The existence of magnetic phase separation between AFM and FM in the lightly doped $Nd_{1-x}Ca_xMnO_{3-\delta}$ was reported by Khomchenko *et al.* [191] from the measurement and analysis of NPD. Here $Nd_{0.92}Ca_{0.08}MnO_{2.98}$ sample was found to consist of 70 % of A-type AFM phase and 30 % FM phase. Nagai *et al.* [192] presented the direct observation of the transverse and sinusoidal structural modulation in charge-orbital ordered manganites $Nd_{1-x}Ca_{1+x}MnO_4$ ($0.55 \leq x \leq 0.75$), by recording the low temperature high-resolution electron microscope images. This observation suggested a charge-orbital density wave of e_g electrons in a single-layered manganites. The destruction of CO and the evolution of FM along with insulator to metal transition were observed in $Nd_{0.5}Ca_{0.5}MnO_3$ by preparing the material in nano-phase form [193].

(Nd, Sr)-Mn-O

First of all Caignaert *et al.* [194] reported magnetic and transport properties on $Nd_{0.7}Sr_{0.3}MnO_3$ compound. They observed FM T_C at around 250 K along with M-I transition temperature at 235 K. Later on, other authors observed FM and metal-insulator (M-I) transitions with T_C in the range of 230 K to 250 K because of its relatively large A site ionic size ($< r_A > =1.212$) compared to (Nd, Ca)-Mn-O series [195-197]. Recently, spin glass like behavior due to freezing of FM clusters was observed from frequency variation of ac susceptibility and 3rd harmonic of ac susceptibility in under doped $Nd_{0.8}Sr_{0.2}MnO_3$ compound [198]. However in half doped $Nd_{0.5}Sr_{0.5}MnO_3$ compound, Kuwahara *et al.* [59] reported a

TH-1060_06612103

field induced insulator to metal transition with first order characteristic behavior. The suppression of resistivity and MR in $Nd_{0.5}Sr_{0.36}Pb_{0.14}MnO_{3-\delta}$ by the application of external pressure was reported by Khazeni *et al.* [199]. The peaks in resistivity and MR corresponding to the FM ordering were found to move towards higher temperature at the rate 20 K/kbar pressure. In half doped $Nd_{0.5}Sr_{0.5}MnO_3$ material, CO has been reported at around 150 K with CE-type AFM structure from the detailed NPD, magnetization, electrical resistivity and electron paramagnetic resonance studies [58, 200-204]. Jung *et al.* [205] have observed the melting of charge-orbital-ordered (COO) state in $Nd_{1/2}Sr_{1/2}MnO_3$ compound through the percolation in the FM metal domains from the analysis of dielectric constant. An interesting feature of metallic state below the T_N of A-type of AFM was reported in $Nd_{0.45}Sr_{0.55}MnO_3$ [206, 207]. For the same composition of Sr, Hayashi *et al.* [208] have observed first order FM transition with a minor hysteresis below the T_N. That was the indication of collapse of d_{x2-y2} orbital ordering as well as the collapse of the A-type AFM spin ordering. However for $x \geq ½$, coexistence of CE-type and A-type AFM ordering was observed from NPD measurements [209, 210], and the electrical conductivity was found to be higher than that of half doped compound. Recently, the existence of COO was reported by using resonant soft x-ray powder diffraction technique [211]. Kimura *et al.* [212] have observed a doping induced crossover from the COO CE-type AFM phase ($0.67 \leq x \leq 0.75$) to charge disordered C-type AFM phase ($0.75 < x < 0.9$) with a phase coexistence in the vicinity of phase boundary ($0.75 \leq x \leq 0.78$) in $Nd_{1-x}Sr_{1+x}MnO_3$ crystals. Nagai *et al.* [213] presented the real-space imaging of COO domains in the tetragonal manganites, $Nd_{1-x}Sr_{1+x}MnO_4$ ($x = 0.8$ and 0.82) from the study of low temperature transmission electron microscope images. The suppression of CO could be observed in $Nd_{1/2}Sr_{1/2}MnO_3$ compound by reducing the particle size down to nano-metric scale [214, 215].

(Nd, Ba)-Mn-O

In $Nd_{1-x}Ba_xMnO_3$ series, even though the $< r_A >$ value is quite large, FM was observed only in a narrow composition range of $x = 0.20$ to 0.40 with a maximum T_C of 146 K for $x = 0.34$ [216, 217]. Troyanchuk *et al.* [217] have reported different magnetic states depending on dopant concentrations in $Nd_{1-x}Ba_xMnO_3$ series; i.e., inhomogeneous AFM in $0 \leq x \leq 0.05$ range, a mixed AFM-FM state in $0.05 < x < 0.10$, a pure FM state in $0.20 \leq x < 0.40$ and an inhomogeneous FM state for $x \geq 0.40$. Troyanchuk *et al.* [218] reported inhomogeneous FM behavior with $T_C = 120$ K and $M_S = 2.8$ μ_B/f.u at 5 K in $Nd_{0.55}Ba_{0.45}MnO_3$ sample. The MR value was found to increase with decrease in temperature and its maximum value at 90 K was found to be 70 % for $H = 9$ kOe. FM insulating state along with negative MR of the order of

TH-1060_06612103

50% for 9 kOe magnetic field was observed in $Nd_{0.75}Ba_{0.25}MnO_3$ compound [219]. Thus, the double exchange (DE) interaction is not purely driven by the $<r_A>$ size or e_g electron bandwidth. Pseudocubic structure from NPD patterns analysis and 3D isotropic FM behavior from EPR patterns analysis were reported on $Nd_{0.75}Ba_{0.25}MnO_3$ [220]. Venkataiah *et al.* [221] have systematically investigated the influence of M-I transition as well as FM-PM transition by varying the average A-site cation radius, $<r_A>$ in $Nd_{0.67}A_{0.33}MnO_3$ (A = Ca, Sr, Pb and Ba) compound. The FM T_C was found to increase from 123 K to 164 K with increase in $<r_A>$ from 1.167 Å for $Nd_{0.67}Ca_{0.33}MnO_3$ to 1.264 Å for $Nd_{0.67}Ba_{0.33}MnO_3$.

(Nd, Pb)-Mn-O

There are a few reports on the single crystal samples of $Nd_{0.7}Pb_{0.3}MnO_3$, where FM and M-I transitions were observed at around 150 K [222-224]. It was also predicted that in these materials, Nd ions order anti-ferromagnetically with spin canting. In $Nd_{1-x}Pb_xMnO_3$ single crystals, Ghosh *et al.* [225] have reported a structural transition from tetragonal symmetry (space group *P4/mmm*) for x = 0.25 to cubic symmetry (space group *Pm3-m*) for x = 0.38. The increase in doping concentration led to the minimization of octahedral distortion and hence to higher crystal symmetry. Colossal electro resistance in FMI state was observed in $Nd_{0.7}Pb_{0.3}MnO_3$ single crystal [224].

Mono valent doped Nd-Mn-O

Recently the mono-valent alkali ion doped, $Nd_{1-x}Na_xMnO_3$ series was studied by a few groups for x= 0.1 to 0.25 and found that these materials exhibit charge ordering at around 180 K followed by a weak FM transition at 110 K [226-228]. They exhibited a semiconducting behavior of electrical resistance without any metal-insulator transition. However, metal-insulator transition could be induced by the application of magnetic field of the order 3T [228]. Li *et al.* [229, 230] reported that $(La_{1-x}Nd_x)_{1-y}Na_yMnO_3$ (y = 0.20 and 0.25) samples exhibited a rhombohedral perovskite structure for $x \leq 0.20$ and distorted orthorhombic structure for $x \geq 0.40$. Srivastava *et al.*[231] have investigated the frequency variation of ac susceptibility of $Nd_{1-x}Ag_xMnO_3$ (x = 0.10 and 0.15) and reported the spin glass like behavior and spin canting due to lower ionic radius of Nd compared to La. In $Nd_{0.5}Ag_{0.5}MnO_3$, Tang *et al.* [232] reported a negative MR~78 % for H = 130 kOe.

Electron Doping

Zhang *et al.* [233] studied the electron doped $Nd_{1-x}Ce_xMnO_3$ compounds, for x=0.04 to 0.10. They have observed FM transition at around 60 K followed by a secondary peak at around 25 K. They have explained their magnetization results based on FM interaction between two sublattices; one having Mn^{3+} ions and other having Mn^{3+} and Mn^{2+} ions.

TH-1060_06612103

Yanagida *et al.* [234] reported FM transition at 65K in single phase $Nd_{0.7}Ce_{0.3}MnO_3$ thin film. The room temperature electrical resistivity values of their samples were reported to be in the order of 10^3 -10^4 Ω-cm.

1.12. Motivation of the Present Thesis Work

As reviewed above, there are several reports on Nd based divalent alkaline earth doped manganites, i.e., $Nd_{1-x}A_xMnO_3$ (A=Sr, Ca, Ba and Pb). The magnetic and transport properties of such materials were found to be quite interesting. The work on mono-valent doping in place of Nd is limited.

The monovalent doping has the advantage of creation of optimum concentration of Mn^{3+}/Mn^{4+} ions with relatively small level of doping. Thus, the lattice distortion can be kept minimum in the monovalent doped materials. In order to understand the effect of crystal structure and lattice distortion on CMR behavior and other magnetic properties, the K-doped Nd-Mn-O series was chosen, where K^{1+} has larger ionic radius (1.38 Å) compared to Nd^{3+} (0.983 Å). On the other hand, the Na^{1+} has comparable ionic radius, i.e., 1.02 Å with that of Nd^{3+}. So, we have taken up a detailed study in $Nd_{1-x}Na_xMnO_3$ series. The magnetic structure of Nd-Mn-O series is quite complicated due to the presence of one more magnetic sublattice, i.e., Nd^{3+} ion. So, it is essential to understand its interaction with Mn ion and is explored in the present thesis from the measurement and analysis of NPD at differeent temperatures. DC magnetization and ac susceptibility measurements were carried out to investigate the nature of magnetic properties and interactions between Mn^{3+} and Mn^{4+} ions for different doping concentrations. Moreover, FM, spin glass like behavior, critical exponent behavior in the vicinity of FM transition, CO, etc. were studied in detail in these materials. Suppression of CO in $Nd_{0.8}Na_{0.2}MnO_3$ compound by varying two parameters, namely particle size down to nano-metric scale and magnetic field up to 10 T were investigated.

The following three series of samples were prepared for the present thesis work,

1. $Nd_{1-x}K_xMnO_3$ (x = 0.10 - 0.30)
2. $Nd_{1-x}Na_xMnO_3$ (x = 0 - 0.20)
3. Nanoparticle samples of $Nd_{0.8}Na_{0.2}MnO_3$

The first two series were prepared to study the effect of A-site ionic size on the magnetic properties of Nd-Mn-O series and to study the role of Nd magnetic moment on the double exchange ferromagnetism. One of the samples in the second series, namely x = 0.20, i.e., $Nd_{0.8}Na_{0.2}MnO_3$ was found to be very interesting with CO behavior. Moreover, it was

TH-1060_06612103

found to exhibit different magnetic ground states such as paramagnetism (PM) → charge-ordering → FM → re-entrant spin glass behavior with decrease in temperature. So, we have taken up this sample for detailed study, by tuning the average particle size down to nano-metric scale.

भारतीय प्रौद्योगिकी संस्थान गुवाहाटी • Indian Institute of Technology Guwahati •

TH-1060_06612103

Chapter 2: Experimental Techniques

Experimental tools are the backbone of an experimentalist and it is essential to understand the mechanism and operational details of equipments to extract best experimental data. The samples for the current investigations were prepared by solid state route and sol-gel methods. For heat treating the materials during the preparations, both homemade and commercial furnaces were used. The details of design and fabrication of homemade furnaces are discussed in this chapter. The prepared materials were characterized by using X-ray diffraction (XRD) to check their phase purity and lattice parameters, chemical titration to determine average Mn valency, scanning electron microscope (SEM) and field emission scanning electron microscope (FE-SEM) to study the microstructure, energy dispersive spectrometer (EDS) analysis for determining sample composition and transmission electron microscope (TEM) to estimate particle size, and to study composition and crystal structure at nano-crystalline level. The electrical transport and magnetic properties were studied by carrying out temperature variations of electrical resistivity, magneto-resistivity, ac susceptibility, dc magnetization, and neutron powder diffraction measurements. The experimental set-ups used for electrical transport and magnetic measurements are also discussed in this chapter.

2.1. Sample Preparation

The most widely used methods for preparing polycrystalline oxides are the solid state reaction route reaction and sol-gel technique. Even though, the desired phase is thermodynamically favored, solids do not usually react together at ambient temperature over laboratory time scales and it is necessary to heat the reactants at high temperatures to overcome the kinetic barriers. The powders of stoichiometric ratio of starting compounds are often pressed into pellets before heating to high temperature to increase the contact between particles. Reaction times are usually several days and it is best to repeat the process to ensure homogeneous samples. The starting materials are usually single cation oxides, carbonates, nitrates or hydroxides which decompose to form oxides when heated. Carbonates are popular for the alkali and alkaline earth elements because they are not hygroscopic and therefore can be weighed accurately in air. During the initial heating or calcination of carbonate mixtures, carbon dioxide is produced and it escapes from the solid. This prevents good sintering of the material into a dense ceramic, requiring an additional heating.

TH-1060_06612103

Sol-gel method is a chemical process, where the nitrates or acetates of cationic materials are dispersed in a solvent and are converted into a gel form through the hydrolysis reaction of polymerization. The heating of the gel leads to combustion reaction, with an end product of fine dry powders in nano-metric scale. The advantage of sol-gel technique compared to the solid state route is as follows. (1) In sol-gel technique, the mixing of the starting materials at the molecular level is possible due to the dispersion of the materials in a solvent. (2) The incorporation of dopant elements evenly to achieve uniform doping on a molecular level is possible. (3) The required temperature for annealing is relatively small compared to the case of solid state route and the diffusion of components is in the nanometer range.

The samples were prepared from the following starting compounds and elements, such as, Neodymium oxide (Nd_2O_3, 99.9%), Potassium Carbonate (K_2CO_3, 99.9 %), Sodium Carbonate (Na_2CO_3, 99.9%) and Manganese Acetate ($C_4H_6MnO_4.4H_2O$, 99.5%).

Solid state reaction:

The stoichiometric ratio of starting compounds and/or elements were weighed using an electronic balance supplied by Mettler Toledo model no. AG135 with an accuracy of ±0.01 mg. The weighed compounds were grinded under the medium of acetone (99%) using an agate mortar and pestle. The homogeneous mixture of starting compounds was transferred to an alumina crucible and was presintered in the temperature range 800 to 900°C for over 24 h followed by furnace cooling to room temperature. The presintered powder was grinded again to get a homogeneous mixture. The presintering was repeated twice. The presintered powder was pressed into cylindrical shape pellets by using a 13 mm die and a hydraulic press supplied by Techno Search instruments, Thane, India with a maximum load of 6 Ton/cm^2. The sintering in pellet form was carried out in a step by step process in air at different temperatures with several intermediate grindings and repelletizing. The final sintering temperatures were different for different series of the samples and these details are discussed in chapters 3, 4, and 5 for respective series of materials.

Sol gel method:

The stoichiometric amounts of starting compounds and/or elements were converted into metal nitrates by adding nitric acid. They were converted into citrate by adding excess amount of citric acid and ethylene glycol. The uniform mixture of the above solution was

TH-1060_06612103

slowly evaporated in a hot plate at 75 to 100°C until a gel was formed. The polymeric gel was completely dried up by keeping at 75°C for 12 hr. The product was heated to 200°C to induce self combustion. The combustion derived fine powder was heat treated at 400°C to decompose the remaining organic reagents. The obtained precursor powder was sintered in pellet form. The final sintering temperatures were different for different series of the samples.

2.2. High Temperature Furnaces

High temperature furnaces were used for material preparation. Homemade muffle furnaces with a maximum operating temperature of 1200°C and commercial high temperature furnaces with the maximum operating temperature of 1400°C were used for sintering the samples. The commercial furnaces were supplied by N. R. Enterprises and Bysakh & Company, Kolkata, India. The furnace supplied by N. R. Enterprises was powered by a thyristor unit of 30 A rating. The temperature was controlled using; West, UK make, PID programmable temperature controller (model no. 6400) with 16 segment programming feature. The platinum versus platinum-rhodium (Platinum + 10 % Rh) thermocouple was used for sensing the temperature. The heating elements were based on Si-Carbide rods. The

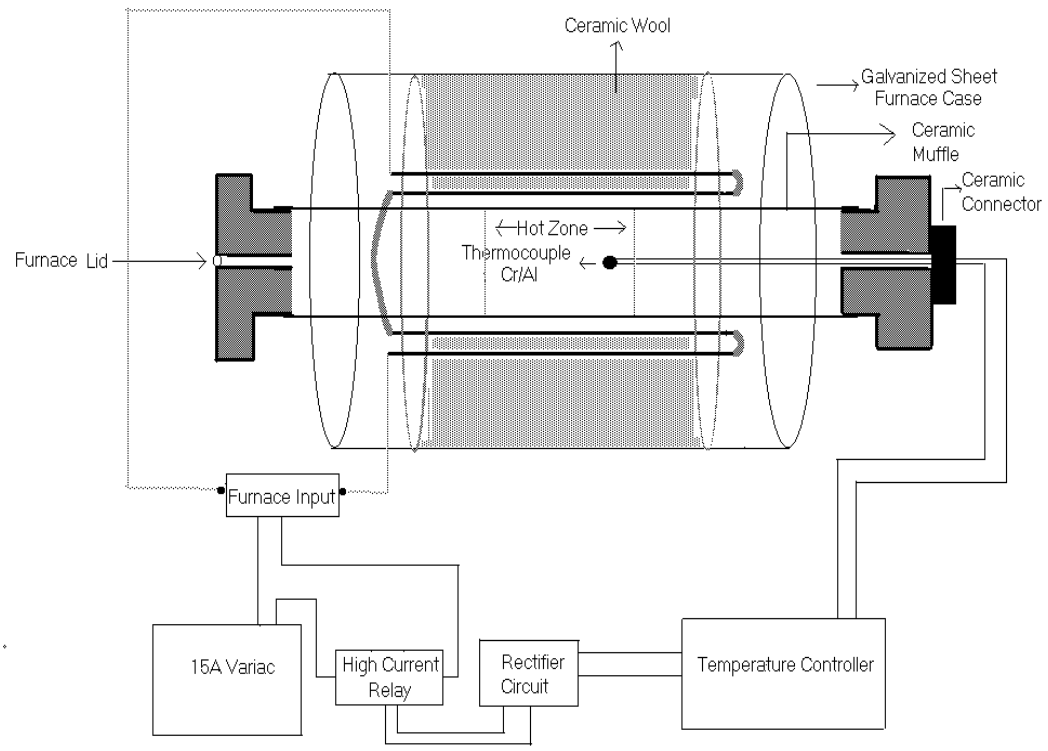

Figure 2.1: Block diagram of the furnace with maximum operating temperature of 1200°C.

TH-1060_06612103

temperature was controlled to an accuracy of ± 1°C. The furnace could be operated up to a maximum temperature of 1400°C. The other furnace supplied by Bysakh & Co. contains (1) a thyristor unit rating of 35 A, (2) a PID programmable temperature controller (model no. PRC-300) with 16 segment programming feature, (3) a platinum versus platinum-rhodium (Platinum + 13 % Rh) thermo couple wire, (4) Si-Carbide rods based heating elements. The maximum operating temperature was 1450°C.

The home made furnace (1200°C) was fabricated using a cylindrical alumina muffle with an inner diameter of 5.8 cm and 50 cm length. Six Si-Carbide rods of 45 cm length each were used as heating element. The muffle loaded with heating elements was housed in a cylindrical container of 50 cm diameter and 50 cm length and it was made up of galvanized aluminum sheet. High temperature ceramic bricks and ceramic wools were used as thermal insulation. Chromel-Alumel (Cr-Al) thermocouple and a commercial on/off type temperature controller were used for temperature measurement and controlling. The input power to the furnace was regulated using a variac (dimmerstat) of 15 A capacity. An external on/off relay (15 A capacity) was used for controlling the power supply to the heater wire. The relay was triggered using the temperature controller. The block diagram of the furnace is shown in figure 2.1. The furnace could be operated up to a maximum temperature of 1200°C. The temperature could be controlled with an accuracy of ± 5°C.

2.3. X-ray Diffraction

The X- ray diffraction technique has been used to study the phase purity and crystal structure of the prepared compounds. Powder X-ray diffraction (XRD) patterns were recorded at room temperature using commercial Seifert-model no. 3003TT or a Bruker model no. D8 X-ray diffractometer by employing CuK_α radiation (1.5418 Å). In the present investigation, all the XRD data were collected with the setting of 30 mA current and 40 kV voltage for X-ray generator. The instrument is based on the Bragg-Brentano geometry as shown in figure 2.2. In this geometry, the source to sample distance and the sample to detector distance are kept equal. A perspex sheet with rectangular groove was used for sample mount, where the powder sample was filled uniformly in the groove. The data were collected in an usual θ-θ scan with an angular speed 1-2^0/minute and a step size of 0.03-0.05°.

The XRD patterns were analyzed with the help of Fullprof program by employing Rietveld refinement technique [235]. The background was refined using a polynomial

TH-1060_06612103

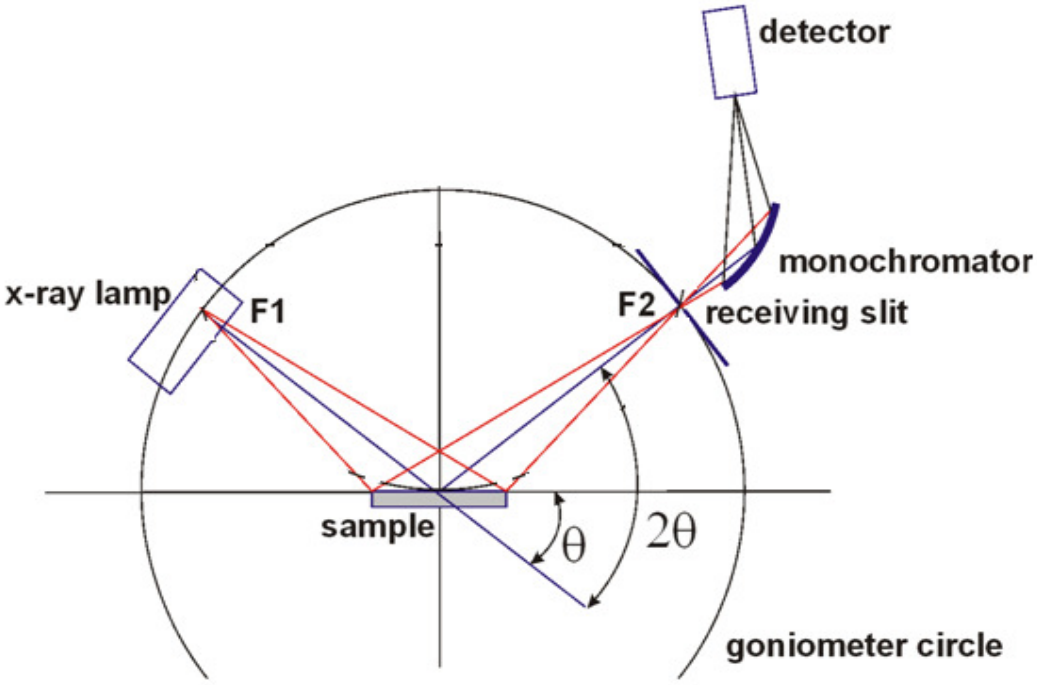

Figure 2.2: Ray diagram of X- ray diffractometer.

function. Pseudo-Voigt function was chosen for peak shape. The global parameters, such as coefficients of background polynomial, scaling factor, half width parameters (u, v, w) and lattice parameters (*a, b, c*) were mainly varied during the refinement. In addition to that nuclear structure variables such as fractional atomic co-ordinates (x, y, z), isotropic displacement (temperature) parameters and occupancy values were varied. Here, occupancy is the chemical occupancy normalized to the multiplicity of the general position of the group. The occupancy of oxygen was taken as 1 for all the refinements and it was not varied during the refinement. The quality of the refinements are known based on the values of reliability factors such as, R_p, R_{wp}, R_{exp}, R_{Bragg}, R_F and χ^2 and they are defined as follows.

$$\text{Profile factor, } R_p = 100\frac{\sum_{i=1,n}\left|y_i - y_{c,i}\right|}{\sum_{i=1,n} y_i} \qquad \text{---------- (2.1)}$$

Here y_i is the observed point (experimental) and $y_{c,i}$ is the calculated point and n represents the number of data points.

TH-1060_06612103

$$\text{Weighted profile factor, } R_{wp} = 100\left[\frac{\sum_{i=1,n}\omega_i\left|y_i - y_{c,i}\right|^2}{\sum_{i=1,n}\omega_i y_i^2}\right]^{1/2} \quad \text{---------- (2.2)}$$

Here $\omega_i = \frac{1}{\sigma_i^2}$, σ_i^2 is the variance of observation y_i.

$$\text{Expected weight factor, } R_{\exp} = 100\left[\frac{n-p}{\sum_{i=1,n}\omega_i y_i^2}\right]^{1/2} \quad \text{---------- (2.3)}$$

Here $(n - p)$ is the number of degrees of freedom. n is the total number of experimental points and p is the number of refined parameters.

$$\text{Reduced chi-square, } \chi^2 = \left[\frac{R_{wp}}{R_{\exp}}\right]^2 \quad \text{---------- (2.4)}$$

$$\text{Bragg factor, } R_B = 100\frac{\sum_h\left|I_{obs,h} - I_{calc,h}\right|}{\sum_h I_{obs,h}} \quad \text{---------- (2.5)}$$

Here h is the vector which levels the Bragg reflections. The $I_{obs,h}$ is the observed integrated intensities and $I_{calc,h}$ is the calculated intensities.

$$\text{Crystallographic } R_F \text{ factor, } R_F = 100\frac{\sum_h\left|F_{obs,h} - F_{calc,h}\right|}{\sum_h F_{obs,h}} \quad \text{---------- (2.6)}$$

Here $F_{obs,h}$ and $F_{calc,h}$ are the observed and calculated structural factors respectively.

Inter atomic distances (bond length) and bond angles were calculated using the refined fractional coordinates and lattice parameters by using Fullprof software.

The average crystallite size (S_C) has been calculated from the peak broadening by using the Scherrer's formula [236]

$$S_C = \kappa\lambda / \beta\cos\theta \quad \text{---------- (2.7)}$$

where, constant k depends upon the shape of the particle(grain) size. Here it is taken as 0.89 by assuming the circular shape of particle, β = Full Width at Half Maximum (FWHM) of intensity versus 2θ profile, λ is the wavelength of the CuK_α radiation and θ is the Bragg's diffraction angle. The instruments broadening effect has been taken into account.

TH-1060_06612103

2.4. Scanning Electron Microscope (SEM)

Recording of microstructural images and compositional analysis have been carried out by using LEO Scanning Electron Microscope (SEM, Leo 1430VP) equipped with Oxford energy dispersive spectrometer (EDS). Basic principles of SEM and EDS analysis are given briefly as following.

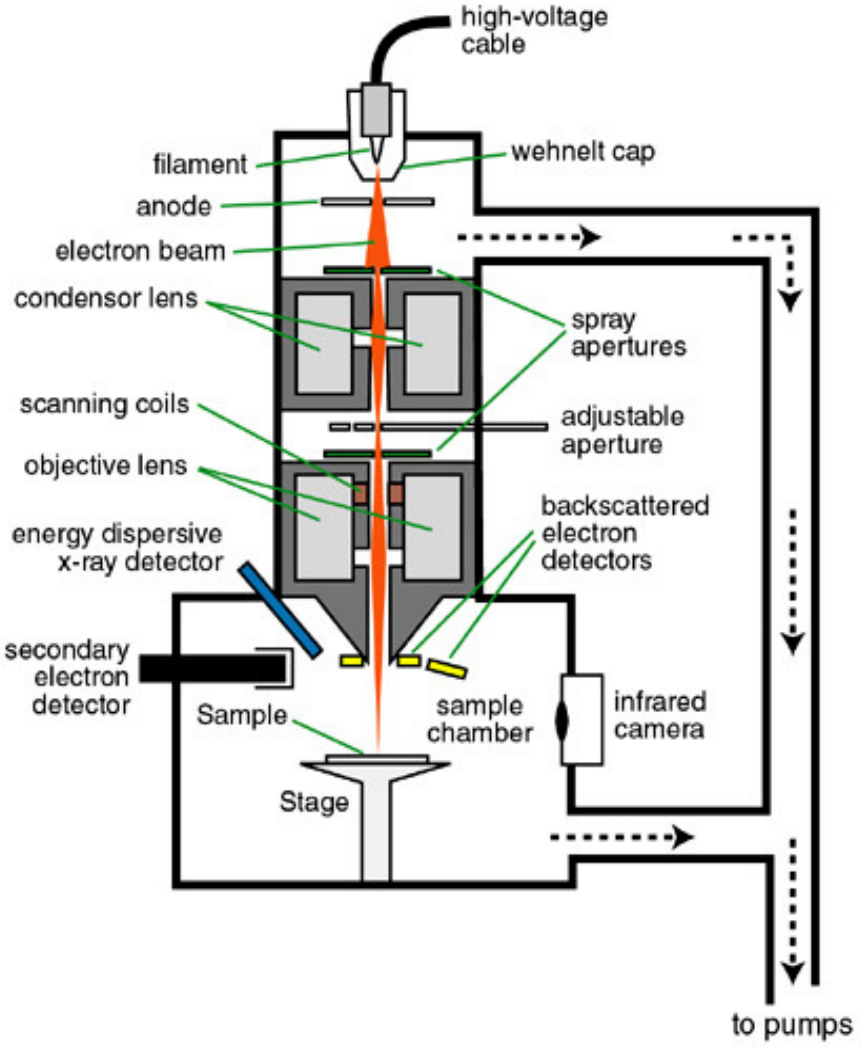

Figure 2.3: Schematic view of scanning electron microscope.

The scanning electron microscope (SEM) is a type of electron microscope that uses electrons to form an image of objects and to study surface morphology, fractured components, foreign particles and residues, etc. The schematic view of SEM is shown in figure 2.3. The thermionically emitted electrons from a tungsten filament are drawn towards anode and were focused by two successive condenser lenses into a beam with a narrow spot

TH-1060_06612103

size (~50 Å). The shorter wavelength of electrons permits image magnifications of up to 100, 000 times in SEM. Pair of scanning coils located at the objective lens deflect the beam either linearly or in raster fashion over a rectangular area of specimen surface. These primary bombarding electrons on the surface of the specimen dislodge electrons from the specimen. Figure 2.4 shows the interaction of electrons with the surface of the sample. Upon electron impingement on the surface, the interaction volume assumes a tear shape. These dislodged electrons are known as secondary electrons, which are attracted and collected by a positively

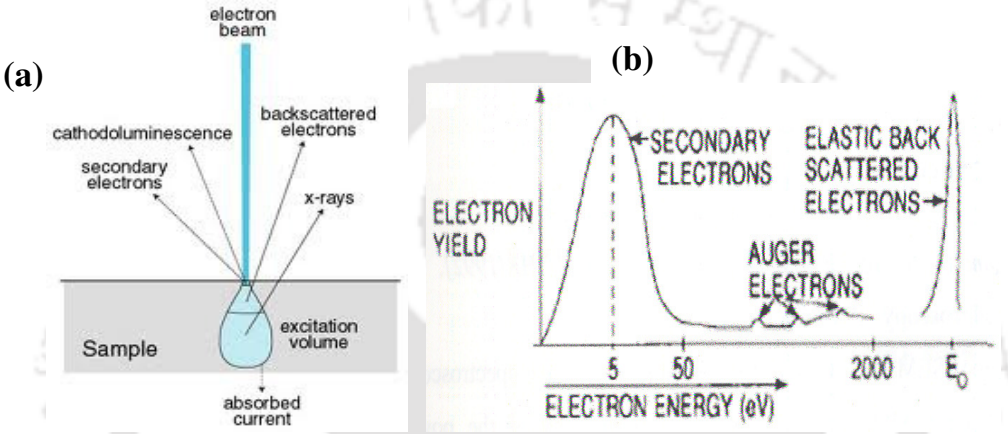

Figure 2.4 : (a) Electron and photons signals emanating from tear-shaped interaction volume during electron beam impingement on specimen surface, and (b) Energy spectrum of electrons emitted from the specimen surface.

biased grid or detector, and then translated into signals. These signals are then amplified, analyzed, and translated into images of the topography being inspected.

Apart from secondary electrons, the back scattered electrons (BSE), characteristic x-rays, light (cathode-luminescence), specimen current and transmitted electrons are produced by SEM. These types of signal require specialized detectors and all such detectors are not present in a single machine. The primary electron beam results in the emission of BSE from the specimen. BSE possess more energy than secondary electrons and have a definite direction. As such, they cannot be collected by a secondary electron detector, unless the detector is directly in their path of travel. All emissions above 50 eV are considered to be BSE. BSE imaging is useful in distinguishing one material from another, since the yield of the collected BSE increases monotonically with the specimen's atomic number

TH-1060_06612103

Z (~ 0.05 $Z^{1/2}$). Backscattered imaging can distinguish elements with atomic number difference of at least 3.

Energy dispersive X-ray spectroscopy (EDS, EDX or EDXRF) is an analytical technique used for the elemental analysis or chemical characterization of a sample. Its characterization capabilities originate from the fact that each element has a unique atomic structure, which emits its unique characteristic X-ray. To stimulate the emission of characteristic X-rays from a specimen, a high energy beam of charged particles such as electrons or protons, or a beam of X-rays, is focused into the sample being studied. At rest, an atom within the sample contains ground state (or unexcited) electrons in discrete energy levels or electron shells bound to the nucleus. The incident beam may excite and eject an electron from an inner shell and it results in a hole or electron vacancy in the shell. An electron from an outer higher-energy shell then fills the hole, and the difference in energy between the higher-energy shell and the lower energy shell is released in the form of an X-ray. The atoms of every element releases X-rays with unique amounts of energy during the above process. Thus, by measuring the value of energy of X-rays being released by a specimen during electron beam bombardment, the identity of the atoms present in the specimen can be established. Thus, we get the EDS spectrum, as an output and it is just a plot of how frequently an X-ray is received for each energy level. An EDS spectrum normally displays peaks corresponding to the energy levels for which the X-rays had been received. Each of these peaks is unique to an atom, and therefore corresponds to a single element. The intensity of the peaks depends on the concentration of the elements present.

In the present work, a thin solid pellet was mounted on carbon coated tape. Our sample was electrically conducting, so the direct SEM and EDS measurements could be carried out without any metal coating.

2.5. Field Emission SEM (FE-SEM)

A FE-SEM is used to visualize very small topographic details on the surface of pellets or fractioned objects. Researchers in biology, chemistry and physics apply this technique to observe structures that may be as small as 1 nanometer. In the present work ZEISS make FE-SEM (ΣIGMA) was used to study the surface morphology of nanocrystalline samples. The resolution of this FE-SEM is 1.3 nm at 50 kV and 2.8 nm at 1 kV.

Field emission (FE) is an emission of electrons induced by external electromagnetic fields. FE can happen due to the promotion of electrons, from the valence to the conduction

TH-1060_06612103

band of semiconductors. The related effect is cold electronic emission, i.e., the emission of electrons in strong static (or quasi-static) electric fields. The electron gun is basically a zirconium oxide coated tungsten (ZrO_2/W) emitter, which operates in a thermally assisted Schotky emission mode. This type of gun provides narrower probing beams as well as high electron energy, resulting in both improved spatial resolution and minimized sample charging and damage.

Electrons are liberated from a field emission source and accelerated in a high electrical field gradient. Within the high vacuum column, these so-called primary electrons are focused and deflected by electronic lenses to produce a narrow scan beam that bombards the object. As a result, secondary electrons are emitted from each spot on the object. The angle and velocity of these secondary electrons depend on the surface structure of the object. A high efficient annular in-lens ac-detector catches the secondary electrons and produces an electronic signal. One more detector, i.e., solid state back scattered detector is used to detect the BSE.

The advantages of FE-SEM over SEM are as follows, (1) FE-SEM produces clearer, less electrostatically distorted images with spatial resolution down to 1 nm. That is 3 to 6 times better than conventional SEM; (2) smaller-area contamination spots can be examined at electron accelerating voltages compatible with Energy Dispersive X-ray Spectroscopy; (3) Closer to the immediate material surface can be probed due to the reduced penetration of low kinetic energy electrons; (4) high quality, low voltage images are obtained with negligible electrical charging of samples. (Accelerating voltages range from 0.5 to 30 kV).

In order to observe FE-SEM for objects, the sample should have electrically conducting. This can be done by coating them with an extremely thin layer (1.5 - 3.0 nm) of gold or carbon by using respective coater. However in the present thesis work, the samples were electrically conducting. A thin layer of powder was spread on a carbon coated tape and was directly mounted for the FE-SEM observation.

2.6. Transmission Electron Microscope (TEM)

Recording of nanocrystalline microstructure has been carried out by using JEOL Transmission electron microscope (TEM, JEOL 2100; TECNAI G^2 F30). Figure 2.5 shows the schematic diagram of TEM. Thermionically emitted electrons from the gun are accelerated to 100 KeV or higher and are first projected onto the specimen by means of the

TH-1060_06612103

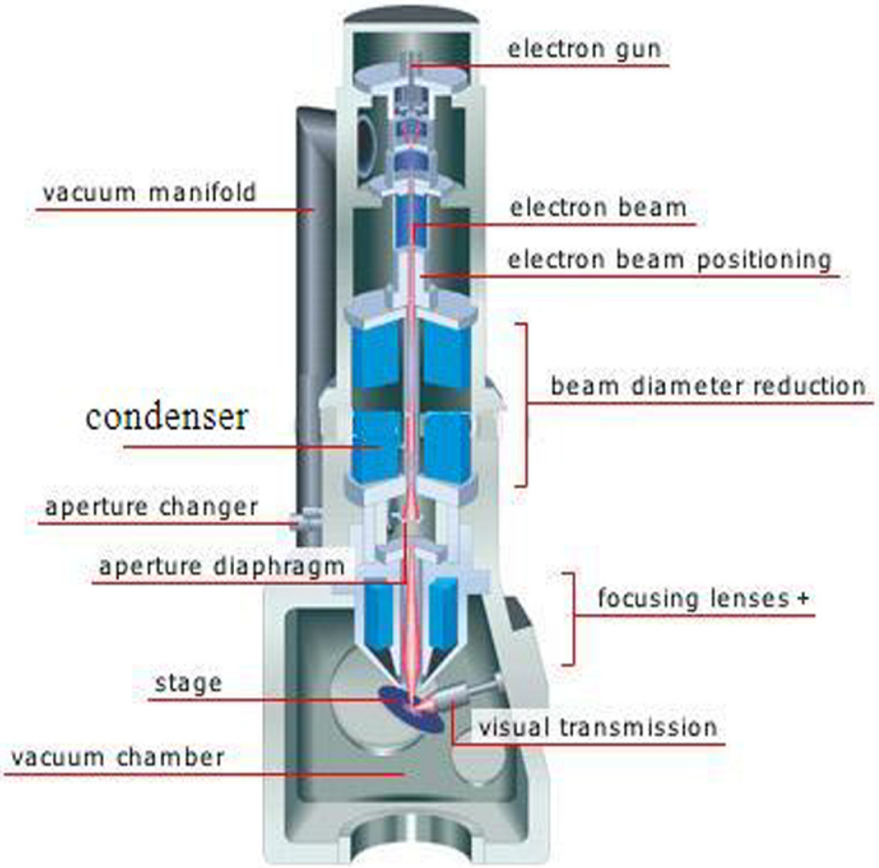

Figure 2.5: Schematic diagram of transmission electron microscope.

condenser lens system. The scattering process experienced by electrons during their passage through the specimen determines the kind of information obtained. Elastic scattering, involving no energy loss, when electrons interact with the potential field of the ion core, gives rise to diffraction patterns. Inelastic interactions between beam and matrix electrons at heterogeneities, such as grain boundaries, dislocations, secondary phase particles, defects, density variations, etc., cause complex absorption and scattering effects, leading to a spatial variation in the intensity of the transmitted beam. Images can be formed in a number of ways. The bright-field image is obtained by intentionally excluding all diffracted beams and only allowing the central beam through the specimen. This is done by placing suitably sized apertures in the back focal plane of the objective lens. Intermediate and projection lenses then magnify this central beam. Dark-field images are also formed by magnifying a single beam; here one of the diffracted beam is chosen by means of an aperture that blocks the central beam and the other diffracted beams. By selected area diffraction, ring like structure is imaged, which corresponds to the particular plane of that element or compound. If only

TH-1060_06612103

diffused rings appear then the system must have single amorphous phase. From the high-resolution TEM (HR-TEM) image, average grain size, and dislocations can be evaluated.

In the present study the powdered sample was first dispersed in ethanol solution and then a drop of the liquid was placed on a carbon coated grid for the TEM observation.

2.7. Neutron Diffraction

In contrast to X-rays, neutron beams are produced by nuclear reactions, such as nuclear fission or fusion, or by spallation of nuclei by accelerated particles. Since, nuclear fusion cannot be controlled sufficiently to produce stable neutron sources, neutrons are mainly produced by fission and spallation sources. In comparison to X-rays, a number of properties of the neutron make it useful for the study of structures of crystalline systems.

- The neutron is an uncharged particle; therefore, it interacts with the nucleus and not the electron cloud. Thus, neutrons have high penetrating power. Unlike in X-rays, where the atomic scattering factor *f* increases with increasing *Z*, for neutrons the scattering is not strongly dependent on the atomic number of an atom. Consequently, neutron diffraction is more sensitive to lighter atoms compared to the X-ray diffraction. Furthermore, neutrons can distinguish isotopes in contrast to X-ray scattering.
- The velocity of neutrons is such that, wavelength of thermal neutrons is comparable to the interatomic distances of atoms. Hence, neutron scattering is useful to study the structure of solids.
- Additionally, the energy of thermal neutrons is comparable to the energy of elementary excitations in matter, making it suitable for the study of dynamic processes.
- An important property of neutrons is that they carry a magnetic moment of $-\gamma\mu_N$, where $\gamma = 1.913$ and $\mu_N = eh/2m_p$ is the nuclear magneton. This interacts with unpaired electrons of magnetic atoms leading to additional scattering from magnetic solids. The resulting scattering from magnetic solids is used for the study of magnetic structure and spin excitations.

2.7.1. Magnetic Diffraction

The interaction between the neutron magnetic moment and the magnetic moment of atom produces neutron magnetic scattering, and it is in addition to the nuclear scattering of

TH-1060_06612103

neutrons. In the paramagnetic state, the magnetic moments of atoms are completely uncoupled to each other and are randomly oriented. According to Halpern and Johnson, for paramagnetic ions, the differential magnetic scattering cross section per unit solid angle, and per atom is given as [237],

$$d\sigma_{pm} = \frac{2}{3} S(S+1) \left(\frac{e^2\gamma}{mc^2}\right)^2 f^2 \quad \text{---------- (2.8)}$$

In this expression, S is the spin quantum number, γ is the magnetic moment of the neutron expressed in nuclear magnetons, and f is an amplitude form factor. Paramagnetic materials scatter neutrons incoherently providing no contribution to the Bragg peaks, as the magnetic spins are randomly orientated in all directions. The occurrence of the form factor (f) in magnetic scattering is in contrast to the absence of such factor for nuclear scattering. This is due to the distribution of electrons having magnetic moment over a whole volume having dimensions comparable to the neutron wavelength. The form factor for the magnetic scattering falls off more rapidly as a function of scattering angle compared to X-ray scattering, because only a few outer orbital unpaired electrons contribute to the magnetic moment. This restricts the range of θ over which significant magnetic intensities can be detected.

Scattering by antiferromagnetic and ferromagnetic materials:

In case of AFM and FM materials, the magnetic moments of the individual ions are oriented in a defined manner, in contrast to their random orientation in space for a paramagnetic material. For a FM system, all the moments in a single domain are parallel, while, in an AFM system, the atoms may be considered to lie on two sublattices whose spins are oppositely aligned. In comparison with the paramagnetic system, the differential magnetic scattering cross section is modified as,

$$d\sigma_{pm} = q^2 S^2 \left(\frac{e^2\gamma}{mc^2}\right)^2 f^2 \quad \text{---------- (2.9)}$$

where, q is the magnetic interaction vector defined as, $q = \varepsilon(\varepsilon, k) - k$, where, k is a unit vector in the direction of the atomic magnetic moment and ε is the scattering vector, as shown in figure 2.6. In general, for an atom in which both spin and orbital moments are present, the spin quantum number is replaced by the total angular momentum J.

If the chemical and magnetic unit cells are of the same size, then the coherent magnetic diffraction peaks will superimpose on the nuclear Bragg peaks. In FM systems, the coincidence of magnetic and nuclear peaks leads to an enhancement in intensity of low angle nuclear Bragg reflections. In AFM compounds, the magnetic unit cell may have dimensions

TH-1060_06612103

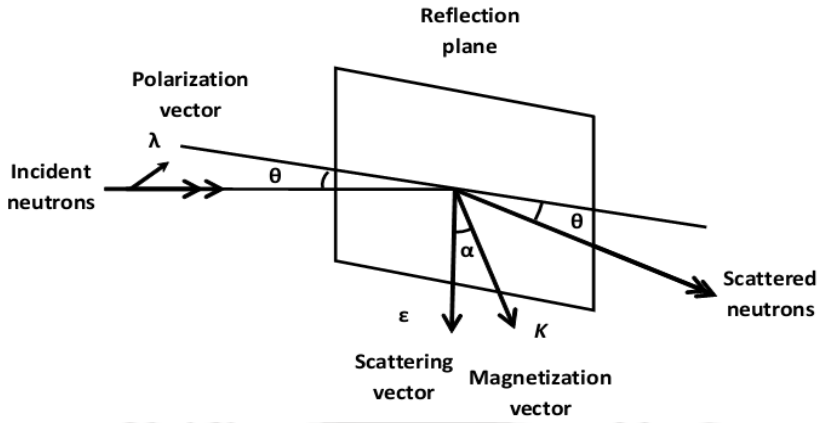

Figure 2.6: Directions of unit vectors *ε, k, λ* described in the text towards magnetic scattering in addition to scattering angle *α, θ*. The *q* lies in the plane of *ε, k* and is perpendicular to *ε* with a magnitude of *sin α*.

different from the chemical one, causing the appearance of superlattice reflections at new positions.

The resultant structure factor is given as, $F^2 = F^2_{nucl} + q^2 F^2_{magn}$. In this expression, F^2_{nucl} is the nuclear structure factor, while F^2_{magn} is the magnetic structure factor defined as,

$$F^2_{magn} = \left|\sum_i p_i \exp(2\pi i(hx_i + ky_i + lz_i))\right|^2 \quad \text{---------- (2.10)}$$

where, $p = (e^2\gamma/2mc^2)g\,J\,f$ *and* $q^2 = 1 - (\varepsilon.k^2) = \sin^2\alpha$. Here, *g* is the Lande splitting factor, *J* is the total angular momentum, and *f* is the amplitude form factor. The occurrence of this form factor in the magnetic scattering is due to the magnetic moments associated with electrons and is different from nuclear scattering. The distribution of these electrons is over a volume of space having linear dimensions, which is comparable with the neutron dimensions. Therefore, if the magnetic moments are parallel to reflecting plane, then *α* will be 90° and *q* = 1 as shown in figure 2.6. On the other hand, if magnetic moments are perpendicular to the reflecting plane, then *α* will be 0° and *q* = 0.

2.7.2. Neutron Powder Diffractometer

The NPD measurements of samples presented in the thesis were carried out on the beam port T-1013 in Dhruva reactor hall at Bhabha Atomic Research Center (BARC), Trombay, Mumbai, India. A schematic diagram of this instrument and the parameters are shown in figure 2.7. The powder diffractometer is based on multi position sensitive detectors (PSDs)

TH-1060_06612103

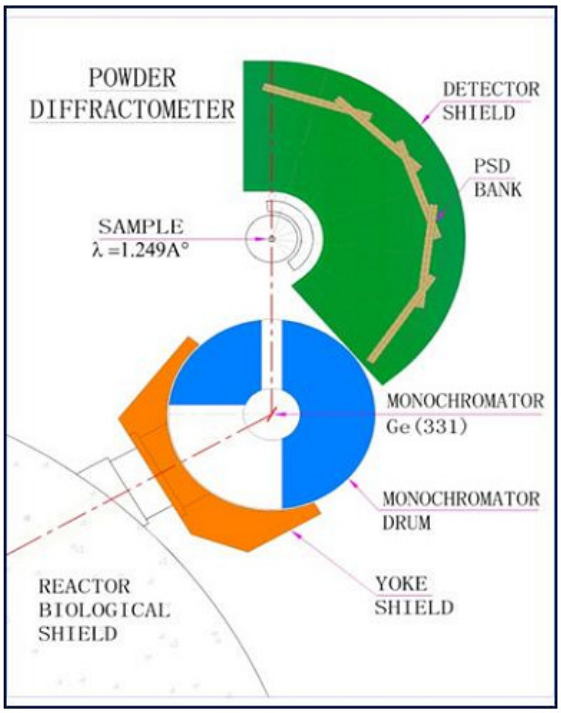

Beam hole no.	T1013
Monochromator	Ge (331)
Wavelength	1.249 Å
Beam size	4.0cm× 1.5 cm
Flux at sample	8.5×10^5 n/cm²/sec
Scattering angle	$4^o < 2\theta < 140^o$
Q range	0.4 – 9.4 $Å^{-1}$
Δd/d	~ 0.8 %
Detector	5 (1d-PSD)
Sample environment	5 – 300K

Figure 2.7: A schematic diagram and the corresponding instrument parameters of neutron powder diffractometer at DHRUVA reactor.

and it covers wide angular range from $4° < 2\theta < 140°$. It employs Ge (3 3 1) monochromator crystal at a takeoff angle of 60° to obtain monochromatic neutron beam of wavelengths λ = 1.249 Å. The neutron flux at the sample is 8.5×10^5 $n/cm^2/sec$. The powdered samples were packed in a cylindrical Vanadium container, attached to the cold finger of Helium closed cycle refrigerator (CCR) cryostat for temperature dependent measurements between 5 and 300K. The advantage of using Vanadium container is that it has negligible coherent scattering cross-section and therefore it does not produce diffraction peaks. The detection system consists of 5 linear PSDs. The PSDs consist of 10 μm diameter Ni-Cr alloy wire having specific resistance of 9Ω/mm [238]. The effective length of the PSD is 875 mm and the diameter of the outer brass tube is 36.5 mm. The filling gas is constituted of ^3He at 3 atm pressure and Kr at 1.5 atm pressure. Kr acts as a stopping gas and limits the range of protons produced during the nuclear reaction.

$$\frac{3}{2}He + \frac{1}{0}n = \frac{1}{1}H + \frac{3}{1}T \qquad \text{---------- (2.11)}$$

The neutron collides with helium gas and produces one proton and a tritium. Clearly the charge and mass number are conserved. The position sensing is based on charge division

TH-1060_06612103

method [239]. Having input from all 5 PSDs, the data acquisition was done with the help of a computer.

2.8. Chemical Titration

The oxidation state of Mn was determined by a chemical titration method, in which the samples were dissolved in dilute sulphuric and phosphoric acids with an addition of excess amount of Mohr salt, $Fe(NH_4)_2(SO_4)_2.6H_2O$ and were titrated against self-indicating potassium permanganate, $KMnO_4$ solution [240, 241]. Here, the valency of Fe and Mn are +2 and +7 respectively. During the titration Fe^{2+} is oxidized to Fe^{3+} and Mn^{7+} is reduced to Mn^{2+}. The reaction is as follows,

$$MnO_4^- + 8H^+ + 5Fe^{2+} \rightarrow Mn^{2+} + 5Fe^{3+} + 4H_2O \quad \text{---------- (2.12)}$$

$$Mn^{7+} + 5e \rightarrow Mn^{2+}$$

$$5Fe^{2+} - 5e \rightarrow 5Fe^{3+}$$

$$Mn^{7+} + 5Fe^{2+} \rightarrow Mn^{2+} + 5Fe^{3+} \quad \text{---------- (2.13)}$$

The normality of Mohr salt and $KMnO_4$ was kept constant during the titration. The normality (N) for any solution is defined as,

$$N = M \times \text{number of reduced valency or oxidized valency} \quad \text{---------- (2.14)}$$

Here M is the molarity of the solution. The molarity of a solution is 1 when the solution is prepared by adding an amount of molecular weight of the sample in 1000 ml of water. To prepare 250 ml solution of y molar concentration, one has to add z_1 gm (z_1 = molecular wt. × 250 × y/1000) of material into 250 ml of water.

Generally, fresh solutions were prepared to perform the titrations. Molecular weight of Mohr salt and $KMnO_4$ are 392.13 gm and 158.04 gm respectively. In a 250 ml volumetric flask, z_1 = 49.016 gm (1/8 of the molecular weight) of Mohr salt was taken and deionized water was added up to the mark on the volumetric flask. It was shaken thoroughly at the time of adding water and it leads to a molarity of 0.5 M (0.5 N). Similarly, in another 250 ml volumetric flask, z_1 = 3.95 gm (1/40 of the molecular weight) of $KMnO_4$ was taken alongwith added deionized water up to the mark of the volumetric flask. It leads to a molarity of 0.1 M (0.5N). So, the normality of the above two solutions was equal. 20 ml of Mohr salt solution was taken in a conical flask with the help of a 20 ml pipette. 2 ml of dilute phosphoric (H_3PO_4) and 2 ml of dilute sulphuric (H_2SO_4) acids were added to it. $KMnO_4$ solution was

TH-1060_06612103

taken in a burette and was titrated against Mohr salt solution and, was shaken at the time of adding. At the end point, faint pink color of Mohr salt solution was turned into a straw color, i.e., all iron was oxidized. The quantity of $KMnO_4$ solution added was determined from the initial and final burette readings. Titration was repeated two times, and the average value has been taken for finding the equivalence of $KMnO_4$ solution (say u_1 ml) for 20 ml of Mohr salt solution. Let u_2 ml of $KMnO_4$ solution is equivalent to 1 ml of Mohr salt.

To standardize the titration procedure, commercially supplied MnO_2 (Mn^{4+}) was used. For determining the valency of Mn in MnO_2, a small amount of known weight of MnO_2 was added into the 20 ml of Mohr salt solution before titration. As a result of the addition of MnO_2, some of the Fe^{2+} ions are oxidized to Fe^{3+} ions. The Mohr salt solution containing MnO_2 was titrated against $KMnO_4$ solution. The consumption of $KMnO_4$ solution (say u_3 ml) was found to be less than the value obtained from the earlier titration, i.e., titration against pure Mohr salt solution. The difference between the equivalent Mohr salt solution (u_1) and the consumption of $KMnO_4$ solution (u_3) can be found and, this quantity of Mohr salt solution is called consumed Mohr salt solution (say u_4 ml). The reduced valency (R_v) of Mn in MnO_2 was calculated using the formula,

$$R_v = \frac{x_1 y_2}{x_2 y_1} \qquad \text{---------- (2.15)}$$

where, x_1 and x_2 are the atomic weight of Mn and Fe respectively. y_1 is the mass of Mn present in the MnO_2 compound added to the Mohr salt solution in gram. y_2 is the mass of Fe present in the consumed Mohr salt solution, i.e., in u_4 ml of Mohr salt solution. So, the actual valency can be calculated as,

$$\text{Mn Valency} = 2 + R_v \qquad \text{---------- (2.16)}$$

2.9. ac Susceptibility Set-up

ac susceptibility technique can be used for studying the magnetic properties of the materials [242-246] and it has advantage over other techniques in terms of cost and one can get additional information such as loss components, etc. The details of ac susceptometer are given as follows. It is basically designed by employing mutual inductance bridge method. It consists of a primary coil and coaxially wound two identical secondary coils as shown in figure 2.8. One secondary coil is used for mounting the sample and is called sample secondary and the other one is reference coil. The primary coil is energized using a sinusoidal signal of desired frequency and voltage, $E = E_0 e^{i\omega t}$. Magnetic field, $H = H_0 e^{i\omega t}$ is generated

TH-1060_06612103

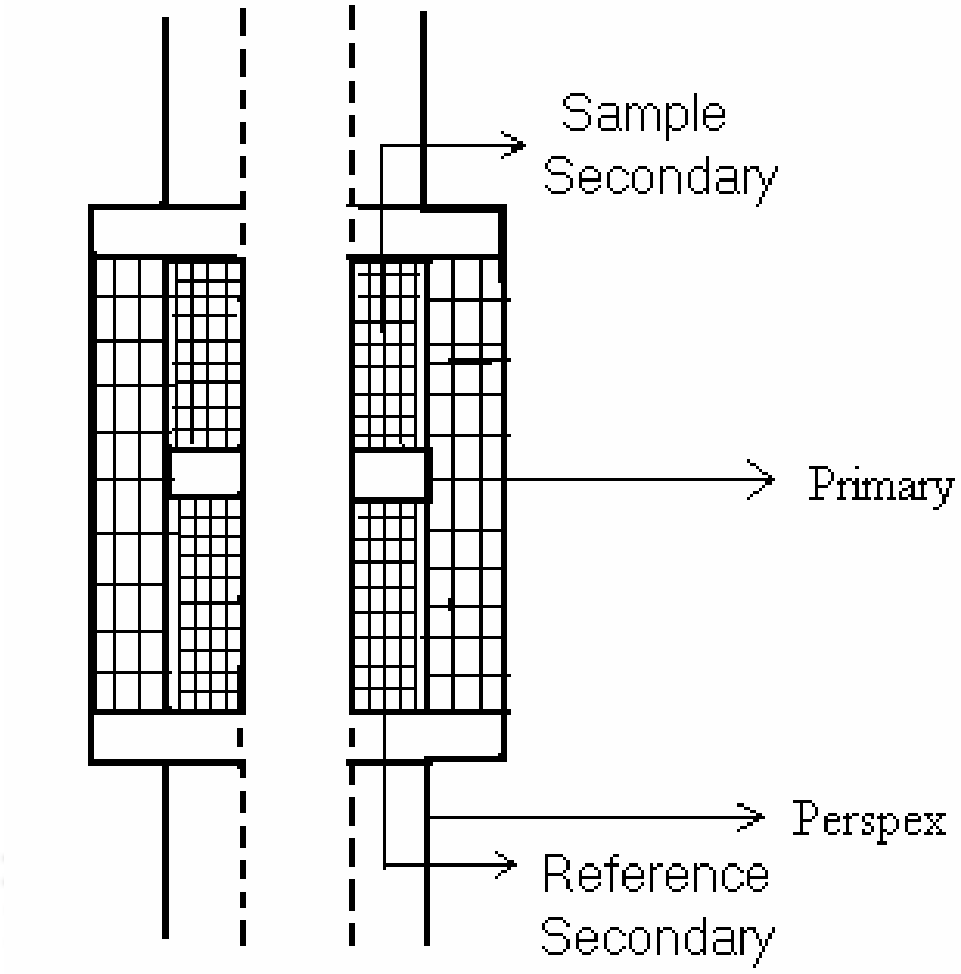

Figure 2.8: Block diagram of Mutual Inductance Coil assembly.

along the axis of the solenoid (primary coil) corresponding to applied voltage in the primary. In the absence of the sample, the induced voltage in each secondary coil would be almost equal and its differential output would be close to zero. When sample is inserted into sample secondary coil, the induced emf, e is a measure of susceptibility of the material, as given in the following expression [247],

$$e = (\alpha n_s V_s \omega \mu_0 H_0)\chi \qquad \text{---------- (2.17)}$$

where, n_s is the number of turns per unit length in the secondary coil; ω is the angular frequency of input signal to primary coil and V_s is the volume of the sample. The filling factor coefficient, α depends on the geometry and dimension of the sample and secondary coils. χ is the susceptibility of the material.

TH-1060_06612103

The outline of the mutual inductance coil assembly is shown in figure 2.8. Two identical secondary coils of length 15 mm each were wound with 39SWG (diameter 0.1312 mm) insulated copper wire on a Perspex tube of outer diameter 12 mm and inner diameter 6 mm. They were separated by a distance of 3 mm along the length of the coil. The primary coil with same SWG was wound over the secondary coils with inner diameter 18 mm and outer diameter 23 mm. The number of turns in each secondary coil was 1370 and that of primary coil was 2689.

The temperature variation down to 20 K was achieved using a closed cycle Helium refrigerator cryostat along with the temperature controller. However, a separate sample insert assembly was fabricated for ac susceptibility measurements. The schematic diagram of the CCR cryostat is shown in figure 2.9. The sample chamber of $1^{//}$ diameter is covered by non-magnetic radiation shield and vacuum shroud as shown in figure 2.9. The sample chamber is cooled with the help of helium exchange gas.

A sample insert assembly attached with a sample holder has been designed and fabricated for quick loading and unloading of samples. The schematic diagram of the sample insert assembly along with Coil housing assembly for mutual inductance bridge is shown in figure 2.10. A non magnetic thin walled stainless steel (SS) tube with outer diameter 10 mm and length 550 mm is coupled to the sample holder made up of Perspex rod of length 100 mm. The bottom part of Perspex rod was made into a flat surface to load the sample and temperature sensor. The other end of the SS tube passing through the Wilson nut is fitted with an electrical feed through and it is used for connecting the sensor leads mounted nearby sample area. Electrical feed through adapter attached to aluminum flange was used for connecting the primary and secondary Coil leads. The position of sample holder can be adjusted with the help of Wilson nut arrangement. A Lakeshore supplied Si diode sensor, which follows a standard curve was mounted in the vicinity of sample position as shown in the figure 2.10.

The block diagram of the ac susceptibility set-up is shown in figure 2.11. The primary coil is connected to the oscillator output of a dual phase lock-in amplifier supplied by Perkin–Elmer, model no. 7265. The maximum oscillator output of lock-in amplifier is 5V (rms). The magnetic field was calculated using the standard relation of the solenoid,

TH-1060_06612103

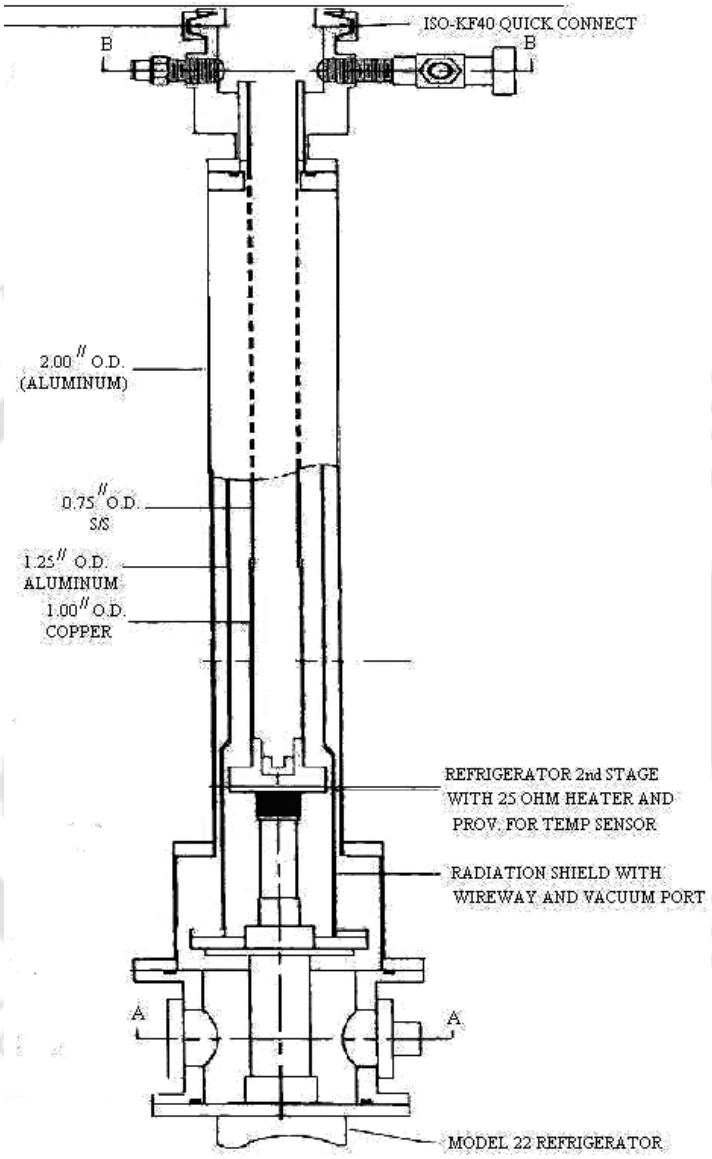

Figure 2.9: Block diagram of CCR cryostat.

TH-1060_06612103

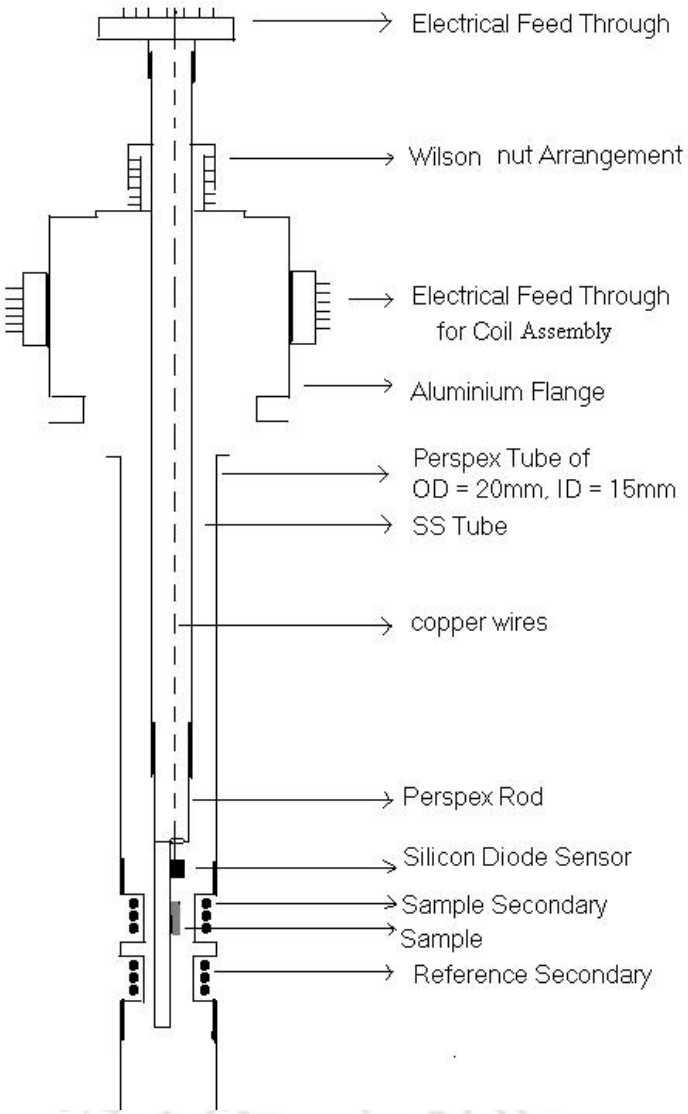

Figure 2.10: Sample insert and Coil housing assembly.

TH-1060_06612103

$$H = \frac{NI}{L} \text{ (A/m)} \qquad \text{---------- (2.18)}$$

or,

$$H = \frac{NI}{L} 4\pi \times 10^{-3} \text{ (Oe)} \qquad \text{---------- (2.19)}$$

Here, N is the total number of turns in the primary coil, I is the amplitude of current flowing through the primary in Ampere and L is the length of primary in meter. The maximum amplitude of magnetic field in the present set-up was found to be around 12 Oe. The output signals of both the secondary coils were connected to the differential input (A-B) of the lock-in amplifier, which can measure the in-phase and out of phase components of ac susceptibility signal simultaneously. For controlling the temperature, Lakeshore supplied silicon diode sensor (model no. DT-470) has been used. This sensor was mounted at the cold tip of the CCR, where a heater wire of 50Ω resistance was also installed. Four leads of the controlling sensor were connected to the A-channel input of the Lakeshore supplied temperature controller model no. 331. The sample temperature was measured using another silicon diode sensor (model no. DT-670) which was connected to the B-channel input of the temperature controller. Both the temperature controller and the lock-in amplifier were connected to a personal computer equipped with a GPIB board for data acquisition. The necessary software in the language of Quick Basic was developed for running the temperature variation of ac susceptibility. The accuracy of temperature measurement was ±50 mK.

To completely separate the real and imaginary components of ac susceptibility, appropriate reference phase angle needs to be set, in the lock-in amplifier. The phase angle ϕ was obtained by adjusting the reference phase in the lock-in amplifier such that the signal of the out of phase (loss/imaginary component) component is zero above the FM transition temperature. One can also numerically separate the real and imaginary components, by measuring the susceptibility in zero phase and using the following expressions [248],

$$\chi' = \chi_0' \cos\phi + \chi_0'' \sin\phi \qquad \text{---------- (2.20)}$$

$$\chi'' = \chi_0'' \cos\phi - \chi_0' \sin\phi \qquad \text{---------- (2.21)}$$

Where χ_0' and χ_0'' are the measured susceptibilities before phase adjustment (at zero phase).

TH-1060_06612103

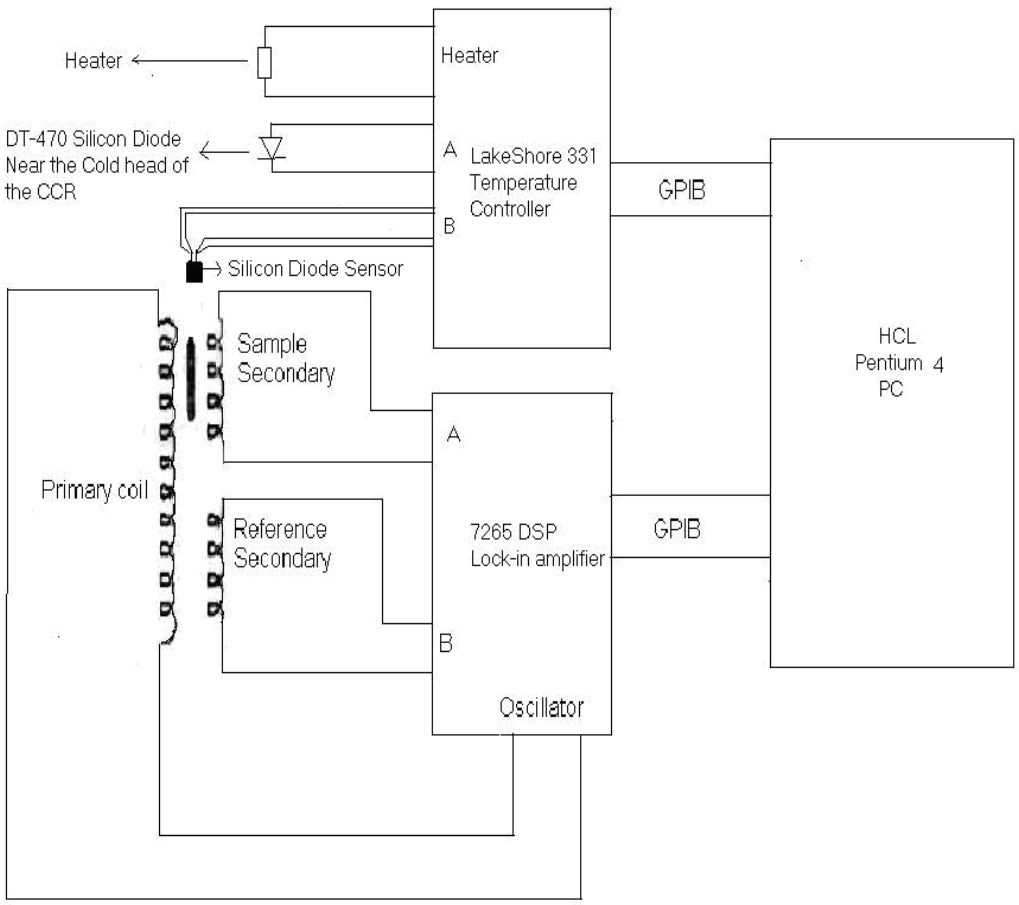

Figure 2.11: Block diagram of ac susceptibility set-up.

AC susceptibility measurement is a compatible technique to probe the associated magnetic phase and its sensitivity towards several influencing factors of a system. Investigation of the nonlinear χ_{ac} is one of the most important tools to understand any magnetic phase transition. In general, the nonlinearity of magnetization (M) can be expanded with the help of power series with respect to an oscillating applied magnetic field (H) as,

$$M = \chi_1 H + \chi_2 H^2 + \chi_3 H^3 + \ldots\ldots\ldots\ldots \quad \text{---------- (2.22)}$$

Here χ_1, χ_2 and χ_3 etc. are, respectively, linear, second and third harmonic susceptibilities. In fact, several subtle features not discernible using linear χ_{ac} can be picked up using nonlinear χ_{ac}. Direct measurement of the non-linear susceptibility, gives the choice to us to clearly distinguish the spin glass freezing from to other non-equilibrium systems like super-paramagnetism. According to the critical behavior of spin glass material, $\chi_3 \propto \varepsilon^{-\gamma}$, where $\varepsilon = (T-T_g)/T_g$ and γ is the critical exponent. The non-linear susceptibility was measured by setting a appropriate harmonic selection in the lock-in-amplifier.

TH-1060_06612103

Calibration of the ac susceptometer was carried out by using the standard paramagnetic salts Gd_2O_3 [249]. Its temperature dependent gram susceptibility is given as, [250]

$$\chi = \frac{45684}{T+18} \times 10^{-6} \text{ c.g.s} \qquad \text{---------- (2.23)}$$

where T is the temperature and in the unit of Kelvin.

2.10. DC Magnetization Measurement

DC magnetization as a function of temperature, field and time was measured by using the vibrating sample magnetometer (VSM) (model no. 7410) made by Lakeshore, and a superconducting quantum interference device (SQUID) magnetometer (Quantum Design) at Institut Neel, CNRS Grenoble, France and a high field magnetometer (developed at Institut Neel, CNRS Grenoble, France).

2.10.1. Vibrating Sample Magnetometer (VSM)

The vibrating sample magnetometer (VSM) has become a widely used instrument for measuring the magnetic properties of a large variety of magnetic materials. The vibrating sample magnetometer (VSM) developed originally by Foner [251] has however, been the most successful for low temperature and high magnetic field studies of correlated electron systems. It has a flexible design and combines high sensitivity with ease of sample mounting and exchange. Samples can be changed rapidly even at any operating temperature. Using a vibrating sample magnetometer, one can measure the DC magnetic moment as a function of temperature, magnetic field and time. So, it allows to perform susceptibility and magnetization studies. Magnetic moments as small as 5×10^{-5} emu are measurable with a VSM [251].

The temperature variations of zero field cooled (ZFC) and field cooled (FC) magnetization (M) were measured by using the Lakeshore, model no. 7410 vibrating sample magnetometer. The temperature variation down to 20 K was achieved using a OXFORD make CCR cryostat (model X 74019-044) along with the temperature controller. The magnetic field was produced by using a 10 $^{//}$ electromagnet. The magnetization loop was measured by varying B up to 2 T. Calibration of the vibrating sample magnetometer was done by measuring the magnetic moment of a standard pure Ni sample. Block diagram of the

TH-1060_06612103

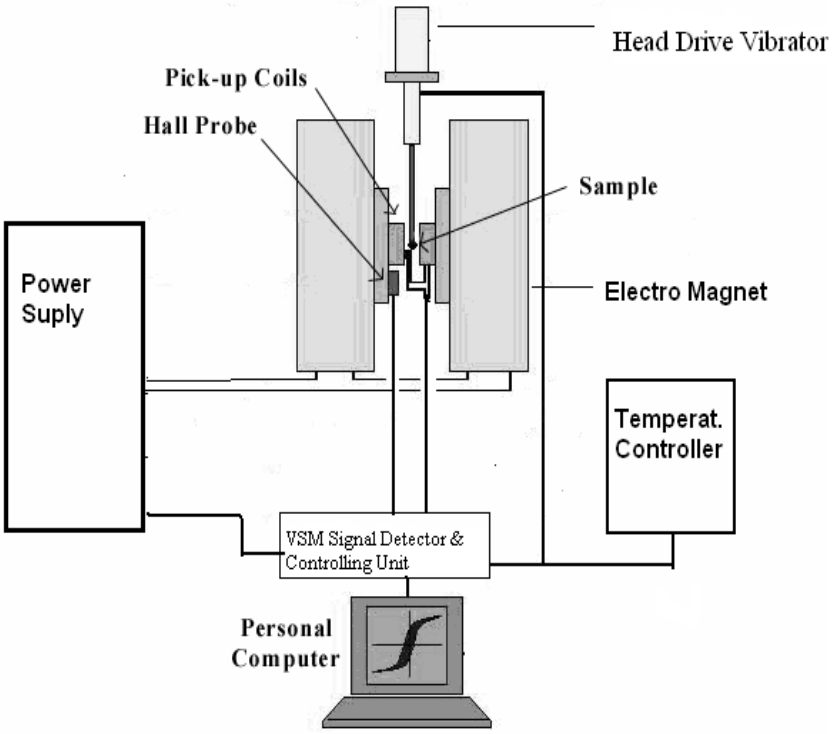

Figure 2.12: Block diagram of the vibrating sample magnetometer.

vibrating sample magnetometer is shown in figure 2.12.

The VSM is based upon Faraday's law, according to which an emf is induced in a conductor by a time-varying magnetic flux. If a sample of any magnetic material is placed in a uniform magnetic field, a dipole moment will be induced. If the sample vibrates with sinusoidal motion, there is some magnetic flux change. This induces a voltage in the pick-up coils, which is proportional to the magnetic moment of the sample. Voltage, V(t) can be detected to a high resolution and accuracy by means of suitable VSM signal detector (e.g. Lock in Amplifier).

2.10.2. SQUID Magnetometer

The magnetization measurements were also carried out by using superconducting quantum interference device (SQUID, MPMS XL 7) magnetometer (Quantum Design) and high field magnetometer (developed at Institut Neel, CNRS Grenoble, France).

The main components of a SQUID magnetometer are: (A) SQUID probe (B) Temperature control system (C) Pick up coil (D) SQUID detection unit (E) Superconducting

TH-1060_06612103

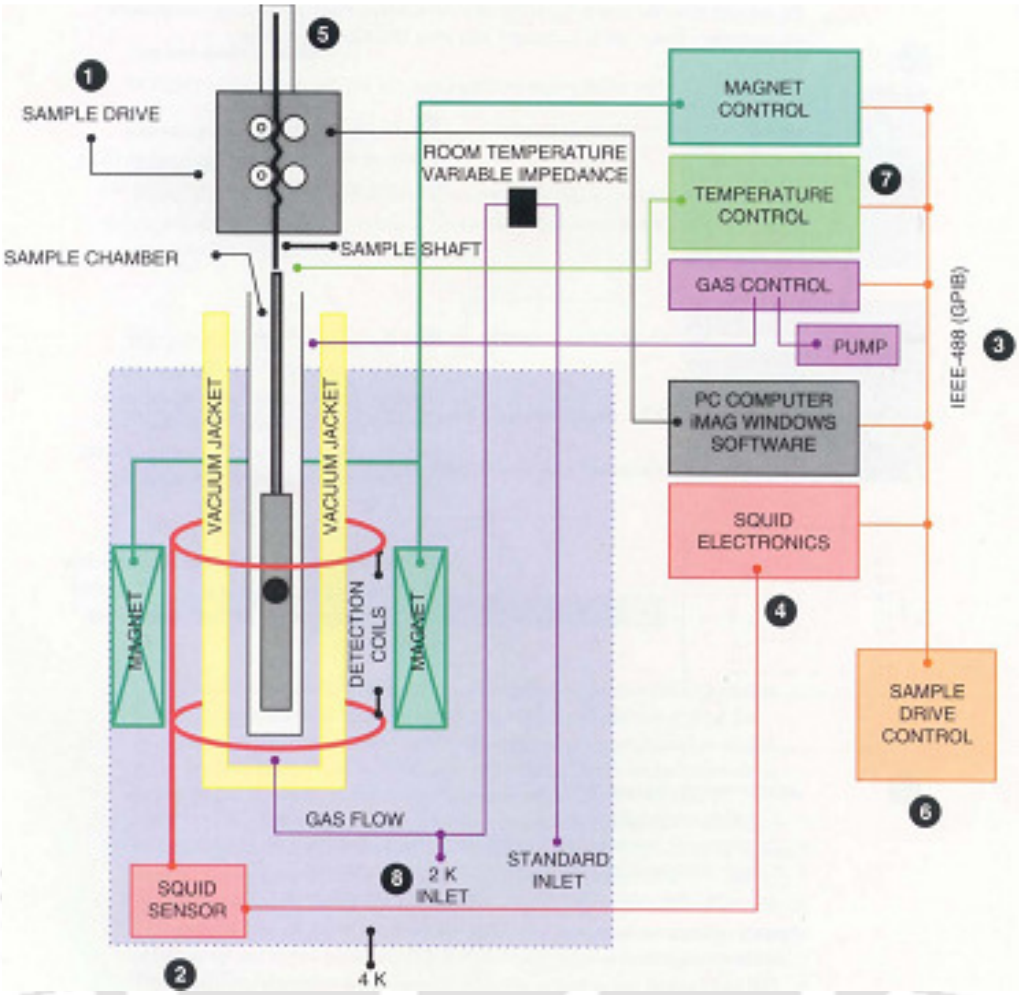

Figure 2.13: Block diagram of the SQUID magnetometer.

magnetic shield. The block diagram for SQUID magnetometer is shown in figure 2.13. A brief detail about these components and the principle of operation of SQUID magnetometer are given below.

(A) SQUID Probe: The SQUID probe as shown in figure 2.14 is inserted in liquid helium dewar. The sample rod is made with an upper section of needle temper type 304 stainless steel and a bottom section of silicon copper alloy. The stainless steel is used for strength, good surface finish and low thermal conductivity. The lower section is made from silicon copper alloy to minimize the magnetic signal in the SQUID detector due to the sample rod. Sample may be mounted on the end of the sample rod by using a plastic drinking straw. The straw has minimal magnetic susceptibility. The sample is wrapped by teflon tape and is

TH-1060_06612103

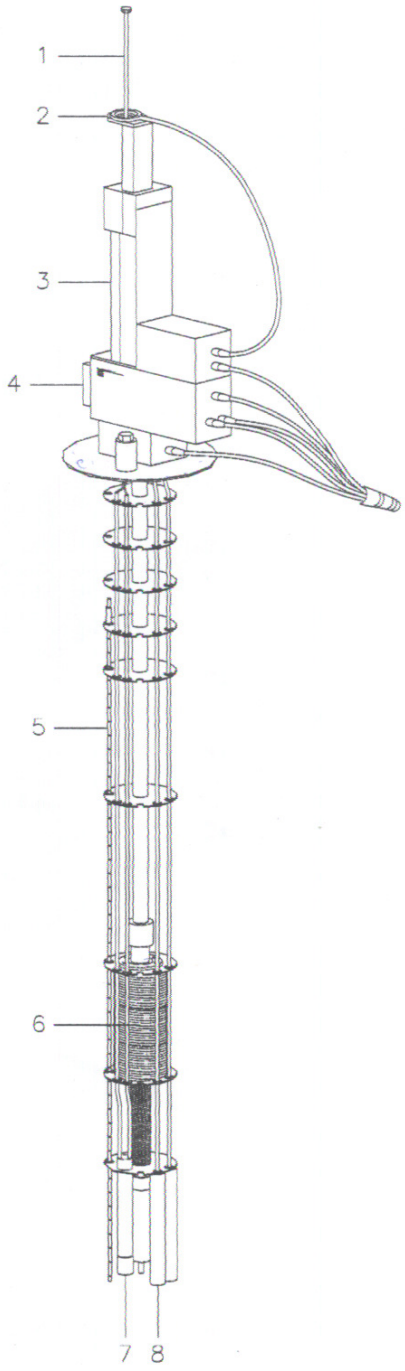

System Components

1. **Sample Rod**
2. **Sample Rotator**
3. **Sample Transport**
4. **Probe**
5. **Helium Level Sensor**
6. **Superconducting Solenoid**
7. **Flow Impedance**
8. **SQUID Capsule**

Figure 2.14: SQUID probe components.

TH-1060_06612103

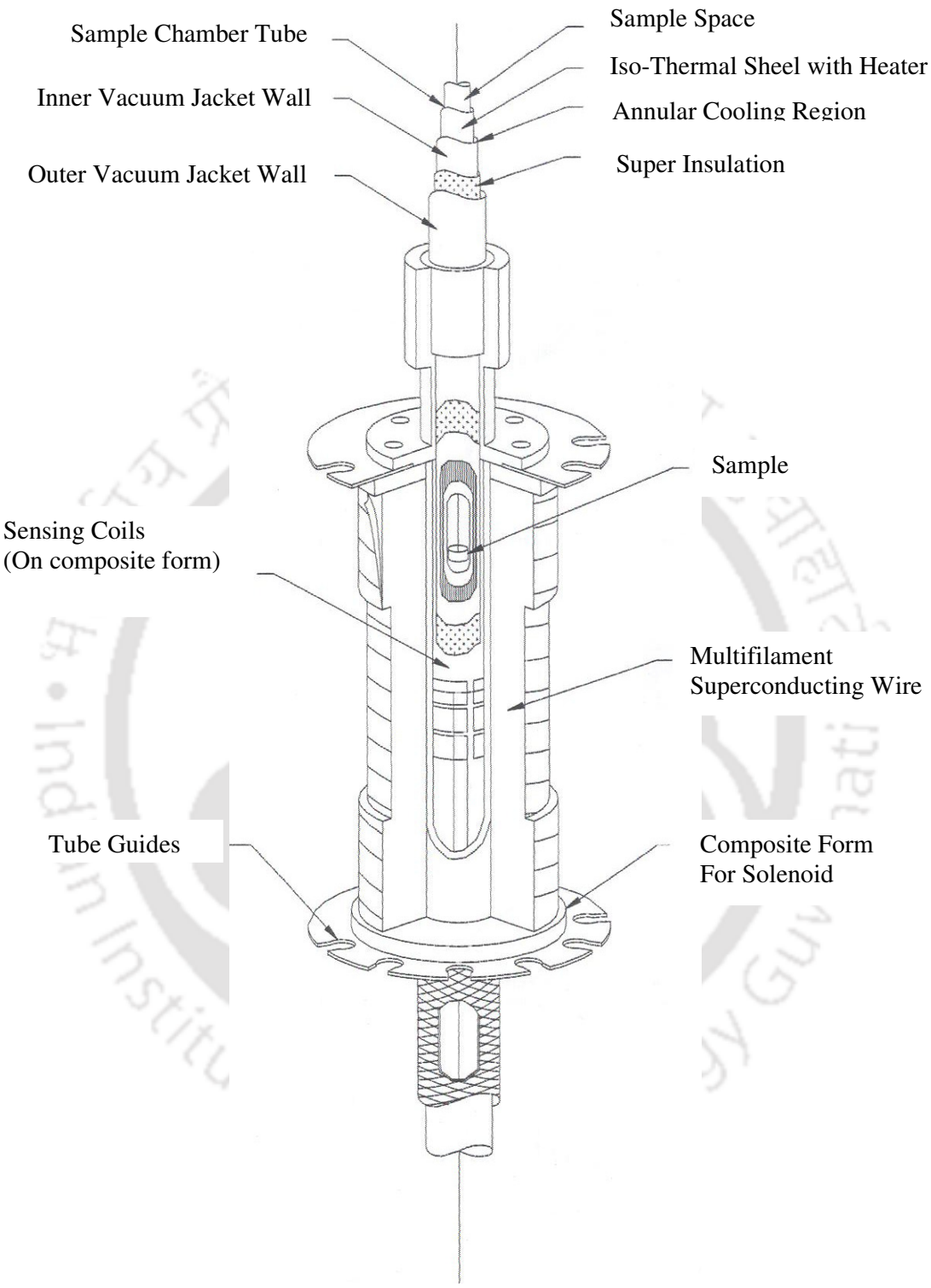

Figure 2.15: Superconducting magnet components.

TH-1060_06612103

inserted tightly in the middle of the plastic straw. Sample rotator helps to rotate the sample at the time of mounting. The sample transport allows for moving the sample in vertical direction, which is required for DC centering. Moreover, the sample centering process includes performing a full length DC scan, adjusting the sample position, and then performing a DC centering scan to get maximum moment from the sample. The helium level in the dewar is monitored with helium level sensor.

A superconducting magnet is a solenoid made up of superconducting wire. This solenoid is kept at liquid helium temperature in a liquid-helium Dewar. The uniform magnetic field is produced along the axial cylindrical bore of the coil. A superconducting magnet requires an appropriate programmable bipolar power supply to operate it. The superconducting magnet system provides reversible field operation up to plus and minus 7 tesla (depending upon the system configuration). The cut view of a superconducting magnet is shown in figure 2.15.

(B) Temperature Control system: Temperature for the SQUID is achieved by components within the Temperature Controller Module (TCM) under the active control of the model 1820R/G bridge, the model 1822 controller, and the control software. Stable and continuous operation at any temperature from 1.9 to 400 K is possible with MPMS system. Temperature sweeps from 0.001 to 10 K /Min are possible, with smooth transition from above or below 4.2 K. The control system utilizes a third order PID feedback technique to maximize response to large changes as well as minimizing temperature variations at any set-point temperature. The block diagram of TCM is shown in figure 2.16. Two negative temperature coefficient (NTC) thermometers are used for temperature sensing; the primary sensor is located at the null point of the SQUID pick up coils, and the secondary sensor is located under the bottom of the sample tube. Both the thermometers are used for temperatures above 14 K, while at temperatures below 14 K, only the bottom thermometer is active. Strong magnetic fields can affect the accuracy of the thermometers at temperatures below 14 K. Only the bottom thermometer is used in this temperature range, since it is shielded from magnetic fields.

Cooling power above 4.2 K is provided by allowing a controlled amount of liquid helium from the dewar to enter the bottom of the cooling annulus. Liquid helium enters through the variable impedance inlet and is called flow impedance. The liquid helium turns into gas, which flows through the cooling annulus and is pumped from the top of the probe by vacuum pump. Longitudinal copper wires along the length of the sample chamber maintain

TH-1060_06612103

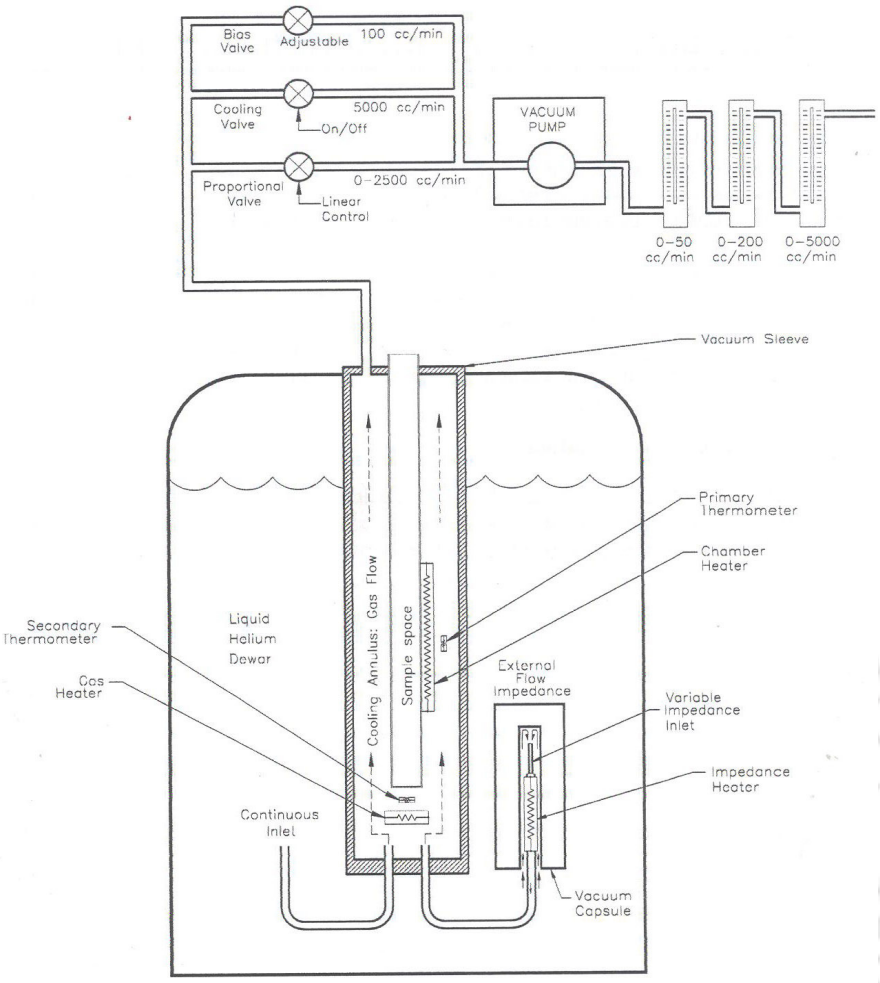

Figure 2.16: Temperature controller module elements.

the thermal uniformity, and a few millimeters pressure of helium gas in the sample chamber provide the thermal contact with the sample.

Sample space heating is accomplished with the use of the gas heater and the chamber heater. The gas heater pre-heats the helium gas by applying power regulated by the system, the gas then surrounds the sample space, transferring thermal energy to the sample tube. The chamber heater directly heats the outside surface of the sample tube in a uniform manner by warming heating coils that are wrapped around the sample space.

(C) Pick up coil: This is a single piece of superconducting wire configured as a second-order gradiometer with a total length of approximately 3 cm as shown in figure 2.17. In this geometry, this pick-up coil system is placed in the uniform magnetic field region of the solenoidal superconducting magnet. The SQUID coils detect the longitudinal component of

TH-1060_06612103

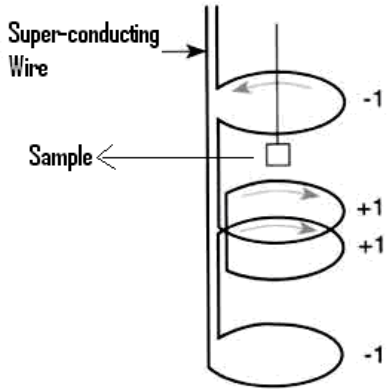

Figure 2.17: Second-order gradiometer superconducting pick-up coils.

the magnetization as the sample is pulled through them. When the sample is pulled up and down, it produces an alternating magnetic flux in the pick up coil which leads to induced emf. Pick-up coil system is connected to the SQUID, which experiences the alternating voltage, depending on the moment of the sample.

(C) SQUID (detection unit): The SQUID detection system consists of SQUID sensing pick-up loops, a superconducting transformer with an RFI shield, and the SQUID amplifier (model 2000) control electronics. The SQUID utilizes the Josephson (the weak link) effect in superconducting ring, where the flux passing through the weak link is quantized. The SQUID consists of a superconducting loop with one (rf SQUID) or two (dc SQUID) weak link

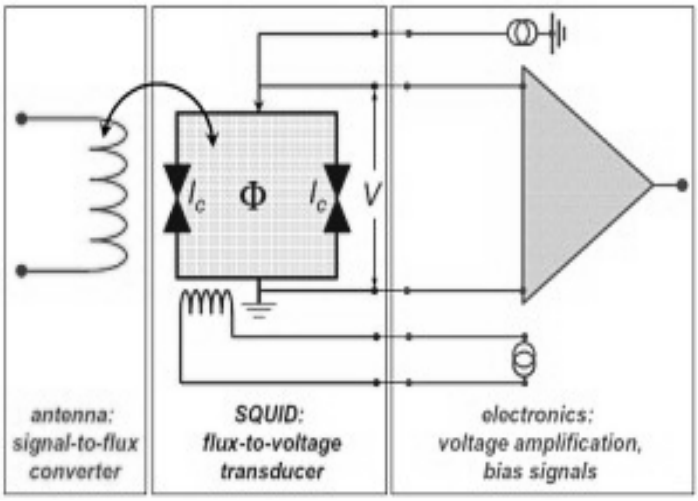

Figure 2.18: SQUID magnetometer-flux-to-voltage converter.

TH-1060_06612103

Josephson junctions. The electrical current density through the Josephson junctions depends on the phase difference in wave functions ΔΦ between two parts of the superconductors. Moreover, the time derivative of ΔΦ is correlated with voltage across the Josephson junctions. A change in the magnetic flux in the pickup coils changes the persistent current in the detection circuit. So, the change in the current in the detection coils produces variation in the SQUID output voltage proportional to the magnetic moment of the sample. The above operation is schematically shown in figure 2.18.

(D) Superconducting magnetic shield: It is used to shield the SQUID sensor from the fluctuations of the ambient magnetic field of the place where the magnetometer is located and from the large magnetic field produced by the superconducting magnet.

Magnetization measurement:

To carry out temperature and field variation of magnetization measurement, initially the sample is mounted at the bottom of the sample rod through a plastic drinking straw as a sample holder as discussed above. The sample chamber is purged three times by helium gas. After sample mounting, the DC centering is needed to gain maximum magnetic moment in the SQUID pick coil. Now the system is allowed to perform *M* versus *T* or *M* versus *H* measurements. The temperature can varied from 1.9 to 400 K with the help of TCM system as discussed in temperature controller system. The magnetic field can be changed in two operating mode, i.e., oscillate and no overshoot. The magnetic field applied to the sample is just due to the current from a Kepco power supply (Model JQE 6-45M-22103) in the magnet in its persistent mode. In persistent mode, during the change in magnetic field, the magnetic field will gradually relax due to the magnetic field lines slowly creeping through the superconducting winding. During *M* versus *H* measurement it is important to choose no overshoot mode.

2.11. Electrical Resistivity and Magneto-Resistivity Measurements

Temperature variation of dc electrical resistivity and transverse magneto-resistivity measurements down to 20 K were carried out to study the electrical transport. For carrying out the above measurements, a top loading helium exchange gas cooled type closed cycle helium refrigerator cryostat fabricated by; Cryo Industries of America, USA using a CTI

TH-1060_06612103

make compressor and cold head motor has been used. The temperature was controlled using a Lakeshore temperature controller, Model no.331 and a Lakeshore calibrated Si-diode sensor mounted on the cold head. The sample can be positioned at the centre of pole face using the Wilson nut arrangement. The pole pieces of $10^{//}$ diameter are tapered to $3^{//}$ diameter. The magneto-resistivity measurements have been carried out by applying a magnetic field strength of 10 kOe (1 T).

Standard linear four probe technique was used to eliminate the contribution from contact resistance and lead resistance coming into picture. Current through the sample was passed using a programmable Keithley constant current source, model no. 224. The voltage drop across the sample was measured using Keithley nanovoltmeter, model no. 2182. To eliminate the thermo-emf generated across the voltage leads, measurements were carried out for both positive and negative currents. The experimental data were collected using a personal computer equipped with GPIB board. The Fabricated sample holder attached to the CCR cryostat for resistivity and Magneto-resistivity measurements is shown in figure 2.19. The necessary software in quick Basic language was developed for temperature controlling and data acquisition using a personal computer.

A typical current of 1 mA was passed through the sample using the above current source, the voltage drop arises at the voltage terminals found on the sample are measured using the Keithley nano-voltmeter. The current was reversed and again voltage drop was measured. From the measured current and voltage the resistance of the sample was calculated. For calculation of electrical resistivity, the dimension of the samples was determined by using a screw gauge and the distance between the voltage leads were measured by using a travelling microscope.

TH-1060_06612103

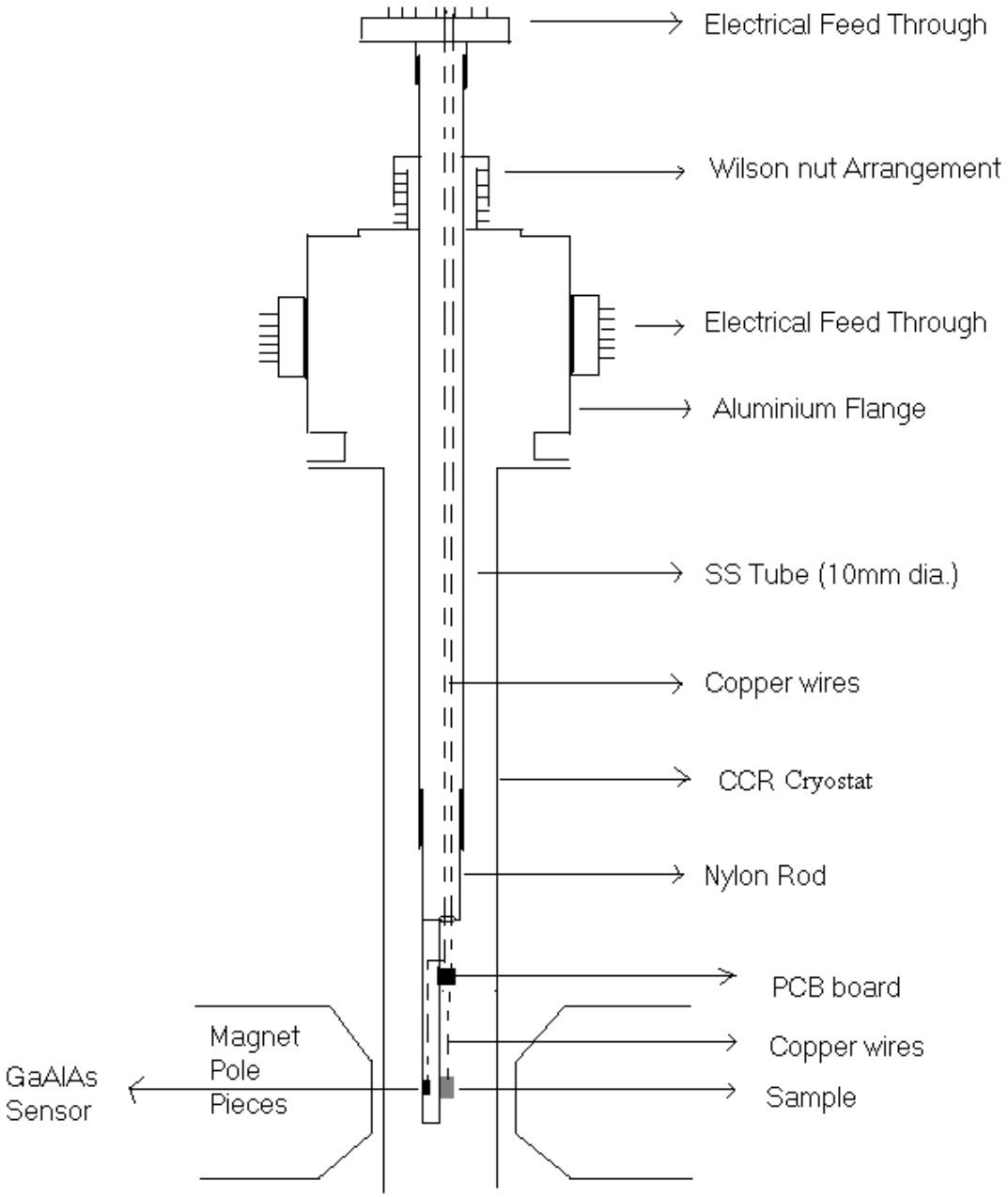

Figure 2.19: Fabricated sample holder attached to the CCR cryostat for resistivity and Magneto-resistivity measurements.

TH-1060_06612103

Chapter 3: (Nd, K)-Mn-O Series

Nd-Mn-O series falls in the category of medium size e_g electron bandwidth and hence the ionic size of doped materials plays a very sensitive and crucial role in tuning the electrical transport and magnetic properties in this system. Even though, there are several reports on divalent alkaline earth doped Nd-Mn-O series, the work on mono-valent doping in place of Nd is limited. The monovalent doping has some advantage over divalent doping. Each doped mono-valent atom oxidizes two Mn ions from Mn^{3+} to Mn^{4+} state. Thus, the optimum ratio of Mn^{3+} and Mn^{4+} ions can be obtained by doping relatively small fraction of monovalent atoms and hence with minimum lattice distortion. The K doping in $La_{1-x}K_xMnO_3$ series has been found to be quite successful in achieving CMR behavior with transition temperature as high as 330K [29, 172, 252]. Magnetoresistance of 40% was reported in the above series for a field of 5.6 T at 300 K. The ionic size of K^{1+} is greater than some of the alkaline earth and other alkali ions, so, the K doped Nd-Mn-O series, i.e., $Nd_{1-x}K_xMnO_3$ compounds for x = 0.10 to 0.30 were prepared. The crystal structure, magnetic structure, magnetic properties and electrical transport properties of $Nd_{1-x}K_xMnO_3$ compounds are presented in this chapter. These materials are found to exhibit interesting magnetic properties such as FM, spin canting and re-entrant spin glass behaviors. The study of critical exponent behavior in the vicinity of FM transition is also presented.

3.1. Sample Preparation and Characterization

Polycrystalline samples of $Nd_{1-x}K_xMnO_3$ (x= 0.10, 0.15, 0.20, and 0.30) were prepared by conventional solid state reaction method. Stoichiometric ratio of Nd_2O_3, K_2CO_3 and manganese acetate with 99.9% purity were weighed and mixed thoroughly under acetone. The mixture was presintered at 300 ^{0}C, 400 ^{0}C, 500 ^{0}C, 600 ^{0}C and 700 ^{0}C for 6 hrs. at each temperature and at 800 ^{0}C for 24 hrs with intermediate grindings. The powdered samples were pressed into pellet form and were sintered at 1000 ^{0}C for 24 h. The final sintering in pellet form was carried out at 1200 ^{0}C for 40 h.

The $Nd_{1-x}K_xMnO_3$ compounds for x = 0.10 to 0.30 are found to be in single phase form as per their XRD patterns. The XRD patterns for these samples are shown in figure 3.1. The patterns could be refined by using *Pnma* space group in orthorhombic cell. The typical XRD patterns alongwith Rietveld refinement are shown in figure 3.2 for x = 0.10 and 0.30 samples. The lattice parameters determined from XRD analysis are given in table 3.1.

TH-1060_06612103

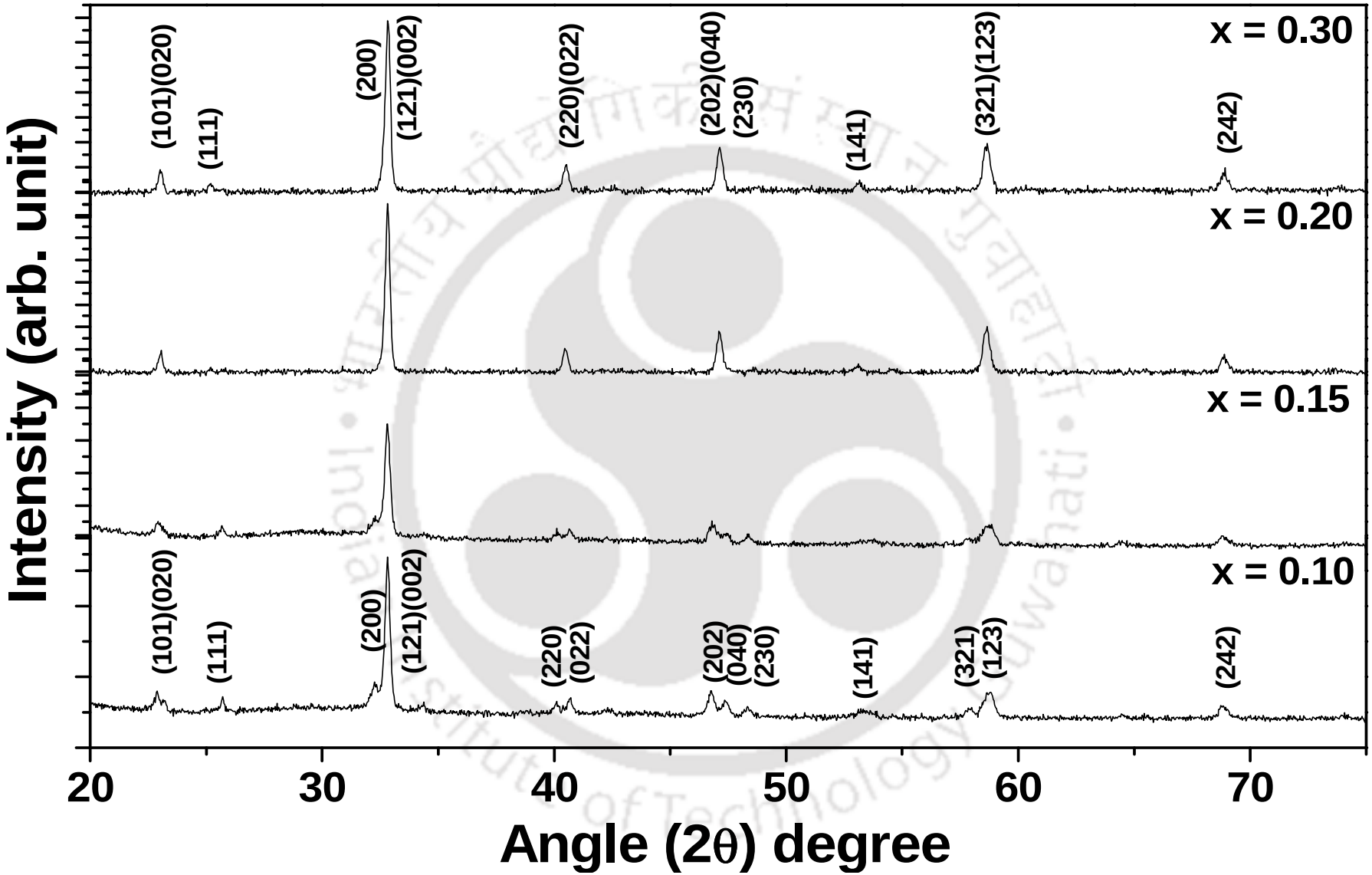

Figure 3.1: XRD patterns of the samples $Nd_{1-x}K_xMnO_3$ for x = 0.10-0.30.

TH-1060_06612103

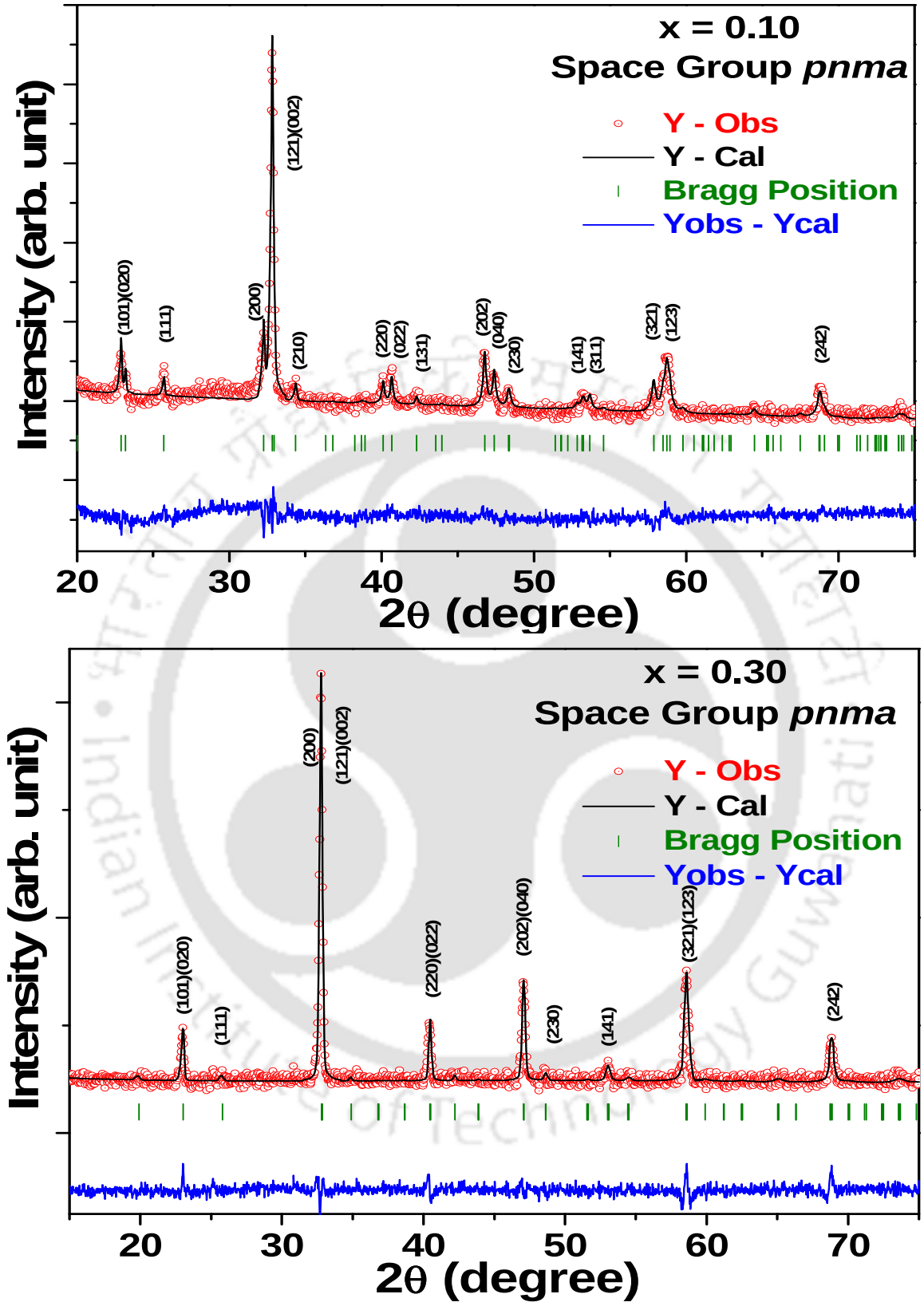

Figure 3.2: XRD patterns for x = 0.10 and x = 0.30 samples. The circles represent experimental points and solid line represents Rietveld refined data. The bottom line shows the difference between experimental and refined data. The marked 2θ positions are the allowed Bragg peaks.

TH-1060_06612103

Table 3.1: Parameters obtained from the Rietveld analysis of XRD patterns of $Nd_{1-x}K_xMnO_3$ (x= 0.10, 0.15, 0.20, & 0.30). The numbers in brackets are estimated errors.

Samples/ parameters	**x = 0.10**	**x = 0.15**	**x = 0.20**	**0.30**
χ^2	1.77	1.70	1.79	2.86
R_p(%)	4.75	4.50	4.85	5.70
a (Å)	5.5521 (0.0015)	5.54654 (0.0026)	5.5498 (0.0031)	5.4563 (0.0030)
b (Å)	7.6731 (0.0022)	7.6813 (0.0036)	7.6828 (0.0043)	7.7248 (0.0012)
c (Å)	5.4405 (0.0014)	5.4441 (0.0021)	5.4525 (0.0026)	5.4660 (0.0025)
Volume (Å)^3	231.7	231.6	231.9	230.4
Mn Valency	3.24	3.35	3.46	3.52

The lattice parameters are found to be larger than those reported for Na and Ag doped Nd-Mn-O series [226-228, 231].The lattice parameters *b* and *c* are found to increase with increase in doping concentration and on the other hand, no such systematic variation in parameter *a* is observed. This can be understood on the basis of competition between larger K^{1+} ions replacing Nd^{3+} ions and the generation of smaller Mn^{4+} ions at the expense of larger Mn^{3+} ions. The Mn-O bond lengths and Mn-O-Mn bond angles are found to in the order of 1.9358 Å and 160°. Even though, the Mn valency is found to increase systematically with doping, the actual Mn valency for a particular doping concentration is found to be marginally larger than that of expected values and such behavior is mainly due to possible oxygen off-stoichiometry. The presence of oxygen off-stoichiometry has been reported by Zhong *et al.* [253], from a systematic measurement of oxygen contents. The average valency of Mn is listed in table 3.1. The systematic increase in Mn valency, with K substitution highlights the formation of Mn^{3+}/Mn^{4+} mixture with increase in Mn^{4+} concentration. SEM micrographs of the above samples are shown in figure 3.3. The microstructure morphology of the samples is found to be uniform with average particle size 400, 450, 270, and 250 nm for x = 0.10, 0.15, 0.20, and x = 0.30 samples respectively. Typical EDS spectrum for x = 0.15 sample is shown in figure 3.4. The chemical compositions determined from EDS analysis are found to be comparable to the nominal starting composition. The cationic ratio for all the samples is given in table 3.2.

TH-1060_06612103

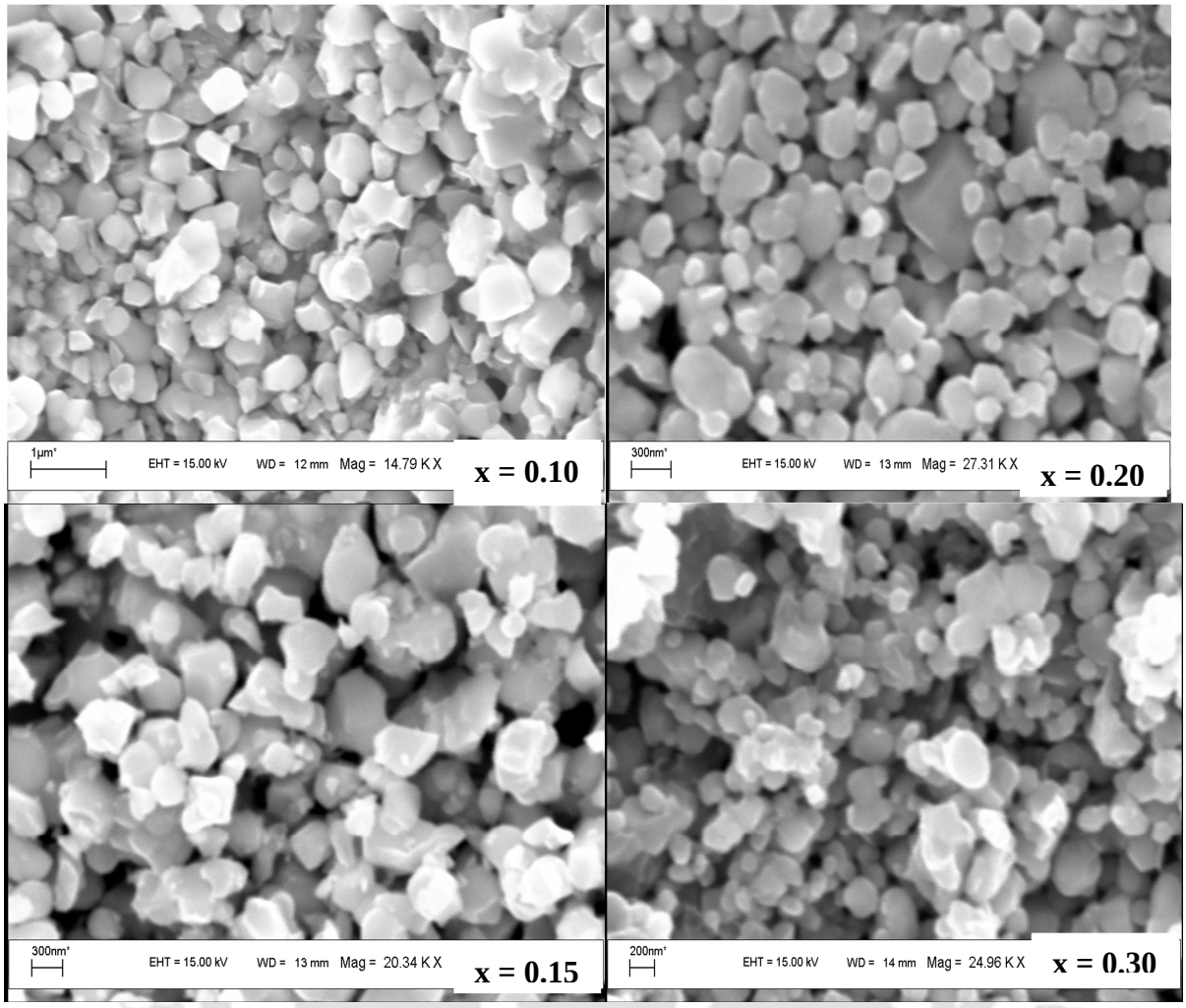

Figure 3.3: SEM images of x = 0.10, 0.15, 0.20 and 0.30 samples.

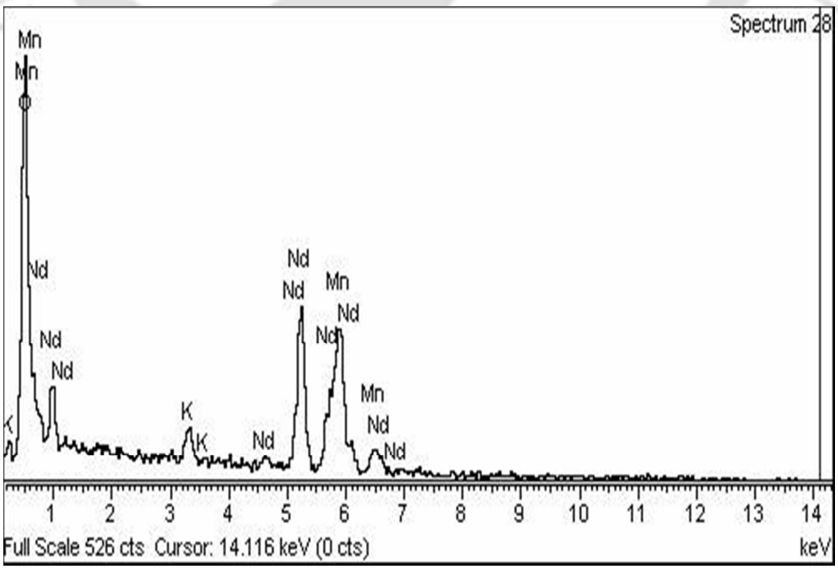

Figure 3.4: Typical EDS spectrum for $Nd_{0.85}K_{0.15}MnO_3$ sample.

TH-1060_06612103

Table 3.2: The cationic ratio determined from EDS analysis for x = 0.10-0.30 samples.

Sample	Calculated Cationic Ratio from EDS		
	Nd	**K**	**Mn**
x = 0.10	0.90	0.07	1.00
x = 0.15	0.84	0.12	1.00
x = 0.20	0.84	0.16	1.00
x = 0.30	0.77	0.23	1.00

3.2. Neutron Powder Diffraction

Neutron powder diffraction (NPD) patterns were recorded at selected temperatures down to 22K for $Nd_{1-x}K_xMnO_3$ series for x = 0.15 and 0.20 samples. The NPD patterns recorded at 300K were refined by considering only the nuclear structure. On lowering the temperature, especially below the transition temperature T_C, enhancement in the intensity of some of the low angle fundamental reflections, (101) (121) are observed and it indicates the ferromagnetic ordering of the sample. The NPD patterns in the low angle region as a function of temperature are shown in figure 3.5 for x = 0.15 and 0.20 samples. The compounds are free from any impurity phase. All the Bragg peaks of x = 0.15 and 0.20 samples could be successfully refined to *Pnma* space group with orthorhombic structure. Typical diffraction patterns along with Rietveld refinement for x = 0.15 and 0.20 samples recorded at 300 K are shown in figure 3.6 (a) and (b) respectively. The refined structural parameters at 300 K are shown in table 3.3. The values of lattice parameters and unit cell volume are found to increase with K doping as a result of larger ionic size of K compared to Nd. The values of lattice parameter are found to decrease rapidly below the FM ordering temperature of 125 K as shown in figure 3.7 (a) and (b) for x = 0.15 and 0.20 samples respectively. Similar behavior is observed for unit cell volume. The same trend in lattice parameters and unit cell volume has been reported for the parent compound $NdMnO_3$ below the AFM ordering temperature, T_N = 78 K [177]. The temperature variation of Mn-O-Mn bond angles are shown in figure 3.7 (c) and (d) for x = 0.15 and 0.20 samples respectively, where a clear increase in average Mn-O-Mn bond angles below the FM T_C is observed and it signifies the strengthening of double exchange interaction. The stoichiometry ratio of the compounds as per the refinement of occupancy values for x = 0.15 and 0.20 samples are $Nd_{0.80}K_{0.15}MnO_{2.97}$ and $Nd_{0.76}K_{0.20}MnO_{3.09}$ respectively.

TH-1060_06612103

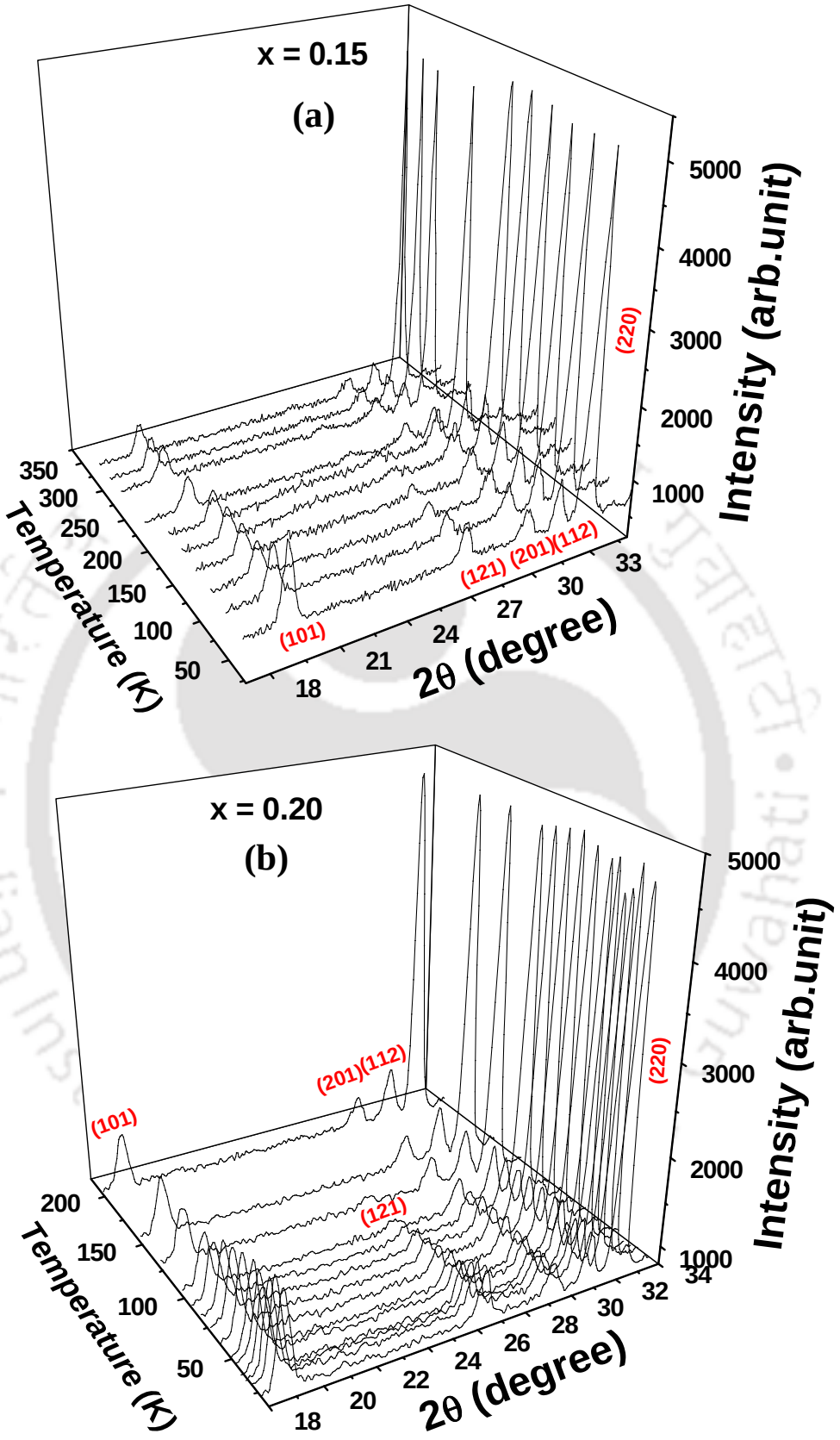

Figure 3.5: Evolution of low angle reflections of neutron diffraction patterns in the temperature range 22-200K for (a) x = 0.15 and (b) x = 0.20 samples.

TH-1060_06612103

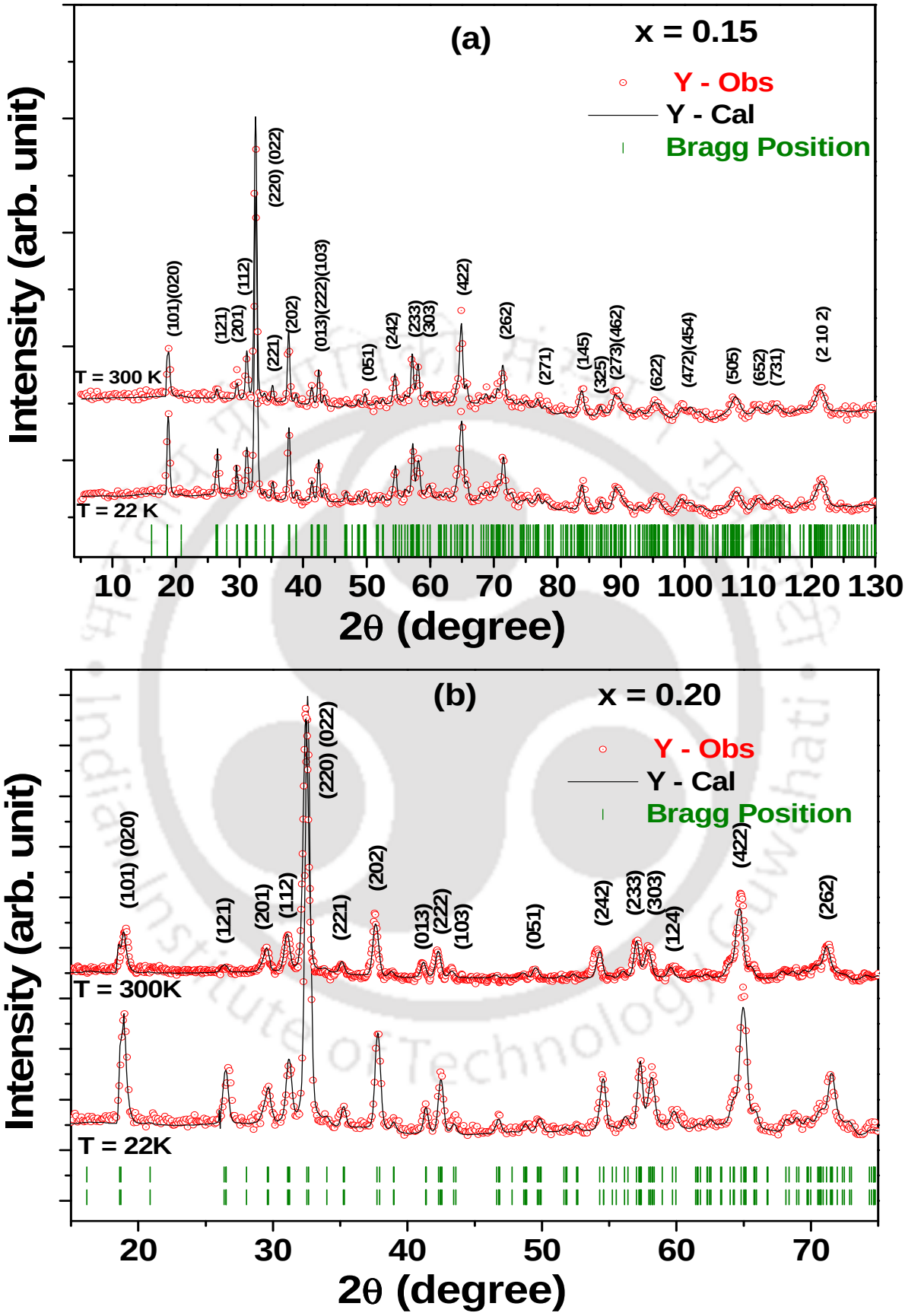

Figure 3.6: Rietveld refinement of neutron diffraction patterns of (a) x= 0.15 and (b) x = 0.20 compound at 300K and 22K.

TH-1060_06612103

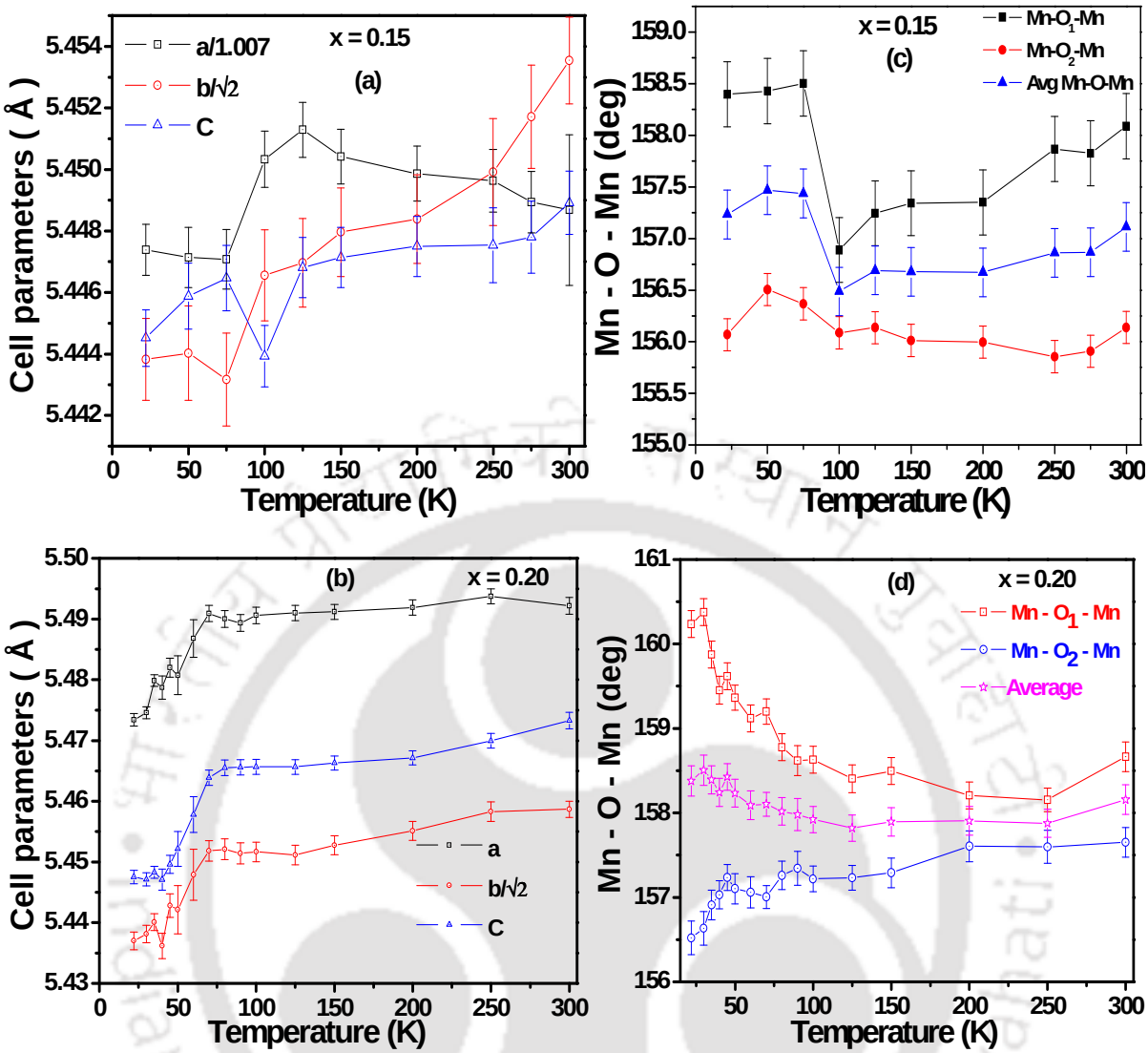

Figure 3.7: Temperature variations of lattice parameters for (a) x = 0.15 and (b) x = 0.20 and Mn-O-Mn bond angles for (c) x = 0.15 and (d) x = 0.20 samples respectively.

The increase in intensity of (101) and (121) peaks with decrease in temperature can be seen from figure 3.5 especially below 125 K depicting the ferromagnetic nature of the sample. We have not observed any new peak corresponding to antiferromagnetic structure. So, the magnetic reflections are dominated by ferromagnetic interactions. The low temperature patterns below 125 K could be refined by taking into account the ferromagnetic phase in addition to the nuclear phase. The Bragg positions for both the nuclear phase and magnetic phase are same. The patterns at low temperature were refined by varying the magnetic moments of Mn ions only. Attempt to refine Nd moments was not successful; so, there was no ordering of Nd moments in the measured temperature range. The NPD patterns along with Rietveld refinement for x = 0.15 and x = 0.20 samples recorded at 22K are shown in figure

TH-1060_06612103

Table 3.3: Structural and magnetic parameters obtained from the Rietveld refinement of the NPD patterns for $Nd_{1-x}K_xMnO_3$ (x = 0.15 and 0.20) compounds at 22 K and 300 K.

Refined Parameter	**x = 0.15**		**x = 0.20**	
	22K	300K	22K	300K
Space group	*Pnma*	*Pnma*	*pnma*	*pnma*
a (Å)	5.4855(08)	5.4868(24)	5.4745(09)	5.4921(13)
b (Å)	7.6975(13)	7.7183(44)	7.6895(14)	7.7185(13)
c (Å)	5.4445(09)	5.4450(30)	5.4471(10)	5.4732(13)
Volume ($Å^3$)	229.89(06)	230.59(21)	229.30(07)	232.02(09)
Mn-O_1(Å)	1.9591	1.9649	1.9509	1.9636
Mn-O_{21}(Å)	1.9766	1.9659	1.9649	1.9439
Mn-O_{22} (Å)	1.9736	1.9754	1.9782	2.0079
Mn-O_1-Mn	158.3	158.24	160.37(15)	158.66(17)
Mn-O_2-Mn	156.06	156.41	156.63(19)	157.65(17)
Mn/μ_B (FM)	2.82(05)	-----	2.59(05)	------
(Nd, K) (x, y, z)	{0.0288(5), ¼, 0.0009(10)}	{0.0155(13), ¼, -0.0046(14)}	{0.0233(2), ¼, 0.0009(3)}	{0.0286(8), ¼, -0.0079(4)}
(Mn) (x, y, z)	{0, 0, ½}	{0, 0, ½}	{0, 0, ½}	{0, 0, ½}
O_1 (x, y, z)	{0.4860(11), ¼, 0.0659(4)}	{0.4857(4), ¼, 0.0651(5)}	{0.4904(7), ¼, 0.0607(3)}	{0.4957(9), ¼, 0.0662(4)}
O_2 (x, y, z)	{0.2871(3), 0.0378(8), 0.7126(12)}	{0.2811(7), 0.0375(9), 0.7159(10)}	{0.2884(10), 0.0386(2), 0.7184(5)}	{0.2828(8), 0.0326(9), 0.7084(4)}

3.6 (a) and (b) respectively. The refinement was carried out by varying the cell parameters, position of the Nd/K and O atoms, occupancy, thermal parameters, orientation and magnitude of magnetic moment of Mn ions. Different choices of magnetic moment orientation were used in the refinement to get the best fit for x = 0.15 and 0.20 samples. The best possible refinement was obtained for the Mn^{3+} magnetic moments oriented in the *ac*-plane of the unit cell. The magnetic structure of x = 0.20 sample at 22 K is shown in figure 3.8. The temperature variations of refined magnetic moment for x = 0.15 and 0.20 samples are shown in figure 3.9. The FM transition at around 120 K could be observed for both x = 0.15 and 0.20 samples. The maximum magnetic moment per Mn ion, obtained from the above refinements, for x = 0.15 and 0.20 samples at 22 K are found to be 2.82(5) μ_B and 2.68(5) μ_B respectively.

TH-1060_06612103

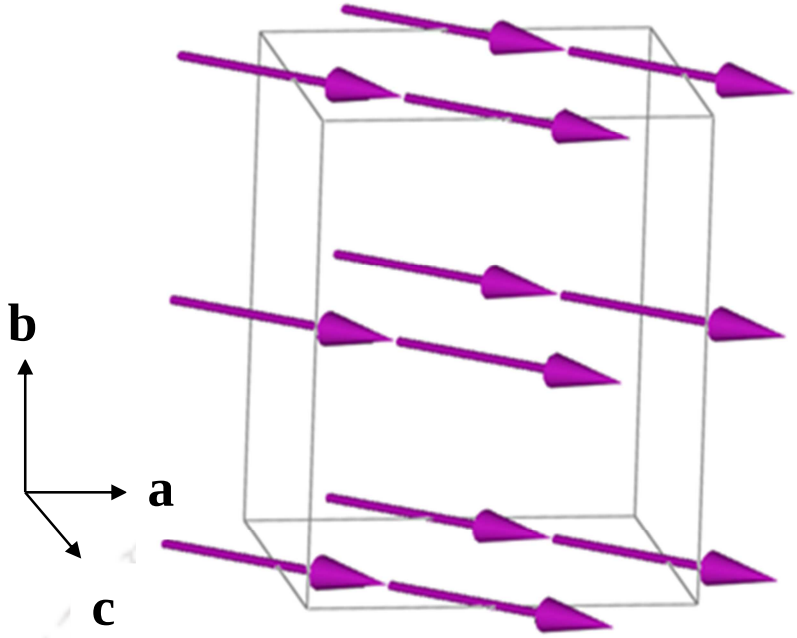

Figure 3.8: Magnetic structure of x = 0.20 sample at 22 K due to the magnetic moment of Mn ions.

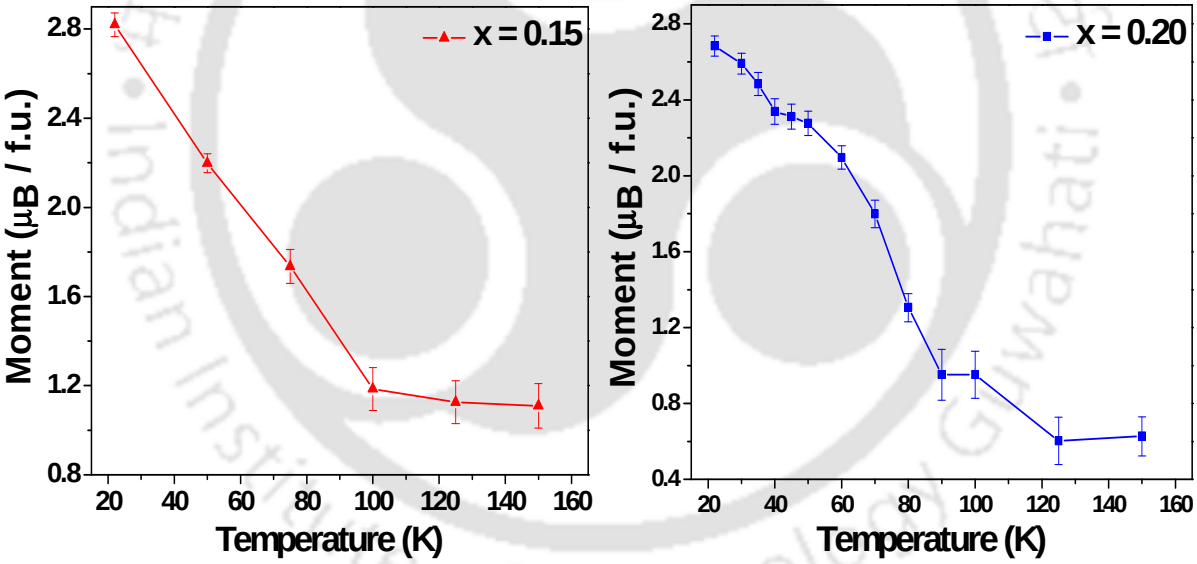

Figure 3.9: Temperature variations of refined magnetic moment for x=0.15 and 0.20 samples.

3.3. Magnetic Properties

The temperature variations of magnetization for x= 0.10, 0.15, 0.20, and 0.30 samples in zero field cooled (ZFC) and field cooled (FC) conditions are shown in figure 3.10. All the K doped materials exhibit PM-FM transition. The values of FM T_C were determined from (*dM/dT*) versus *T* plots and they are tabulated in table 3.4. They are found to increase with increase in doping concentration and are found to be in the range of 116 K to 128 K. The

TH-1060_06612103

observed T_C values in the present (Nd, K)-Mn-O series are found to be smaller than those of K-doped La based series. i.e., (La, K)-Mn-O [253-255]. It is mainly due to the larger A site ionic size of La-Mn-O series. However, the percentage of increase in T_C for x = 0.10 to 0.15 is comparable to that reported in (La, K)-Mn-O series [254]. Moreover, no appreciable variation in T_C is observed for x > 0.15 and similar trend has been observed by Zhong *et al.* [253] in (La, K)-Mn-O system. The magnitude of irreversible magnetization, $\Delta M = (M_{FC} - M_{ZFC})$ is found to increase with increase in doping concentration, i.e., in correlation with increase in Mn^{4+} concentrations. One of the reasons could be due to the presence of competing anti-ferromagnetic interaction in Mn^{4+}-O-Mn^{4+} networks. Typical plot of $\Delta M/M_{ZFC}$ versus temperature for x = 0.20 sample is shown in figure 3.10 (e), where we can see a clear peak in the vicinity of FM transition followed by a continuous increase in irreversible magnetization. Such an increase in $\Delta M/M$ with decrease in temperature below the FM T_C was observed in all other samples with different x values. Temperature variations of dc inverse susceptibility in the paramagnetic region were fitted to Curie-Weiss law and are shown in figure 3.11. The estimated parameters such as Curie temperature θ_C, and effective paramagnetic moment, μ_{eff} are given in table 3.4. The θ_C values are found to be about 20 K higher than the respective FM T_C determined from dM/dT vs. T plots. Theoretical effective magnetic moment (μ_{th}) can be calculated using the relation,

$$\mu_{th} = \sqrt{x_1\mu_1^2 + x_2\mu_2^2 + x_3\mu_3^2} \qquad \text{---------- (3.1)}$$

Here x_1, x_2, x_3 are the concentrations of Nd^{3+}, Mn^{3+}, Mn^{4+} ions and μ_1, μ_2, μ_3 are their respective theoretical magnetic moments. Here μ_1, μ_2, and μ_3 are taken as 3.63 μ_B, 4.9 μ_B and 3.87 μ_B respectively. The experimental μ_{eff} values are found to be considerably higher than those of μ_{th} as shown in table 3.4 and it could be mainly due to the presence of some isolated FM clusters.

The M-H loops recorded at 78 K for different samples are shown in figure 3.12. The saturation magnetization (M_S) value is found to increase with increase in doping concentration up to x = 0.20 and beyond which it is found to decrease. It can be understood in terms of enhanced double exchange interaction, as a result of generation of Mn^{4+} ions. However beyond the optimum Mn^{4+} concentration, M_S value decreases. The complete saturation of magnetization was not achieved even for x = 0.20; so, there is a presence of linear contribution. The M_S values were determined after subtracting the linear contribution in the high field region and they are given in table 3.4. The maximum M_S value observed for x = 0.20 sample is still considerably lower than the expected spin only contribution of M_S value

TH-1060_06612103

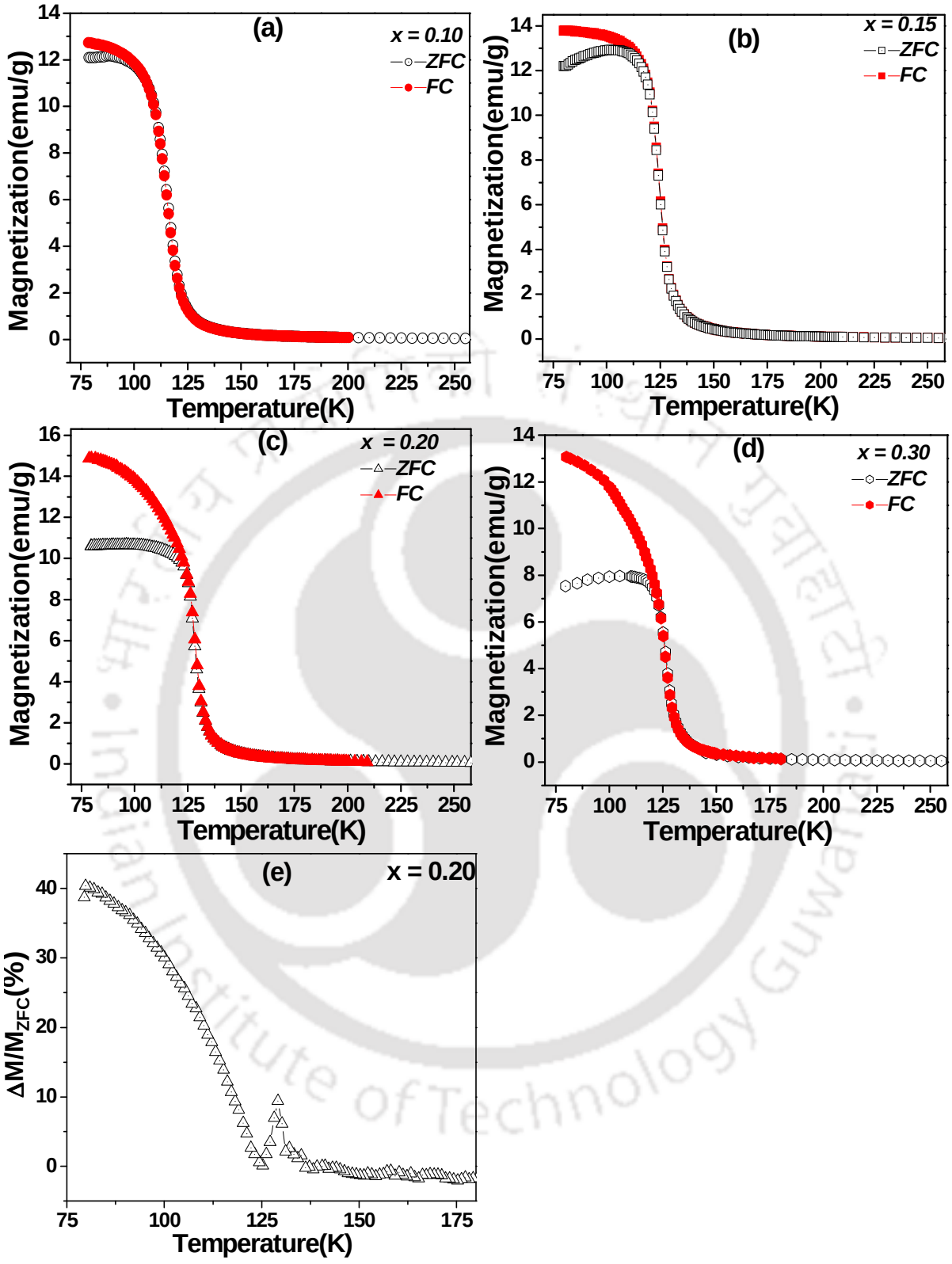

Figure 3.10: Temperature variations of magnetization for both zero field cooled (ZFC) and field cooled (FC) conditions for (a) x = 0.10, (b) x = 0.15, (c) x = 0.20 and (d) x = 0.30 samples. Figure (e) shows the temperature variation of irreversibility magnetization ($\Delta M/M_{ZFC}$) for x = 0.20 sample.

TH-1060_06612103

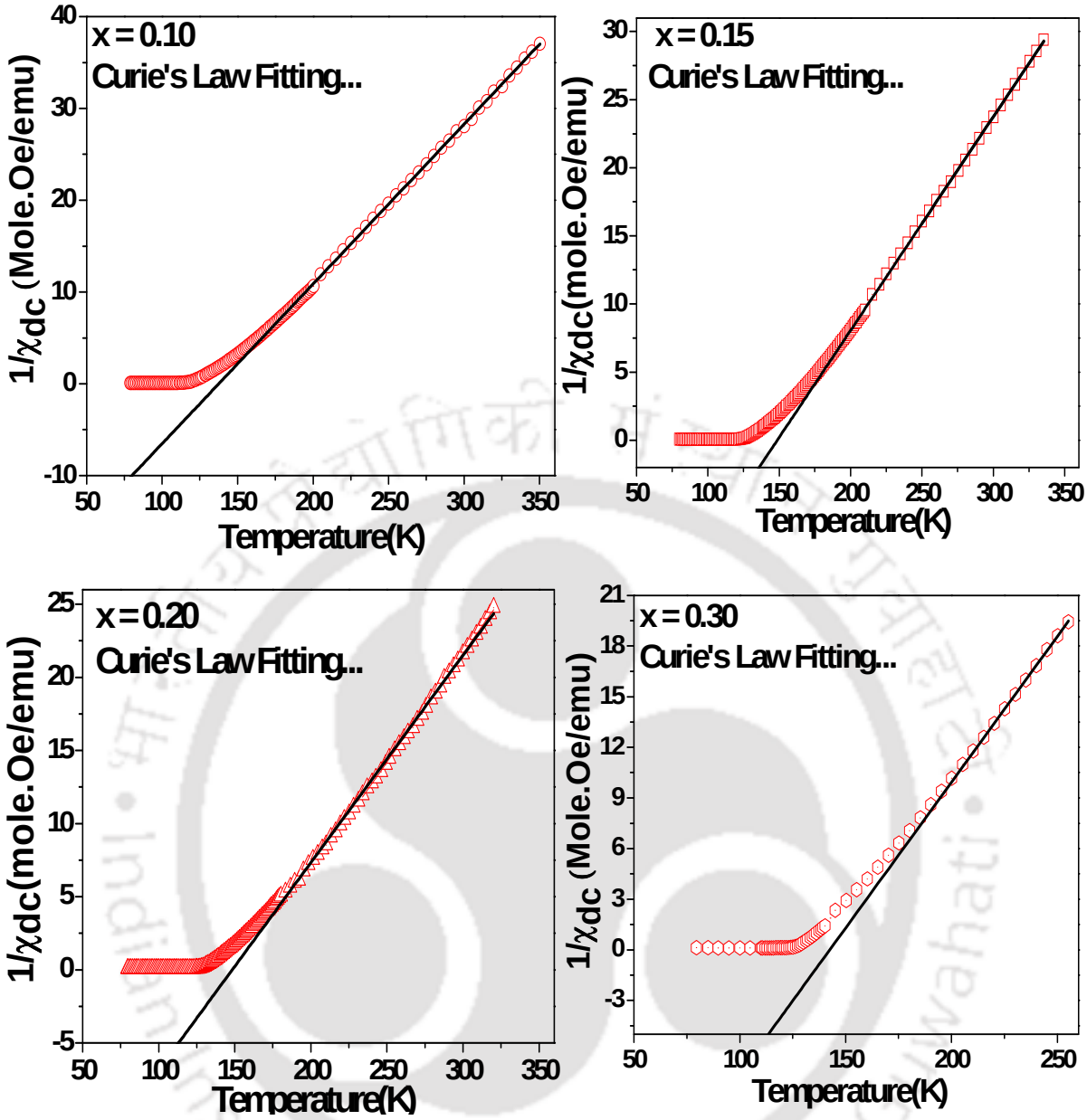

Figure 3.11: Temperature variations of inverse dc susceptibility along with Curie Weiss law fit for x = 0.10, 0.15, 0.20 and 0.30 samples.

for the optimum doped material. However, it is found to be greater than that observed in (Nd, Ag)-Mn-O [231] at a given temperature T = 78 K and is comparable to that of (Nd, Na)-Mn-O system at 50 K [228]. The lack of hysteresis loss indicates the soft magnetic properties of the materials. By following ref. [231], the effective magnetic spin (S_{eff}) towards the double exchange ferromagnetic interaction was determined by analyzing the initial magnetization data in-terms of Brillouin function model. The field variation of magnetization after subtracting the linear contribution was fitted to Brillouin function model by taking into

TH-1060_06612103

Table 3.4: Parameters obtained from magnetization measurement and analysis. T_C is the ferromagnetic transition temperature. θ_c and C are Curie temperature and curie constants respectively. M_S & S_{eff} are saturated magnetic moment and effective magnetic spin respectively.

Samples/ parameters	**x = 0.10**	**x = 0.15**	**x = 0.20**	**x = 0.30**
T_c(K)	116	124	128	127
θ_c(K)	136	145	148	135
C (emu K/ mole Oe)	5.74	6.37	6.71	5.78
μ_{eff}(μ_B)	6.77±0.02	7.13±0.43	7.32±0.08	6.79±0.22
μ_{th}(μ_B)	5.67	5.56	5.46	5.27
M_S(μ_B/f.u)	2.16	2.52	2.84	2.33
S_{eff}	1.48	1.58	1.65	1.60

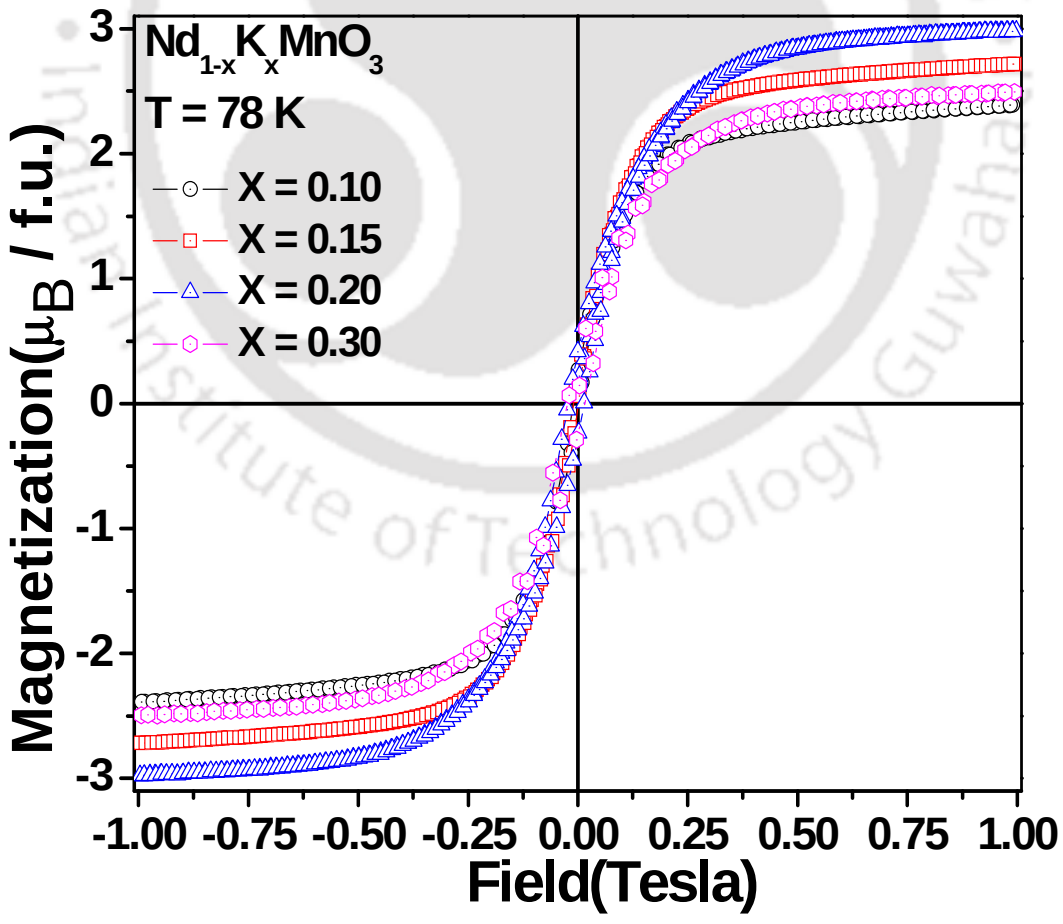

Figure 3.12: Magnetization versus magnetic field for x= 0.10, 0.15, 0.20, & 0.30 samples.

TH-1060_06612103

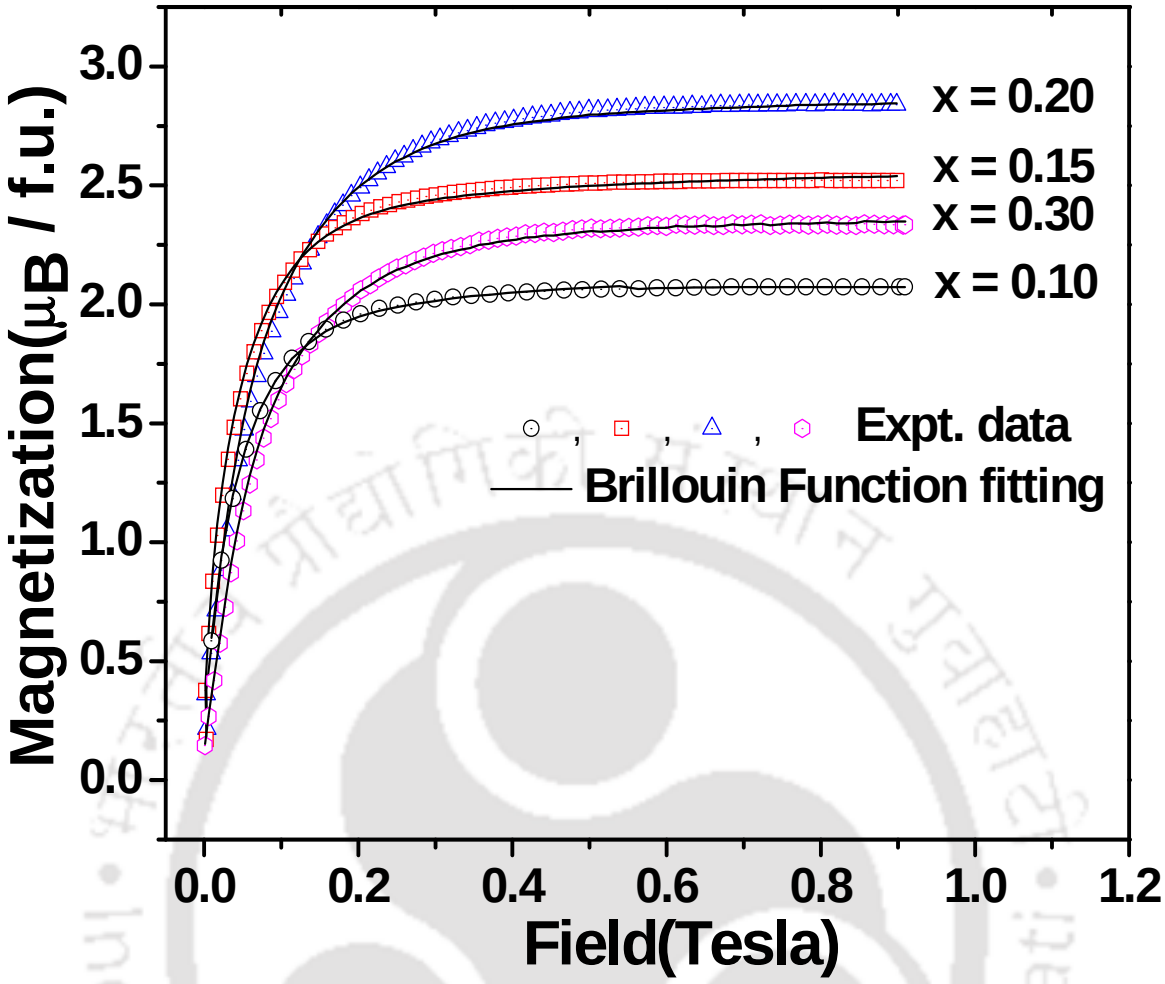

Figure 3.13: Brillouin function fitting of magnetization data at T = 78 K (after subtracting the linear part) for x = 0.10, 0.15, 0.20, & 0.30 samples.

account the FM interaction.

$$M = M_0 B_S(x) \qquad \text{---------- (3.2)}$$

where, $$B_S(x) = \frac{1}{|S_{eff}|}\left[\left(S_{eff}+\frac{1}{2}\right)Coth\,x\left(S_{eff}+\frac{1}{2}\right)-\frac{1}{2}Coth\frac{x}{2}\right] \qquad \text{----------(3.3)}$$

Here, $M_0 = Ng\mu_B S_{eff}$, $x = \frac{g\mu_B}{kT}B$, and $B=B_a+\lambda M$. λ is the Weiss molecular field constant for ferromagnetic interaction. We have carried out the fit by assuming the λ values determined from the FM T_C and Curie constant C ($T_C = \lambda C / \mu_0$) for different samples. Plots of initial magnetization curves along with Brillouin function fitting are shown in figure 3.13. We can see that the fitted data closely follow the experimental data. The fitted values of S_{eff} are given in table 3.4 and they are found to increase with increase in doping concentration. The S_{eff} values are comparable to that reported on (Nd, Ag)-Mn-O compounds [231].

TH-1060_06612103

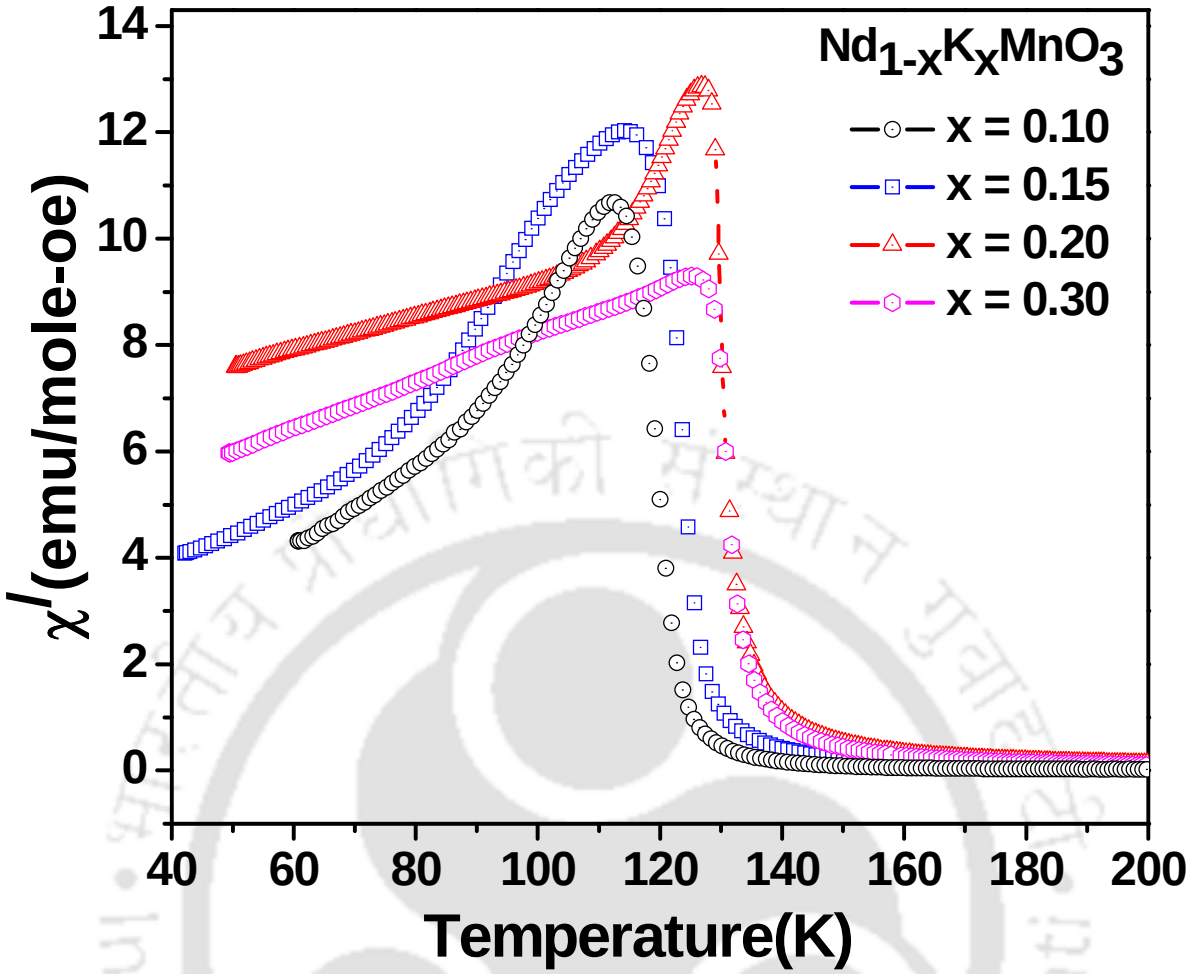

Figure 3.14: Temperature variation of linear ac susceptibility (χ_1') of $Nd_{1-x}K_xMnO_3$ (x=0.10, 0.15, 0.20, & 0.30).

The temperature variations of in-phase linear ac susceptibility (χ'_1) are shown in figure 3.14 for x = 0.10, 0.15, 0.20, & 0.30 samples. The measurements were carried out up to 300 K and for clarity, the data are shown only up to 200K. Even though, all the K-doped samples exhibit PM to FM transition; the lower doped samples, such as x = 0.10 and x = 0.15 exhibit strong peak effect and the magnitude of susceptibility falls sharply as the temperature is lowered beyond the FM T_C. On the other hand, for x ≥ 0.20, even though there is a peak effect in the vicinity of T_C, the signal does not fall rapidly with decrease in temperature. The decrease in χ' is generally explained on the basis of inherent magnetic anisotropy; however, additional mechanism such as competing AFM may play a role for lower doped materials, where the sharp fall is observed. $1/\chi'_1$ versus T plots of above samples exhibit linear behavior with positive Curie temperature values and are shown in figure 3.15 for x = 0.20 and 0.30 samples.

TH-1060_06612103

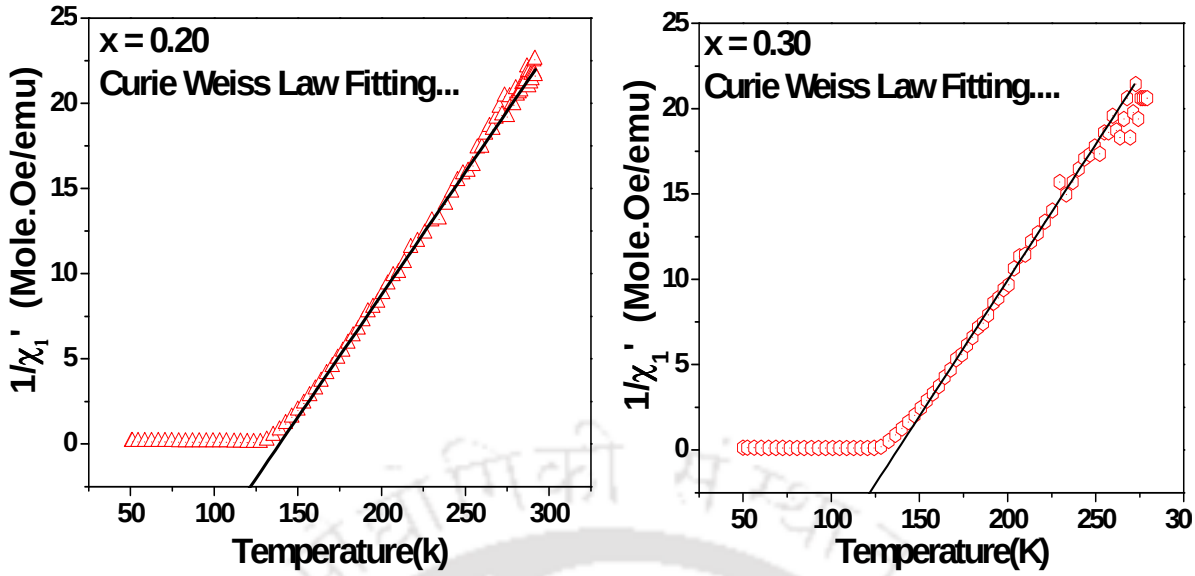

Figure 3.15: Temperature variations of inverse ac susceptibility ($1/\chi_1'$) along with Curie Weiss law fitting, for x = 0.20 and 0.30 samples.

3.3.1. Re-entrant Spin Glass Behavior (RSG)

We have carried out frequency variation of linear susceptibility and temperature variation of third harmonic ac susceptibility and, magnetic relaxation measurements in one of the samples, i.e., x = 0.15, to understand the mechanism of magnetic frustration. The temperature variations of inphase (χ_1') and out of phase (χ_1'') components of linear susceptibility are shown in figure 3.16. The χ_1'' vs. T plot exhibits two peaks, one in the vicinity of the FM transition and the other coinciding with observed low temperature fall in χ_1'. The inset of figure 3.16 shows the plot of $d\chi_1'/dT$ versus temperature and it exhibits two peaks. The sharp negative peak can be attributed to FM T_C and the minor broad positive peak can be attributed to the spin glass (SG) like behavior as discussed in the following paragraphs.

The plots of χ_1'' versus temperature at frequencies 233, 333, 1333 and 3333Hz are shown in figure 3.17 and they exhibit double peaks. The high temperature peak is found to be independent of frequency and it signifies the FM transition. The low temperature peak is found to shift towards higher temperatures with increase in frequency and it highlights the spin relaxation phenomenon; so, it is taken as spin glass freezing temperature T_f. The spin glass transition temperature T_g was determined by extrapolating the plot of frequency (f) variation T_f to $f = 0$, as discussed in refs [231, 256, 257] and it is shown in the inset of figure 3.17. T_f versus frequency was found to follow a linear behavior and the T_g value was found to be 97.6 ± 0.1 K. The dynamic property of spin glass was analyzed based on the

TH-1060_06612103

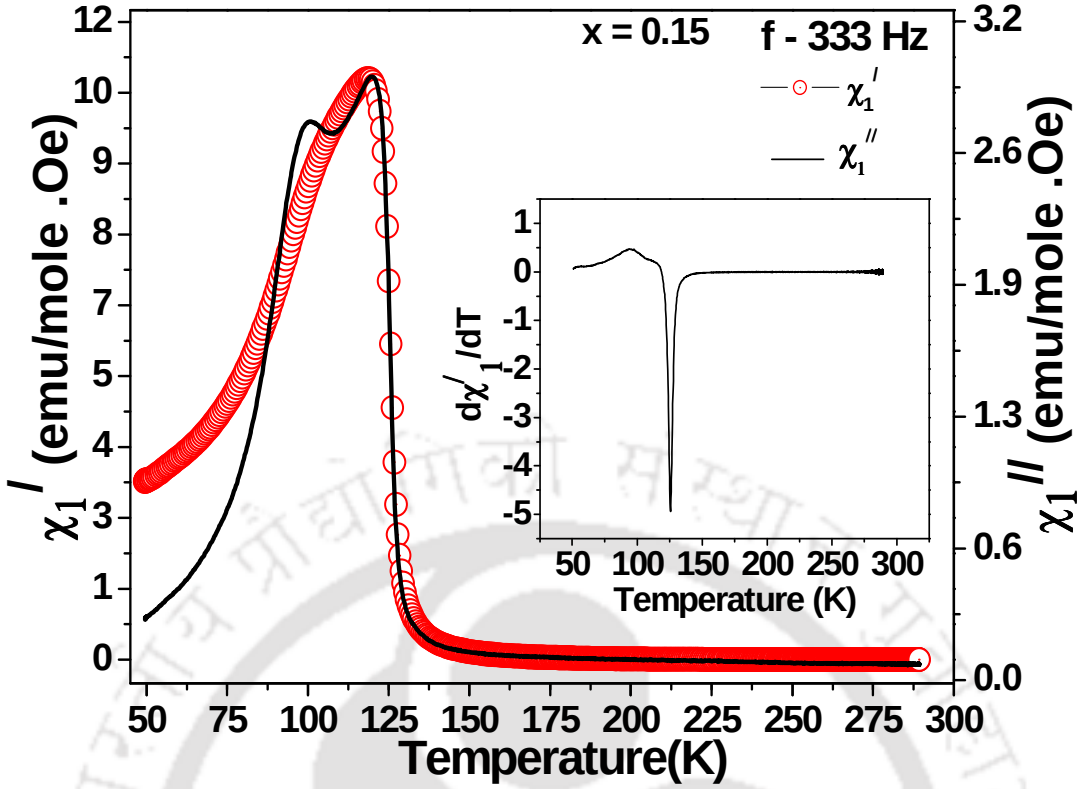

Figure 3.16: Plots of χ_1' and χ_1'' versus temperature (T). Inset shows temperature variation of $d\chi_1'/dT$.

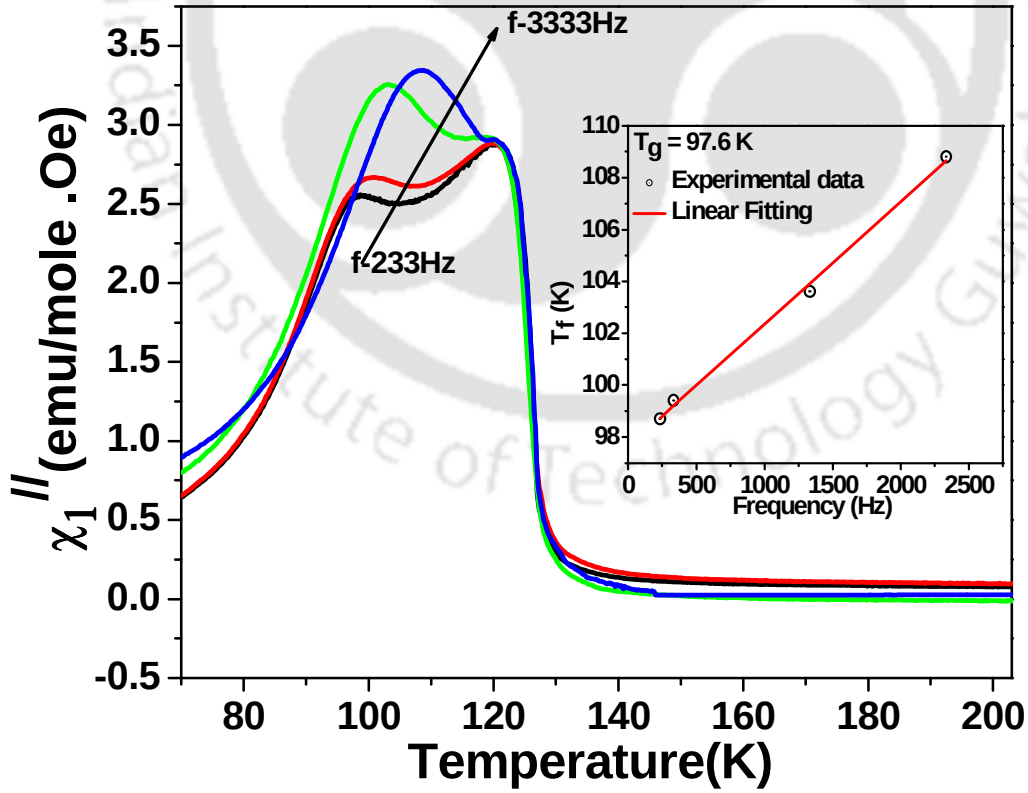

Figure 3.17: χ''_1 versus temperature (T) measured at frequencies f = 233 Hz, 333 Hz, 1333 Hz and 3333 Hz and the inset shows T_f versus frequency.

TH-1060_06612103

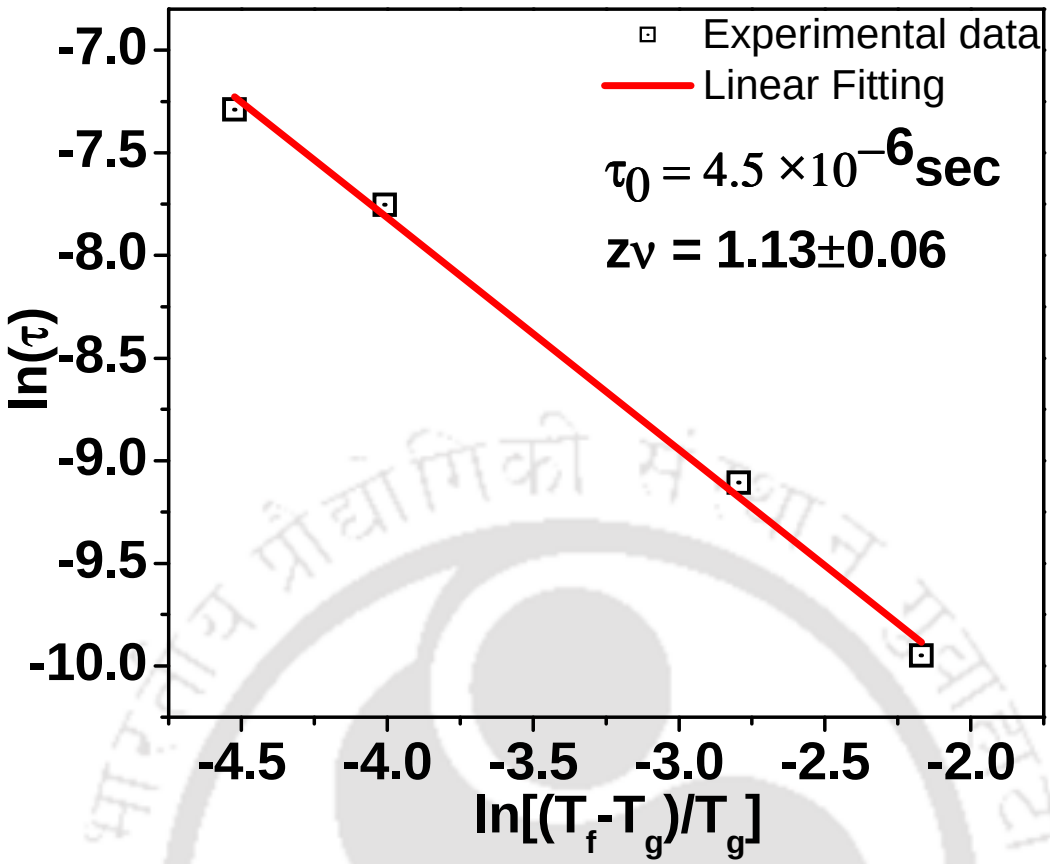

Figure 3.18: Plot of $ln(\tau)$ versus $ln[(T_f-T_g)/T_g]$ along with theoretical fit.

conventional power law model [81] as mentioned in eqn. 1.5 and for easy reference the equation is reproduced below.

$$\frac{\tau}{\tau_0} = \left[\frac{T_f - T_g}{T_g}\right]^{-z\nu} \quad \text{----------} \quad (3.4)$$

Here, τ is the relaxation time corresponding to the measured frequency ($\tau = 1/f$), τ_0 is the characteristic time scale for spin dynamics and $z\nu$ is the critical exponent. The plot of $ln(\tau)$ versus $ln[(T_f - T_g)/T_g]$ is shown in figure 3.18 and the fitted data using eqn. (3.4) are shown as solid line. τ_0 and $z\nu$ were taken as free parameters of the fit and these values are found to be τ_0 = (4.5±1.6) $\times 10^{-6}$ sec and $z\nu$ = 1.13 ±0.06. The observed τ_0 and $z\nu$ values are comparable to those reported by Cao *et al.* [190] in $(Nd, Sm)_{0.5}Ca_{0.5}MnO_3$ system and Cr doped (La, Ag)-Mn-O system [256]. Such a high value of τ_0 ($1.5 \pm 0.02 \times 10^{-5}$ sec) has been also reported recently in $LaCo_{0.5}Ni_{0.5}O_3$ system [258].

Third harmonic susceptibility measurement was carried out to unambiguously distinguish between spin glass behavior and super-paramagnetic behavior; since, in both

TH-1060_06612103

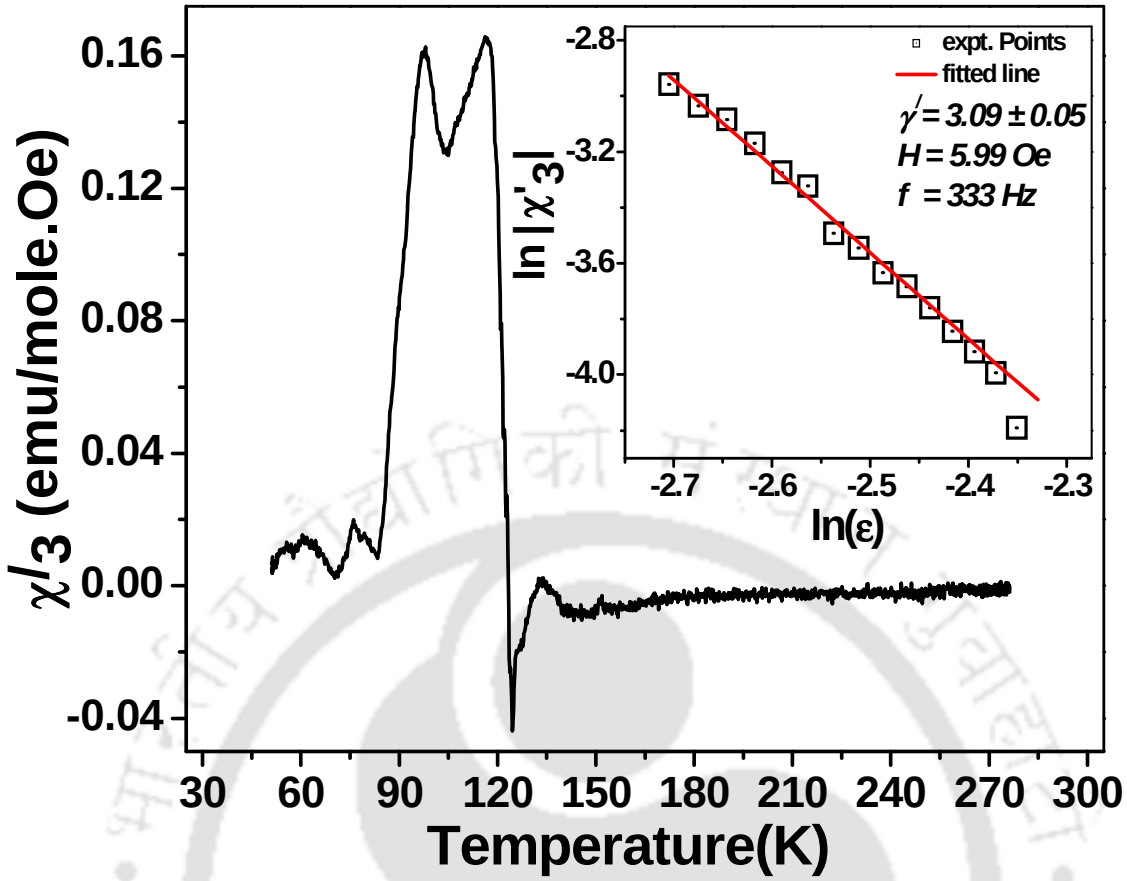

Figure 3.19: Third harmonic ac susceptibility (χ'_3) versus *T* for the sample x = 0.15 and the inset shows the plot of ln $|\chi'_3|$ versus *ln* ε along with the linear fit.

cases, similar frequency dependent fundamental susceptibility is generally observed. The plot of temperature variation of third harmonic ac susceptibility χ'_3 is shown in figure 3.19 for this sample. It exhibits a sharp negative peak at 124 K and it coincides with the ferromagnetic transition temperature. The low temperature peak observed at 98 K is closely comparable to that observed from χ'' vs. *T* plot (figure 3.16) and is attributed to the spin glass transition temperature. In spin glass materials, χ'_3 is expected to follow the critical scaling relation, $\chi'_3 \alpha \varepsilon^{-\gamma'}$. Here, the reduced temperature $\varepsilon = (T-T_g)/T_g$ and γ' is the characteristic critical exponent for spin glass transition. The plot of $ln|\chi'_3|$ versus $ln(\varepsilon)$ is shown in the inset of figure 3.19 and it exhibits a linear behavior. The critical exponent value determined from the linear fit is found to be γ' = 3.09 ± 0.05. The γ' value is found to be comparable to that reported for conventional spin glass system, such as Ni-Mn [87] and manganites [101, 259]. Thus, the present sample exhibits PM-FM transition followed by low temperature re-entrant spin glass transition.

TH-1060_06612103

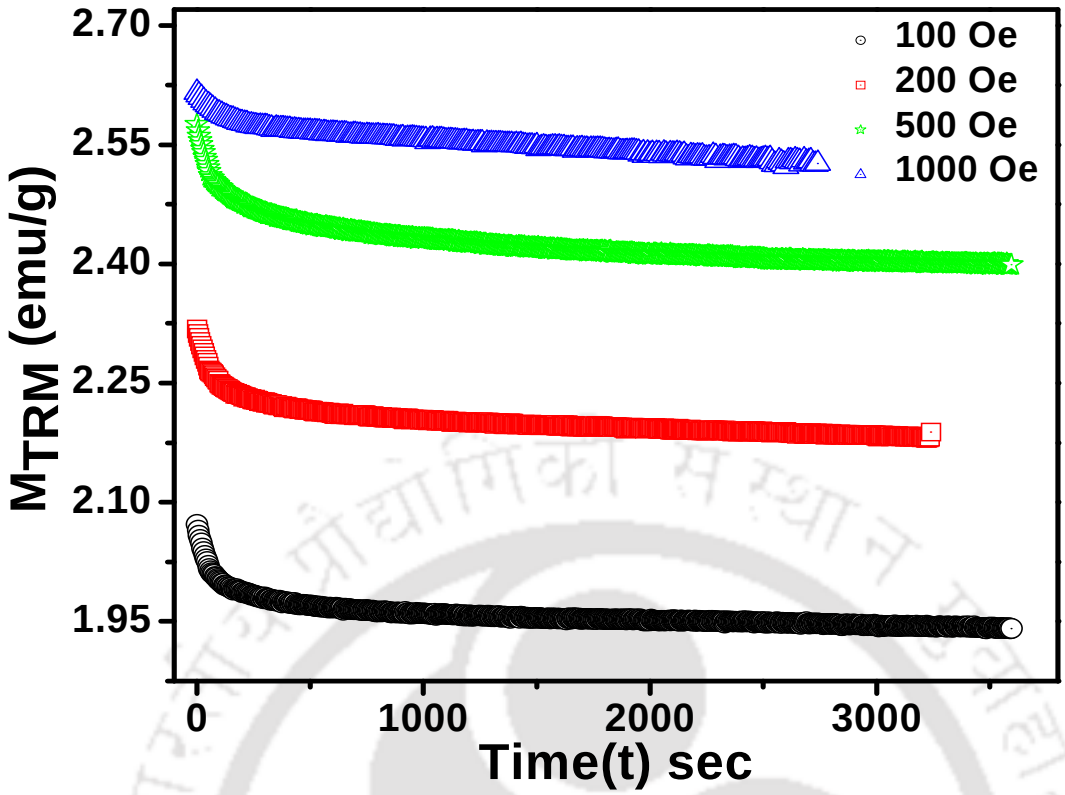

Figure 3.20: The relaxation of thermoremanent magnetization measured for different magnetic fields.

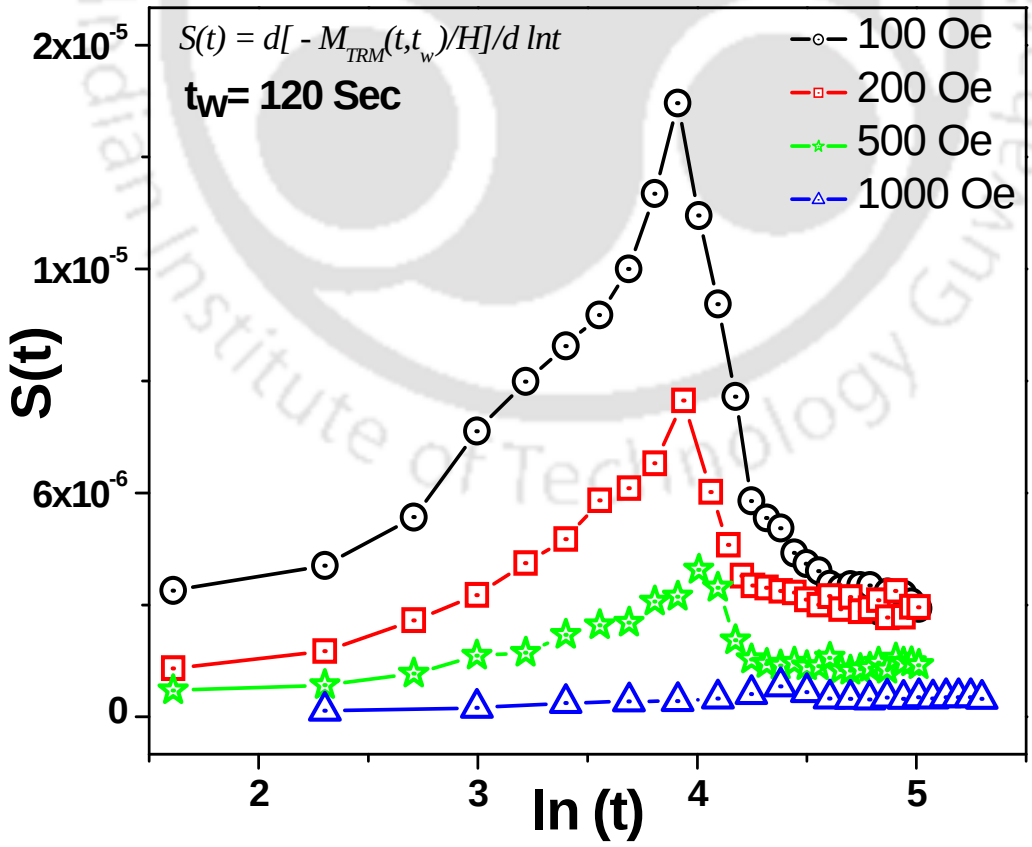

Figure 3.21: Relaxation rate *S(t)* versus *ln(t)* for different magnetic fields.

TH-1060_06612103

The aging behavior is the general characteristics of spin glass system and that could be analyzed from thermoremanent magnetization measurement; where, the sample is cooled in a magnetic field through the spin glass transition temperature T_g to the measuring temperature T. After waiting for a time (t_w), the magnetic field is cut off and the decay of magnetization is measured. This generates a response function called spin relaxation rate S and it is defined in section 1.7 and eqn. 1.14 is reproduced here,

$$S(t) = \frac{d\left[\frac{-M_{TRM}(t,t_W)}{H}\right]}{d \ln t} \qquad \text{----------} \quad (3.5)$$

Here, $M_{TRM}(t,t_w)$ is the thermoremanent magnetization at time t after cutting the magnetic field to zero. The M_{TRM} was measured for four different fields and is shown in figure 3.20 as a function of time. All the measurements were carried out at a predetermined temperature, i.e., $0.80T_g$ and the waiting time (t_w) was 120 sec. The response function $S(t)$ is plotted as a function of $ln(t)$ for different magnetic field as shown in figure 3.21. They exhibit peaks at a t value comparable to the waiting time t_w. The magnitude of peaks is found to decrease with increase in magnetic field. The aging effect is found to collapse for H = 1000 Oe. Similar variation of $S(t)$ is reported in refs [102, 260] for $Eu_{0.5}Ba_{0.5}MnO_3$ and $La_{0.7-x}Y_xCa_{0.3}MnO_3$ samples. The applied magnetic field reduces the depth of the trap by an amount E_Z, called Zeeman energy, which helps the spins to escape towards a region of more favorable magnetization. The time corresponding to the peak in $S(t)$ function is defined as the effective time, t_{eff} and is given by $ln(t_{eff} / t_w) = - E_z / K_BT$ [92]. The E_Z values for different cooling fields are tabulated in table 3.5. The Zeeman energy E_Z can be equated to $\sqrt{NH(m\mu_B)}$. Here N is the number of spins, which are effectively blocked together and $m\mu_B$ is the effective moment of one spin entity. We have taken $m\mu_B$ as $6.37\mu_B$ as obtained from Curie –Weiss law fit. N was extracted and is found to be in the order of 10^6 for H = 200Oe, The N values as tabulated in table 3.5 are found to reduce from 10^6 to 10^4 as the applied field is increased

Table 3.5: Parameters obtained from magnetic relaxation measurements.

Field(Oe)	**E_z (10^{-16} erg)**	**N (10^5)**	***ξ (Å)***
100	94	25	325
200	92	6	206
500	84.7	0.8	103
1000	43.6	0.05	----

TH-1060_06612103

from 100 to 500 Oe and it can be explained as a result of increase in Zeeman energy. The above N values are found to be comparable to those of $Eu_{0.5}Ba_{0.5}MnO_3$ sample [102]. The range of correlation length, ξ was estimated by using the relation $N = \alpha\xi^3$, by assuming the clusters are in spherical shape. 'α' is the geometrical factor and is taken as 2. The ξ values are found to decrease with increase in applied field and are listed in table 3.5. These values are found to be an order of magnitude larger than those reported for $Eu_{0.5}Ba_{0.5}MnO_3$ system [102]. The listed values are in consistent with the large τ_0 value obtained from frequency dependent susceptibility. Thus, the above analysis suggests that the observed spin glass behavior is not due to the frustration in atomic scale rather it is due to cluster formation.

3.3.2. Critical Exponent Behavior

The critical exponent behavior was analyzed in the vicinity of FM T_C to find out the nature of magnetic interaction in the present series of samples. We have chosen two higher concentration of K-doped samples, namely x = 0.20 and 0.30. The magnetization measurements were carried out for the above samples taken in spherical shape. Initially, the sample was cooled down to the measuring temperature in the absence of any external magnetic field. The sample temperature was allowed to stabilize within an error of ±0.05 K. The magnetic field was varied slowly with a sweeping rate of 1.5 mT/sec. Isothermal magnetization as a function of magnetic field was measured at different temperatures with 1 K interval, in the immediate vicinity of T_C, i.e., 120 K ≤ T ≤ 130 K and with 2 K interval outside that region. The entire critical region (110 -140 K) was covered to see the continuous transition from PM to FM state. The effective intrinsic magnetic field $H = (H_{ext} - DM)$, was used for the scaling analysis. Here D is the demagnetization factor and is taken as 1/3 for spherical samples. H_{ext} is the external applied field. Figure 3.22 (a) and (b) show the isothermal magnetization curves for x = 0.20 and x = 0.30 samples in the temperature range 110 K to 140 K. A gradual transition from FM to PM state with increase in temperature could be clearly seen.

Typical plots of M^2 versus H/M for a few selected temperatures close to the T_C are shown in figure 3.23 for x = 0.20 and 0.30 samples. These plots exhibit parallel sets of straight lines in high field region with a positive slope, confirming the second order nature of the magnetic phase transition. In order to obtain the reliable values of critical exponents, one has to determine the spontaneous magnetization, M_S $(0, T)$, and the zero-field inverse susceptibility, $\chi_0^{-1}(0, T)$, accurately. We have obtained these values by following the

TH-1060_06612103

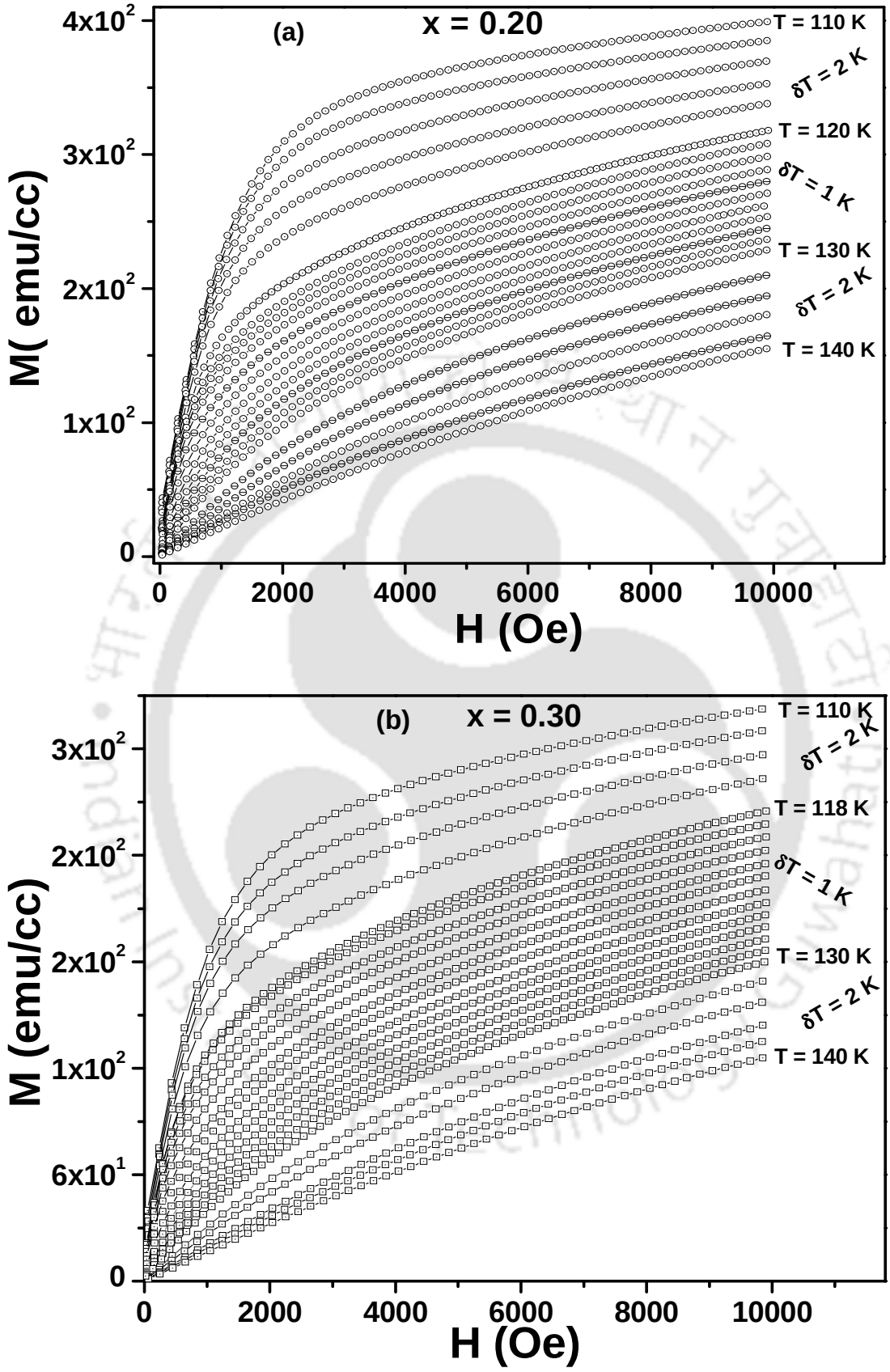

Figure 3.22: Isothermal magnetization as a function of magnetic field for (a) x = 0.20 and (b) x = 0.30 samples.

TH-1060_06612103

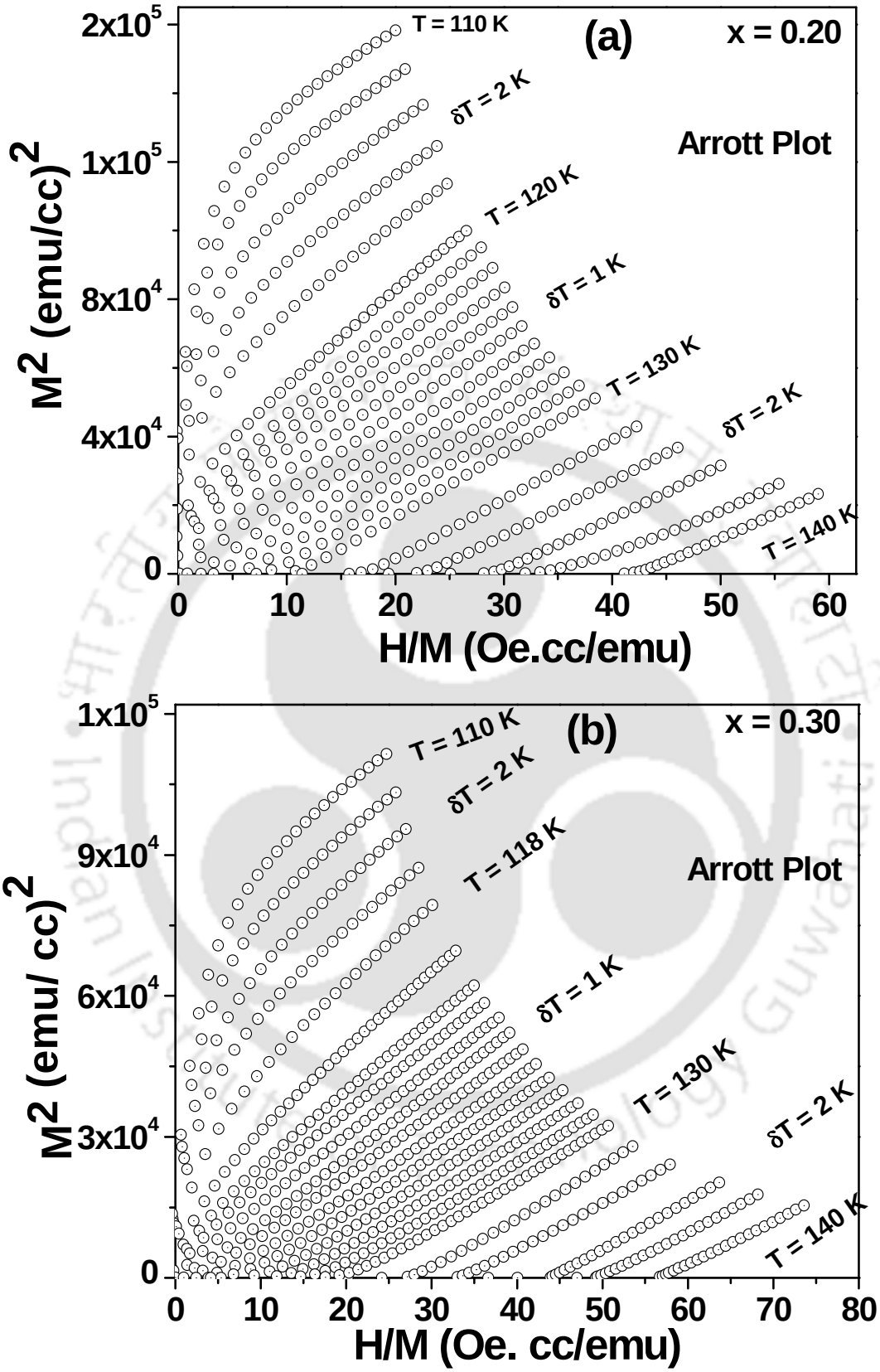

Figure 3.23: Arrott plots (M^2 versus H/M) of (a) x = 0.20 and (b) x = 0.30 samples in the temperature range 110 to 140 K.

TH-1060_06612103

modified Arrott plot (MAP) method, as described by Kim *et al.* [121]. The expression corresponding to modified Arrott plot as mentioned in equation (1.20) is reproduced here,

$$\left(\frac{H}{M}\right)^{1/\gamma} = \frac{(T - T_C)}{T_1} + \left(\frac{M}{M_1}\right)^{1/\beta} \qquad \text{---------- (3.6)}$$

MAP plots were generated by appropriately selecting the right β and γ values, such that the plots are linear. Subsequently, $M_s(T)$ values were determined by extrapolating the high-field data of $M^{1/\beta}$ versus $(H/M)^{1/\gamma}$ to $(H/M)^{1/\gamma} = 0$. Similarly $\chi_0^{-1}(T)$ values were determined by extrapolating the high field data of the above curve to $M^{1/\beta} = 0$. T_C value was determined from the temperature corresponding to the $M^{1/\beta}$ versus $(H/M)^{1/\gamma}$ curve passing through the origin. The $M_s(T)$, $\chi_0^{-1}(T)$ and the isothermal magnetization at the critical temperature $M(H, T = T_C)$ follow the power law behavior with the respective critical exponents β, γ and δ as given in section 1.8 and for easy reference they (eqn. 1.17-1.19) are reproduced as below,

$$M_S(T) \propto |\varepsilon|^{-\beta} \qquad \varepsilon < 0 \qquad \text{---------- (3.7)}$$

$$\chi_0^{-1}(T) \propto |\varepsilon|^{\gamma} \qquad \varepsilon > 0 \qquad \text{---------- (3.8)}$$

$$M(H, T = T_C) \propto H^{\frac{1}{\delta}} \qquad \varepsilon = 0 \qquad \text{---------- (3.9)}$$

where, $\varepsilon = (T - T_C)/T_C$ is the reduced temperature. By plotting $ln(M_s)$ versus $ln(\varepsilon)$ for $\varepsilon < 0$, and $ln(\chi_0^{-1})$ versus $ln(\varepsilon)$ for $\varepsilon > 0$ and fitting them to linear relation as per eqns. 3.7 and 3.8, a new set of β and γ values were obtained. The above process was repeated continuously until consistent values of β and γ were obtained. By fitting $ln(M)$ versus $ln(H)$ data at $T = T_C$, the critical exponent δ was determined. The values of β, γ and δ determined for both the samples are listed in table-3.6. These critical exponent values are close to those values predicted by the mean-field model. MAP plots for selected temperatures close to T_C are shown in figure 3.24 (a) and (b) for x = 0.20 and 0.30 respectively. The observed linear behavior at higher field of MAP plots confirms the validity of the mean-field model in the present set of samples. The extracted values of M_S and χ_0^{-1} from the MAP for both the samples are plotted as a function of temperature as shown in figure 3.25 and 3.26. The solid lines passing through the data points are the least square fit to the data using eqns. (3.7) and (3.8) and they follow experimental data closely. Plots of $ln(M_S)$ versus $ln(\varepsilon)$ and $ln(\chi_0^{-1})$ versus $ln(\varepsilon)$ are shown as insets in figure 3.25 and 3.26. The isothermal *M-H* curves at $T = T_C$ along with theoretical fit are shown in figure 3.27 for both the samples. The insets show the same data in logarithmic scale. The value of $\delta - (1+\gamma/\beta)$ is found to be -0.004 (-0.002) for x = 0.20 (0.30) sample, which is close to zero as per the Widom relation.

TH-1060_06612103

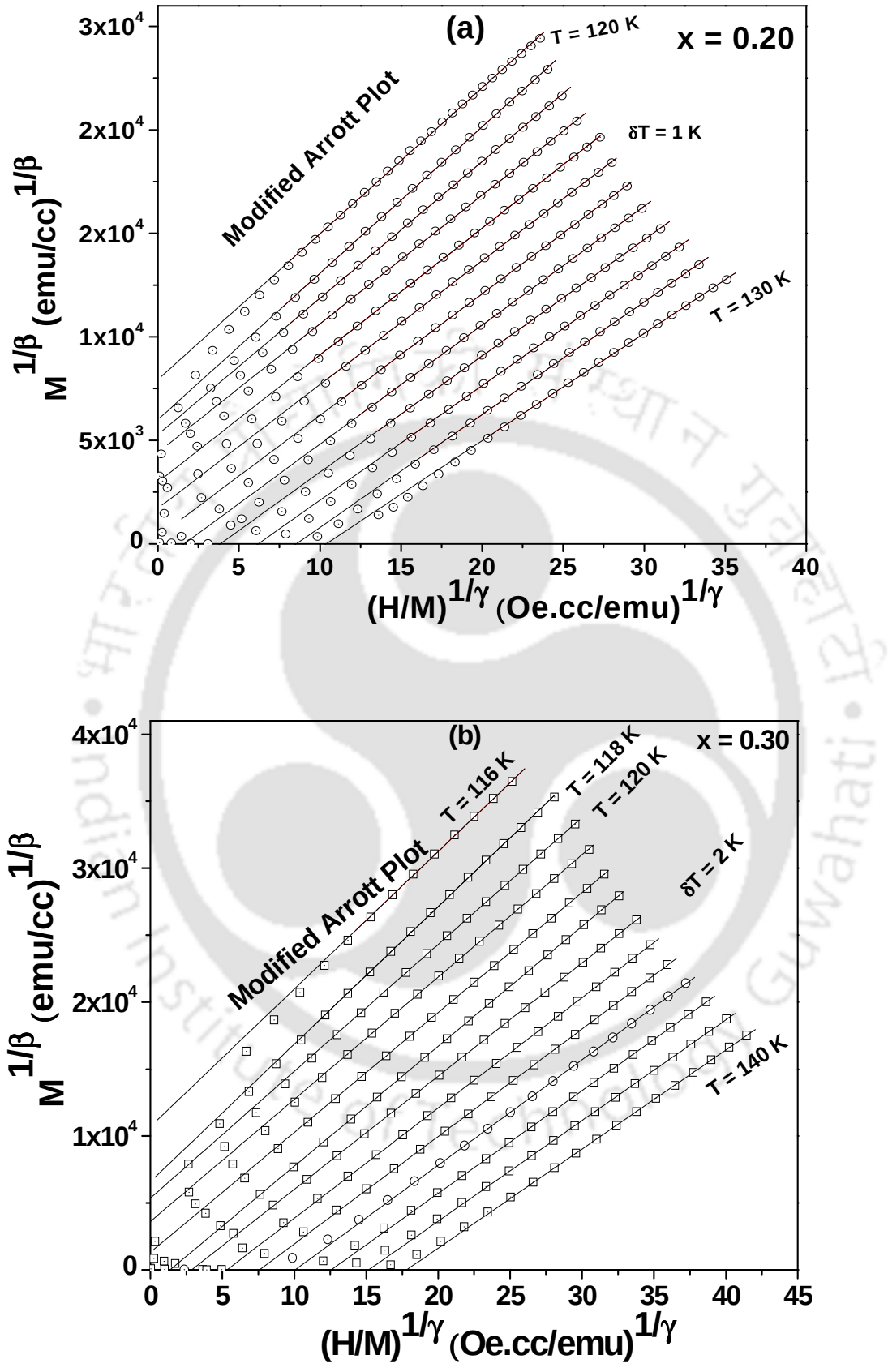

Figure 3.24: Modified Arrott plots $M^{1/\beta}$ versus $(H/M)^{1/\gamma}$ for (a) x = 0.20 (β = 0.57, γ = 1.04) and (b) x = 0.30 (β = 0.53, γ = 1.07) samples.

TH-1060_06612103

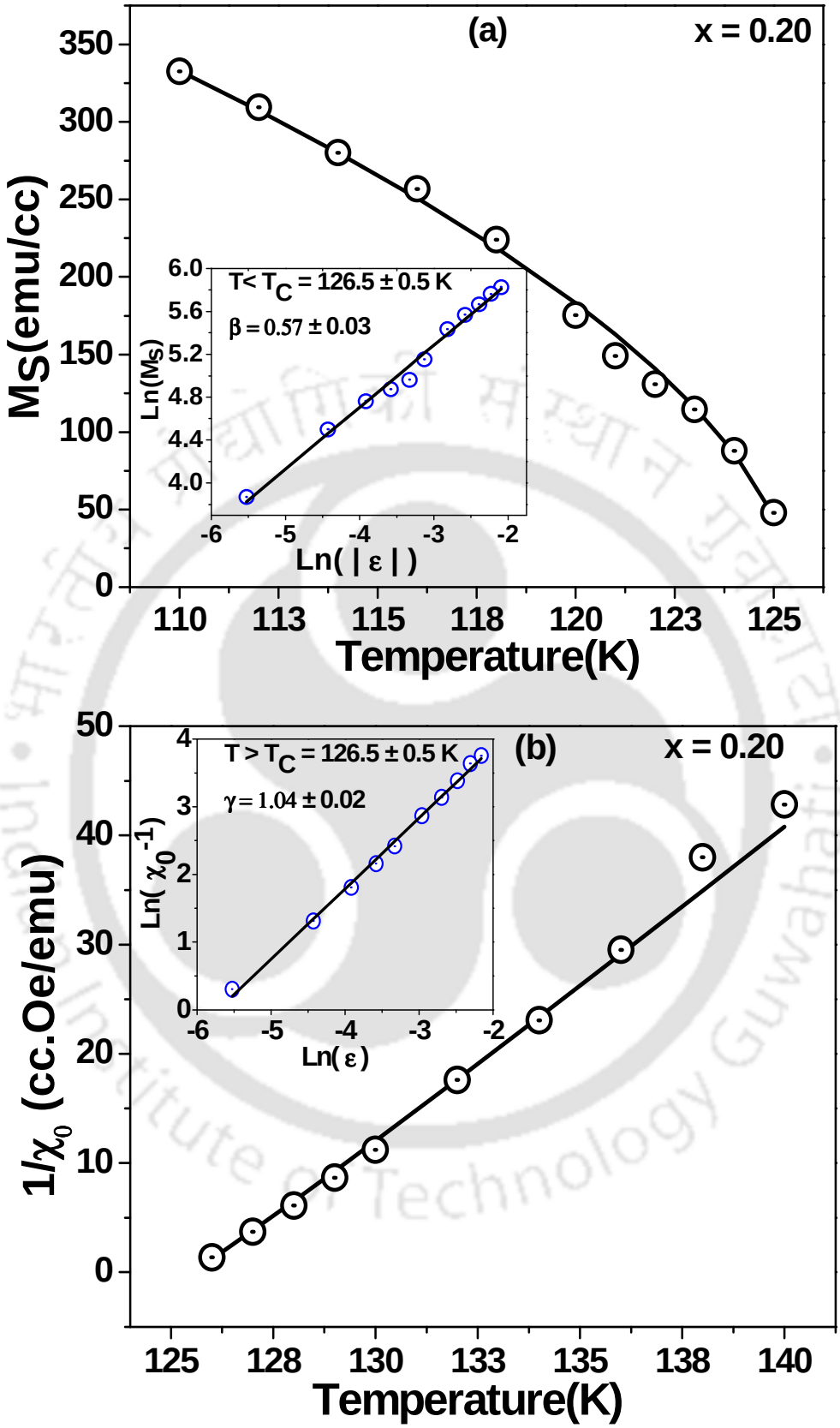

Figure 3.25: Temperature variations of (a) spontaneous magnetization (M_S *(0, T)*) and (b) the zero-field inverse susceptibility (χ_0^{-1}) for x = 0.20 sample. Insets show the same data plotted in logarithmic scale.

TH-1060_06612103

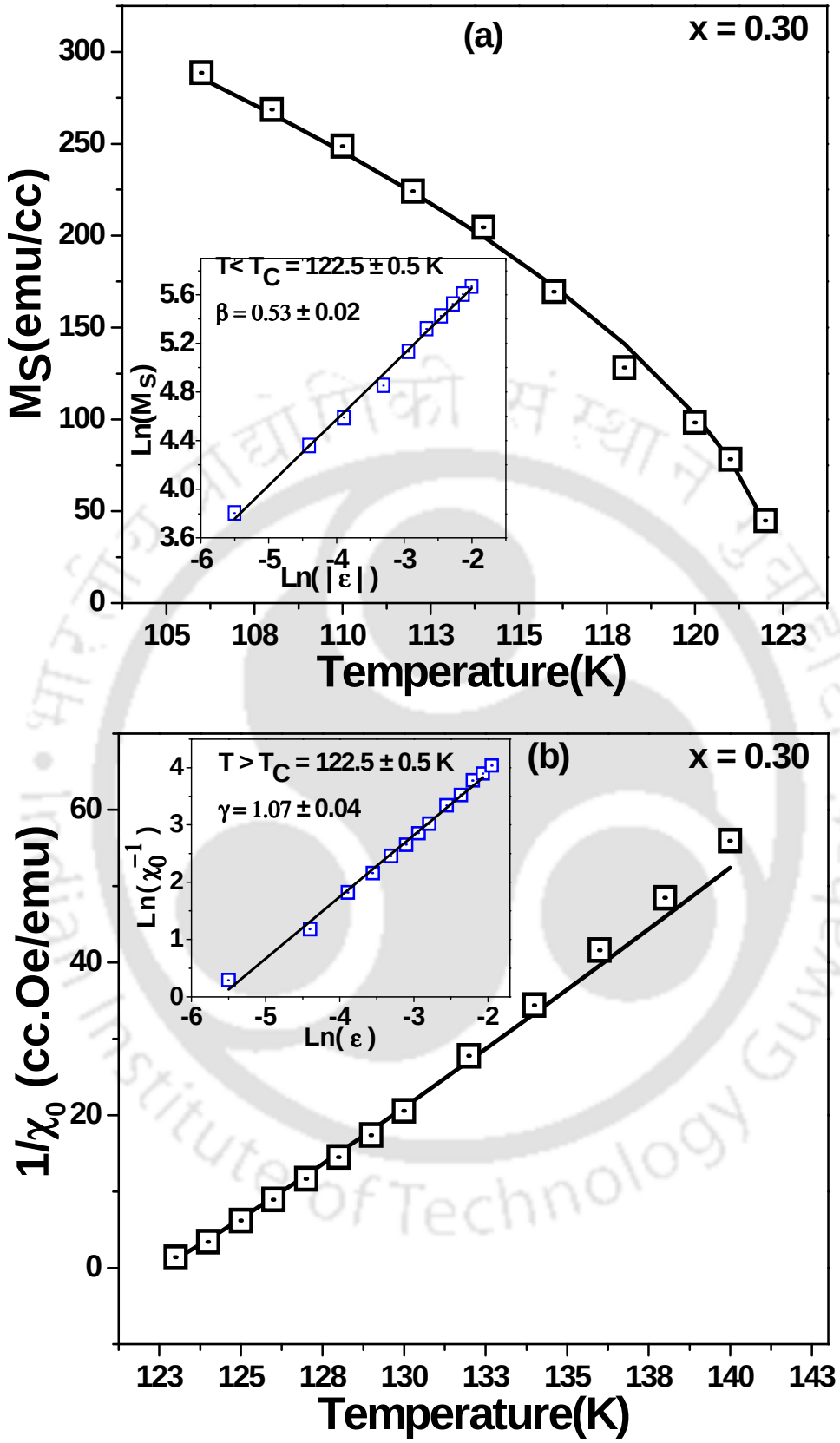

Figure 3.26: Temperature variations of (a) spontaneous magnetization ($M_S(0, T)$) and (b) the zero-field inverse susceptibility (χ_0^{-1}) for x = 0.30 sample. Insets show the same data plotted in logarithmic scale.

TH-1060_06612103

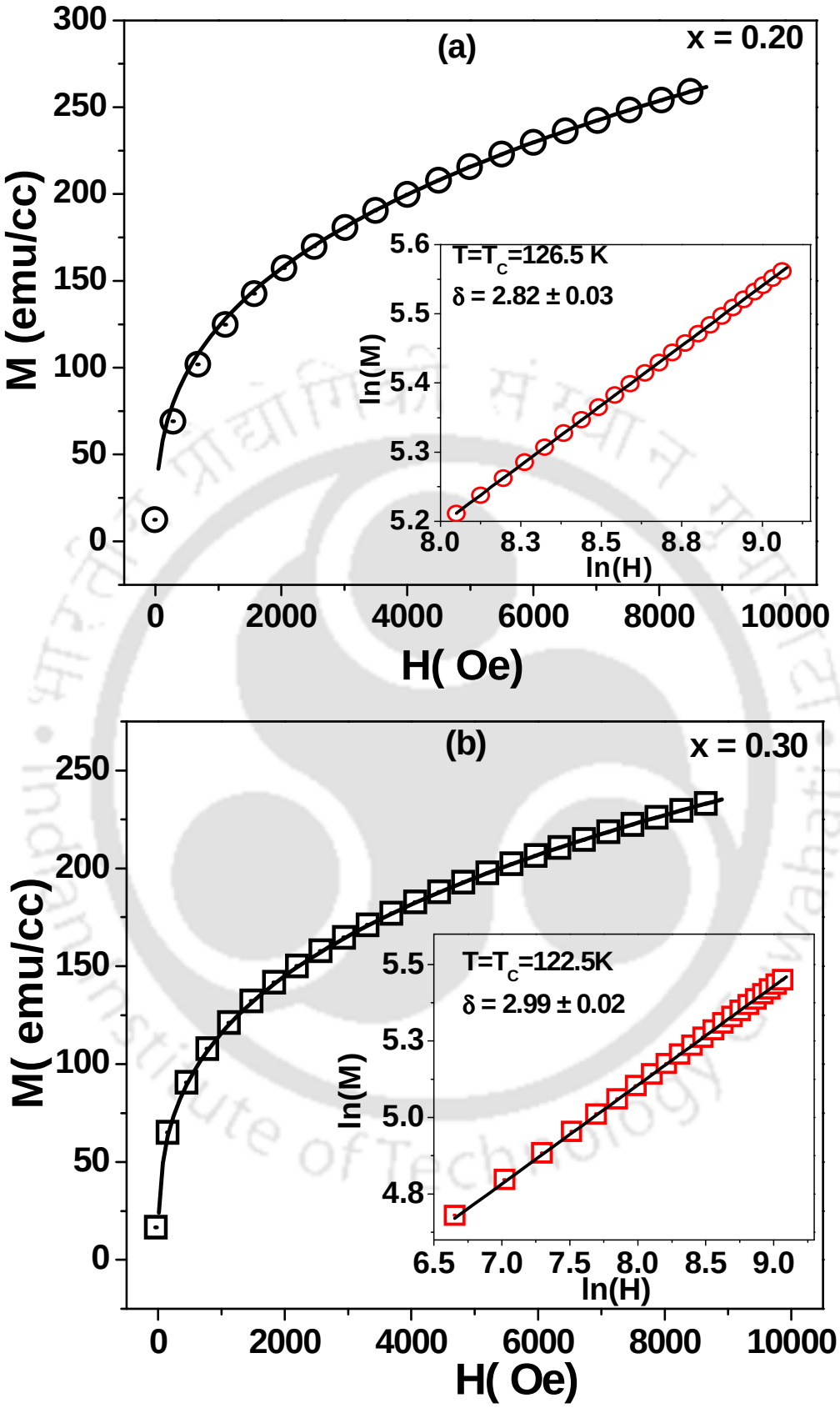

Figure 3.27: Isothermal magnetic curves at $T = T_C$ for (a) x = 0.20 and (b) x = 0.30 samples. The insets show these plots in logarithmic scale, along with the fitted data shown as solid lines.

TH-1060_06612103

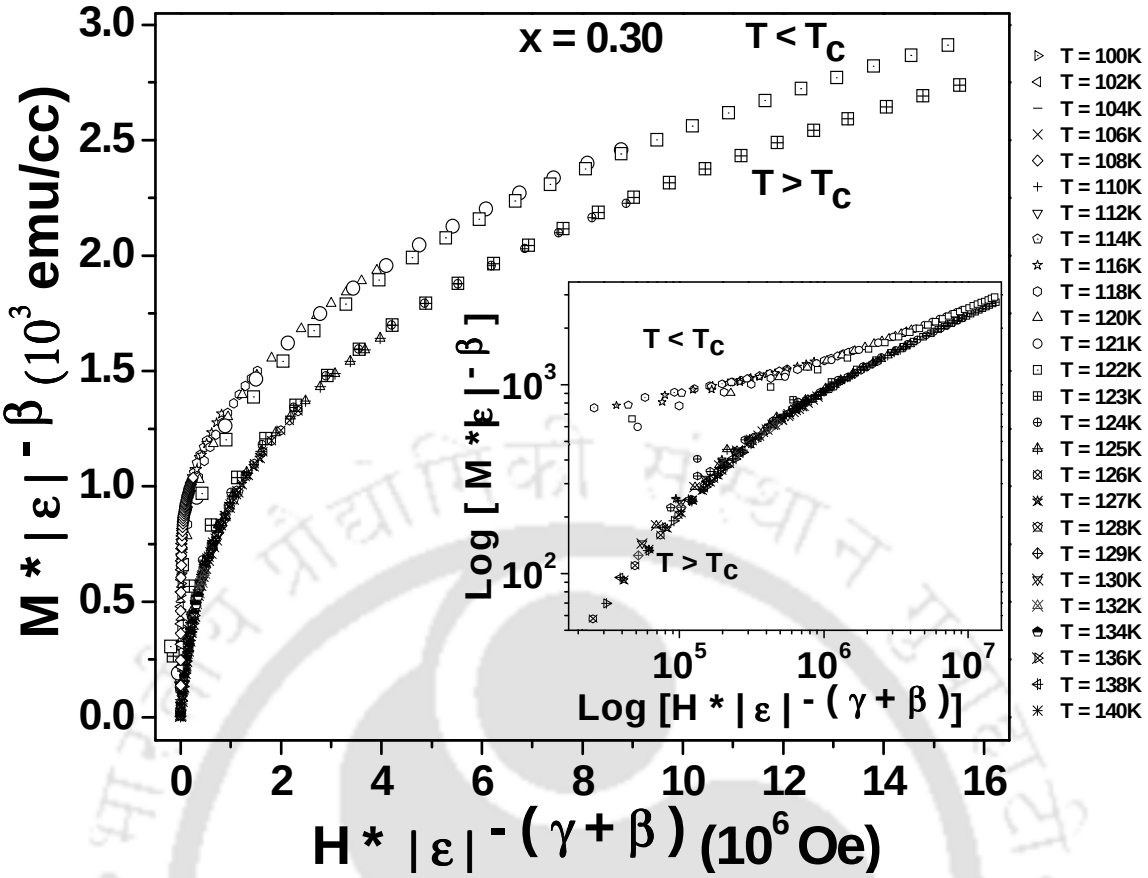

Figure 3.28: Scaling plot *of* $M|\varepsilon|^{-\beta}$ *versus* $H|\varepsilon|^{-(\beta+\gamma)}$ with β, γ and δ values from final iteration for x = 0.30 sample. Different symbols represent data taken at different temperatures. Inset shows the plots in double logarithmic scale.

The static scaling hypothesis predicts that $M(H, \varepsilon)$ is an universal function of ε and H as mentioned in eqn. 1.21 and for easy reference the equation is reproduced here,

$$M(H,\varepsilon)|\varepsilon|^{-\beta} = f_{\pm}\left(H|\varepsilon|^{-(\beta+\gamma)}\right) \qquad \text{---------- (3.10)}$$

where, f_+ and f_- are regular analytical functions for $\varepsilon > 0$ and $\varepsilon < 0$, respectively. According to eqn. (3.10), plots of $M(H, \varepsilon)|\varepsilon|^{-\beta}$ versus $H|\varepsilon|^{-(\beta+\gamma)}$ would lead to universal curves, one for temperatures $T > T_C$ $(\varepsilon > 0)$ and the other for $T < T_C$ $(\varepsilon < 0)$. Figure 3.28 shows the scaling plot on a linear scale and the inset shows the same data in a logarithmic scale. All the data points in the entire range of variables simply fall into two curves, depending upon the sign of ε. This shows that the critical exponent values and T_C obtained from the present investigation are reasonably accurate.

The critical exponent values obtained for the present set of samples and the values predicted by the mean-field [127], tricritical mean-field [261], 3D Heisenberg [127]

TH-1060_06612103

Table 3.6: Comparison of critical parameters for double-exchange ferromagnets $Nd_{1-x}K_xMnO_3$ (x = 0.20 & 0.30) with values predicted for different theoretical models and other Nd-Mn-O based manganites reported in literature. The abbreviations M, SC and PC refer magnetization, single crystal sample and polycrystalline sample, respectively.

Material	Ref.	Technique	T_C(K)	β	γ	δ
$Nd_{0.80}K_{0.20}MnO_3$ (PC)	This Work	Bulk M	126.5±0.5	0.57±0.03	1.04±0.02	2.82±0.03
$Nd_{0.70}K_{0.30}MnO_3$ (PC)	This Work	Bulk M	122.5±0.5	0.53±0.02	1.07±0.04	2.99±0.02
Mean-Field Model	[127]	Theory	--	0.5	1.0	3.0
Tricritical Mean-field	[261]	Theory	--	0.25	1	5
3D Heisenberg Model	[127]	Theory	--	0.365	1.336	4.80
3D Ising Model	[127]	Theory	--	0.325	1.241	4.82
$Nd_{0.6}Pb_{0.4}MnO_3$ (SC)	[262]	Bulk M	156.4	0.374±0.006	1.329±0.003	4.54±0.10
$Nd_{0.7}Sr_{0.3}MnO_3$ (SC)	[263]	Bulk M	203.6±0.3	0.57±0.01	1.16± 0.03	3.03±0.03
$Nd_{0.6}Sr_{0.4}MnO_3$ (PC)	[264]	Bulk M	--	0.51±0.02	1.01± 0.03	3.13±0.02

TH-1060_06612103

and 3D Ising [127] models are listed in table 3.6. The exponent values obtained from the present analysis are close to the values predicted by the mean-field model, signifying the presence of the long range FM interactions. According to DE theory, the extended states are favorable due to the kinetics of e_g electrons and hence a long range universality class is expected. It is important to note that the values of β and δ are close to the values reported previously for $Nd_{0.7}Sr_{0.3}MnO_3$ single crystal [263]. Similarly, the critical exponent values of polycrystalline $Nd_{0.6}Sr_{0.4}MnO_3$ sample [264] follow the mean-field model, indicating that the present result on (Nd,K)-Mn-O series is consistent with those reported for (Nd,Sr)-Mn-O series [264]. The observed long range FM interaction can be attributed to the formation of FM clusters just above T_C. The FM clusters provide an average exchange field in the system which in turn facilitates the FM alignment of bulk magnetic spins in the critical region. The signature of FM clustering was observed from the analysis of magnetic susceptibility in the PM region [265]. The effective magnetic moment was found to be higher than that of theoretical value. Generally, it is difficult to arrive at a conclusion about the nature of the magnetic phase transition, since the predicted critical exponent values for different theoretical models are quite close to each other as shown in table 3.6. However in the present set of samples, all the three critical exponent values are unambiguously close to those values predicted by the mean-field model. The consistent results obtained on two different samples of the same series, clearly demonstrate the mean-field behavior of FM interaction in (Nd, K)-Mn-O compounds.

3.3.3. Magnetocaloric Effect

In order to evaluate the magnetocaloric effect (MCE) for the present materials, isothermal magnetization as a function of magnetic field was measured for x = 0.20 and 0.30 samples in the temperature range of $T_C \pm 25$ K. We have calculated the change in magnetic entropy (ΔS_M) due to the applied magnetic field up to 1 T by using the relation [266].

$$\left|\Delta S_M\right| = \sum_i \frac{M_i - M_{i+1}}{T_{i+1} - T_i} \Delta H_i \qquad \text{----------} \qquad (3.11)$$

where M_i and M_{i+1} are the magnetization values measured at temperatures T_i and T_{i+1} respectively. The magnetic entropy change ΔS_M, calculated according to eqn. 3.11, is plotted against temperature as shown in figure 3.29. The maximum value of $\left|\Delta S_M\right|$ is found to be 1.67 and 1.37 J/Kg K for x = 0.20 and x = 0.30 samples respectively. The $\left|\Delta S_M\right|$ values are comparable to those reported for (La, Ca)-Mn-O series at 1T magnetic field [266]. The value

TH-1060_06612103

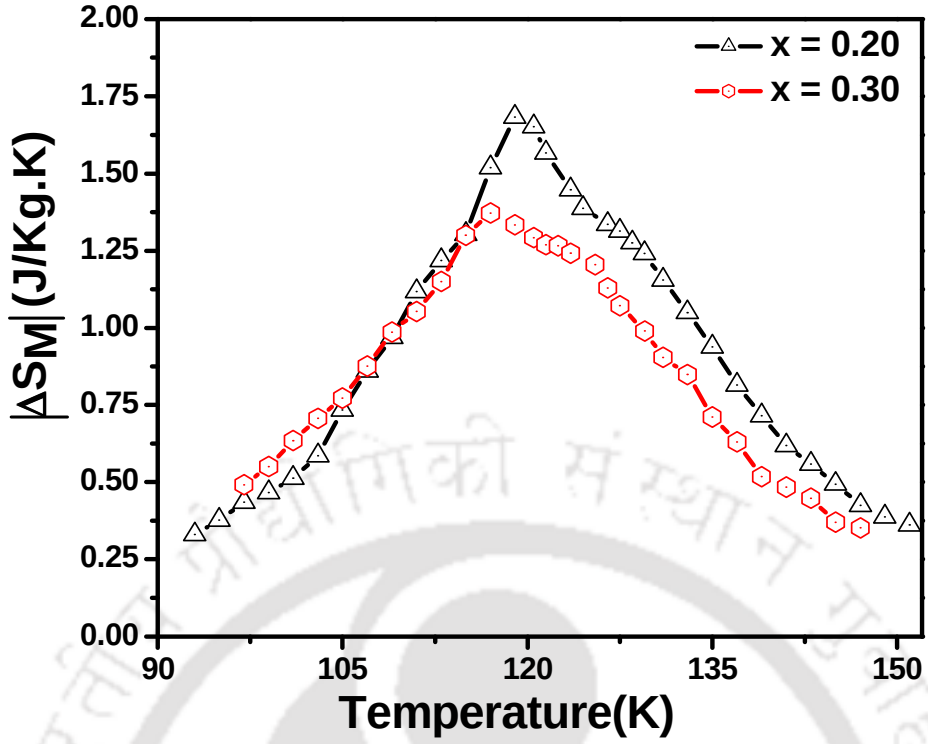

Figure 3.29: The change in entropy $|\Delta S_M|$ for 1 T field as a function of temperature for x = 0.20 & 0.30 samples.

of $|\Delta S_M|$ observed in the present series in the vicinity of T_C is comparable to that reported by Das and Dey [254] in $La_{1-x}K_xMnO_3$ (x = 0.05, 0.10 and 0.15) series.

3.4. Transport Properties

Temperature variation of electrical resistivity (ρ) was measured in the absence and the presence of 1 T magnetic field, and are shown in figure 3.30 for x = 0.10, 0.15, 0.20 and 0.30 samples. Higher concentration of K-doped samples (x = 0.20 & 0.30) show the metal-insulator transition at around 120 K. The metal insulator transition temperatures (T_{MI}) obtained in the absence and the presence of applied magnetic field are tabulated in table 3.7. The observed metallic behavior could be understood due to the strengthening of DE interaction. By application of 10 kOe magnetic field, the resistivity peak at T_{MI} is suppressed significantly along with the shifting of T_{MI} towards higher temperature. However for samples with lower doping of K concentration (x = 0.10 and 0.15), semiconducting behavior was observed down to 50 K. Below that temperature, the resistivity was higher than 10 mega Ohm and was going beyond the measuring range of instruments. The absence of M-I transition in these samples can be understood as a result of lack of percolation threshold of DE-FM interaction.

TH-1060_06612103

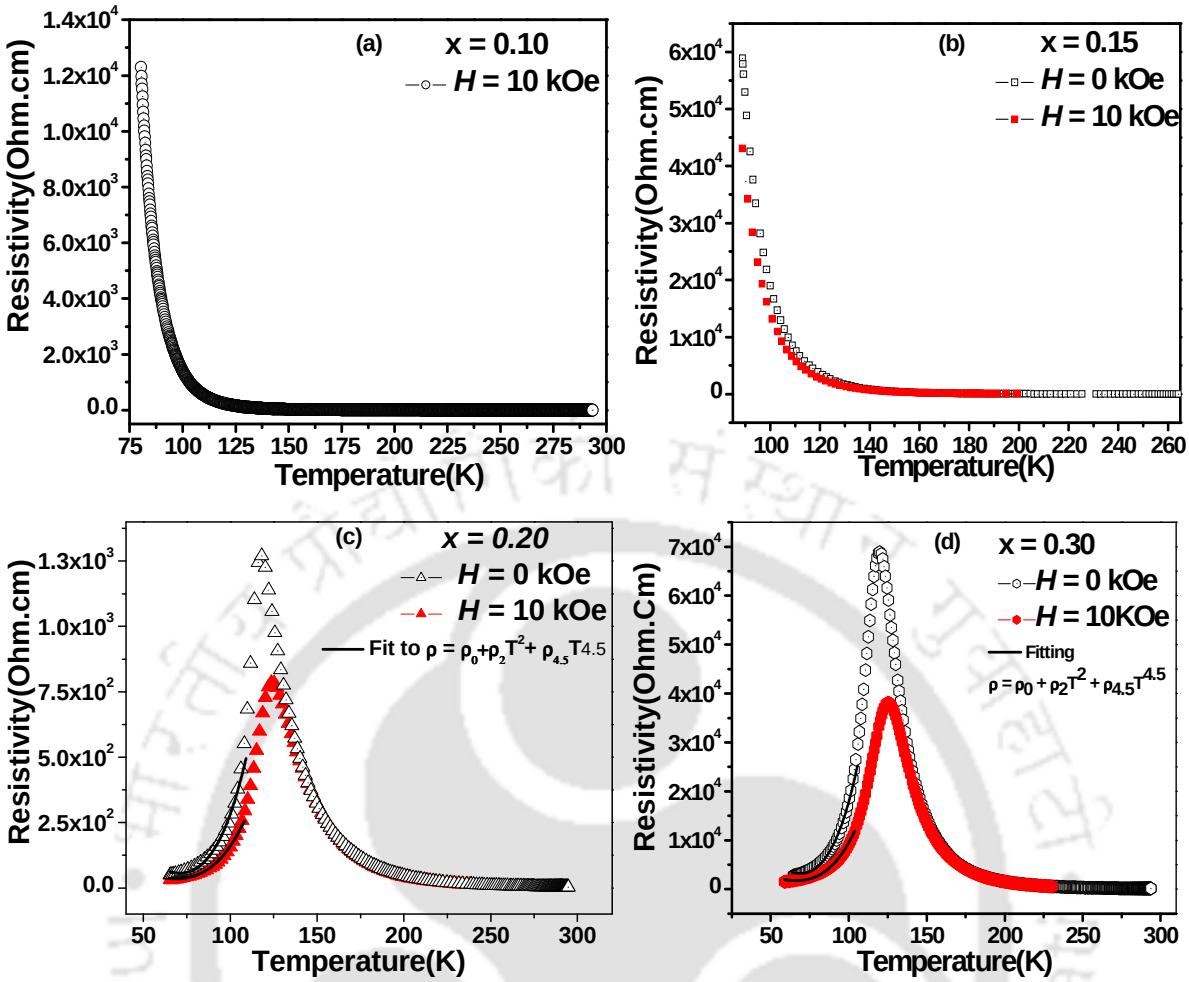

Figure 3.30: Temperature variations of electrical resistivity in the absence and the presence of applied magnetic field for $Nd_{1-x}K_xMnO_3$ (x = 0.10, 0.15, 0.20 and 0.30).

The temperature variation of magneto-resistivity (MR) was calculated using the relation, $(\Delta\rho/\rho_o) = (\rho_H-\rho_o)/\rho_o$. Here ρ_H is the resistivity in the presence of magnetic field and ρ_0 is the resistivity in the absence of magnetic field at a given temperature. The temperature variation of negative MR $(-\Delta\rho/\rho_0)$ is shown in figure 3.31 for x = 0.15, 0.20 and 0.30 samples. The observed (-MR) values are found to be 27%, 59% and 57% for x = 0.15, 0.20 and 0.30 samples respectively. MR peaks have been observed in the vicinity of ferromagnetic transition temperature (FM T_C) observed from dc magnetization measurements.

The electrical resistivity in the metallic region for the samples x = 0.20 and 0.30 were analyzed by using eqn. 1.23, i.e.,

$$\rho(T) = \rho_0 + \rho_m T^m + \rho_n T^n \qquad \text{----------} \qquad (3.12)$$

where, ρ_0 is the temperature-independent residual resistivity due to scattering by impurities, defects, grain boundaries, and domain walls, etc. Here m and n are exponents and their values

TH-1060_06612103

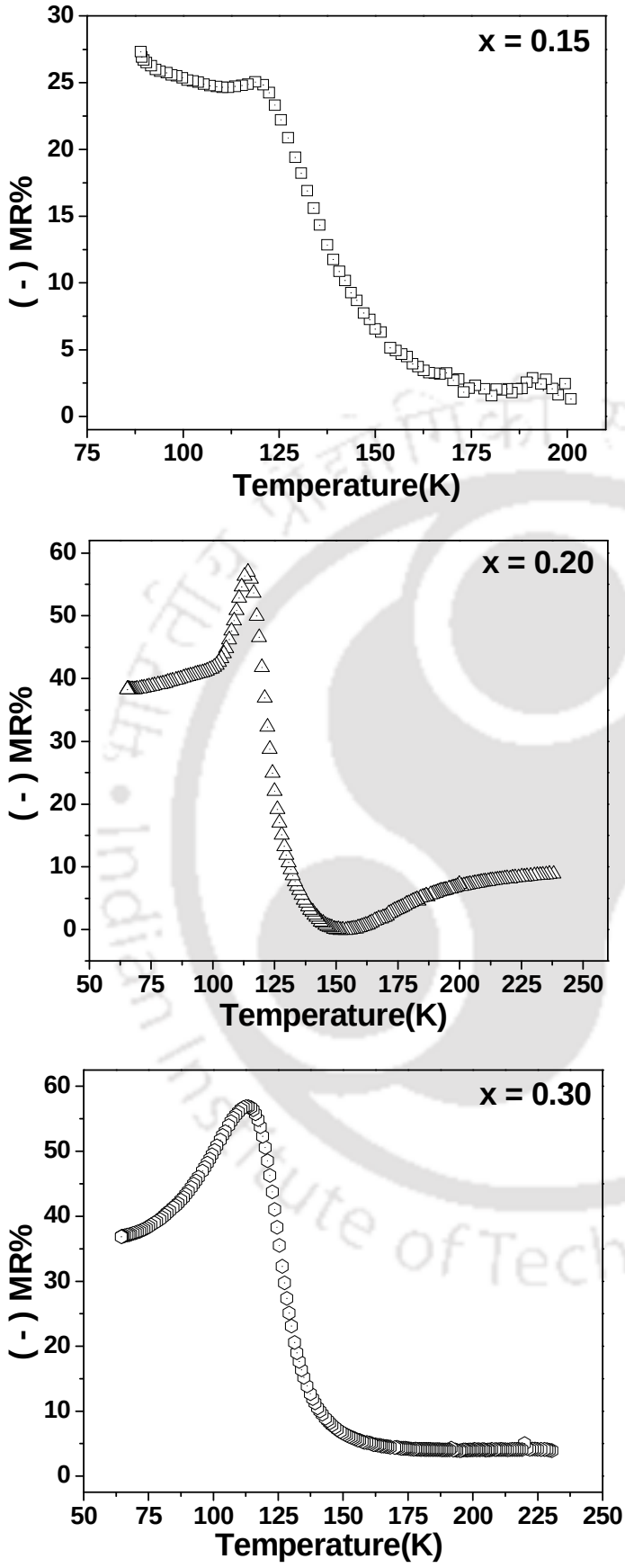

Figure 3.31: Temperature variations of magneto-resistivity ($-\Delta\rho/\rho_0$) for x = 0.15, 0.20 and 0.30 samples.

TH-1060_06612103

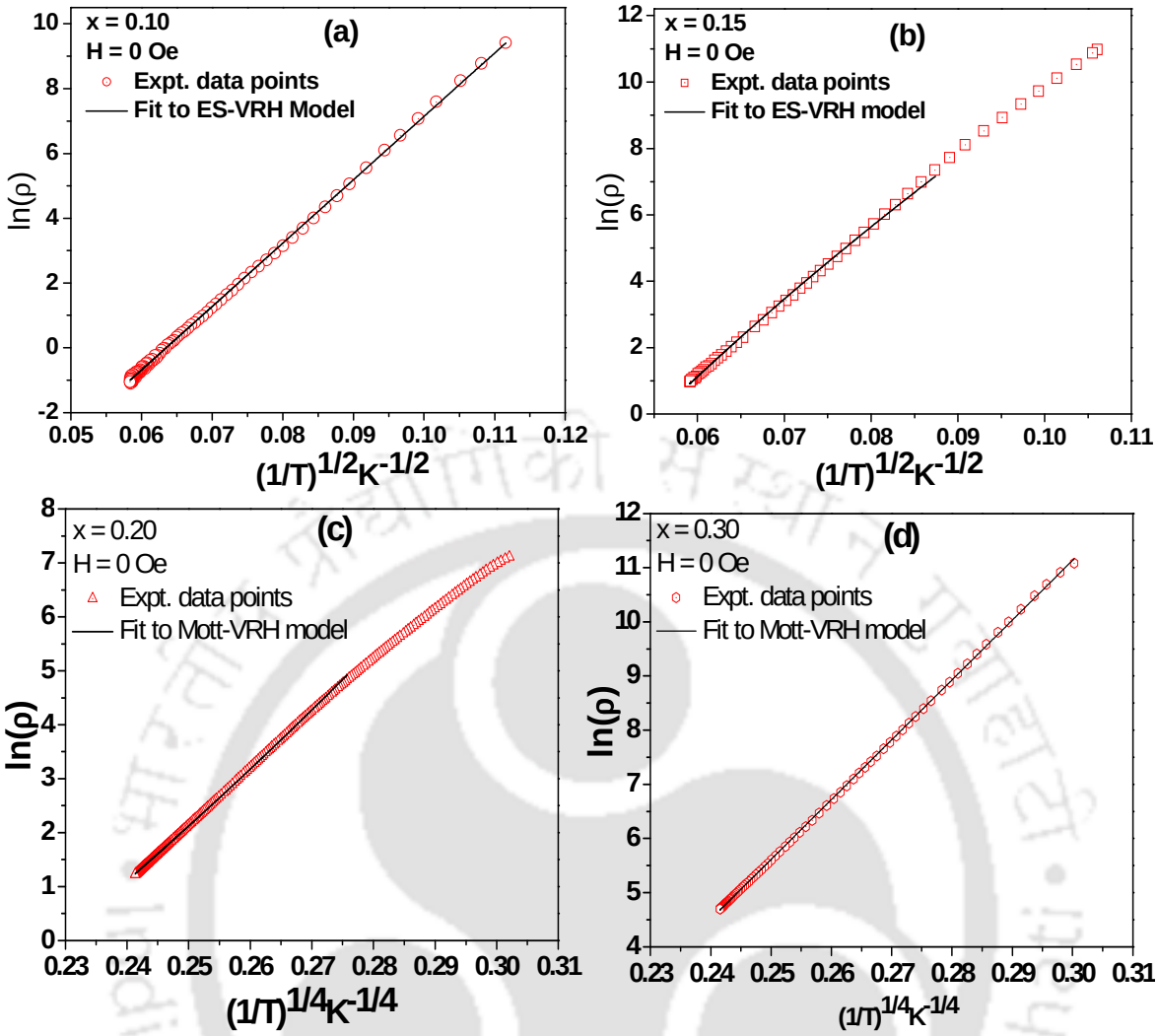

Figure 3.32: (a) & (b) ln (ρ) vs. $(1/T)^{1/2}$ for x = 0.10 & 0.15 samples, (c) & (d) ln (ρ) vs. $(1/T)^{1/4}$ for x = 0.20 & 0.30 samples in the absence of magnetic field. The solid lines are fit to ES-VRH model for x = 0.10 & 0.15 and Mott-VRH model for x = 0.20 & 0.30 samples.

Table 3.7: Parameters obtained from the resistivity analysis in metallic region.

Para-meters	ρ_0(×10 ^{4}Ωcm)		ρ_2(Ωcm K^{-2})		$\rho_{4.5}$ (Ωcm K$^{-4.5}$)		T_{MI}(K)		(-) **MR(%)**
Samples	H = 0 Oe	H=10 kOe	H = 0 Oe	H=10 kOe	H = 0 Oe	H=10 kOe	H = 0 Oe	H=10 kOe	
x = 0.20	0.024	0.011	-0.068	-0.03	7.15E-7	3.52E-7	117	124	59
x = 0.30	1.29	0.55	-3.70	-1.56	4.19E-5	1.95E-5	120	126	57

TH-1060_06612103

Table 3.8: Parameters obtained from the resistivity analysis in the semiconducting region for $H = 0$.

Samples Parameters	**x = 0.10**	**x = 0.15**	**x = 0.20**	**x = 0.30**
rmsd (Mott-VRH)(%)	0.074	0.066	0.017	0.020
rmsd (ES-VRH) (%)	0.051	0.024	0.021	0.035
T_{0m}($\times10^{8}$K)	-----	-----	1.214	1.488
ρ_{om} ($\times10^{-11}$Ωcm)	-----	-----	3.392	27.924
R_h(300K) (Å)	-----	-----	42.569	44.784
E_{hm} (300K)(mev)	-----	-----	162.89	171.37
$N(E_F)$ ($\times10^{25}$ev^{-1}m^{-1})	0.886	0.771	1.89	1.54
T_{0s}($\times10^{4}$)(K)	3.826	5.048	----	----
ρ_{oES} ($\times10^{-5}$ Ωcm)	0.044	0.0445	----	---
ε_r	2.71	2.055	----	----

are generally 2, 2.5, 3 or 4.5 depending upon the nature of scattering mechanism. The resistivity data were analyzed by taking different values of m and n. Better fit was obtained for m = 2 and n = 4.5 and the fitted data are shown as solid lines in figure 3.30 (c) and (d). The fitted parameters for H = 0 and 10 kOe are listed in table 3.7. Thus, the electrical resistivity in metallic region can be explained by the magnon scattering mechanism for the samples x = 0.20 and 0.30 samples.

The resistivity data of x = 0.20 and 0.30 samples for H = 0, in the semiconducting region, i.e., for $T > T_{MI}$ was analyzed by using Mott variable range hopping (Mott-VRH) and Efros-Shklovskii VRH (ES-VRH) models as discussed in section 1.9.3. Similarly, the resistivity data of x = 0.10 and 0.15 samples were analyzed in the entire measured temperature range. The resistivity data of x = 0.20 and 0.30 samples for $T > T_{MI}$ could be fitted to Mott-VRH model with relatively low root mean square deviation value. The Mott-VRH model equation as explained in section 1.9.3 is reproduced as follows,

TH-1060_06612103

$$\rho = \rho_{0m} \exp\left(\frac{T_{0m}}{T}\right)^{1/4} \quad \text{---------- (3.13)}$$

Here ρ_{0m} is the Mott residual resistivity and T_{0m} is the Mott characteristic temperature. The $ln(\rho)$ versus $(1/T)^{1/4}$ plots in figure 3.32 (c) and (d) show linear behavior and the fitted data are shown as solid line. The density of states in the vicinity of the Fermi level ($N(E_F)$), hopping distance, $R_{hop}(T)$ and hoping energy $E_{hop}(T)$ have been estimated from the fitted parameters and using the relations discussed in section 1.9.3 are given as follows.

$$N(E_F) = \frac{18}{k_B T_{0m} a^3} \quad \text{---------- (3.14)}$$

$$R_{hop}(T) = \frac{3}{8} a \left(\frac{T_{0m}}{T}\right)^{1/4} \quad \text{---------- (3.15)}$$

$$E_{hop}(T) = \frac{1}{4} k_B T^{3/4} T_{0m}^{1/4} \quad \text{---------- (3.16)}$$

Here a is the localization length and k_B is the Boltzmann constant. By following Viret *et al.* [267], a is taken as 4.5Å in the above calculations. The value of Mott residual resistivity, ρ_{0m}, Mott characteristic temperature, T_{0m}, hopping length $R_{hop}(K)$, hopping energy etc. are tabulated in table 3.8 for x = 0.20 and 0.30 samples. However, the semiconducting behavior of x = 0.10 and 0.15 samples are best fitted to ES-VRH model as given below (reproduced from eqn. 1.34).

$$\rho = \rho_{0s} \exp\left(\frac{T_{0s}}{T}\right)^{1/2} \quad \text{---------- (3.17)}$$

where, ρ_{0s} is the ES residual resistivity and T_{0s}, the ES characteristic temperature is defined as,

$$T_{0s} = \frac{\beta_1 e^2}{k_B a 4\pi\varepsilon_0\varepsilon_r} \quad \text{---------- (3.18)}$$

Here a is the localization length, ε_r is the dielectric constant and β_1 is a numerical constant = 2.8. The $ln(\rho)$ versus $(1/T)^{1/2}$ plots in figure 3.32 (a) and (b) show linear behavior and the fitted data are shown as solid line. The fitted parameters are tabulated in table 3.8.

3.5. Conclusions

In summary, we have prepared single phase samples of K doped series, i.e., $Nd_{1-x}K_xMnO_3$ for x = 0.10 to 0.30. The neutron powder diffraction (NPD) measurements were carried out down

TH-1060_06612103

to 22 K for x = 0.15 and 0.20 samples. The room temperature NPD patterns could be refined by including only the nuclear structure of *Pnma* space group in orthorhombic cell. The NPD patterns at low temperature could be refined by considering both nuclear structure and magnetic reflections based on ferromagnetic structure. The magnetic moments of Mn ions are found to be aligned in the *ac*-plane. All K-doped samples exhibit PM to FM transition, with transition temperature ranging from 116 to 128 K as per magnetization measurements. The saturation magnetization value, M_S was found to increase with increase in doping concentration and the result was consistent with the estimated moments from the analysis of NPD patterns. The field variation of magnetization could be fitted to Brillouin function model by considering the FM interaction. The effective magnetic spin, S_{eff} for FM contribution has been estimated and those values were found to increase with increase in doping concentration.

The temperature and frequency variations of measured ac susceptibility in x = 0.15 sample were analyzed to study the spin glass behavior. The spin glass behavior was also studied by recording the third harmonic ac susceptibility and thermo remanent magnetization. A critical exponent of 3.2 was observed from the analysis of third harmonic susceptibility. The origin of spin glass behavior was found to be due to the freezing of clusters rather than magnetic frustration at atomic scale.

The critical exponent behavior was analyzed for two samples with x = 0.20 and 0.30. Isothermal magnetization was measured as a function of field in the vicinity of FM transition. They were analyzed in terms of modified Arrott plot method and the estimated critical exponents β = 0.57±0.03, γ = 1.04±0.02, and δ = 2.82±0.03 were found to be close to the mean-field model values. The observed static scaling plot clearly showed the estimated critical exponents are accurate.

The present materials are found to exhibit magneto-caloric effect with typical change in entropy for 1 T field as 1.67 J/Kg K and 1.37 J/Kg K for x = 0.20 and x = 0.30 samples respectively. Metal-insulator transitions in the vicinity of FM T_C and colossal magnetoresistivity of the order of 60% for 1 T magnetic field have been observed.

TH-1060_06612103

Chapter 4: (Nd, Na)-Mn-O Series

The ionic radius of Na^{1+} ion is 1.02 Å and is comparable to that of Nd^{3+} (0.983 Å). So it would be very interesting to study the doping of monovalent Na in place of Nd in $NdMnO_3$ series. Unlike $Nd_{1-x}K_xMnO_3$ and $Nd_{1-x}Ag_xMnO_3$ series, the effective A-site ionic size is relatively low. (Nd, Na)-Mn-O series with 20 and 25 % of Na doping was studied by Li and his group [226, 227] and they reported charge ordering at 155 and 180 K respectively, followed by a weak FM transition at around 110 K. Tang *et al.* [228] showed that $Nd_{1-x}Na_xMnO_3$ for x = 0.1 to 0.25 exhibit FM insulating behavior. PM to FM transition along with spin glass like transition and the signature of spin canting have been reported in 'Ag' doped $NdMnO_3$ compound [231]. Transition from FM-insulating state to FM-metallic state and colossal magnetoresistance of the order of 60% were observed in $Nd_{1-x}K_xMnO_3$ (x = 0.10 – 0.30) series as presented in chapter-3. A reduction in Jahn-Teller distortion of MnO_6 octahedra and the transition from A-type AFM structure to pseudo CE-type structure were reported in Na doped $PrMnO_3$ [52]. In order to systematically study the structural and magnetic properties of Na-doped Nd-Mn-O series, $Nd_{1-x}Na_xMnO_3$ compounds were prepared for x = 0 to 0.20. It is found that the system undergoes a transition from AFM phase (for x = 0) to charge ordered state (for x = 0.20) through DE FM phase (for x = 0.10 and 0.15). We have systematically studied the magnetic dynamics in the CO/AFM system, where, different magnetic ground states were found to be dominant at different temperature regions. In this chapter, the magnetic properties determined from the analysis of magnetization and NPD patterns recorded on $Nd_{1-x}Na_xMnO_3$ samples are presented.

4.1. Sample Preparation and Characterization

Polycrystalline samples of $Nd_{1-x}Na_xMnO_3$ (x = 0, 0.05, 0.10, 0.15, and 0.20) were prepared by conventional solid state reaction method. Stoichiometric ratio of Nd_2O_3, Na_2CO_3 and manganese acetate with 99.9% purity were weighed and mixed thoroughly under acetone. The mixture was presintered at 300 ^{0}C, 400 ^{0}C, 500 ^{0}C, 600 ^{0}C and 700 ^{0}C for 6 hrs. at each temperature and at 800 ^{0}C for 24 hrs with intermediate grindings. The powdered samples were pressed into pellet form and were sintered at 1000 ^{0}C for 24 h. The final sintering in pellet form was carried out at 1200 ^{0}C for 40 h.

The prepared samples of $Nd_{1-x}Na_xMnO_3$ series for x = 0 to 0.20 are found to be in single phase form as per the XRD results. The XRD patterns for these samples are shown in

TH-1060_06612103

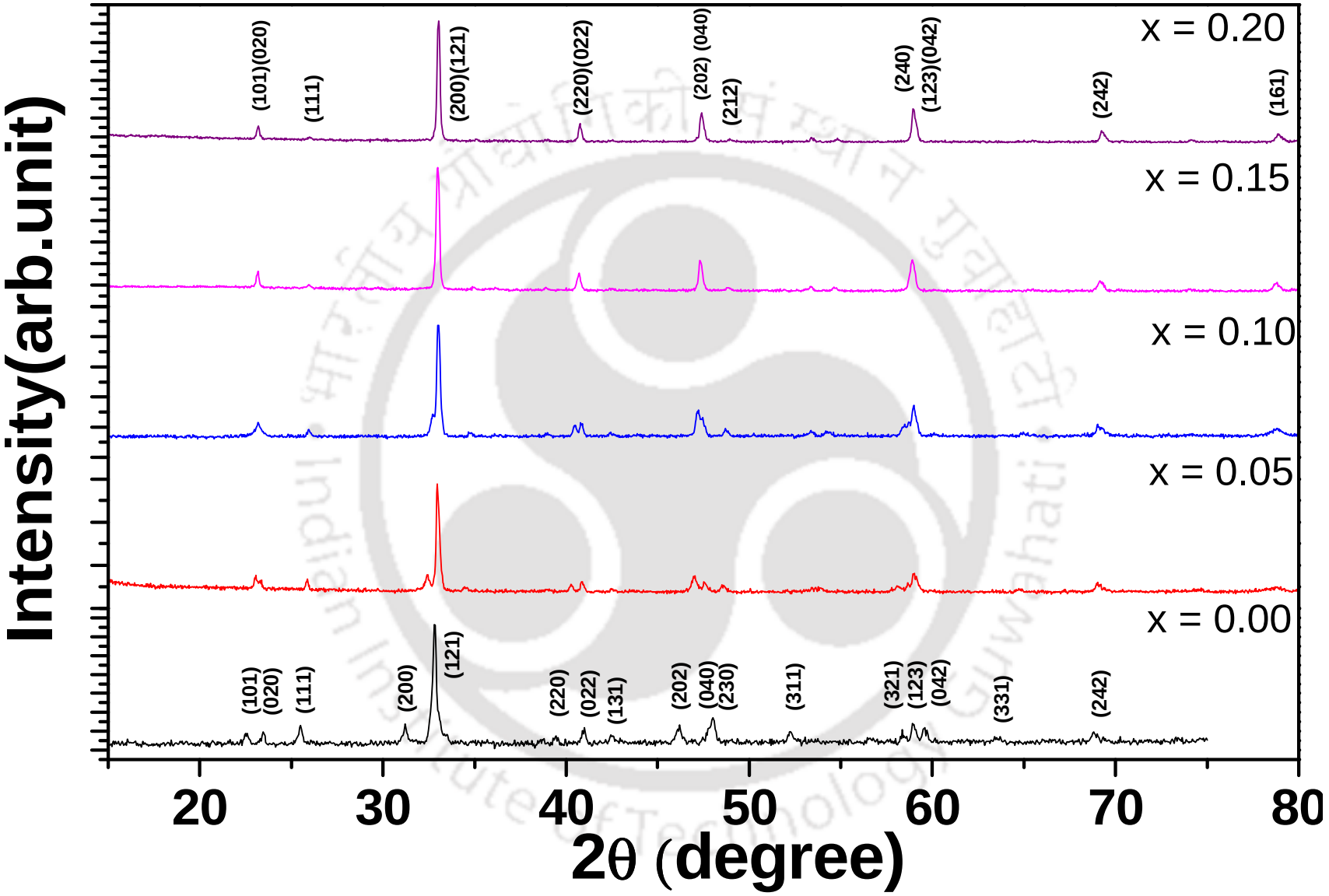

Figure 4.1: XRD patterns of $Nd_{1-x}Na_xMnO_3$ for x = 0.0, 0.05, 0.10, 0.15, and 0.20.

TH-1060_06612103

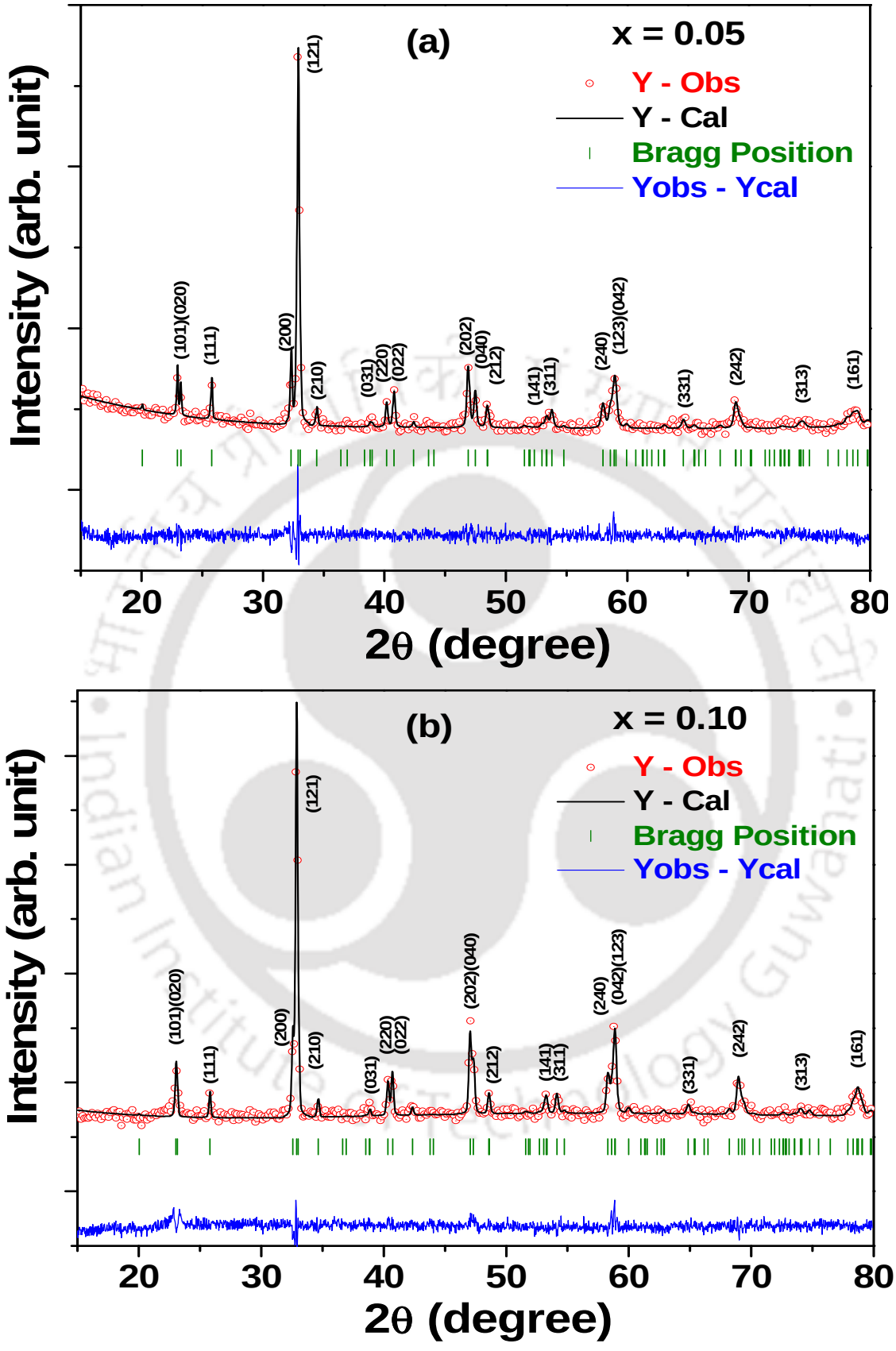

Figure 4.2: XRD patterns alongwith Rietveld refinement of the samples (a) x = 0.05 and (b) x = 0.10.

TH-1060_06612103

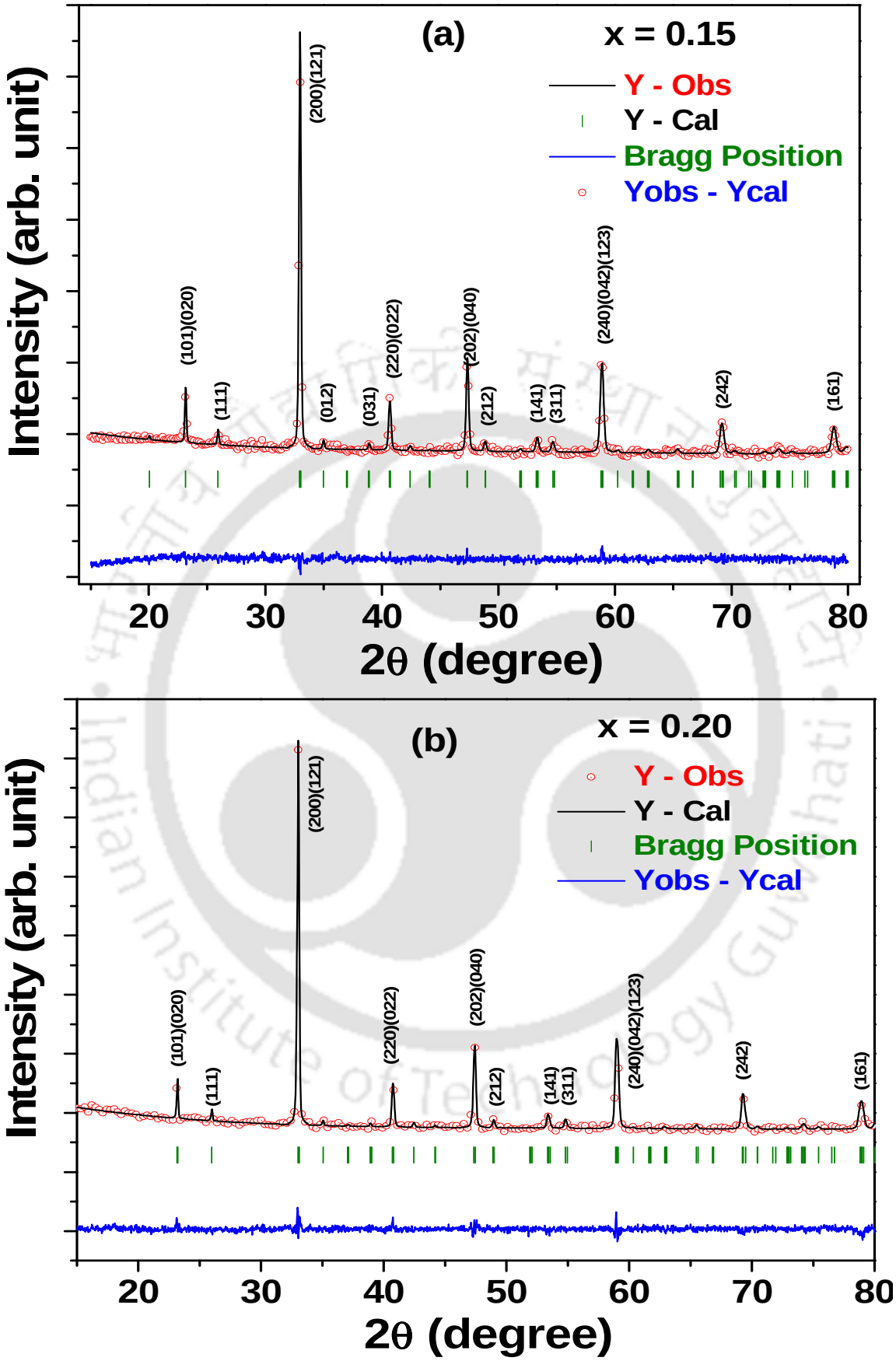

Figure 4.3: XRD patterns alongwith Rietveld refinement of the samples (a) x = 0.15 and (b) x = 0.20.

TH-1060_06612103

Table 4.1: Parameters obtained from the Rietveld analysis of XRD patterns of $Nd_{1-x}Na_xMnO_3$ (x = 0, 0.05, 0.10, 0.15 & 0.20). The numbers in brackets are estimated errors.

Sample / **Parameter**	**x = 0.0**	**x = 0.05**	**x = 0.10**	**x = 0.15**	**x = 0.20**
Space group	*Pnma*	*Pnma*	*Pnma*	*Pnma*	*Pnma*
Chi^2	1.27	0.84	0.78	0.58	0.77
R_{Brag}	15.6	10.8	11.9	7.26	7.37
R_f	20.3	12.5	13.4	8.96	8.35
R_p	5.15	4.44	3.54	2.98	3.37
R_{wp}	6.44	5.57	4.51	3.74	4.30
R_{exp}	5.72	6.79	5.09	4.88	4.87
a (Å)	5.7132(15)	5.5346(9)	5.4950(7)	5.4374(10)	5.4243(5)
b (Å)	7.5608(18)	7.6520(13)	7.6769(9)	7.6746(20)	7.6750(7)
c (Å)	5.4025(13)	5.4157(9)	5.4221(6)	5.4205(11)	5.4061(5)
Volume (Å^3)	233.37(10)	229.3(07)	228.7(05)	226.2(08)	225.07(03)

figure 4.1. As the doping concentration increases, some important fundamental reflections such as (101) and (200) are found to shift towards higher angle and finally merging with (020) and (121) reflections respectively. This signifies the decrease in unit cell volume. These patterns could be refined by using *Pnma* space group in orthorhombic cell. XRD patterns alongwith Rietveld refinements are shown in figure 4.2 and 4.3 for x = 0.05 to 0.20 samples. The lattice parameters determined from the XRD analysis are given in table 4.1. The typical lattice parameters for x = 0.15 are *a* = 5.4374Å, *b* = 7.6746 Å and *c* = 5.4205 Å. The lattice parameters are found to be comparable to those of previous report on Na-doped samples and Ag-doped Nd-Mn-O series [231]. The lattice parameters are mostly, found to decrease with increase in doping concentration. However, the *b* value is found to increase up to x = 0.10, and then it remains constant for further increase in x-value. SEM micrographs recorded for the above samples are shown in figure 4.4. The microstructure morphology of the samples are found to be uniform and the average particle size is found vary from 1.5 to 2.5 μm. Typical EDS spectrum for x = 0.20 sample is shown in figure 4.4 (f). The chemical compositions determined from EDS analysis are found to be comparable to the nominal starting composition. The average valency of Mn ions are found to be 3.06, 3.18, 3.34, 3.39 and 3.46 for x = 0, 0.05, 0.10, 0.15, and 0.20 samples respectively. The systematic increase

TH-1060_06612103

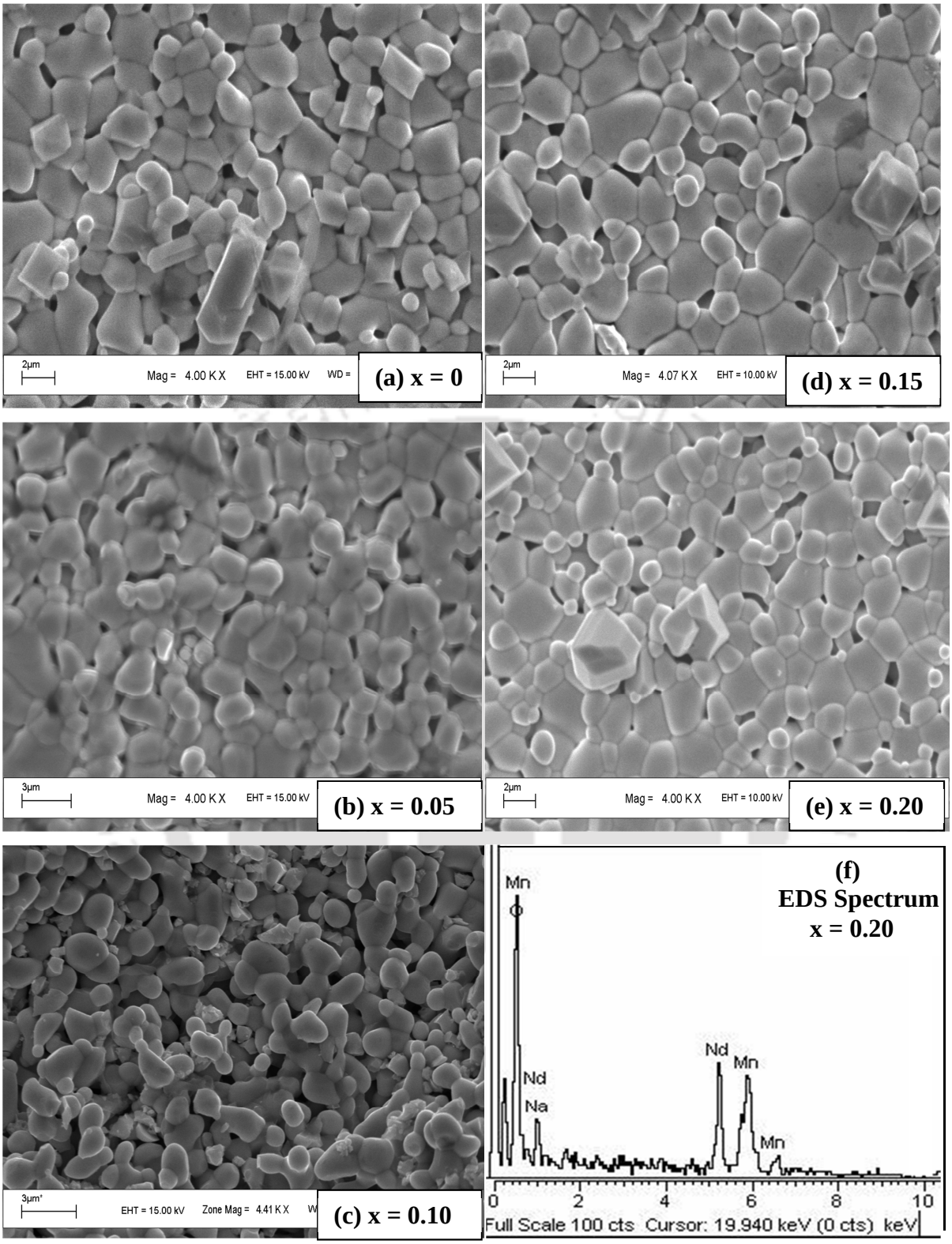

Figure 4.4: SEM micrographs of (a) x = 0, (b) x = 0.05, (c) x = 0.10, (d) x = 0.15, and (e) x = 0.20 samples. Figure (f) shows typical EDS spectrum for x = 0.20 sample.

TH-1060_06612103

in Mn valency with Na substitution highlights the formation of Mn^{3+}/Mn^{4+} mixture with increase in Mn^{4+} concentration. Even though, the valency of Mn is found to increase with increase in doping, but its actual value for a particular doping concentration is found to be more than that of expected value and such behavior can be explained as mainly due to possible oxygen off-stoichiometry.

4.2. Magnetic Properties

Figure 4.5 shows the temperature variation of magnetization of x = 0, 0.05, 0.10, 0.15 and 0.20 samples in zero field cooled (ZFC) and field (FC) conditions for an applied magnetic field of 20 mT. The parent compound, x = 0 exhibits a peak at around 75 K and it can be attributed to the AFM ordering of Mn ions. In addition to that, a sharp fall in magnetization value and leading to negative values is observed at 15 K as shown in figure 4.5 (a). The irreversibility between ZFC and FC magnetization can be seen for $T < T_N = 75$ K. Another interesting feature is that at 15 K, the FC curve exhibits a sharper fall with large negative values of magnetization compared to that of ZFC case. Such magnetization values can be interpreted in terms of ferrimagnetic coupling between two magnetic sublattices, namely Mn and Nd ions. The samples for x = 0.05 to 0.15 exhibit PM to FM transition followed by a low temperature spin glass like transition at 40 K. The FM T_C was found to be in the range of 101 K to 113 K and they are shown in figure 4.5 (b)-(d). The FM T_C values are comparable to other monovalent alkali-ion doped $NdMnO_3$ compounds [228, 231, 265]. The dc inverse susceptibility in the paramagnetic region was fitted to Curie-Weiss law by varying the parameters, Curie constant C and Curie temperature θ_C. The effective paramagnetic moment, μ_{eff} was estimated from the fitted values of C and using the relation, $C = (N\mu_{eff}^2/3k_B)$, where N is Avogadro number and k_B is Boltzmann constant. The estimated values of θ_C and μ_{eff} are given in table 4.2. The θ_C values are found to be about 20 K higher than the respective FM T_C determined from dM/dT vs. T plots. Theoretical effective magnetic moment (μ_{th}) can be calculated using the relation,

$$\mu_{th} = \sqrt{x_1\mu_1^2 + x_2\mu_2^2 + x_3\mu_3^2} \qquad \text{----------} \qquad (4.1)$$

Here x_1, x_2, x_3 are the concentrations of Nd^{3+},Mn^{3+}, Mn^{4+} ions and μ_1, μ_2, μ_3 are their respective paramagnetic moments. Here μ_1, μ_2, and μ_3 are taken as 3.63 μ_B, 4.9 μ_B and 3.87 μ_B respectively. The μ_{eff} values are found to be considerably higher than those of μ_{th} as shown in table 4.2 and it could be mainly due to the presence of some isolated FM clustering.

TH-1060_06612103

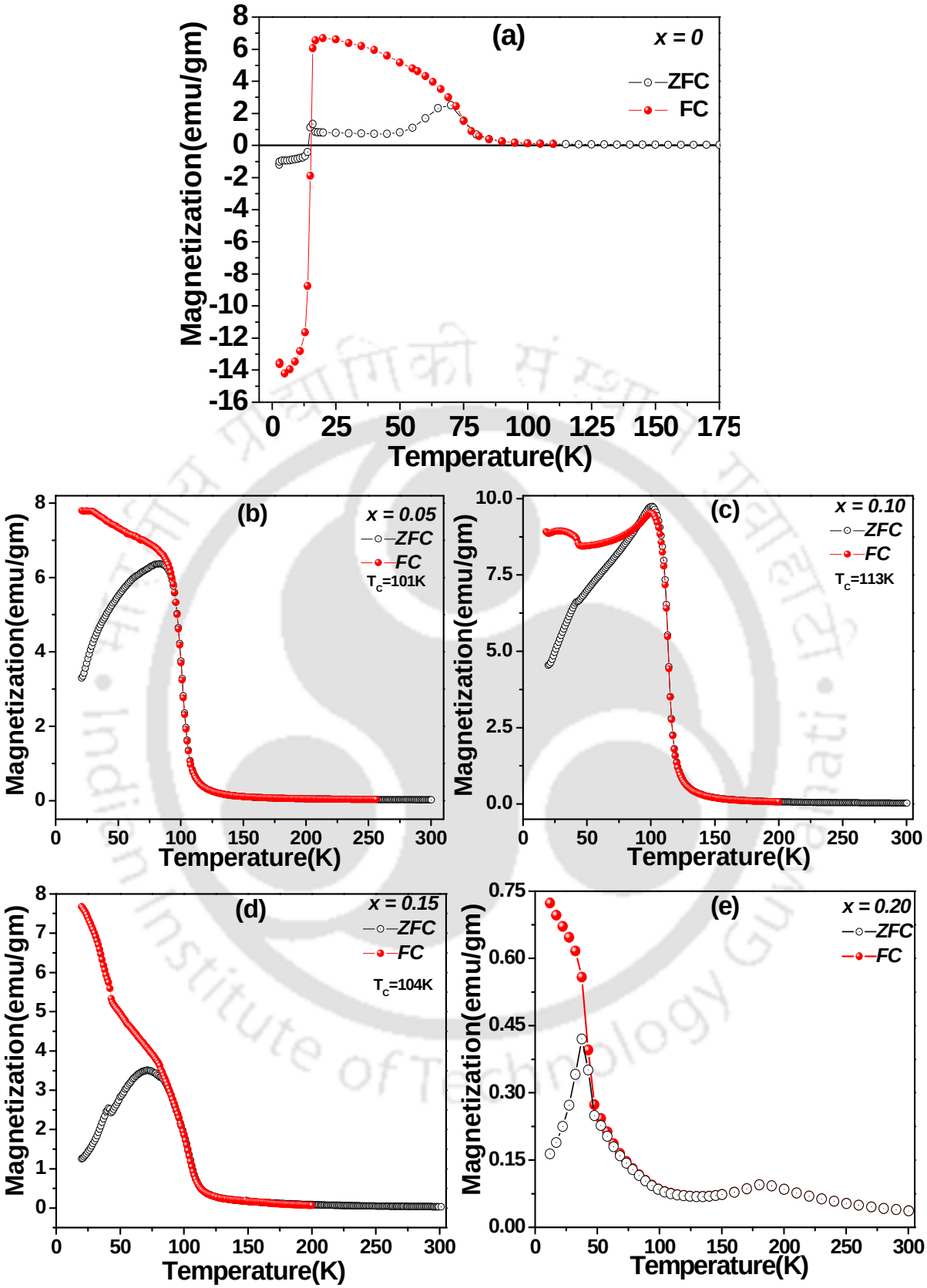

Figure 4.5: Temperature variations of magnetization in zero field cooled (ZFC) and field cooled (FC) conditions for (a) x = 0, (b) x = 0.05, (c) x = 0.10, (d) x = 0.15, and (e) x = 0.20 samples.

TH-1060_06612103

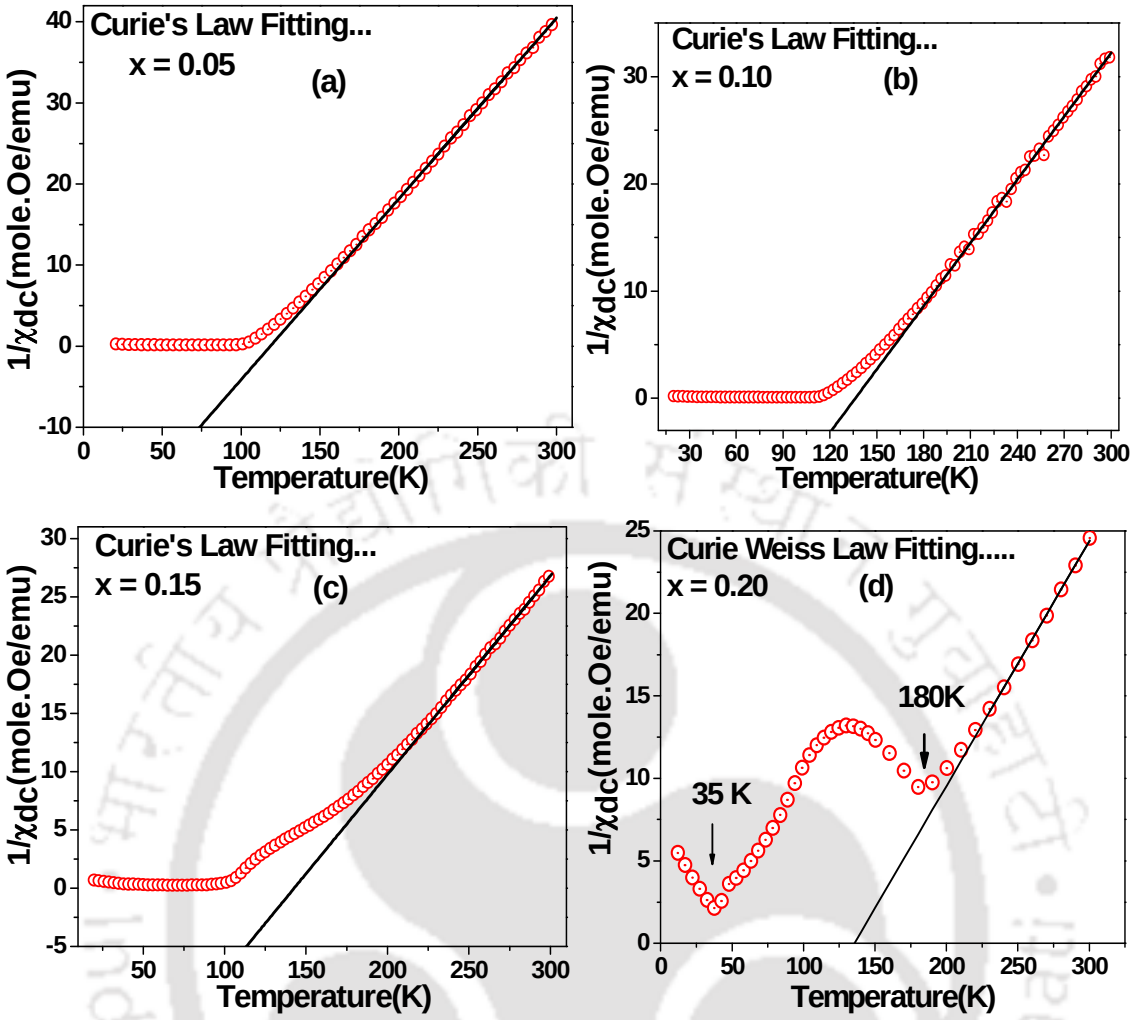

Figure 4.6: Temperature variations of inverse dc susceptibility for (a) x = 0.05, (b) x = 0.10, (c) x = 0.15, and (d) x = 0.20 samples. The fitted data using Curie Weiss law are shown as solid lines.

Table 4.2: Parameters obtained from magnetization measurement and analysis. T_C is the ferromagnetic transition temperature. θ_c and C are Curie temperature and curie constants respectively. M_S is saturated magnetic moment.

Samples/ parameters	***x = 0***	***x = 0.05***	***x = 0.10***	***x = 0.15***	***x = 0.20***
T_C (K)	75	101	113	104	43
θ_c(K)	76	118	136	143	135
C(emuK/moleOe)	4.09	4.48	5.08	5.87	6.73
μ_{eff}(μ_B)	5.71±0.14	5.98±0.03	6.21±0.06	6.68±0.12	7.33±0.15
μ_{th}(μ_B)	6.09	5.96	5.83	5.69	5.37
M_S(μ_B/f.u)	2.6	4.0	4.3	2.2	4.2

TH-1060_06612103

The magnitude of irreversible magnetization, $\Delta M = (M_{FC} - M_{ZFC})$ is found to increase with increase in doping concentration, i.e., in correlation with increase in Mn^{4+} concentrations. One of the reasons could be due to the presence of competing anti-ferromagnetic interaction in Mn^{4+}-O-Mn^{4+} networks. The x = 0.10 sample having the Mn valency of 3.34 exhibits the highest FM T_C and can be explained in terms of the presence of 34% of Mn^{4+} ions, which is close to the optimum value in manganites. The low temperature peak at 40 K, which is attributed to the spin glass like transition is found to be more prominent for x = 0.15. It can be understood on the basis of presence of competing AFM interaction due to the increase in concentration of Mn^{4+} ions beyond the optimum value of 33%. The Curie-Weiss law fits of x = 0.05 and 0.10 samples show clear PM to FM transitions as displayed in figure 4.6 (a) and (b). However, the $1/\chi$ versus temperature plot of x = 0.15 sample deviates from linearity at around 180 K as shown in figure 4.6 (c).

A large reduction in magnitude of magnetization has been observed for the increase in Na concentration to 20% and it is attributed to the transition from ferromagnetic insulating state for x < 0.20 to charge ordered state for x = 0.20. It is clearly seen from figure 4.5 (e) that x = 0.20 sample exhibits a broad hump at 180 K and is attributed to charge ordering transition temperature, T_{CO}. A similar behavior has been reported in $Pr_{0.75}Na_{0.25}MnO_3$ system at T ≈ 220 K [268]. The Mn^{3+}/Mn^{4+} ratio for this compound is 54:46, which is quite close to half doped charge ordered system. Hence, the Mn^{3+} and Mn^{4+} ions arrange orderly and, it gives rise to a charge ordered state below 180 K. The T_{CO} is comparable to that observed by Liu. *et al.* [226] in $Nd_{0.75}Na_{0.25}MnO_3$. A secondary rise in magnetization below 100 K followed by a sharp peak at around 40 K is observed. It can be ascribed to the presence of weak FM followed by competing magnetic interaction such as re-entrant spin glass (RSG) and AFM behavior. This can be substantiated from the observed large irreversibility between ZFC and FC magnetization, especially below 40 K. Figure 4.6 (d) shows the inverse susceptibility along with Curie-Weiss law fit for x = 0.20 sample. The presence of CO transition can be clearly seen and the impending weak FM is manifested from the positive value of the Curie temperature. Thus, the anomaly observed for x = 0.15 and 0.20 samples from χ and $1/\chi$ versus T plots can be attributed to charge ordered insulating state.

In order to understand the complex magnetic properties of x = 0.20 sample, we have carried out *M-T* measurement under different magnetic fields ranging from 1 T to 7 T as shown in figure 4.7. The applied magnetic field is found to enhance the low temperature FM phase with a large increase in the magnitude of magnetization along with shift in FM T_C towards higher temperature, i.e., 85 K for H = 1 T to 166 K for H = 7 T. The sharpness of the

TH-1060_06612103

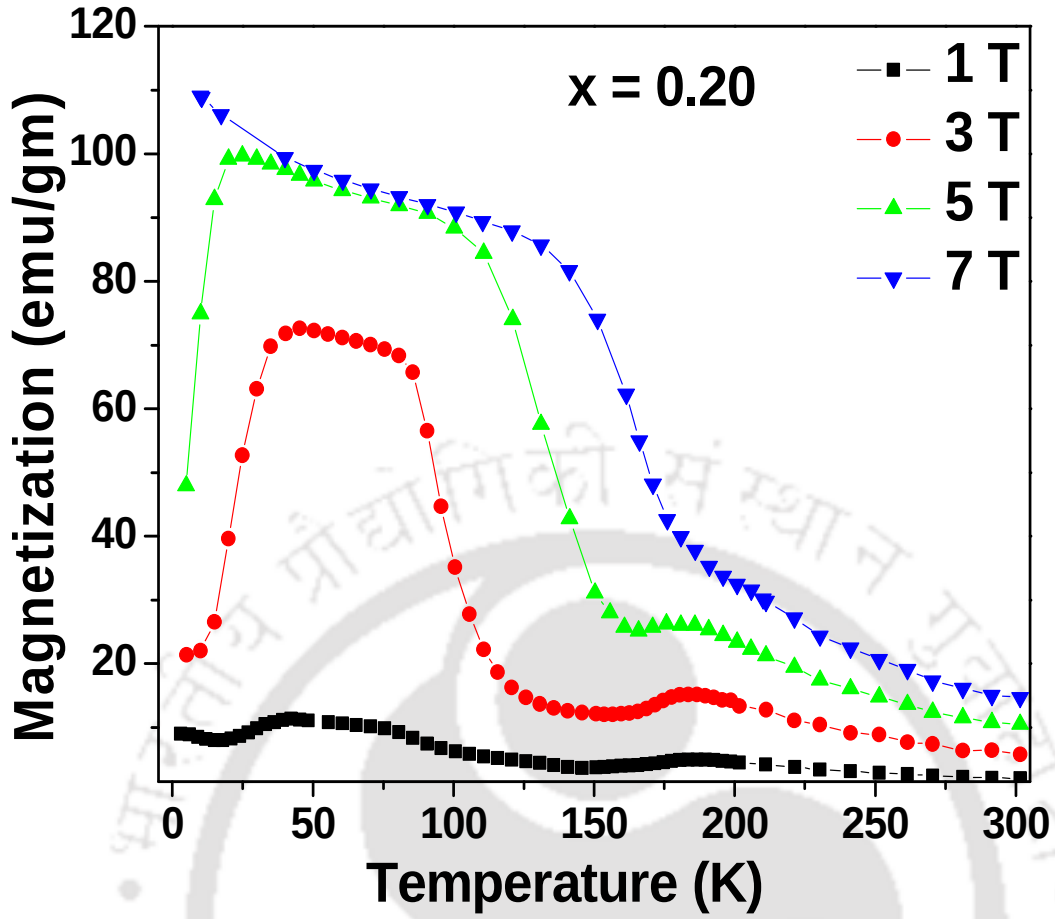

Figure 4.7: Temperature variation of zero field cooled (ZFC) magnetization of x = 0.20 sample, for different applied magnetic fields.

FM transition is also found to decrease, i.e., the width of the FM transition estimated from the full width half maximum of *dM/dT* versus *T* is found to increase from 17 K for H = 1 T to 24 K for *H* = 7 T. Inspite of large increase in FM contribution, no saturation of FM signal was observed even at temperatures for below the FM T_C. This signifies the presence of other competing magnetic interaction or the partial polarization of Nd moment with increase in applied magnetic field and decrease in temperature. Unlike the high temperature CO-AFM phase, the low temperature AFM/RSG phase transition is found to be field dependent. Moreover, the sharp fall in magnetization observed at low temperature due to the possible spin glass like behavior is shifted further downwards and ultimately it disappears for *H* = 7 T. Thus, the applied magnetic field tends to stabilize the FM phase at the expense of other competing magnetic phase. On the otherhand, the CO transition temperature observed at 180 K is found to be field independent and it could be seen prominently up to the magnetic field of 5 T. The disappearance of CO transition for *H* = 7 T could be either due to the quenching of charge-ordering or the merging of the CO transition with the enhanced FM signal.

TH-1060_06612103

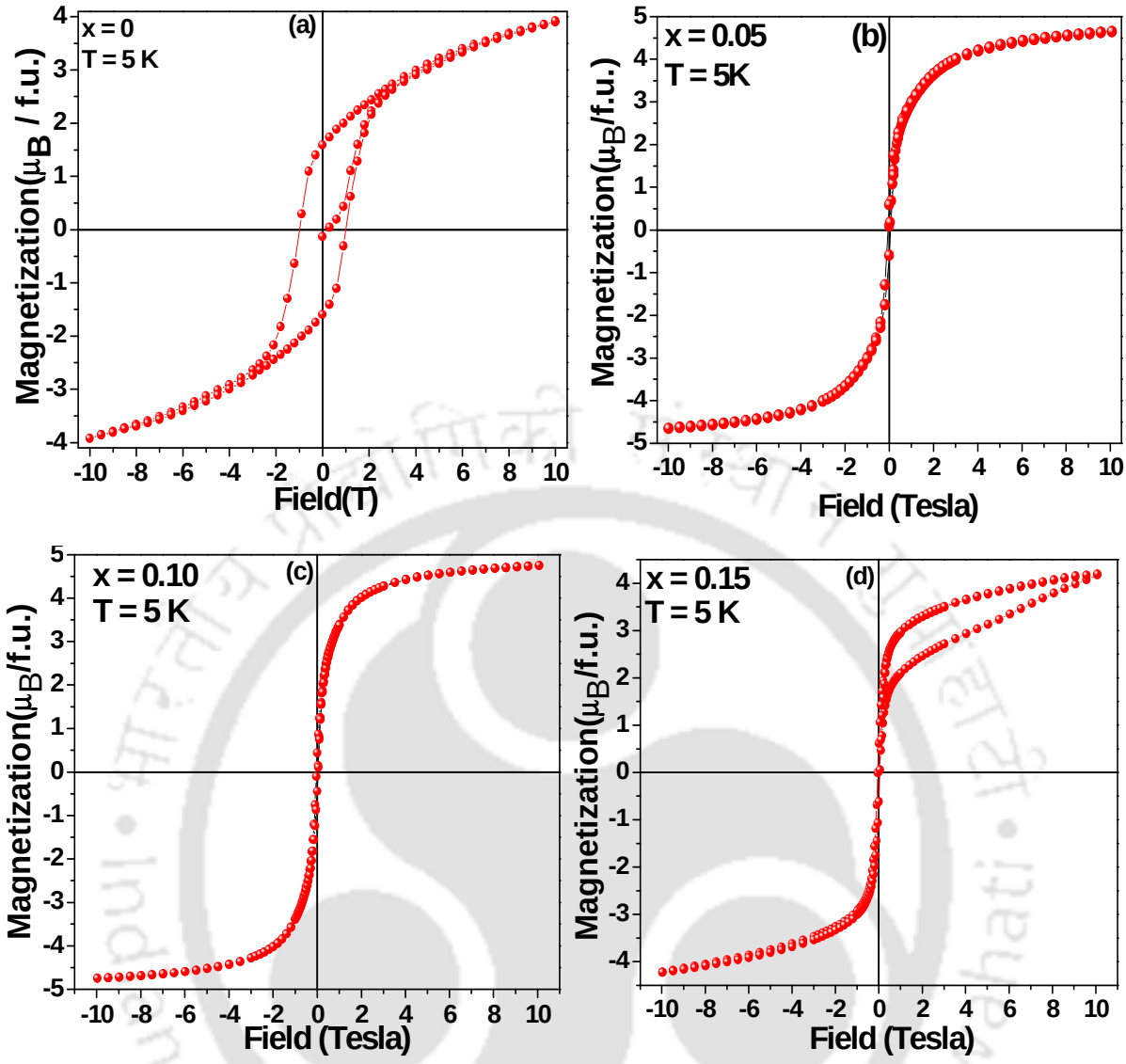

Figure 4.8: Magnetization loop measured at 5 K for (a) x = 0.0, (b) x = 0.05, (c) x = 0.10 and (d) x = 0.15 samples respectively.

We have carried out the measurement of field variation of magnetization up to ±10 T at 5 K for x = 0 to 0.20. The measurements were performed after cooling the sample from 300K under zero magnetic field condition. The *M-H* loops recorded at 5 K for x = 0, 0.05, 0.10, and 0.15 samples are shown in figure 4.8 (a)-(d). The parent compound, i.e., x = 0 exhibits a high coercive field of 1 T. The magnetization is not found to saturate even for a field of 10 T as shown in figure 4.8 (a) and it indicates the dominant AFM interactions. However, the observed remanent magnetization of 1.5μ_B/f.u suggests the coexistence of FM and AFM ordering. It is difficult to estimate the ferromagnetic contribution of 'Nd' moment at 5 K quantitatively from this measurement alone. The saturation magnetization (M_S) was determined by fitting the magnetization data to the following equation,

TH-1060_06612103

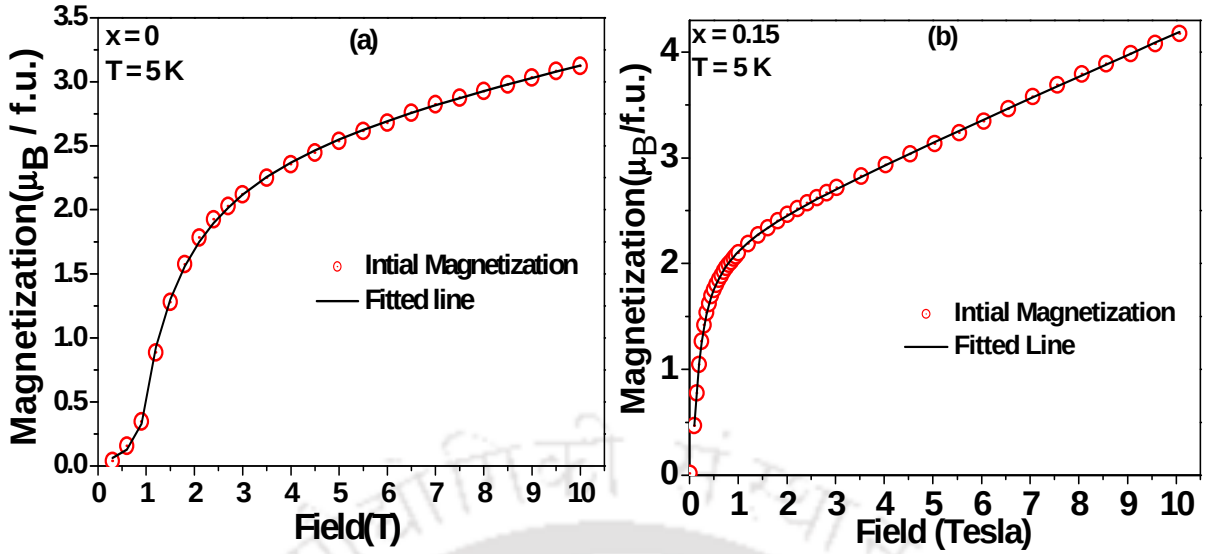

Figure 4.9: Field variations of initial magnetization for (a) x = 0 and (b) x = 0.15 samples. The solid lines are fitted data to eqn. 4.2.

$$M(H) = M_S\left[1 - \frac{a}{H} - \frac{b}{H^2}\right] + \chi_d H \qquad \text{----------} \qquad (4.2)$$

where, χ_d is the high field differential susceptibility and *a* and *b* are constants. The initial magnetization curves alongwith the fitted data to the above equation are shown in figure 4.9 (a) and (b) for x = 0 and 0.15 samples respectively. The saturation magnetization (M_S) values for different samples are given in table 4.2. The x = 0.05 and 0.10 samples exhibit normal ferromagnetic behavior. The M_S values of x = 0.05 and 0.10 samples are found to be larger than the values corresponding to Mn ions and it suggests the ferromagnetic contribution from 'Nd' ion at low temperature. The initial curve of x = 0.15 sample is found to be outside the magnetization loop and no saturation of magnetization is observed as shown in figure 4.8 (d). The value of M_S determined from initial curve is found to be quite small compared to the expected value of 3.7 μ_B.

The *M-H* curves of x = 0.20 sample at different temperatures show very interesting features as shown in figure 4.10 (a) to (d). It exhibits normal PM linear *M-H* curve for $T >$ 180 K. However, at 130 K it exhibits a linear behavior up to a threshold magnetic field (H_{C1}) of 4.5 T and then it undergoes a field induced magnetic phase transition into a FM state with a hysteresis. The M_S value at this temperature is found to be 3.2 μ_B/f.u. The above phase transition is found to be a reversible one both for the ascending and descending branches of the magnetization curve. It may be noted that we have not observed any FM transition in the *M-T* curve recorded above 130 K. The slope of the linear region in the initial magnetization

TH-1060_06612103

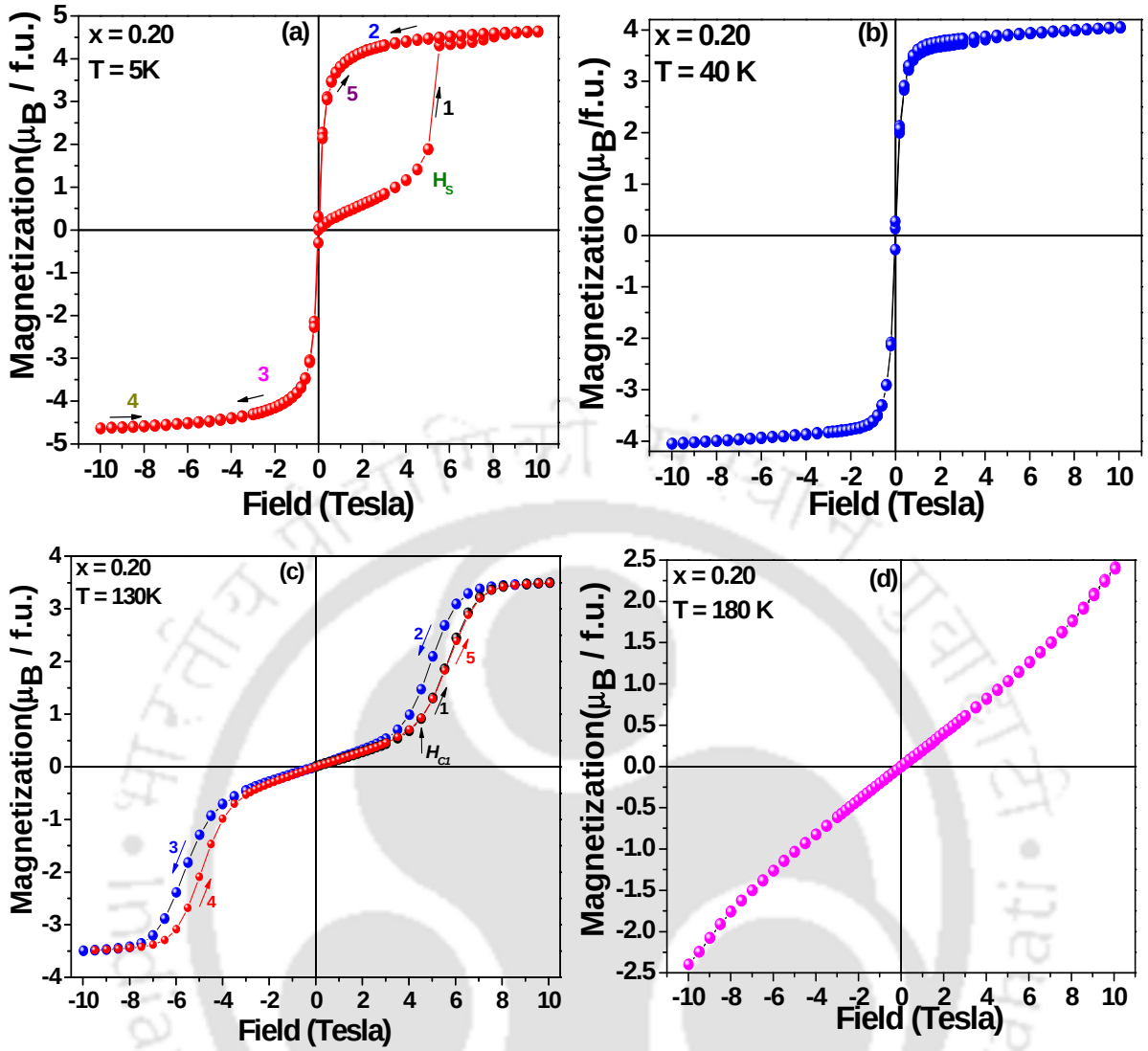

Figure 4.10: Magnetization versus magnetic field at different temperatures for x = 0.20 sample.

curve, at 130 K was determined by a least square fit to a linear relation and was compared to the expected theoretical value $C/T = (\mu_0 N \mu_{eff}^2)/3k_BT$. Here μ_{eff} is the effective paramagnetic moment. From the above calculation, it is concluded that around 24% of Mn ions do not take part in the CO and exhibit spin canting. The *M-H* curve recorded at 40 K, i.e., below the FM T_C exhibits a clear FM behavior with a M_S value of 3.7 μ_B/f.u and it signifies the domination of double exchange FM interaction at this temperature. The *M-H* loop recorded at 5 K, which is below the CO, FM and RSG transitions exhibits a distinct behavior as shown in figure 4.10 (a). The initial magnetization was increasing slowly and linearly up to a characteristic field (H_S) of 5 T, beyond which a first order transition into the FM state with a sharp jump in *M* value from 1 μ_B/f.u to 4.2 μ_B/f.u is observed. It is attributed to the field

TH-1060_06612103

induced quenching of CO or spin glass behavior and, stabilization of FM phase. Unlike at 130 K, here the field induced FM transition is an irreversible process, with a distinct initial curve seen outside the loop. This type of spin flip behavior is usually observed in metamagnetic transitions [188, 269]. The rather large M_S value observed at 5 K, is attributed to the contribution from spin canted Nd ions. It is observed that the M^2 vs. H/M curve exhibits a negative slope for H < 5 T and positive slope for H > 5 T. The negative slope is attributed to the first order behavior and the positive slope is attributed to the second order behavior [270]. Thus at 5 K, for an applied field H < 5 T, the material remains within the characteristics feature of CO-AFM behavior. However for H > 5 T, it undergoes irreversible transition into the FM state. Hence by applying a threshold field one can switch on the spin flip and drive the system into the robust FM state. Thus, a field induced cross-over from CO to FM phase is observed in the present sample. The field induced CO/AFM – FM metamagnetic transition could be explained due to the competition between magnetic energy and elastic energy. The magnetic energy favors alignment of FM clusters and the elastic energy is analogous to elastic strain at the individual AFM/FM domain wall interfaces.

4.3. Neutron Powder Diffraction

4.3.1. Crystal Structure

NPD patterns were recorded at selected temperatures down to 5 K for x = 0, 0.15 and 0.20 samples of $Nd_{1-x}Na_xMnO_3$ series. These samples are found to crystallize with an orthorhombic structure in *Pnma* space group. The NPD data of x = 0 sample recorded at 300 K is shown in figure 4.11 for lower angle region. The Rietveld refinement of the NPD data recorded at 300 K was carried out by varying cell parameters, position of the Nd/Na and O atoms, occupancy, and thermal parameters. Figure 4.12(a) shows the NPD pattern of the parent compound (x = 0) at 300 K along with the results of the Rietveld refinement. All the Bragg reflections could be indexed and the structure is comparable to the distorted orthorhombic perovskite $GdFeO_3$ compound. The refined structural parameters at 300 K determined from this analysis are summarized in table 4.3. The typical values of lattice parameters are found to be a = 5.7200(13) Å, b = 7.5729(22) Å and c = 5.4075(12) Å for x = 0 sample. This is in good agreement with those reported by Munoz *et al.*[177]. The decrease in unit cell volume with increase in doping concentration is observed. This can be understood as a result of generation of Mn^{4+} ions at the expense of Mn^{3+} ions. The ionic size mismatch is quantitatively expressed in terms of a parameter called variance, σ^2. This can be expressed as

TH-1060_06612103

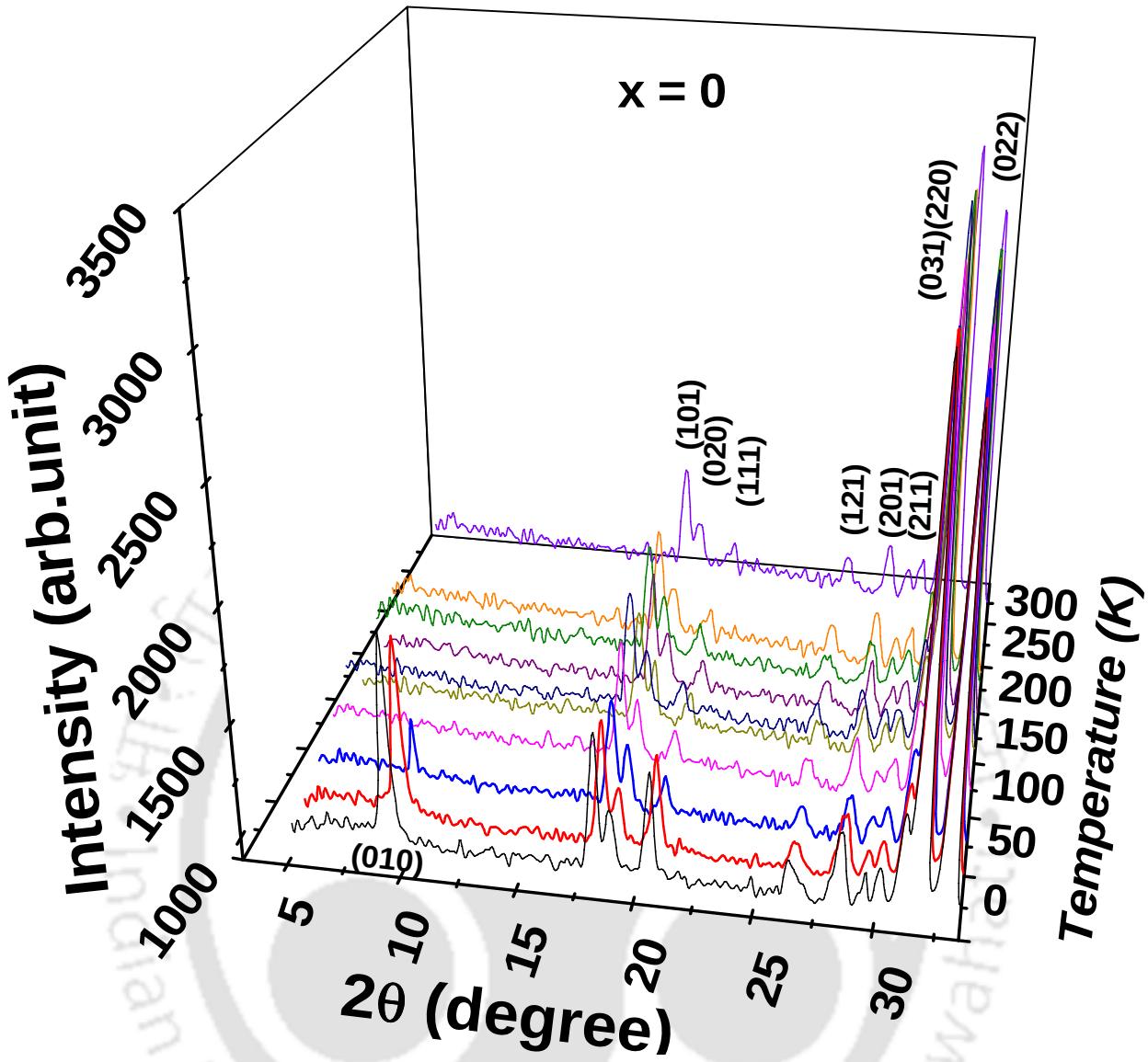

Figure 4.11: Evolution of low angle reflections of neutron diffraction patterns in the temperature range 5 -300K for x = 0.0 sample.

$\sigma^2 = \sum x_i r_i^2 - < r_A >^2$, where x_i is the fractional occupancy of the A site ion, r_i is the corresponding ionic radius and $< r_A >$ is the average size of A-site cation. The σ^2 values of x = 0.15 and 0.20 samples are found to be comparable to that of the charge ordered $La_{0.5}Ca_{0.4}Sr_{0.1}MnO_3$ compound [271]. This larger value of size disorder could plausibly be responsible for the coexistence of FM and AFM phases [272]. The Mn-O bond lengths of MnO_6 octahedra exhibit the characteristics of Jahn-Teller distortion with one pair of long apical Mn-O bond length (> 2.0 Å) and two pairs of shorter planner bond lengths (< 2.0 Å). δ_{JT} is the measure of Jahn-Teller distortion and is quantitatively determined by using the relation [273],

TH-1060_06612103

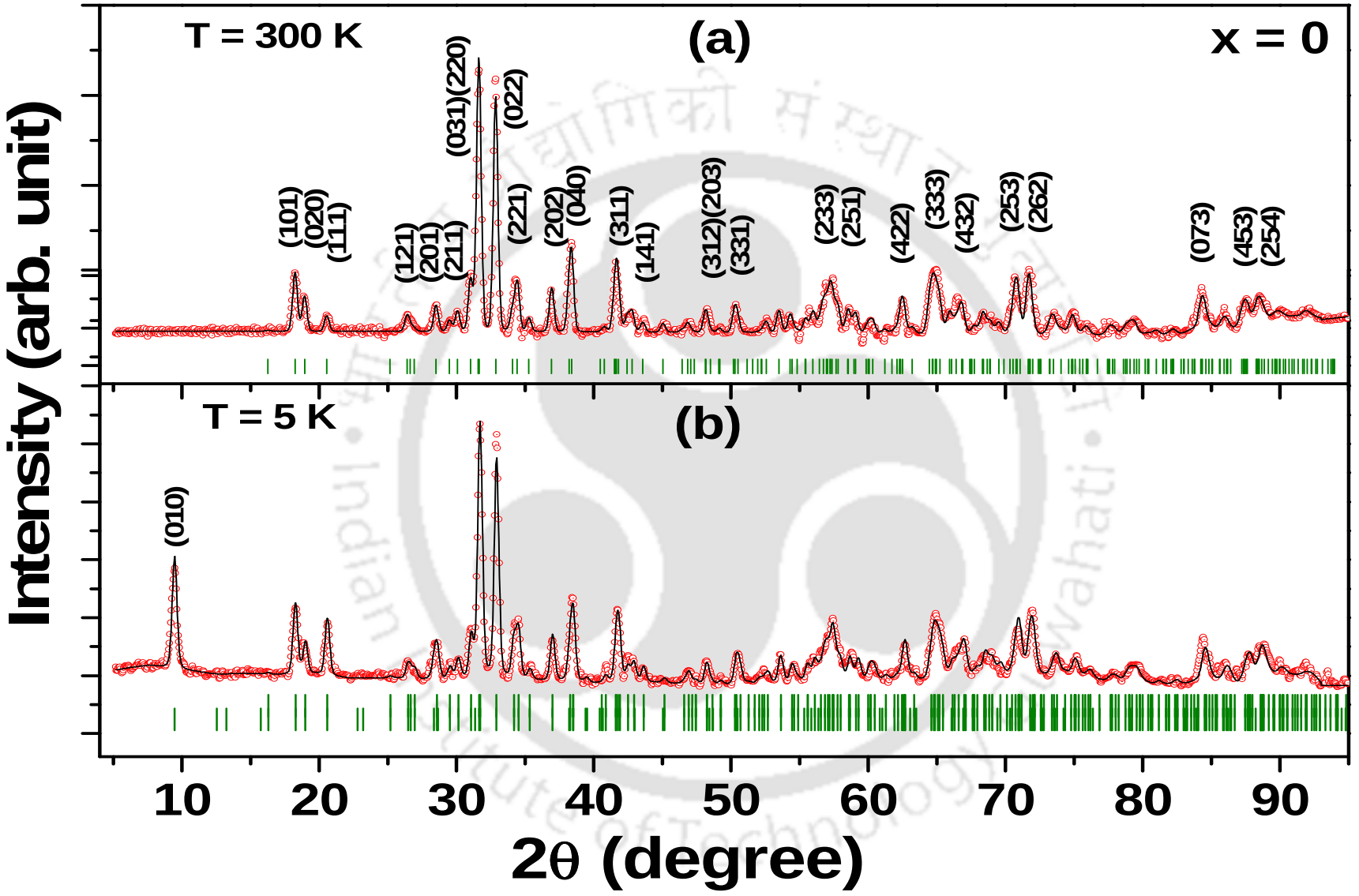

Figure 4.12: Neutron powder diffraction patterns of x = 0 along with Rietveld refinement at (a) 300 K and (b) 5 K.

TH-1060_06612103

Table 4.3: Structural parameters obtained from the Rietveld refinement of the NPD patterns for $Nd_{1-x}Na_xMnO_3$ (x = 0, 0.15 and 0.20) compounds at 300K.

Refined Parameters	**x = 0**	**x = 0.15**	**x = 0.20**
χ^2	2.12	2.35	2.86
R_p	4.24	3.90	4.79
R_{wp}	5.25	5.41	6.48
R_{Bragg}	17.24	10.8	16.1
R_f	15.25	8.03	10.6
a (Å)	5.7200(13)	5.4537(9)	5.4297(14)
b (Å)	7.5729(22)	7.6805(14)	7.6674(19)
c (Å)	5.4075(12)	5.4315(9)	5.4225(19)
Volume ($Å^3$)	234.24(10)	227.51(07)	225.76(10)
Mn-O_1(Å)	1.9454	1.9526	1.9398
Mn-O_{21}(Å)	2.1505	2.0030	1.9795
Mn-O_{22} (Å)	1.9230	1.9459	1.9565
Nd-O_1(Å)	2.4405	2.5060	2.4889
Nd-O_{21}(Å)	2.5778	2.6762	2.6427
Nd-O_{22} (Å)	2.3761	2.3790	2.3427
Mn-O_1-Mn (deg)	153.3	159	162.2
Mn-O_2-Mn (deg)	151.1	154.1	154.2
< r_A > (Å)	1.163	1.175	1.18
$\sigma^2\times10^{-3}$ $(Å)^2$	0	0.921	1.156
δ JT (Å)	0.102	0.040	0.016
(Nd, Na) (x, y, z)	{0.0632(15), ¼, 0.9818(17)}	{0.0305 (7), ¼, 1.0060 (15)}	{0.0261 (9), ¼} 0.9976 (23)}
(Mn) (x, y, z)	{0, 0, ½}	{0, 0, ½}	{0, 0, ½}
O_1 (x, y, z)	{0.4863 (15), ¼, 0.0815(13)}	{0.4864(11), ¼, 0.0638(15)}	{0.4906(16), ¼, 0.0544 (17}
O_2 (x, y, z)	{0.3128(15) 0.04174(13) 0.7127(17)}	{0.2942(7), 0.0407(7), 0.7130(8)}	{0.2901(12), 0.0419(9), 0.7128(14)}
Occupancy	**{**$Nd_{0.92}MnO_{2.93}$}	{$Nd_{0.85}Na_{0.15}MnO_{3.02}$}	{$Nd_{0.82}Na_{0.20}MnO_{3.06}$}
Mn Valency	3.06	3.33	3.46

TH-1060_06612103

Table 4.4. Structural and magnetic parameters obtained from the Rietveld refinemer of the NPD patterns for $Nd_{1-x}Na_xMnO_3$ (x = 0, 0.15 and 0.20) compounds at 5K.

Refined Parameters	**x = 0**	**x = 0.15**	**x = 0.20**
χ^2	1.45	3.3	2.91
R_p	2.85	4.33	4.75
R_{wp}	3.62	5.78	6.57
R_{Bragg}	10.9	10.7	9.31
R_f	7.85	7.03	6.88
a (Å)	5.7068(6)	5.4498(8)	5.4259(10)
b (Å)	7.5472(10)	7.6608(14)	7.6547(11)
c (Å)	5.4004(6)	5.4166(9)	5.4259(9)
Volume (Å^3)	232.60(5)	226.15(6)	225.35(06)
Mn-O_1(Å)	1.9420	1.9459	1.9470
Mn-O_{21}(Å)	2.1850	2.0119	1.9602
Mn-O_{22} (Å)	1.9075	1.9354	1.9578
Nd-O_1(Å)	2.4101	2.4344	2.4893
Nd-O_{21}(Å)	2.6113	2.6674	2.6704
Nd-O_{22} (Å)	2.3510	2.3551	2.3712
Mn-O_1-Mn (deg)	152.6	159.6	158.7
Mn-O_2-Mn (deg)	150.1	153.4	156.6
Mn (μ_B/f.u) AFM	M_x(2.59(03)), M_y(-1.57(1))	1.03(8)	3.10(3)
Mn (μ_B/f.u) FM	------	M_x(-1.78(5)), M_y(1.95 (5))	-----
Nd (μ_B/f.u) FM	1.39(1)	------	-----
(Nd, Na) (x, y, z)	{0.0603 (8), ¼, 0.9864(10)}	{0.0329(6), ¼, 1.0009 (16)}	{0.0254(7), ¼} 0.9943(21)}
(Mn) (x, y, z)	{0, 0, ½}	{0, 0, ½}	{0, 0, ½}
O_1 (x, y, z)	{0.4790(11), ¼, 0.0821(10)}	{0.4849(10), ¼, 0.0617(12)}	{0.4971(6), ¼, 0.0660(12}
O_2 (x, y, z)	{0.3140(7) 0.0453(6) 0.7134(8)}	{0.2977(7), 0.0405(6), 0.7119(8)}	{0.2852(9), 0.0380(8), 0.7150(11)}

TH-1060_06612103

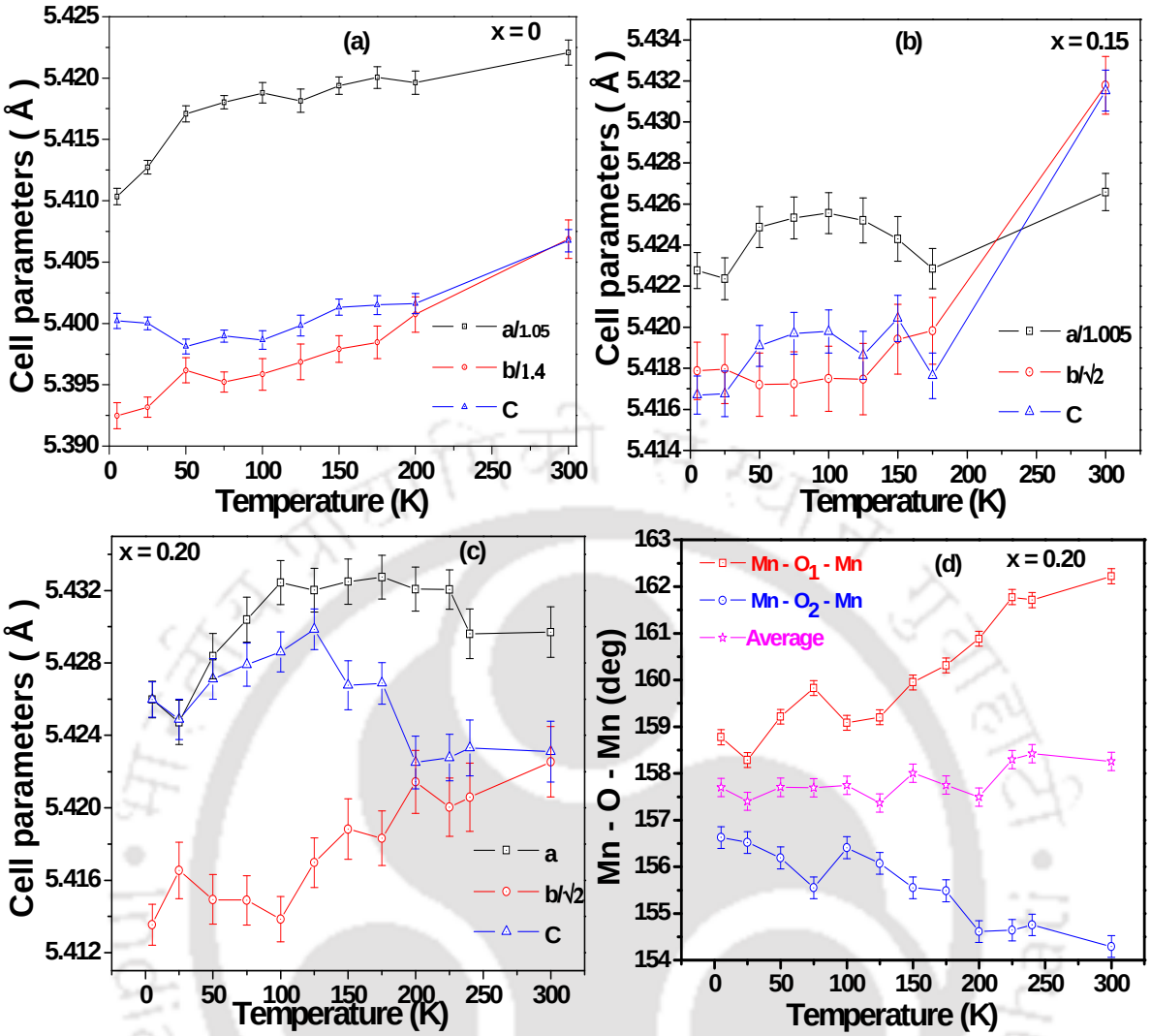

Figure 4.13: Temperature variations of (a) lattice parameters for x = 0 sample, (b) lattice parameters for x = 0.20 sample, (c) Mn-O bond lengths for x = 0.20 sample and (d) Mn-O-Mn bond angles for x = 0.20 sample.

$$\delta_{JT} = \sqrt{\left[\frac{1}{3}\sum_i \{(Mn-O)_i - \langle Mn-O\rangle\}^2\right]} \quad \text{----------} \quad (4.3)$$

The parent compound shows a strong Jahn-Teller distortion of the octahedra. The distortion is found to decrease with increase in Na concentration. The Mn-O-Mn bond angle is found to increase with increase in Na concentration and it leads to enhancement of FM T_C. The stoichiometry ratio of the compounds as per the refinement of occupancy values for x = 0, 0.15 and 0.20 samples are tabulated in table 4.3. The x = 0 sample exhibits vacancy at oxygen and Nd sites. The average Mn valency values obtained from the chemical titration are listed in table 4.3. We have also estimated the valency of Mn ions from the occupancy values obtained from the analysis of neutron diffraction patterns and are found to be comparable to

TH-1060_06612103

those obtained from chemical titration. The systematic increase in Mn valency with Na substitution highlights the formation of Mn^{3+}/Mn^{4+} mixture with increase in Mn^{4+} concentration.

NPD patterns were recorded at various temperatures down to 5 K for the above samples. The refined parameters determined from NPD analysis at 5 K are given in table 4.4. The temperature variations of lattice parameters for x = 0 sample are shown in figure 4.13 (a). The lattice parameters are found to decrease with decrease in temperature and at around 50 K a clear change of slope is observed, where a steeper decrease in *a* and *b* parameters are seen. Similar trend was observed in the temperature variation of unit cell volume. The observed behavior is comparable to those reported in references [177, 178] for $NdMnO_3$ sample. The lattice parameters for x = 0.15 sample exhibit the regular behavior of thermal expansion and is shown in figure 4.13 (b). However, the lattice parameters for x = 0.20 sample exhibit an anomalous behavior at 180 K as shown in figure 4.13 (c). A distinct increase in *a* & *c* parameters and decrease in *b* parameters are seen below 180 K. This behavior is usually observed in systems having CE-type antiferromagnetic ordering or pseudo CE-type antiferromagnetic ordering; which is associated with the orbital ordering of d_z^2 orbital in the *a*-*c* plane. This indicates the presence of orbital ordering in this compound below T~200 K. The average Mn-O bond length values are found to be almost temperature independent. The Mn-O_1-Mn and Mn-O_2-Mn bond angles exhibit opposite effect, while the former one decreases considerably below T_{CO} and the latter one increases in the same temperature region as shown in figure 4.13 (d).

4.3.2. Magnetic Structure

4.3.2.1. x = 0 (A-type AFM phase)

The evolution of low angle portion of the NPD patterns for x = 0 sample in the temperature range 5-300 K are shown in figure 4.11. The NPD data in the temperature range 75-300 K could be refined by using only the nuclear structure in *Pnma* space group. As the temperature is decreased below 75 K, the parent compound, x = 0 exhibits an increase in intensity of fundamental {(101) (020)}, (111), (121) and (201) reflections. The increase in intensity of the (111) and (201) reflections indicates the onset of ferromagnetic transition and they are the allowed reflections in *Pnma* space group. In addition to these fundamental reflections, one prominent super-lattice reflection (010) is also observed. The temperature variations of integrated intensity of some of these reflections having magnetic contribution are shown in

TH-1060_06612103

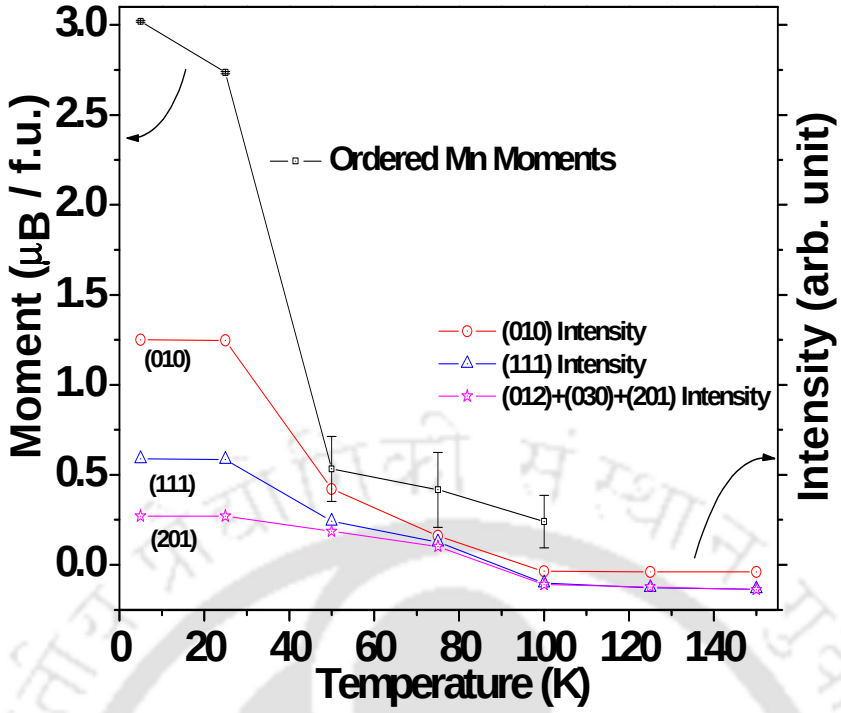

Figure 4.14: Temperature variations of refined magnetic moment and integrated intensity of different reflections for x = 0 sample.

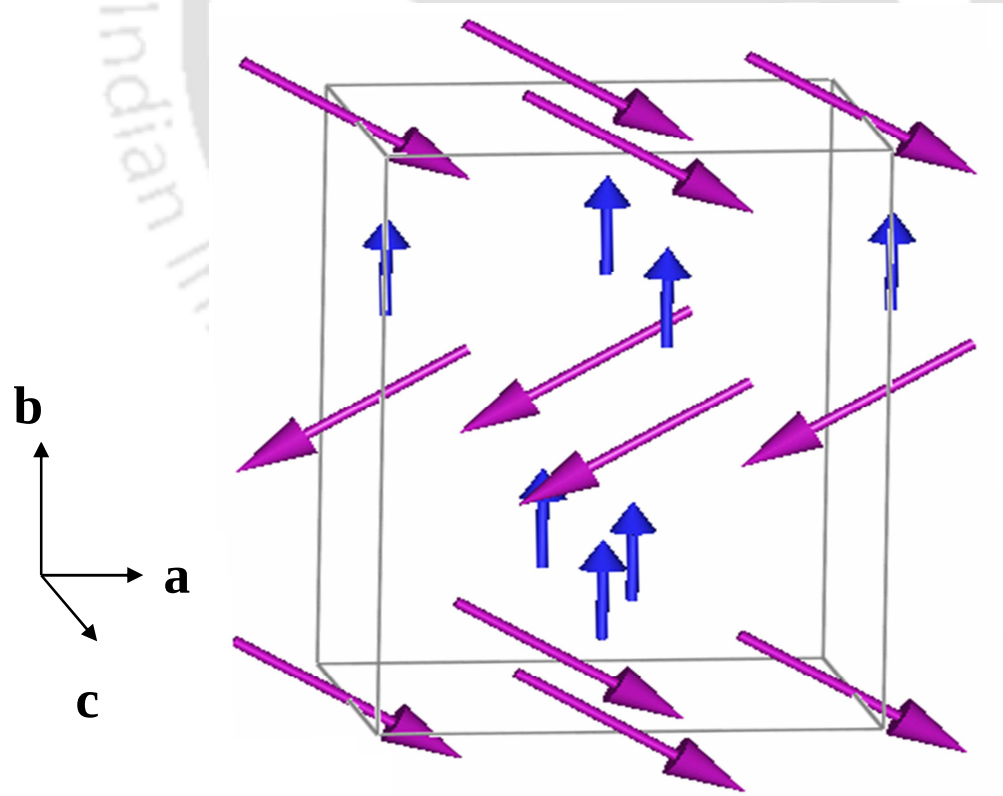

Figure 4.15: Magnetic structure of x = 0 sample at 5 K. The magnetic moment of Nd spin and Mn spins are shown in blue (small arrow) and purple colors (Bigger arrow) respectively.

TH-1060_06612103

figure 4.14. These observations are similar to those reported by Munoz *et al.* [177] in $NdMnO_3$ sample. The size of the chemical and the magnetic cells are found to be same. The low temperature NPD patterns, i.e., for T < 75 K could be refined by including suitable magnetic phase together with the nuclear phase of *Pnma* space group. The magnetic cell was refined in the *P-1* space group. The NPD pattern at 5 K was refined using a model very similar to that reported by Munoz *et al.* [177]. The NPD data along with Rietveld refinement for x = 0 sample at 5 K is shown in figure 4.12 (b). The moments of both Mn and Nd sites were refined. Different choices of magnetic moment orientations were used in the refinement to get the best fit. We have found that the moment of the Mn ions were slightly canted away from the *ac*-plane. Therefore, two components of the moment were taken, namely *x*-component along *a*-axis and *y*-component along *b*-axis. The *x*-components are coupled ferromagnetically within the plane and antiferromagnetically between the planes along the *b*-axis. The *y*-components are coupled ferromagnetically both within the plane and between the planes. The Nd moment is found to be coupled ferrimagnetically to the *y*-component of the Mn moment. Our results are in small disagreement with the analysis of Munoz *et al*. [177]. They found that the coupling between Mn and Nd spins was ferromagnetic, whereas our analysis shows that it is ferrimagnetic. The magnitudes of moment due to Mn and Nd at 5 K are 3 μ_B and 1.3 μ_B, respectively. The refined magnetic moment components at 5 K are tabulated in table 4.4. The temperature variation of refined magnetic moments are shown in figure 4.14 for x = 0 sample. The magnetic structure is shown in figure 4.15. The magnetic moment values are comparable to those observed by Munoz *et al.* [177]. The magnitude of Mn moment is found to be lower than that of expected moment for Mn^{3+} ions. This could be either due to the incomplete ordering of Mn atoms at 5 K or due to the presence of considerable concentration of Mn^{4+} ions due to oxygen off-stoichiometry. The observed magnetic moment value from the above refinement is comparable to that of M_S value obtained from *M-H* loop measurement.

4.3.2.2. x = 0.15 (Spin canted FM phase)

Figure 4.16 shows the evolution of low angle portion of the NPD patterns for x = 0.15 sample in the temperature range 5-300 K. The increase in intensity of (101) and (121) peaks with decrease in temperature below 80 K depicts the ferromagnetic nature of the sample. In comparison to x = 0 sample, we have not observed any superlattice reflections corresponding to A-type AFM behavior. However at 5 K, three weak super lattice reflections (0 0 ½),

TH-1060_06612103

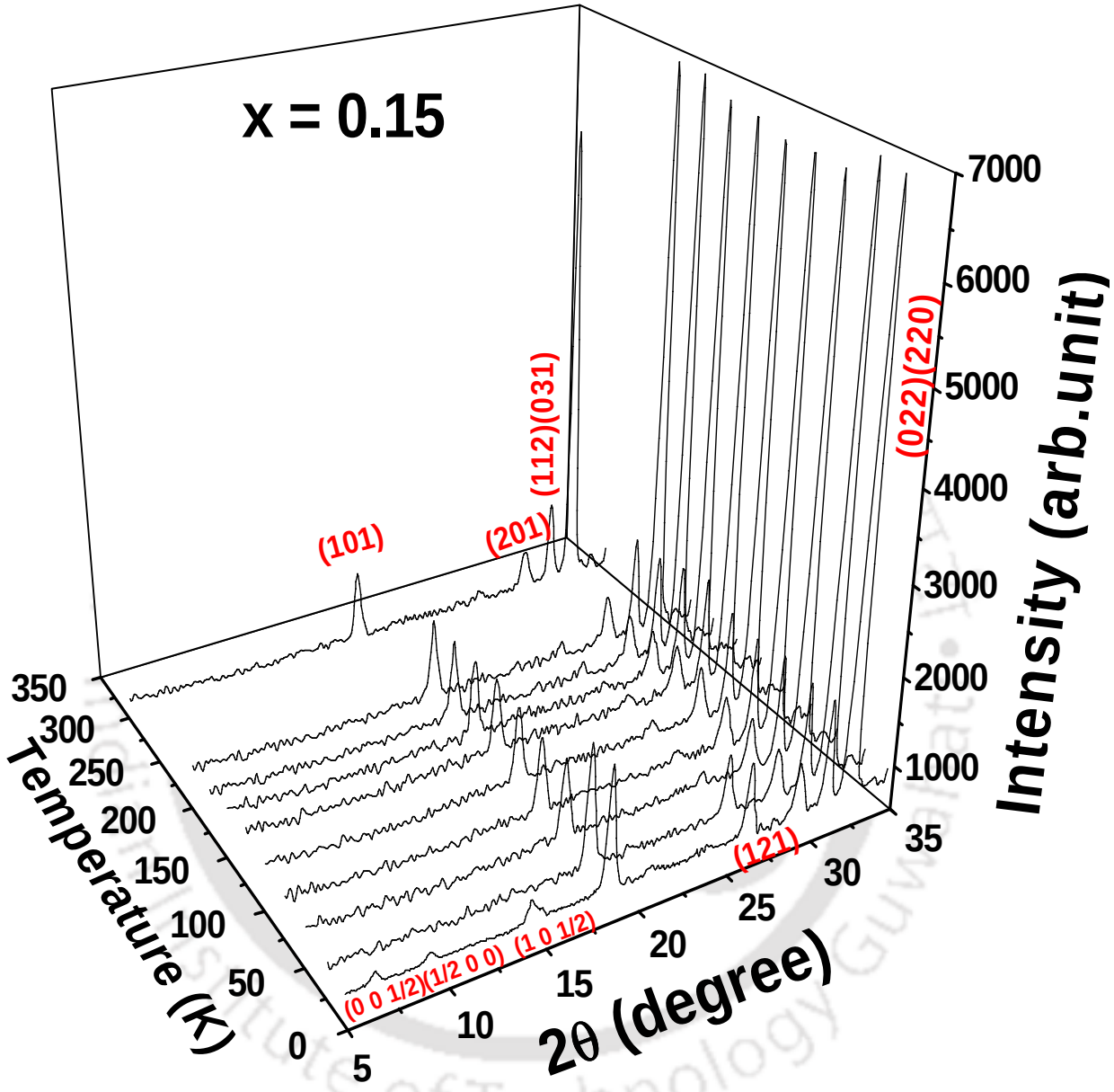

Figure 4.16: Evolution of low angle reflections of neutron diffraction patterns in the temperature range 5 -300K for x = 0.15 sample.

TH-1060_06612103

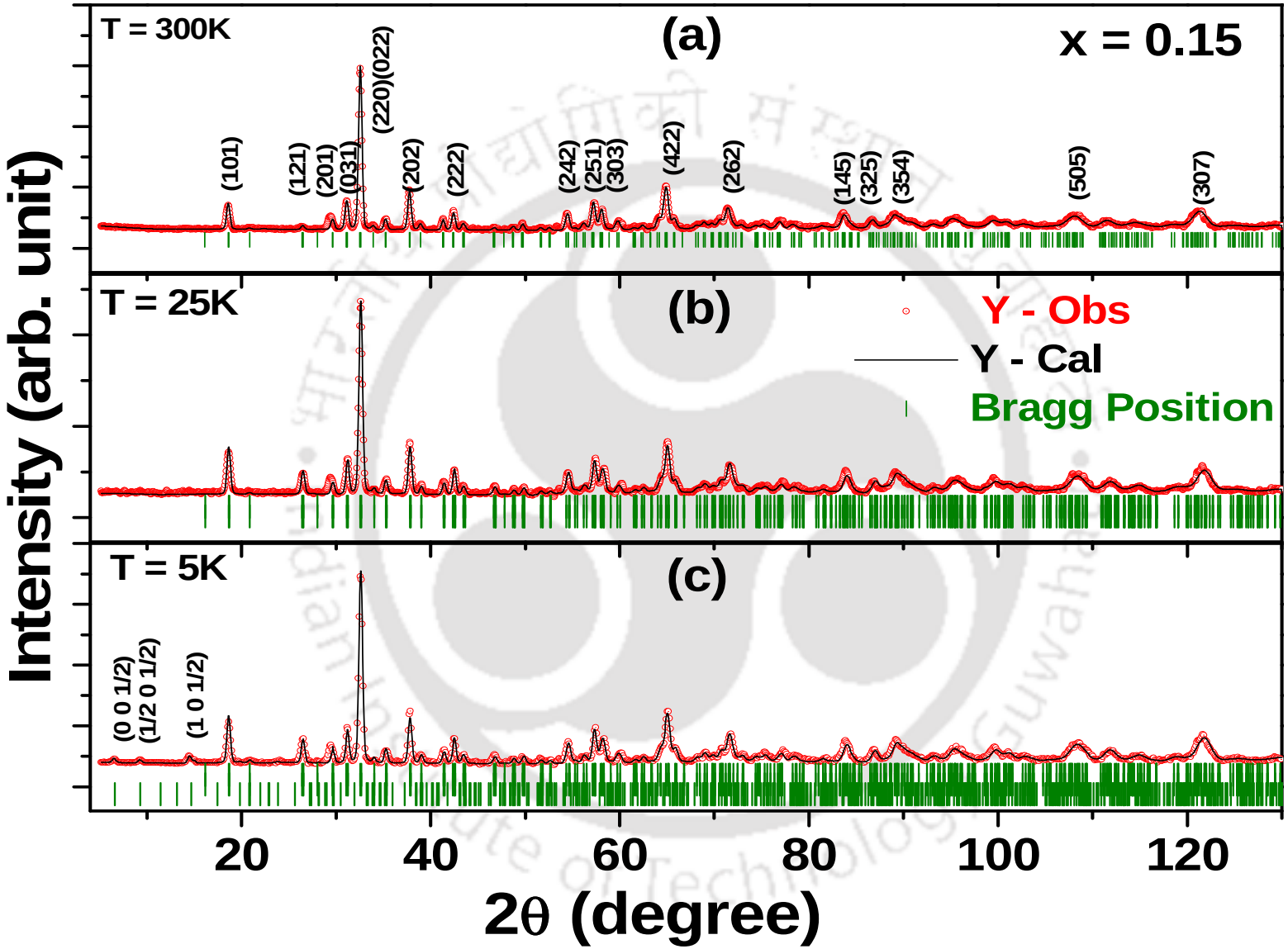

Figure 4.17: Neutron powder diffraction patterns for x = 0.15 sample along with Rietveld refinement at (a) 300 K, (b) 25 K and (c) 5 K.

TH-1060_06612103

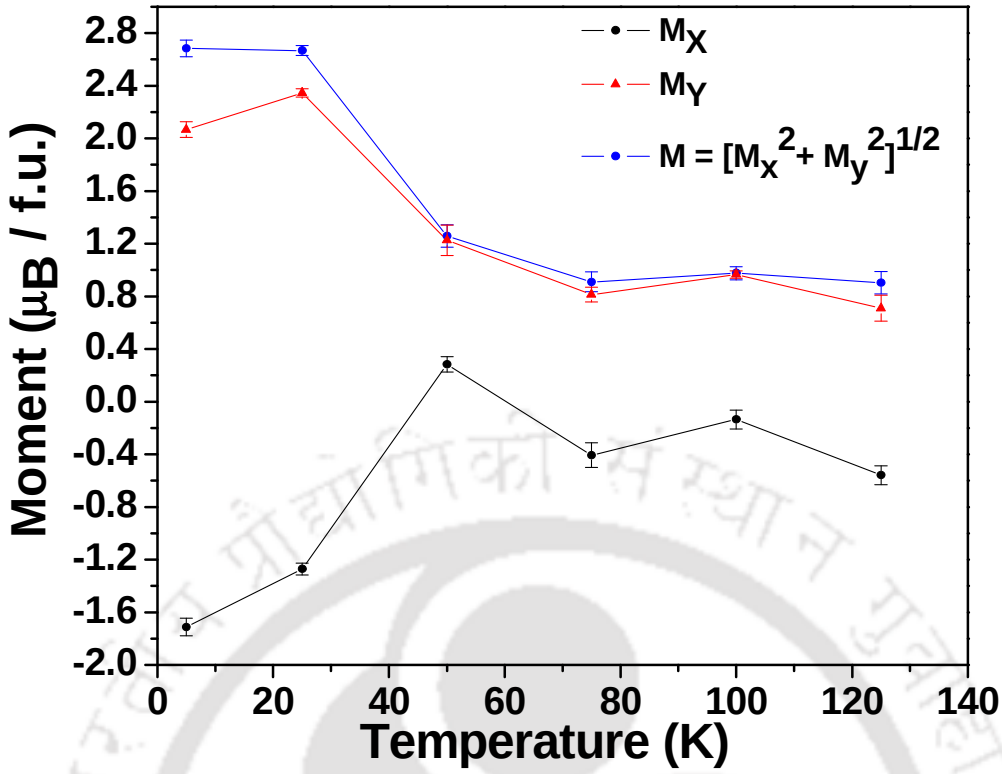

Figure 4.18: Temperature variation of refined magnetic moments of x = 0.15 sample.

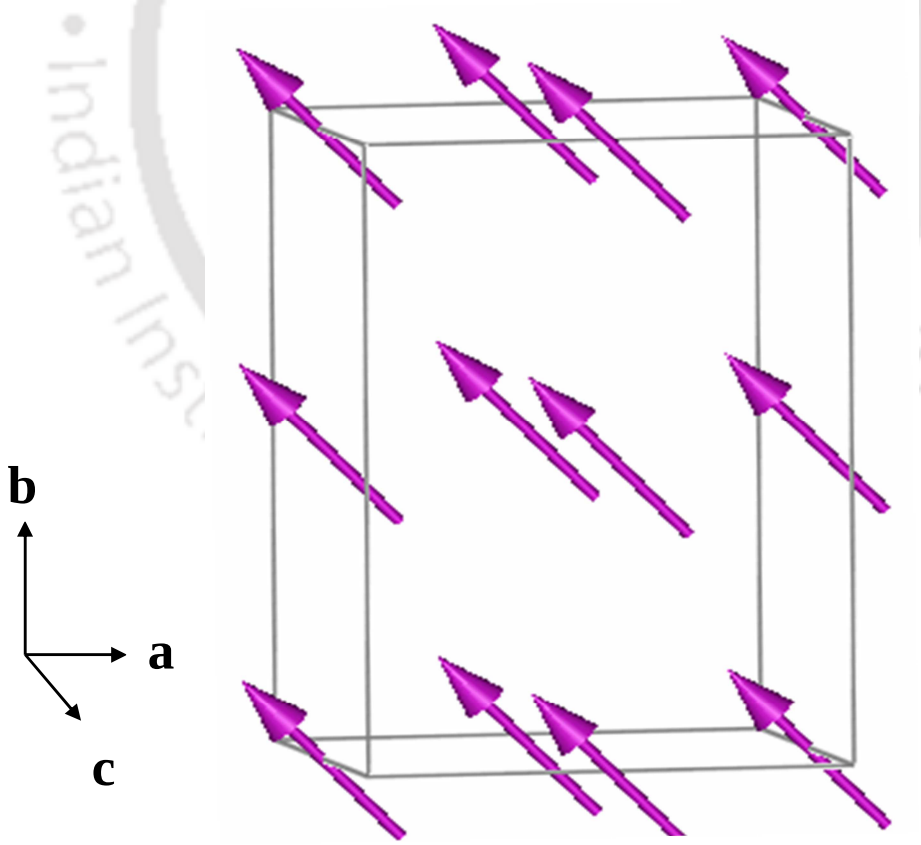

Figure 4.19: Magnetic structure of x = 0.15 sample at 25 K due to Mn ions.

TH-1060_06612103

(½ o ½), and (1 0 ½) are observed at 2θ = 6.5°, 9.5°, and 14.5° respectively. Figure 4.17 shows the NPD patterns along with Rietveld refinement at three different temperatures (a) 300 K, (b) 25 K and (c) 5 K for x = 0.15 sample. The NPD data in the temperature range 100-300 K could be refined by using only the nuclear structure in *Pnma* space group. The low temperature patterns below 80 K could be refined by taking into account the ferromagnetic phase in addition to the nuclear phase. The Bragg positions for the nuclear and magnetic phases are found to be same. So, the magnetic reflections are dominated by ferromagnetic interactions. The patterns at low temperature were refined by varying the magnetic moments of Mn ions. We have also attempted to vary the Nd moment and no ordering of Nd ion was observed. Different choices of magnetic moment orientation were used in the refinement to get the best fit. The best possible refinement was obtained by varying the moments M_x and M_y simultaneously. The observed super lattice reflections corresponding to 2θ = 6.58, 9.28 and 14.68 at 5 K can be indexed as (0 0 ½), (½ 0 ½) and (1 0 ½) respectively. The NPD data at 5 K was successfully modeled by using two magnetic phases, one FM and another AFM phase. The AFM phase could be refined to the pseudo CE-type AFM structure in the $P2_1/m$ space group. Therefore, the low intensities of AFM reflections with pseudo CE-type structure signifies that the x = 0.15 sample re-enters into the charge ordered phase. We have discussed more about charge ordered phase and pseudo CE-type structure in x = 0.20 sample. The temperature variations of refined *x*-component magnetic moment (M_x), *y*-component moment (M_y) and the net magnetic moment (M) corresponding to the FM phase are shown in figure 4.18. The FM spin canted structure for x = 0.15 sample at 25 K is shown in figure 4.19. The refined magnetic moment components per Mn ion corresponding to the FM structure at 5K are found to be M_x = -1.78(05) μ_B, M_y = 1.95(05) μ_B. The magnetic moments corresponding to Mn^{3+} and Mn^{4+} ions in pseudo CE-type AFM structure are found to be 1.11(07) μ_B, 0.94(09) μ_B respectively.

4.3.2.3. x = 0.20 (Charge ordered phase)

Figure 4.20 shows the evolution of low angle portion of the NPD patterns for x = 0.20 sample in the temperature range 5-300 K. The NPD data in the temperature range 200-300 K could be refined by using only the nuclear structure in *Pnma* space group. Below T = 125 K, the integrated intensity of some of the forbidden Bragg reflections (0 0 ½), (½ 0 ½) and (1 0 ½) at 2θ = 6.57°, 9.30° and 14.73° respectively were observed and were found to increase with decrease in temperature. This is the characteristics of the AFM-CO. Further decrease in

TH-1060_06612103

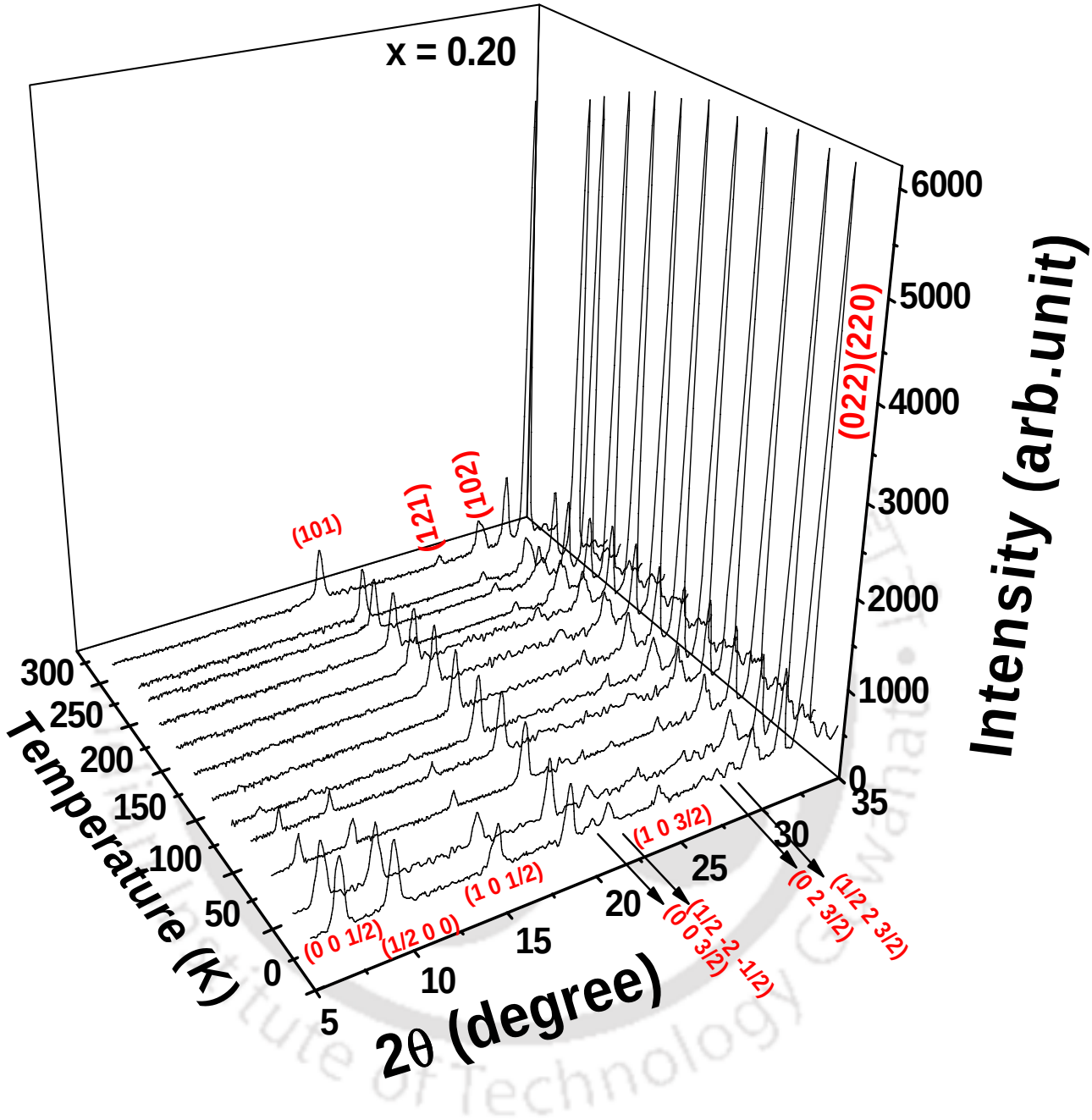

Figure 4.20: Evolution of low angle reflections of neutron diffraction patterns in the temperature range 5 -300K for x = 0.20 sample.

TH-1060_06612103

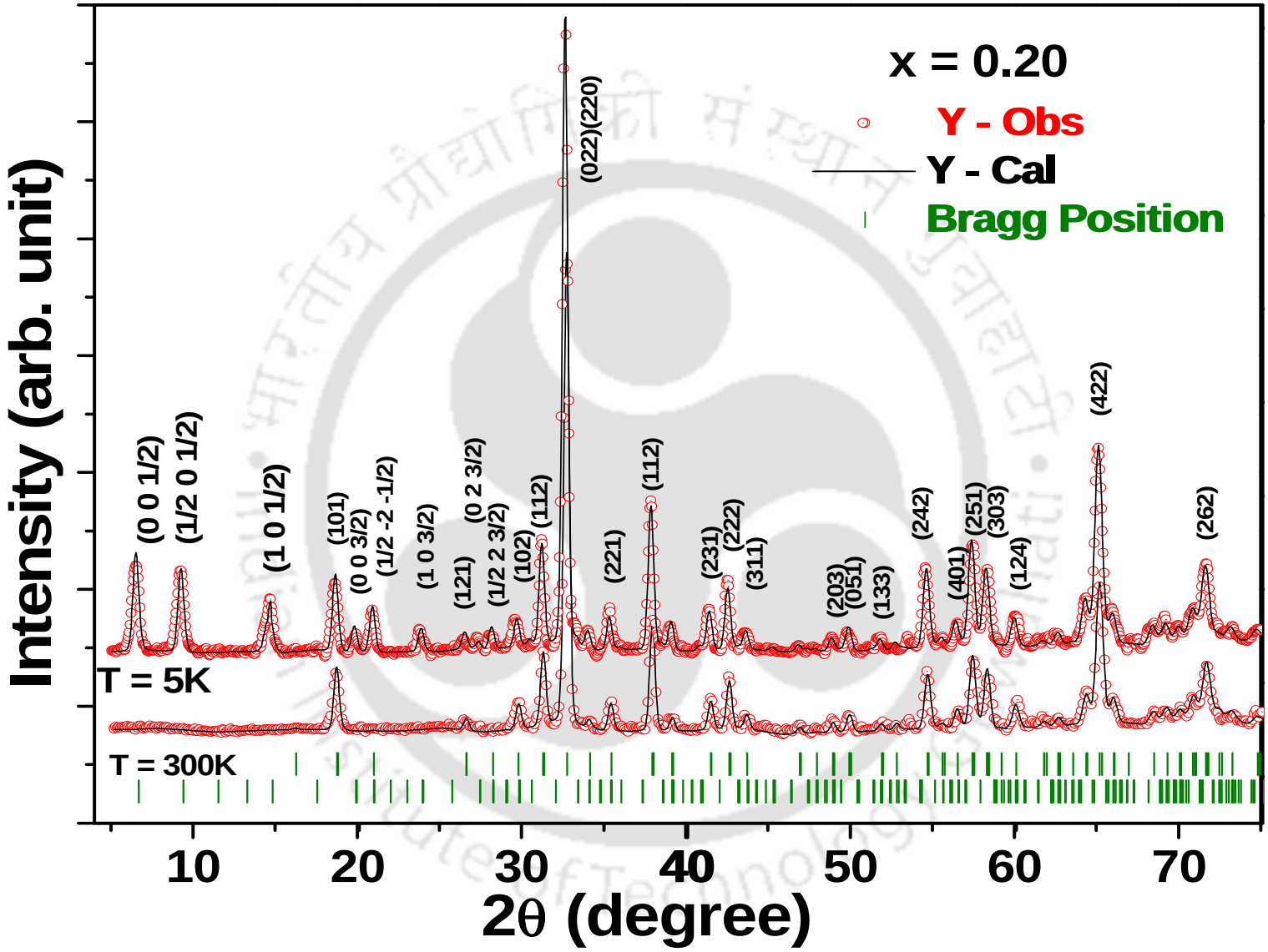

Figure 4.21: Neutron powder diffraction patterns along with Rietveld refinement for x = 0.20 sample at 5 K and 300 K.

TH-1060_06612103

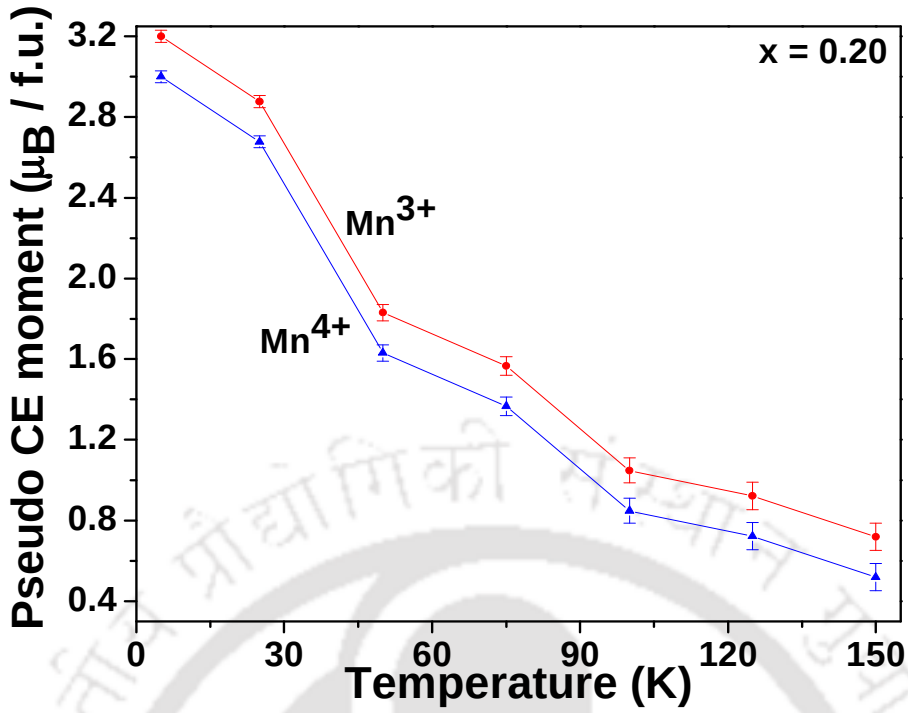

Figure 4.22: Temperature dependent refined magnetic moment corresponding to Mn^{3+} and Mn^{4+} ions in pseudo CE-type structure for x = 0.20 sample.

temperature below 50 K, some more super lattice reflections (0 0 3/2), (-1/2 -2 -1/2), (1/2 0 3/2), (0 2 3/2), (1/2 2 3/2) at 2θ = 19.8°, 20.93°, 23.85°, 27.37° and 28.18° respectively were observed with less intensity. The above super lattice reflections show that *k* is even integer, which is associated with pseudo CE-type AFM ordering [274]. In the CE-type AFM ordering, the *k* is always odd. The common feature between pseudo CE-type and CE-type ordering is AFM arrangement with in the plane. However, the inter planner arrangement along *b*-axis is ferromagnetic in pseudo CE-type magnetic structure and antiferromagnetic in CE-type magnetic structure. In the present case, the absence of *k* = odd reflections rules out AFM coupling between adjacent *a*-*c* planes. So, these superlattice reflections are successfully indexed to a *2a*×*b*×*2c* cell, having a pseudo CE-type structure. We have not observed any increase in intensity of fundamental reflections, i.e., (1 0 1), (1 2 1) and (1 0 2), which indicates the absence of weak FM in such zero magnetic field environment. The low temperature NPD data could be successfully refined by introducing pseudo CE-type AFM structure in the $P2_1/m$ space group and is shown in figure 4.21 for 5 K. In this structure, two different Mn sublattices, i.e., Mn^{3+} and Mn^{4+} occupy two distinct sites. The Mn^{3+} sublattice is associated with the propagation vector k_1 = (0 0 ½) and Mn^{4+} is associated with k_2 = (½ 0 ½). The arrangement of Mn ions in this superstructure is the direct evidence of the charge ordered

TH-1060_06612103

state. The temperature variations of pseudo CE-type moments corresponding to two different Mn sublattices are shown in figure 4.22. The maximum refined magnetic moment for Mn^{3+} sublattice is found to be 3.20(05) μ_B and that of Mn^{4+} sublattice is 3.00(02) μ_B. The net refined magnetic moment value at 5 K is tabulated in table 4.4. The difference between the Mn^{3+} and Mn^{4+} moments describes that the Mn ion concentrations are away from 1:1 ratio and is consistent with titration results.

4.3.3. Discussion of NPD analysis

A systematic change in crystal structure and magnetic structure is observed for different concentration of Na in $Nd_{1-x}Na_xMnO_3$ system. $NdMnO_3$ crystal structure is found to be similar to that of $LaMnO_3$. The lattice parameters are obeying the relation $b/\sqrt{2} \leq c \leq a$ and are corresponding to the orthorhombic distorted crystal structure. The elongation and contraction of Mn-O bond lengths suggest the presence of buckling of MnO_6 octahedra due to cooperative Jahn-Teller distortion. The magnetic structure of $NdMnO_3$ compound follows the same A-type AFM ordering as reported in $LaMnO_3$. In A-type AFM structure, the Mn spins are ordered ferromagnetically along *ac*-plane and the coupling between the planes is AFM along *b*-direction. Here in this report, we have observed the moments of Mn ions are slightly canted away from the *ac*-plane. At low temperature (< 15 K), one more magnetic sublattice, i.e., Nd ion is getting ordered and it is coupled ferrimagnetically with Mn ion. However, Munoz *et al.*[177] have observed that the coupling between Nd and Mn ion was of FM in nature. The magnetic structure of Na doped $NdMnO_3$ system is completely different from that of parent compound. The x = 0.15 sample exhibits ferromagnetism with spin canted structure below 80 K. However at 5 K, the system reenters into the charge ordered state and could be confirmed from the observed three weak super lattice reflections at lower angles of NDP pattern. These super lattice peaks could be successfully refined by including pseudo CE-type AFM structure. So at low temperature, the hole rich compound coexists with the spin canted FM and CO AFM. Thus, the existence of magnetic phase separation (PS) scenario could be understood in this sample. The evolution of this PS can be due to either electronic or structural PS [182]. The $Nd_{0.8}Na_{0.2}MnO_3$ compound, i.e., x = 0.20 exhibits charge ordered state with pseudo CE-type AFM structure below 125 K. Thus in the present system, CO is observed without complete half doping. Basically the half doped manganites exhibit CE-type AFM ordering as in $La_{0.5}Ca_{0.5}MnO_3$ [17], $Pr_{0.5}Ca_{0.5}MnO_3$ [56], and $Nd_{0.5}Ca_{0.5}MnO_3$ [188], etc. According to Kajimoto *et al.*[210], the energy difference between the A-type AFM

TH-1060_06612103

ordering and CE-type AFM ordering is very small. In a comprehensive report, they have observed CE-type AFM ordering in $Nd_{0.5}Sr_{0.5}MnO_3$ and a coexistence of CE-type and A-type ordering for little higher concentration of Sr [210]. It has been reviewed in literature that the magnetic structure of CO manganites having doping concentration, away from half doping are following pseudo CE-type AFM ordering. Cox *et al.* [275] reported that $Pr_{0.7}Ca_{0.3}MnO_3$ compound exhibited CO phenomena below 180 K and the Mn spins were found to follow the pseudo CE-type structure. The monovalent doped $Pr_{1-x}Na_xMnO_3$ series were reported to exhibit a transition from A-type AFM ordering for x = 0 to the pseudo CE-type AFM ordering for x = 0.20 through a spin canted arrangement for x = 0.025 and 0.05 [52]. Pseudo CE-type structure has been also observed from neutron diffraction study of charge ordered phase of $Bi_{0.75}Sr_{0.25}MnO_3$ [276]. A direct evidence of CO transition around 170 K was observed in $Nd_{0.75}Na_{0.25}MnO_3$ from electron diffraction measurement [277].

4.4. Transport Properties

The temperature variation of electrical resistivity was measured down to 50 K for x = 0.05 to x = 0.20 samples. Below certain temperature, the resistivity was too large and could not be measured. The increase in resistivity values with decrease in temperature was observed with a variation of five to six orders of magnitude. The resistivity value was found to decrease with increase in Na concentration up to 15% and for further increase in Na concentration, it was found to increase. It is not surprising because the substitution of monovalent alkali-metal ions Na^{1+} leads to enhanced DE interaction, and the resistivity value is lowered. Different models were tried in order to get the best fit of resistivity data in large temperature range. Adiabatic small Polaron (ASP) hopping model was found to fit the data well. According to ASP model [154],

$$\rho = \rho_0 T \, exp^{\frac{E_{hop}}{K_B T}} \qquad \text{----------} \qquad (4.4)$$

here, ρ_0 residual resistivity and E_{hop} is the hopping energy. Figure 4.23 shows ln(ρ/*T*) versus 1000/*T* for all samples along with the fit to ASP model. However, the resistivity data of x = 0.20 sample were found to exhibit a change of slope at around 130 K, which is some what comparable to the end of CO transition.

TH-1060_06612103

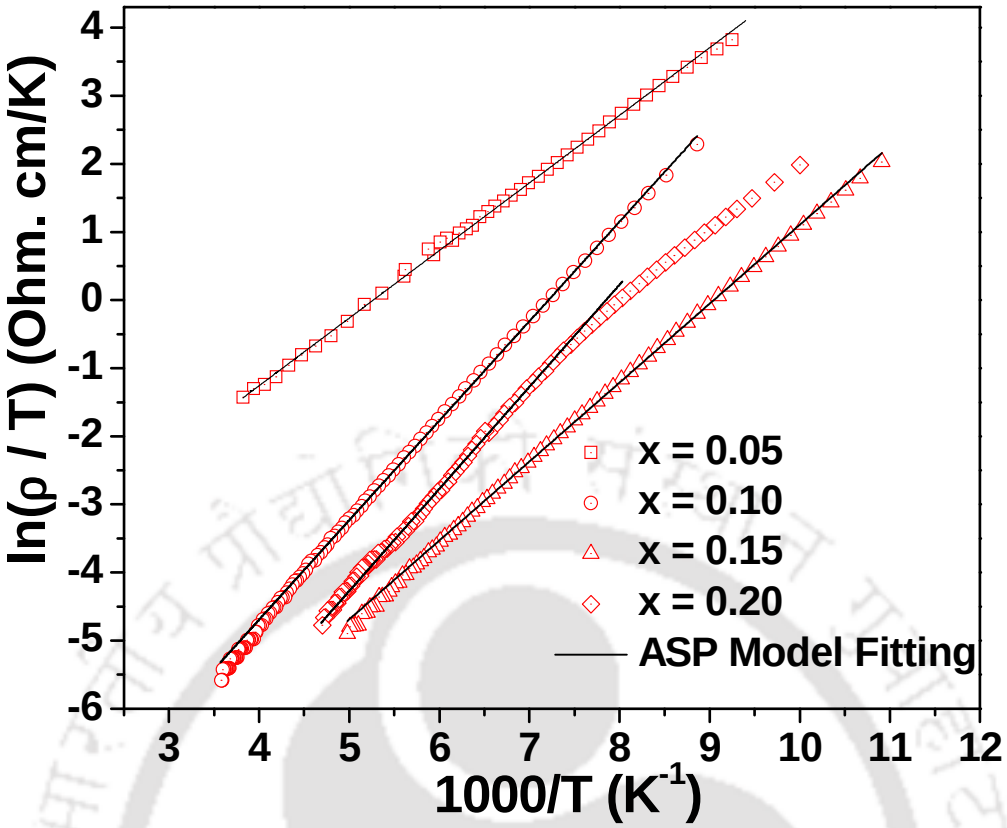

Figure 4.23: *ln (ρ/T)* versus *1000/T* for x = 0.05 to 0.20 samples.

4.5. Conclusions

In summary, we have prepared single phase samples of Na-doped series, i.e., $Nd_{1-x}Na_xMnO_3$ for x = 0 to 0.20. The Na-doped Nd-Mn-O series exhibit PM to FM transition for x = 0.05 to 0.15 with a maximum T_C of 113 K. They also show the signature of the presence of competing AFM and re-entrant spin glass like behavior below 40 K. However, x = 0.20 sample exhibits a CO transition at 180K, followed by a weak ferromagnetic behavior below 100 K and spin glass like transition at around 40 K. The saturation magnetization of x = 0.05, 0.10 & 0.15 samples after subtracting the linear contribution are found to be 4, 4.3 and 3.3 μ_B respectively at 5 K and such a large value is explained on the basis of contribution from magnetic 'Nd' ion. The magnetic dynamics of x = 0.20 sample was studied by recording *M-H* curve at different temperatures, covering different magnetic ground state conditions. A magnetic field induced reversible transition from charge ordered phase to ferromagnetic phase was observed at 130 K. However at 5 K, such transition was found to be irreversible, i.e., ferromagnetic phase is stabilized at the expense of other competing magnetic interactions beyond a characteristic field of 5 T. This transition is found to be first order in nature.

TH-1060_06612103

The crystal and magnetic structures of Na doped $NdMnO_3$ (x = 0, 0.15 and 0.20) compounds were studied by recording neutron powder diffraction patterns down to 5 K. The samples were found to be crystallized in *Pnma* space group. The patterns at low temperature could be refined by considering both nuclear and magnetic reflections based on different magnetic structures. The lattice parameters were found to reduce sharply below the ordering temperature for the x = 0 sample. However in x = 0.20 sample, the *b* parameter was found to shrink, when the temperature was reduced below 180 K and a moderate expansion of *a* and c parameters was observed. It reveals the presence of pseudo CE-type AFM ordering. The magnetic structure of x = 0 sample could be refined by including A-type AFM ordering at $T <$ 75 K with canting of Mn moments away from the *ac*-plane. The ferrimagnetic coupling of Nd moments with Mn ions was observed for $T \leq 15$ K. On the otherhand, the x = 0.15 sample showed a spin canted ferromagnetism. However, three superlattice reflections of very weak intensities were observed at 5 K and could be refined to the pseudo CE-type charge ordered phase. The coexistence of canted ferromagnetism and charge ordered phase could be confirmed from the high field magnetization measurements. So, they could be explained on the basis of magnetic phase separation. So, the NPD patterns of the CO x = 0.20 sample could be refined in terms of pseudo CE-type AFM structure with $P2_1/m$ space group for $T \leq 125$ K. The maximum refined moment for Mn^{3+} sublattice was found to be 3.20(05) μ_B and for Mn^{4+} ions, it was found to be 3.00(02) μ_B.

TH-1060_06612103

Chapter 5: Charge Order Suppression in $Nd_{0.8}Na_{0.2}MnO_3$

In order to study the suppression of charge ordering and the mechanism of magnetic dynamics, one needs to apply large magnetic field of the order of 10 T or higher in magnetization and resistivity measurements. To overcome such restriction in the measurements, the geometrical and chemical environment at the surface of the CO or AFM materials is tuned by many researchers. The CO phenomena were studied by varying the particle size from bulk to nano-metric scale in (La, Ca)-Mn-O systems by a few groups [278-281]. They have observed a decrease in T_{CO} value and increase in FM fraction with decrease in particle size. The disappearance of CO and the appearance of cluster glass FM phase has been reported, when the particle size of half doped (Pr, Ca)-Mn-O is reduced to 20-30 nm [281-284]. They were explained in terms of core-shell model and the increased surface charge density of nanoparticles. In $Nd_{0.5}Ca_{0.5}MnO_3$ compound, Rao *et al.* [193] reported the complete suppression of the CO phase and the emergence of FM metallic phase, when the particle size was reduced to 20 nm scale and a similar behavior was reported by Liu *et al.*[285].

The bulk $Nd_{0.8}Na_{0.2}MnO_3$ compound is known to exhibit charge-ordering at around 180 K [227, 286]. In order to understand the particle size effect on the magnetic properties of the CO phase in (Nd, Na)-Mn-O system, $Nd_{0.8}Na_{0.2}MnO_3$ samples were prepared under different annealing conditions such that particle size can be varied from a few hundred nanometer size to a few tens of nanometer size. Detailed temperature and field variations of magnetization measurements were carried out for H up to 10 T.

5.1. Sample Preparation and Characterization

Nanoparticle samples of $Nd_{0.8}Na_{0.2}MnO_3$ were prepared by sol-gel method. The stoichiometric amounts of Nd_2O_3, Na_2CO_3 and Mn-Acetate were converted into metal nitrates by adding nitric acid. They were converted into citrate by adding excess amount of citric acid and ethylene glycol. The uniform mixture of the above solution was slowly evaporated by heating the solution in the temperature range 75 to 100°C with the help of a hot plate, until a gel was formed. The polymeric gel was completely dried up, by keeping at 75°C for 12 hr. The product was heated to 200°C to induce the self combustion. The combustion derived fine

TH-1060_06612103

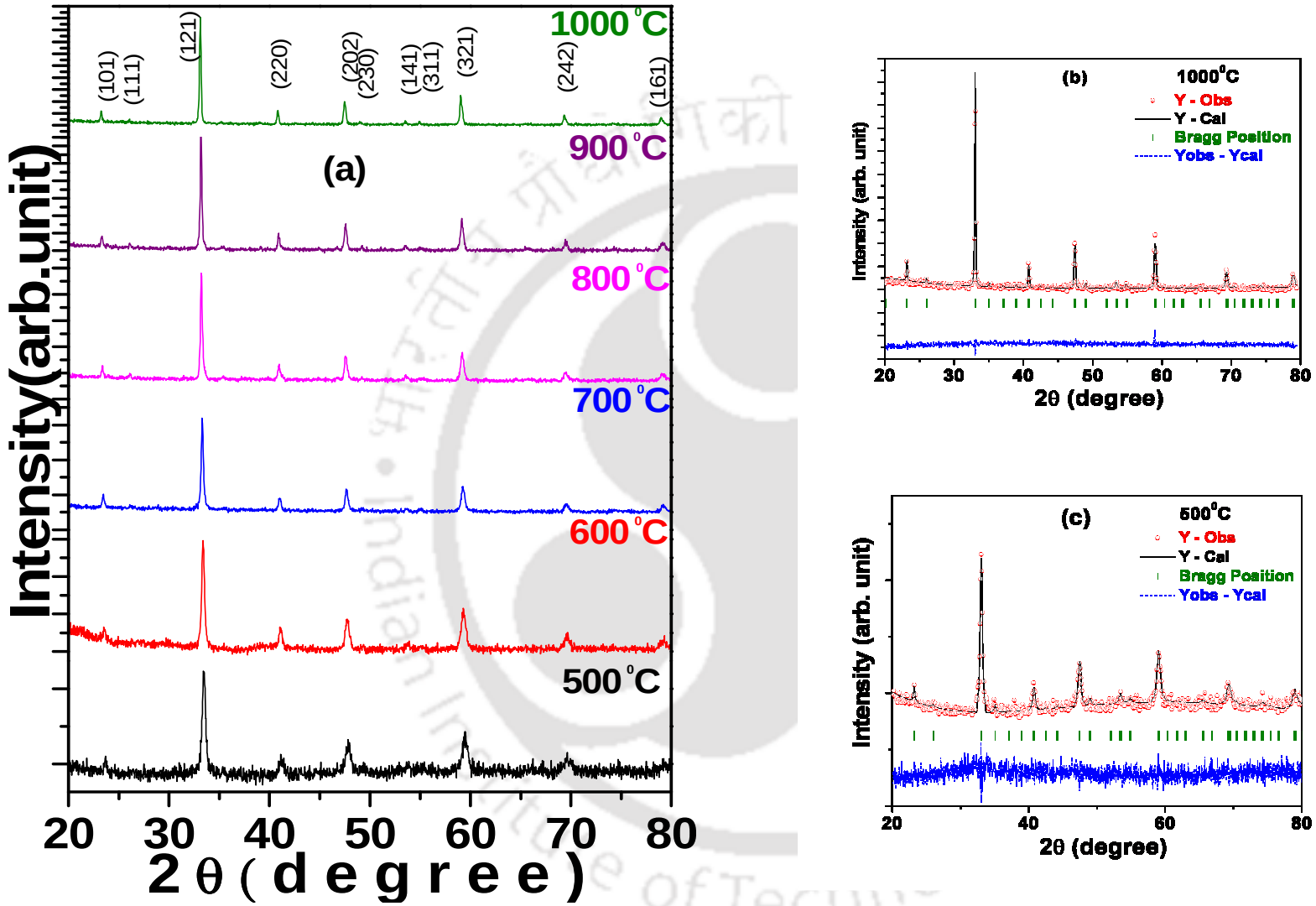

Figure 5.1: (a). X-ray diffraction patterns recorded at room temperature for $Nd_{0.8}Na_{0.2}MnO_3$ samples prepared under different annealing temperatures. Typical XRD patterns along with Rietveld refinement are shown for samples annealed at (b) 1000°C and (c) 500°C temperatures.

TH-1060_06612103

powder was heat treated at 400°C to decompose the remaining organic reagents. The obtained precursor powder was separated into several parts and they were annealed at different temperatures from 500°C to 1000°C with 100°C interval to get samples with different average particle sizes.

The samples of $Nd_{0.8}Na_{0.2}MnO_3$ prepared under different annealing temperatures ranging from 1000°C to 500°C are found to be in single phase form. The XRD patterns of these samples are shown in figure 5.1 (a). These patterns could be refined by using the *Pnma* space group in orthorhombic cell. The typical XRD patterns, along with Rietveld refinement are shown in figure 5.1 (b) and (c) for samples annealed at 1000°C and 500°C respectively. Broadening and shifting of XRD peaks towards higher 2θ angles are observed with decrease in annealing temperature. The above observation suggests that the decrease in annealing temperature leads to decrease in crystallite size and lattice parameter values. It is comparable to the result of $La_{0.5}Ca_{0.5}MnO_3$ nanoparticles [280]. The typical lattice parameters for 1000°C annealed sample are found to be a = 5.4216(8) Å, b = 7.6722(10) Å, c = 5.4048(7) Å and those of 500°C annealed sample are a = 5.3986(12) Å, b = 7.6302(13), c = 5.3612(11) Å. Such a variation of lattice parameters is also reported in $La_{0.25}Ca_{0.75}MnO_3$ and $Pr_{0.5}Ca_{0.5}MnO_3$ compounds [279, 283]. The microstructural images obtained from FE-SEM are shown in figure 5.2 for different samples. The typical particle size distribution obtained from FE-SEM images are shown in figure 5.3 for 800˚C and 700˚C annealed samples. The average particle size values are found to be 700, 250, 140, 80, 50, 30 nm for the samples annealed at 1000°C, 900°C, 800°C, 700°C, 600°C, and 500°C respectively. Hereafter, in the following text, the samples prepared under different annealing temperatures are referred in terms of their particle sizes D, i.e., D = 700, 250, 140 nm, etc.

Typical TEM images of 800°C (140nm) and 700°C (80 nm) annealed samples are shown in figure 5.4. The particles of 800°C sample are found to be in spherical shape with some agglomeration as shown in figure 5.4 (a). High resolution TEM images were recorded on the above nanoparticle samples and the typical image is shown in figure 5.4 (b), where we can see the crystalline strip of (111) plane and the d-spacing is comparable to that of XRD results. The 700°C annealed sample is found to be in the form of nano-rods with average length and thickness of the order of 80 nm and 20 nm respectively as shown in figure 5.4 (c). The selected area diffraction pattern recorded for the sample D = 80 nm shows polycrystalline nature and when it is focused on a single particle, it exhibits the characteristic feature of single crystalline particle as shown in figure 5.4 (d). The average particle size (D)

TH-1060_06612103

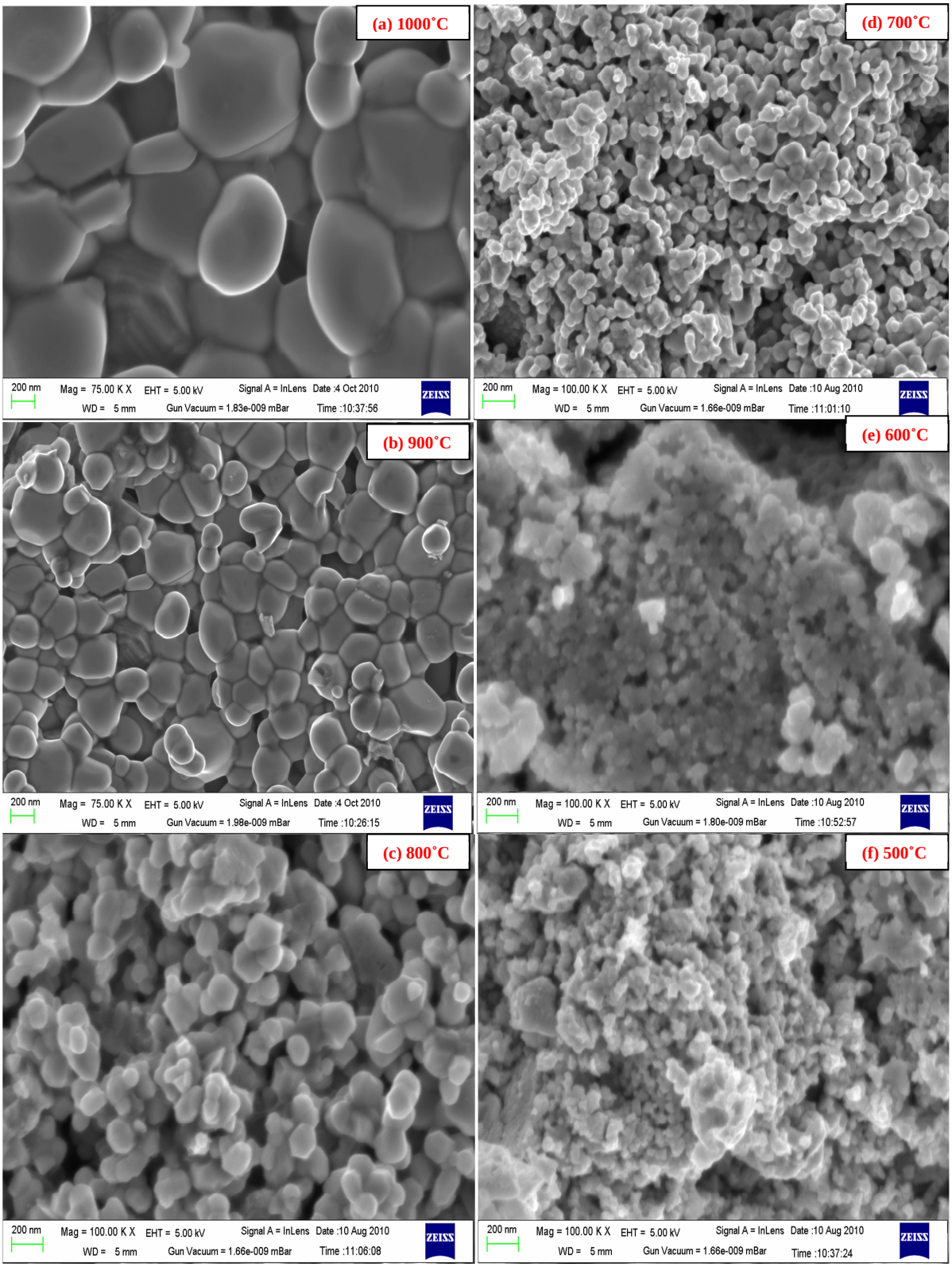

Figure 5.2: FE-SEM micrographs of $Nd_{0.8}Na_{0.2}MnO_3$ samples annealed at 1000 °C to 500 °C.

TH-1060_06612103

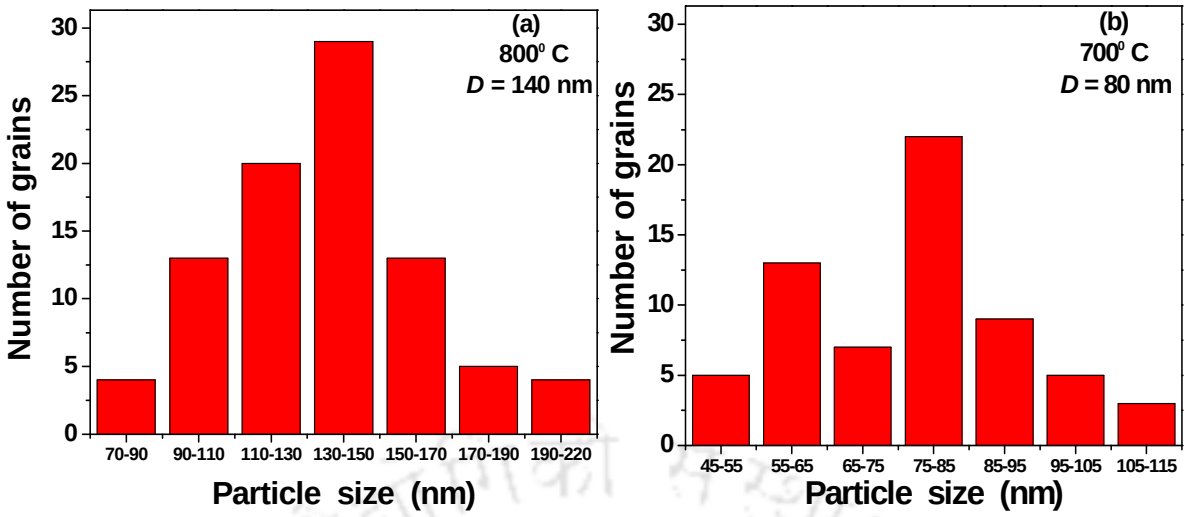

Figure 5.3: Particle size distribution plot for (a) 800°C and (b)700°C annealed samples from FESEM micrographs.

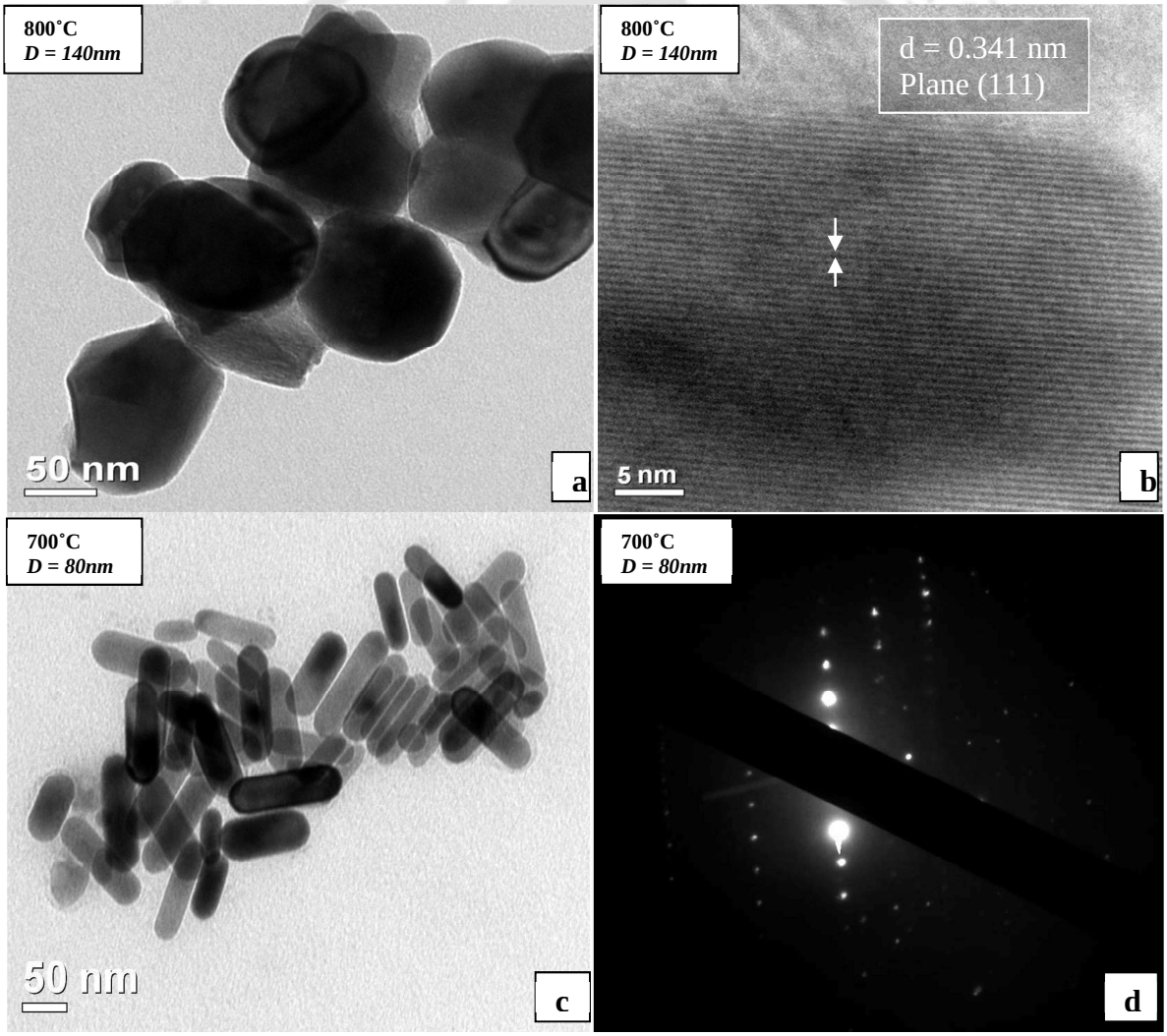

Figure 5.4: (a)-(b) TEM and HRTEM images of 800˚C annealed sample; (c) and (d) represent the TEM image and SAD pattern of 700˚C annealed sample.

TH-1060_06612103

obtained from the TEM analysis is found to be comparable to that obtained from the analysis of FE-SEM images. The average valency of Mn ions obtained from the chemical titration is found to be constant and close to 3.47 for samples prepared under different annealing conditions. This value is found to be slightly larger than that of expected value as per the doping concentration and is mainly due to possible oxygen off- stoichiometry. Thus, the average Mn^{4+}/Mn^{3+} ratio for this series is 47:52, which is quite close to the half doped charge-ordered system.

5.2. Temperature Variation of Magnetization and Magnetic Relaxation at Low Field

Temperature variations of magnetization in zero field cooled (ZFC) and field cooled (FC) conditions for an applied field of 20 mT are shown in figure 5.5 for samples with different particle sizes ranging from D = 700 nm to D = 30 nm. For D = 700 nm, the sample exhibits a transition from paramagnetic insulating state to CO state with decrease in temperature and is seen as a broad hump at 195 K as shown in figure 5.5 (a). A secondary rise in magnetization below 130 K, followed by a sharp peak at around 40 K is observed. They can be ascribed to the presence of weak FM followed by competing AFM interaction and re-entrant spin glass (RSG) like behavior. This argument can be substantiated from the observed large irreversibility between ZFC and FC magnetization data especially below 40 K. A similar behavior has been reported in $Pr_{0.50}Ca_{0.50}MnO_3$ compound of particle size 300 nm [283] and bulk compound of $Pr_{0.75}Na_{0.25}MnO_3$ [268]. The inset of figure 5.5 (a) shows the plot of dM/dT versus temperature and it exhibits two peaks. A sharp negative peak observed at 42 K can be attributed to FM or FM cluster-glass (CG) transition temperature, T_{CG} and a minor broad positive peak observed at 35 K can be attributed to RSG behavior. The CO ground state seen in D = 700 nm sample could be suppressed by reducing the average particle size. We can see from figure 5.5 (a) to (f) that the CO transition observed at around 195 K is suppressed gradually with decrease in particle size. For $D \leq 80$ nm, we do not see any hump at $T \approx 195$ K and it indicates the complete suppression of CO. On the other hand, we can see a clear shift in FM-CG transition towards higher temperature with decrease in particle size, i.e., 42 K for 700 nm to 84 K for 50 nm. The variations of T_{CG} and T_{SG} as a function of particle size are shown in figure 5.6 (a). Plots of inverse susceptibility as a function of temperature are shown in figure 5.6 (b) and (c) for different samples. In nanoparticle samples, the $1/\chi$ vs. T plots are found to be linear down to FM – T_{CG}. The magnitude of ZFC magnetization (M_P) corresponding to the peak is found to increase with decrease in particle

TH-1060_06612103

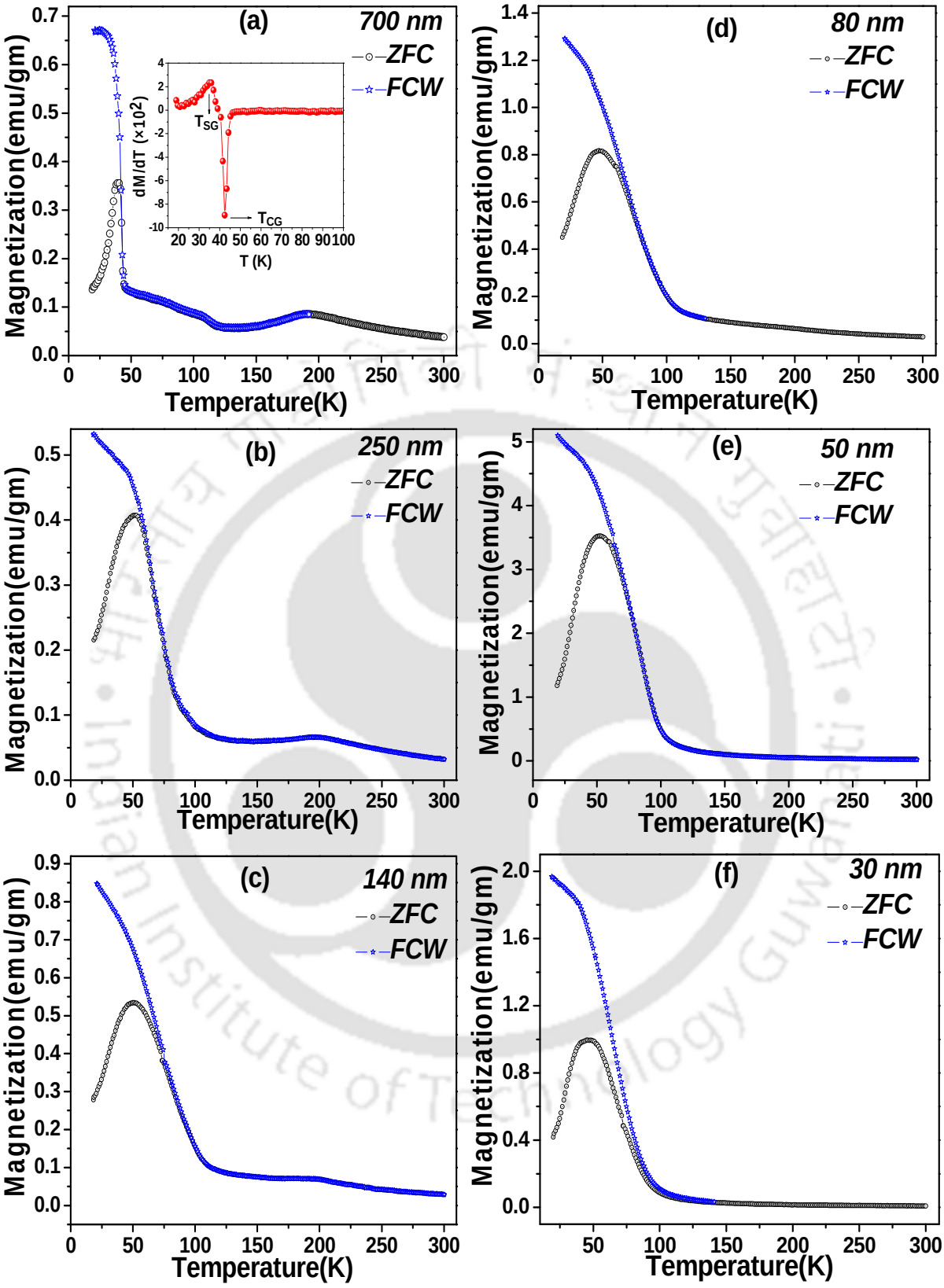

Figure 5.5: (a)-(f) Temperature variations of magnetization for both zero field cooled (ZFC) and field cooled warming (FCW) conditions at 20 mT field for $Nd_{0.8}Na_{0.2}MnO_3$ samples with different particle sizes.

TH-1060_06612103

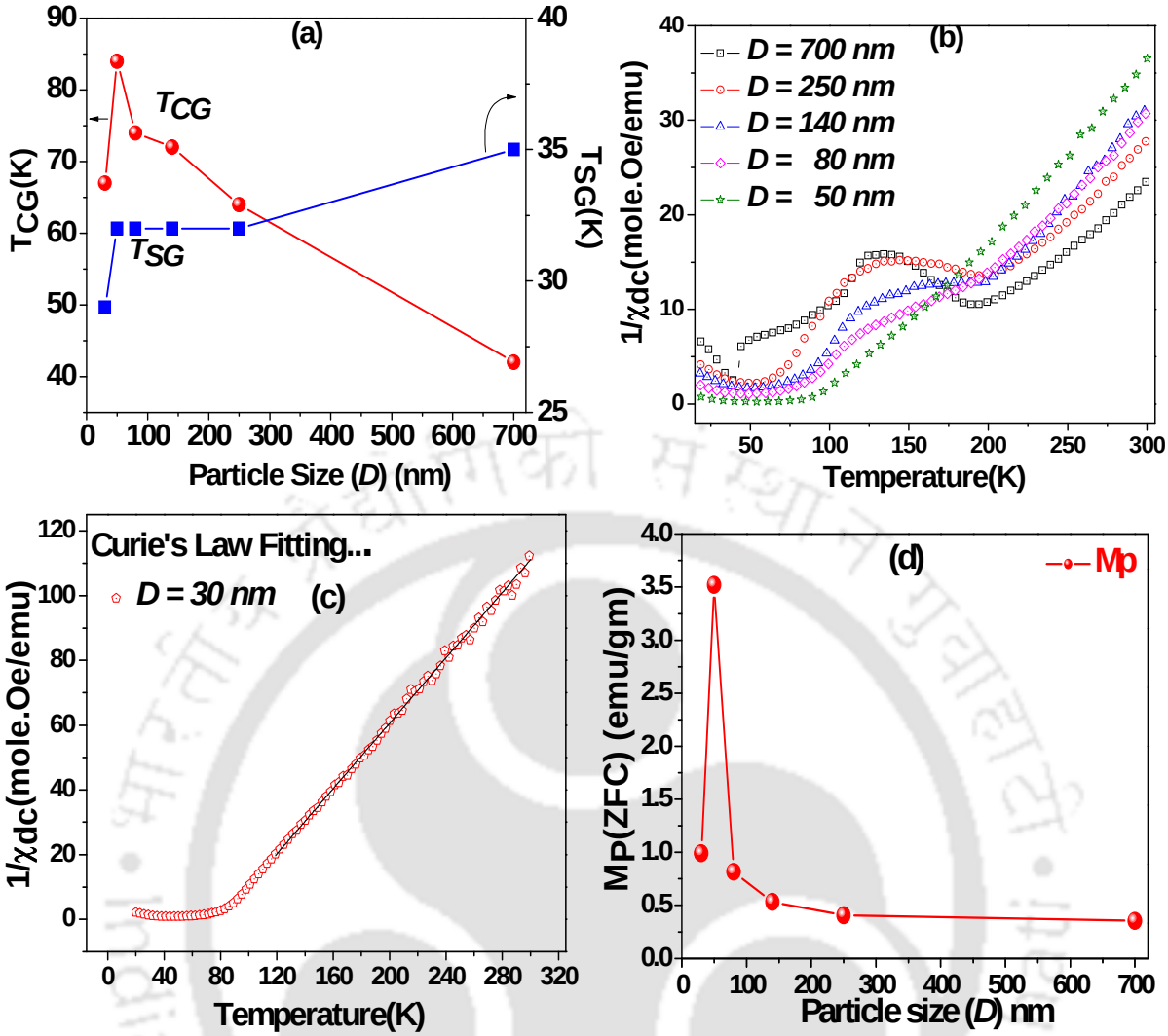

Figure 5.6: (a) particle size variation of FM cluster glass transition temperature (T_{CG}) and the spin glass transition temperature (T_{SG}); (b) and (c) temperature variation of inverse susceptibility for different samples and (d) particle size variation of peak magnetization in ZFC curve (M_P).

size, due to the enhanced FM and it is found to be maximum for D = 50 nm sample (3.5 emu/gm) as shown in figure 5.6 (d). However, the M_P value was found to decrease for further decrease in particle size, i.e., D = 30 nm.

The suppression of charge-ordered state with reduction in average particle size to nano-metric scale in $Nd_{0.8}Na_{0.2}MnO_3$ samples can be explained in terms of evolution of spin configuration resulting from the surface effect. The bulk $Nd_{0.8}Na_{0.2}MnO_3$ compound exhibits a distinct sequence of multiple magnetic transitions like PM-CO-FM-RSG. The *M-T* curve of D = 700 nm sample is very similar to that of bulk compound [227, 286] in $Nd_{0.8}Na_{0.2}MnO_3$ system. The decrease in particle size is expected to increase the surface to volume fraction

TH-1060_06612103

and correspondingly the uncompensated surface spin concentration increases. This leads to the frustration of AFM ordering. On the otherhand, the canting of spins on the surface of the nanoparticles gives rise to enhanced FM. The unscreened Coulomb potential at the surfaces of the nanoparticles is also expected to enhance the surface charge density, which in turn enhances the double exchange FM interaction.

Thus, the observed magnetization behavior with decrease in particle size can be explained in terms of the core-shell model proposed by Bhowmik *et al*. [287], where, the CO-AFM core is surrounded by spin canted surface spins, which contribute to FM. However, with increase in surface to volume ratio to a critical value, it is expected that, the shell containing many spins would be in random orientation and such random orientations lead to net reduction in magnetization as observed for D = 30 nm sample. Moreover, the competing interaction between AFM core and FM shell leads to magnetic frustration, namely re-entrant spin glass behavior.

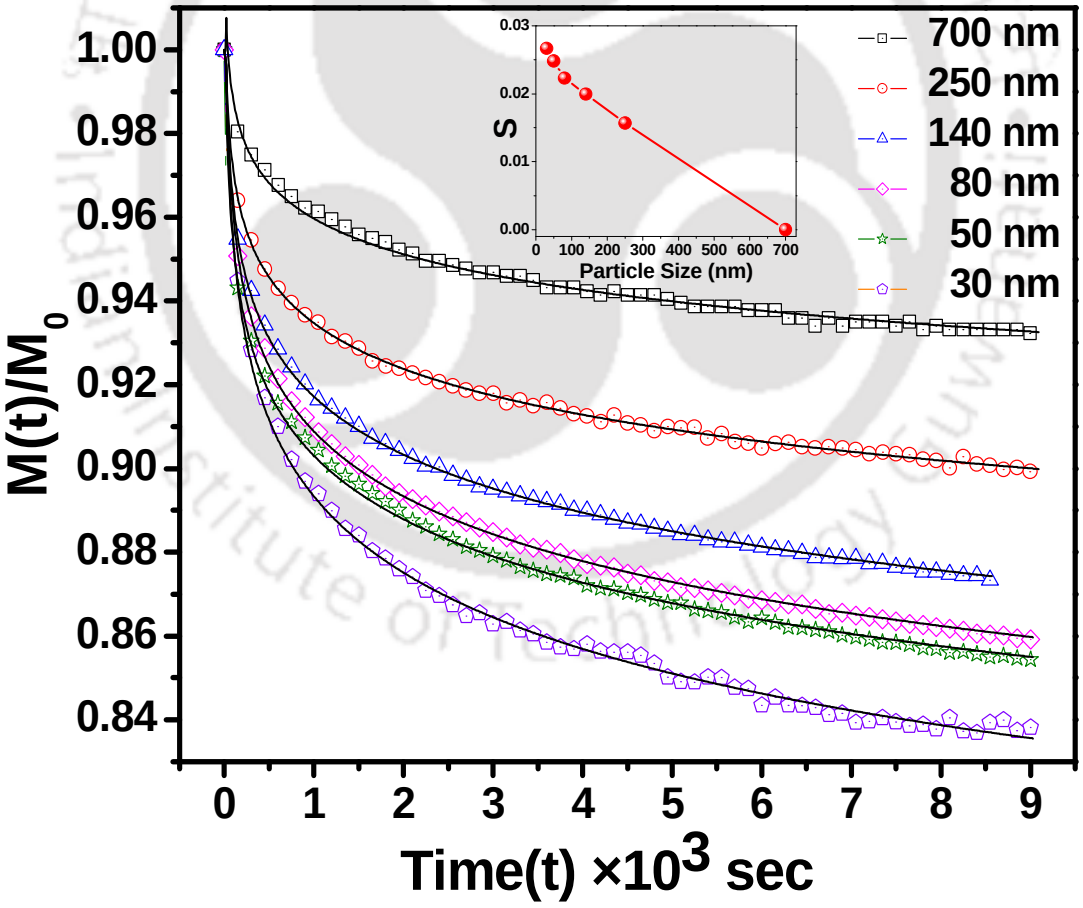

Figure 5.7: Normalized thermo-remanent magnetization as function of time for $Nd_{0.8}Na_{0.2}MnO_3$ samples of different particle sizes. The solid lines represent the fit to the logarithmic decay function. The inset shows S as function of particle size.

TH-1060_06612103

In order to understand the magnetic frustration and the magnetic cluster glass phase, magnetic relaxation measurement was carried out at 20 K, i.e., is below the FM-CG transition temperature, T_{CG}. Samples were cooled from 300 K to 20 K in the presence of 20 mT magnetic field. The magnetic field was cut off after a waiting time of t_w = 120 s, then the thermo-remanent magnetization *M(t)* was measured as a function of time. The plots of normalized thermo-remanent magnetization, *M(t)/M(0)* as function of time are shown in figure 5.7 for different samples, where *M(0)* is the magnetization at t = 0 s. The increase in magnetization relaxation rate with decrease in particle size can be seen. The experimental data were analyzed in terms of logarithmic decay function, $M(t) = M_0 [1- S \log_{10}(t/\tau)]$ [288, 289]. Here S is a constant and is a measure of relaxation rate and τ is the time constant. The thermal energy, which favors the faster relaxation of magnetization and the pinning energy are the two competing factors that influence the S value. The particle size variation of S value is shown in the inset of Fig. 5. The maximum rate of relaxation was observed for D = 30 nm sample. The observed S value is comparable to that of other CO system [290]. The increase in rate of relaxation with decrease particle size signifies the characteristic feature of glassy behavior of the nanoparticles.

5. 3. High field *M-T* Measurements

In order to further understand the interesting magnetic phase transition in the nanoparticles of $Nd_{0.8}Na_{0.2}MnO_3$, we carried out *M -T* measurements at higher magnetic field, i.e., H = 1 T. The field is chosen such that it is higher than the anisotropic field and lower than the field required to quench the charge-ordering. The measurements were carried out under three different experimental conditions, namely zero field cooled warming (ZFC), field cooled warming (FCW) and field cooled cooling (FCC). The *M* vs. *T* plots of various samples are shown in figure 5.8. For D = 700 nm, a pronounced CO transition at $T_{CO} \approx$ 195 K followed by FM transition with T_C = 85 K is observed. Unlike the case of H = 20 mT as shown in figure 5.5 (a), here the FM T_C is much higher. The sharp low temperature peak observed at 40 K for H = 20 mT is smeared into a shoulder due to the enhanced FM for H = 1 T. Another important difference is the observed upward trend of M for T < 25 K and can be explained in terms of polarization of Nd moment due to the large applied field. Unlike the case of 20 mT, here the bifurcation of ZFC and FCW curves is shifted to the FM T_C due to the CG nature of the FM interaction. In FCC case, CO transition is found to be broadened and the FM T_C is also shifted towards low temperature. However, for T < 25 K, both the FCW and FCC curves

TH-1060_06612103

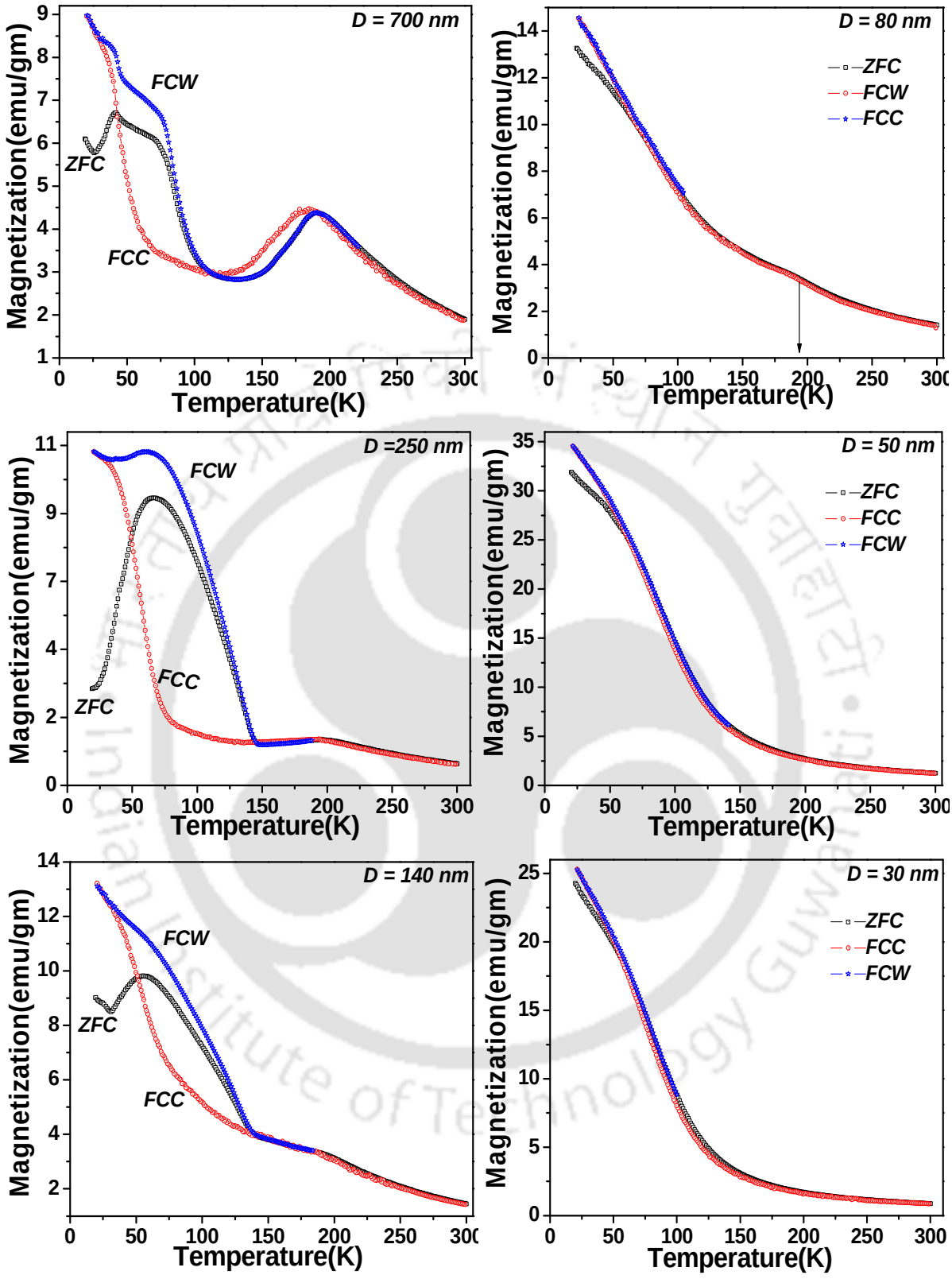

Figure 5.8: Temperature variations of magnetization for zero field cooled (ZFC), field cooled cooling (FCC) and field cooled warming (FCW) conditions at 1 Tesla magnetic field for $Nd_{0.8}Na_{0.2}MnO_3$ sample with different particle sizes.

TH-1060_06612103

merge against each other. The large hysteresis effect observed between FCW and FCC curves is due to the first order and glassy nature of FM transition.

The *M-T* plot of D = 250 nm sample shows the large suppression and broadening of CO transition. The FM T_C and the magnitude of magnetization are found to increase considerably compared to D = 700 nm (bulk) sample. However, the FM transition is found to be broadened due to the considerable contribution from surface spins. Similar behavior is observed for D = 140 nm sample except that hysteresis between FCW and FCC is reduced. For D < 80 nm, the CO transition is completely suppressed and a small bifurcation between ZFC and FCW curves is observed especially for T < 50 K, i.e., below the AFM transition temperature. Moreover, no hysteresis behavior is observed between the FCW and FCC, so the materials basically exhibit FM behavior. A maximum magnetization of 35 emu/gm is observed for D = 50 nm sample. However, for further decrease in particle size to 30 nm, the maximum magnetization value decreases and the trend remains same comparable to the case of H = 20 mT measurement. So, out of all prepared samples, the sample with bulk particle size 700 nm exhibits stronger CO ground state with T_{CO} = 195 K. In comparison to (La, Ca)-Mn-O and (Pr, Ca)-Mn-O series, the present CO phase is expected to fall in between the above two series in terms of e_g – electron bandwidth. The former is the large bandwidth material with inherent tendency to stabilize the FM phase easily and the later series is more robust CO phase. So, it is worthwhile to study the robustness of the CO phase in the present (Nd, Na)-Mn-O series having medium e_g electron bandwidth.

5.4. *M-H* loops and *H-T* Phase Diagram

M-H loops were recorded at T = 5 K for applied fields H = ±10 T for samples with different particle sizes. They are shown in figure 5.9. The initial curve of D = 700 nm sample as shown in figure 5.9 exhibits a linear behavior up to a characteristic field of H_S. For the applied field H_S = 3.5 T, a sharp jump in magnetization from 0.7 μ_B to 4 μ_B is observed. Since, this sample is comparable to any bulk material in terms of its particle size, such a sharp jump in the magnetization will not be possible unless the entire AFM or re-entrant spin glass (RSG) domain is driven into the FM state. Further increase in applied field leads to a marginal increase in magnetization from 4 μ_B to 4.2 μ_B. The cycling of the field is unable to bring the system back into the AFM/RSG state and they remain as a FM phase. We have not observed any saturation of magnetization value even for H = 10 T. However, magnetization value

TH-1060_06612103

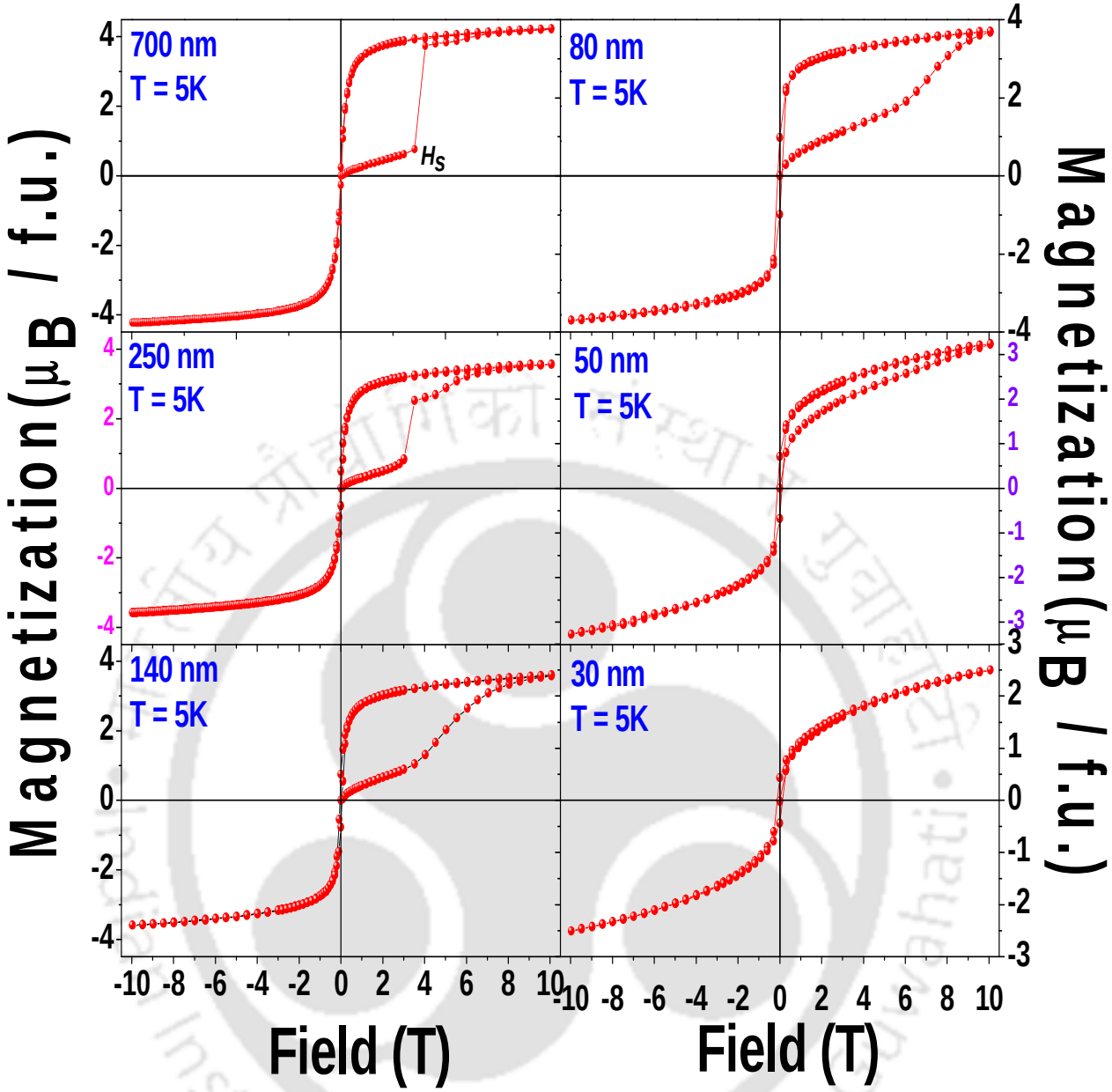

Figure 5.9: The magnetization curve measured at 5K for different particle size samples.

at 10 T, M (10 T) is found to be quite large compared to the magnetic moment due to the spin only contribution of Mn^{3+}/Mn^{4+} ions, which is expected to be ~3.5μ_B. Such a large M value can be understood in terms of partial polarization of magnetic moment of Nd ion. So, basically in the bulk sample, irreversible field induced AFM/RSG to FM transition is observed. The initial curve of D = 250 nm sample also exhibits a sharp jump in magnetization at H_S = 2.8 T, however the shift in magnetization at this field, ΔM_C = 1.8 ± 0.03 μ_B is quite small compared to the case of 700 nm sample. However the secondary rise in M, for $H > H_S$ is found to be more appreciable compared to that of D = 700 nm sample, i.e., ΔM_S = 0.5 ± 0.01 μ_B. This can be easily explained in terms of increased surface contribution

TH-1060_06612103

in D = 250 nm sample compared to that of 700 nm sample. This can be explained in the light of core-shell model [287]. The spin flip of cores occurs abruptly in a co-ordinated manner and on the otherhand, due to spin canting on the surfaces of nanoparticles, they gradually tend to align with increase in applied field. So, ΔM_C / (ΔM_C+ ΔM_S) and ΔM_S / (ΔM_C+ ΔM_S) are the measure of core and surface contribution respectively and, these values for D = 700 nm are found to be 0.86 ± 0.01 & 0.14 ± 0.04. These values for D = 250 nm are found to be 0.61 ± 0.03 & 0.40 ± 0.05 respectively. For $D \leq$ 140 nm, we have not observed any sharp change in magnetization at the field corresponding to spin-flip transition, rather it is found to increase gradually up to the maximum applied field of H = 10 T. This trend clearly explains the domination of surface contribution, where the FM alignment is due to the spin canting of shell and no longer, the low field linear region is observed due to the weakening of AFM interaction as a result of domination of magnetic spins in shell. Further reduction in particle size below 50 nm, we see a smooth Langevin type behavior of *M-H* curve due to the complete quenching of charge-ordering. However, the magnetization value at 10 T is continued to decrease with decrease in particle size. It highlights the presence of surface spin disorder. Such phenomenon is observed due to the presence of large number of surface spins with a wide variation in the angle between the nearest neighbour magnetic spins and it leads to reduction in net magnetic moment and, their spin polarization. Thus, the *M-H* loop measurements at 5 K with different particle sizes show the transition of magnetic ground state from AFM/RSG state in bulk sample to canted FM in nanoparticle sized samples.

In order to clearly understand the magnetic ground states of samples with different particle sizes, before and after the spin flip process, we have replotted the *M-H* curves especially for the low field region, i.e., for $H < H_S$ as shown in figure 5.10 (a). Here, we can see that with decrease in particle size, there is an increase in M value for a particular H value. The saturation magnetization M_{SI} before the spin flip process was determined by fitting the magnetization curves to $M(H) = M_{SI}\,[1 - a/H - b/H^2] + \chi_d H$, where χ_d is the high field differential susceptibility and, a and b are constants. The M_{SI} values are plotted as a function of particle size as shown in figure 5.10 (b). The sharp rise in M_{SI} value especially for $D \leq$ 140 nm shows the predominant FM nature of nanoparticle materials. We have also determined the saturation magnetization, M_{SF} after the spin reversal, i.e., by extrapolating the high field *M-H* curves for $H >> H_S$ to H = 0. These values are referred as M_{SF} and are shown as a function of particle size in figure 5.10 (b). Unlike the case of M_{SI}, here, we can see that M_{SF} value decreases with decrease in particle size and one can see a steep fall in M_{SF}

TH-1060_06612103

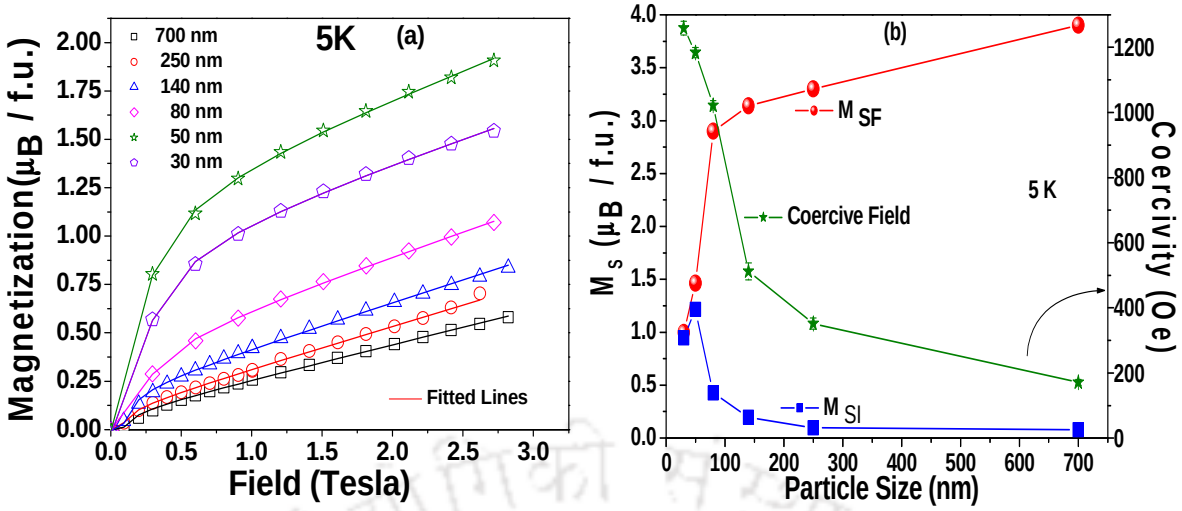

Figure 5.10: (a) The reproduced plot of initial magnetization from figure 5.9 for low field, $H < H_S$ along with fitted data shown as solid lines. (b) The variation of saturation magnetization M_{SI} ($H < H_S$), M_{SF} ($H > H_S$) and coercive field with particle size at 5 K.

value especially for D < 140 nm. Even though the charge-ordering is suppressed and FM is introduced in nanoparticle materials, the variation of M_{SF} value with D suggests that the AFM is quenched due to the surface disordering of magnetic spins. The above observation contradicts the result reported on CO $La_{0.5}Ca_{0.5}MnO_3$ system [280]. The main reason for such a difference is that in $La_{0.5}Ca_{0.5}MnO_3$ system, the CO transition occurs below the FM T_C. However here, the CO occurs at higher temperature. The coercive field as a function of particle size is shown in figure 5.10 (b), and it is found to increase with decrease in particle size. It also supports the argument of particle size induced surface disordering and increase in magnetic anisotropy with decrease in particle size.

In order to understand the magnetic dynamics and construct the *T-H* phase diagram, we have carried out *M-H* loop measurement at different temperatures for D = 700, 250, 140 and 80 nm samples. Figure 5.11 shows *M-H* curves at different temperatures for D = 700 nm sample. The *M-H* curve at 210 K shows a clear PM behavior. When the temperature is reduced to 200 K, which is close to the CO transition, we can see a field induced transition from CO-AFM to a weak FM at around 8 T. The *M-H* curve is found to be completely reversible including the above field induced transition. The above trend continues down to 170 K except that the field induced CO-AFM to FM transition occurs at a lower field. The decrease in above threshold field values with decrease in temperature can be understood in terms of decrease in competing thermal energy. The observed saturation magnetization (M_S) at 170 K is found to be 62% of that of expected value. The *M-H* loop observed

TH-1060_06612103

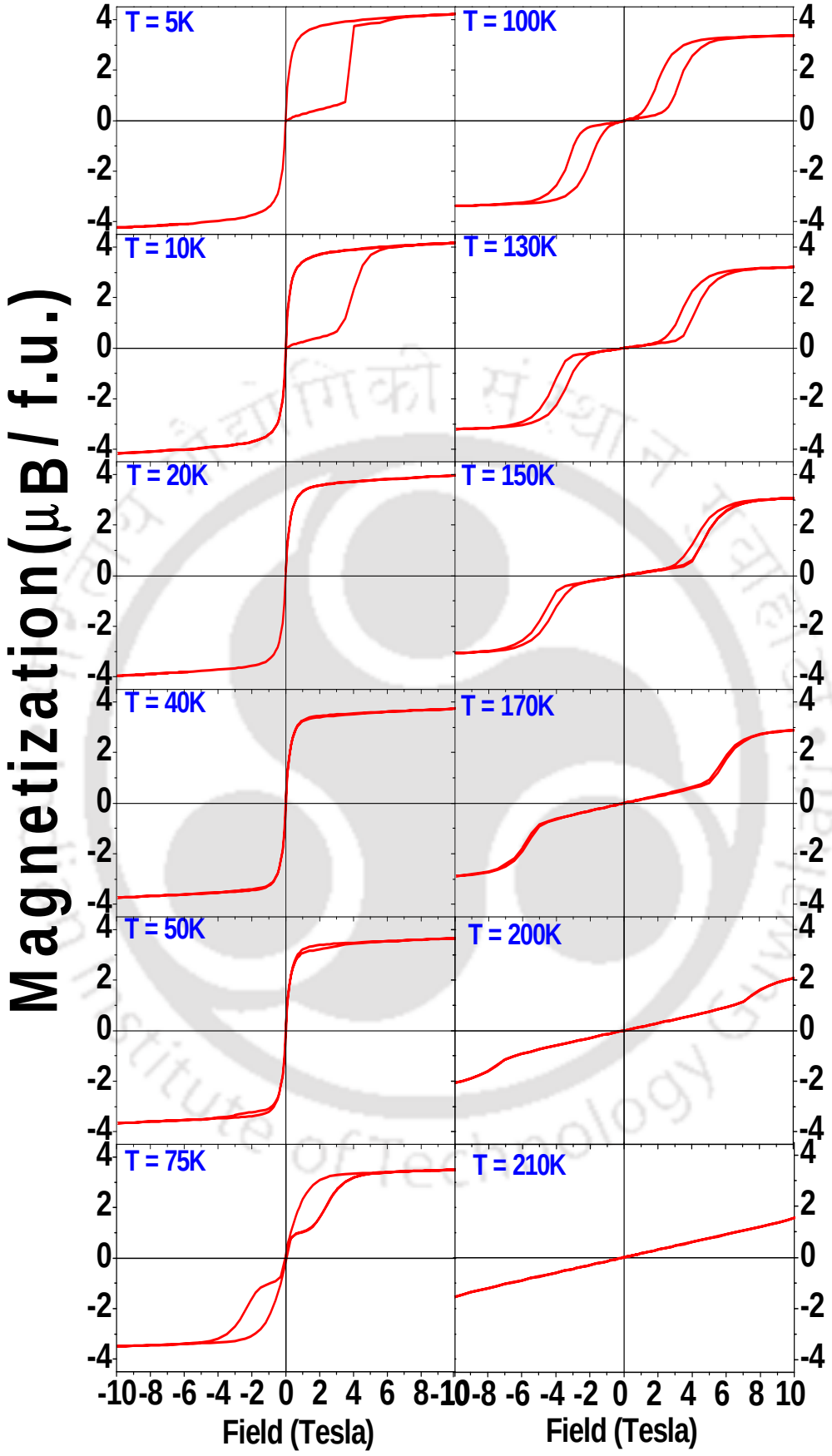

Figure 5.11: Field variation of magnetization at different temperature for 700 nm sample

TH-1060_06612103

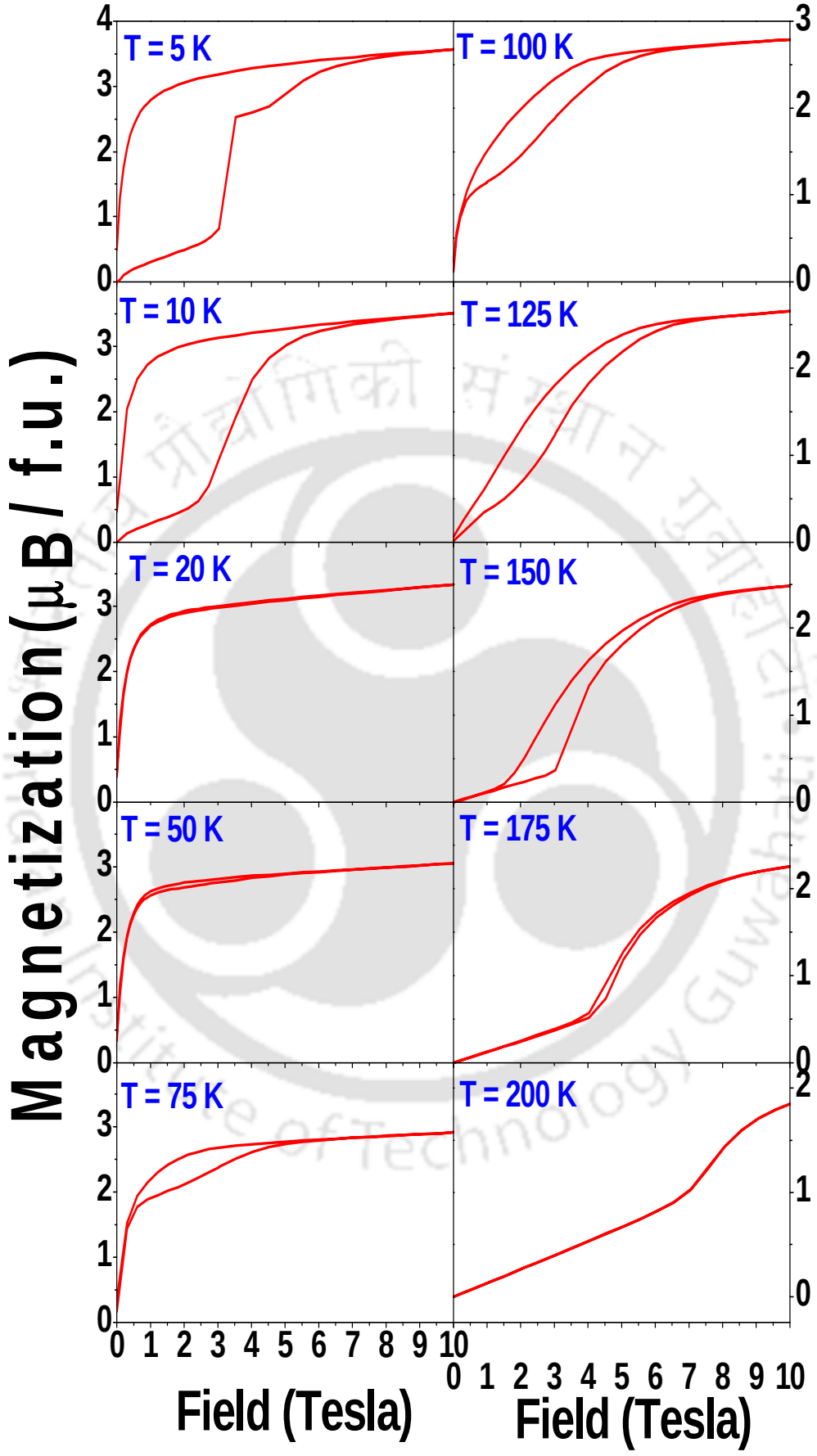

Figure 5.12: Field variation of magnetization at different temperature for 250 nm sample.

TH-1060_06612103

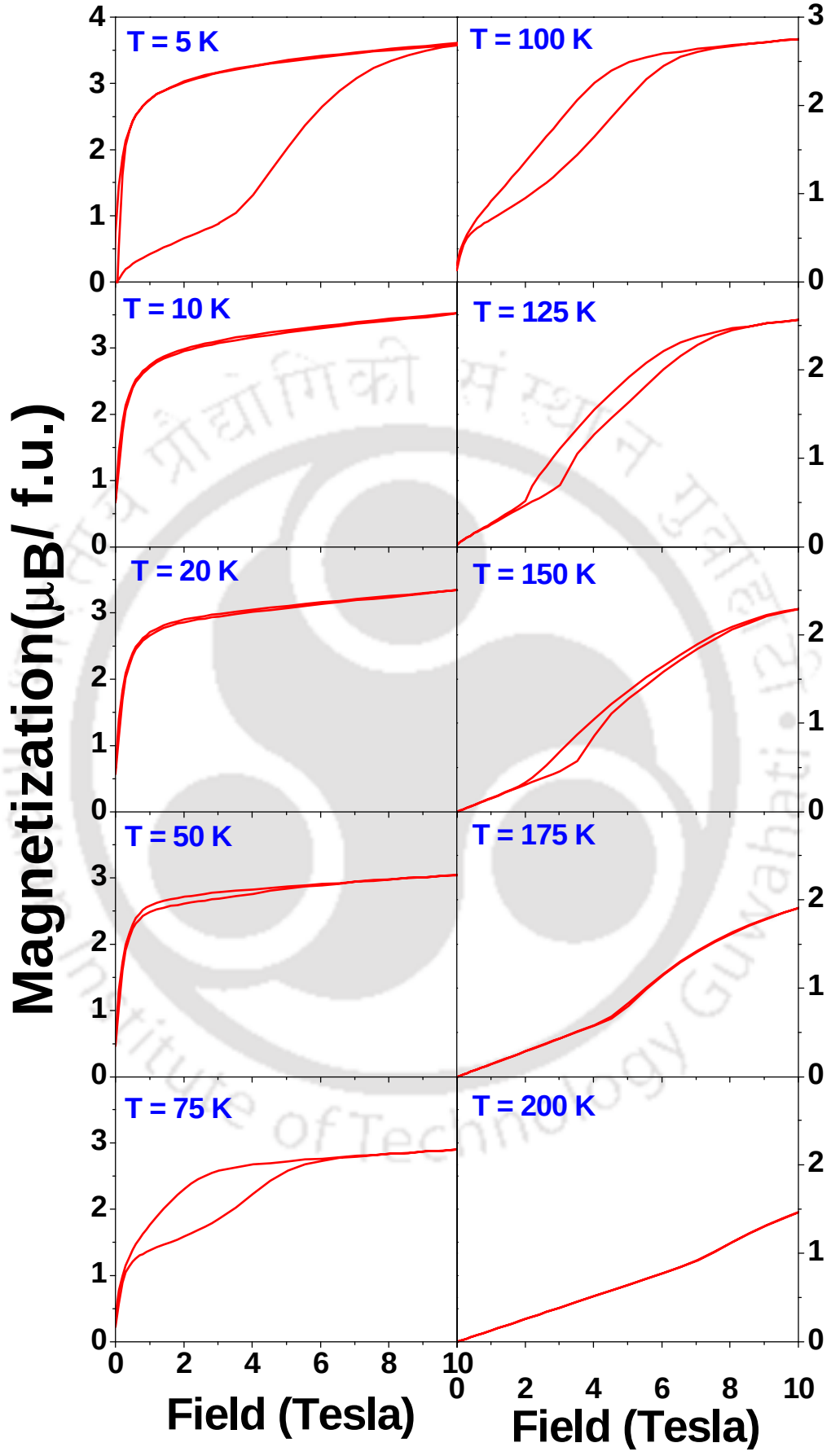

Figure 5.13: Field variation of magnetization at different temperature for 140 nm sample.

TH-1060_06612103

at 150 K exhibits hysteresis behavior within the FM phase, i.e., unlike for $T \geq 170$ K, the threshold field value is found to be different for field increasing and decreasing cycle. Thus even though the field induced AFM-FM transition is found to be a reversible one, the threshold field value for the ascending branch (H_{C1}) is found to be higher than that of descending branch (H_{C2}) of the *M-H* curves. Similar trend of *M-H* curve can be seen down to 75 K and the threshold field value continues to decrease with decrease in temperature. The *M-H* loop measured at 50 K shows the typical behavior of FM ground state, without any trace of AFM or other competing interactions. The magnetization is found to almost saturate for $H > 2$ T, and the small linearity observed in *M-H* curve at this temperature can be attributed to the PM contribution from Nd moment. The saturation magnetization after subtracting the linear contribution is found to be 3.4 μ_B/f.u, which is quite close to the expected magnetization due to spin only contribution of Mn ions. This trend continues down to 20 K. At 10 K, the magnetic ground state is found to be AFM or spin frozen state. This re-entrant AFM like behavior can be attributed to spin glass like state due to the presence of competing AFM and FM interaction. The magnetization value increases linearly up to a characteristic field $H_S = 3$ T and a sudden spin flip leading to a FM phase can be seen. The characteristics feature of this H_S field and magnetization response are found to be quite different from the behaviors observed in the temperature region, $75 \leq T \leq 150$ K. It is distinct from the decrease in H_C value observed with decrease in temperature; secondly, once the spins are flipped into FM state, they are irreversible for the subsequent field cycling. On the other hand, in the temperature range $75 \leq T \leq 150$ K, a field induced FM transition is found to revert back to AFM, when the field is decreased below the threshold field. The *M-H* loop measured at 5 K is found to exhibit similar behavior as that of $T = 10$ K and is already discussed in detail.

The typical *M-H* loops recorded for samples, i.e., $D = 250$ nm and 140 nm are shown in figure 5.12 and figure 5.13 respectively. The *M-H* loop of $D = 250$ nm sample follows similar behavior as that of $D = 700$ nm sample. For $D = 140$ nm, we can see that the system passes through different magnetic ground states, namely PM for $T > 200$ K, CO-AFM for $75 < T < 200$ K, FM for $50 < T < 10$ K and spin frozen state for $T = 5$ K. However, the notable difference is that the shift of the spin frozen state to lower temperature. The field induced AFM to FM transition is found to be broader. Moreover, the magnetization at 10 T is found to be considerably smaller than that of their respective bulk counterpart at a specific temperature. These characteristic features can be understood in terms of enhanced surface contribution, where the magnetic spins are canted or disordered.

TH-1060_06612103

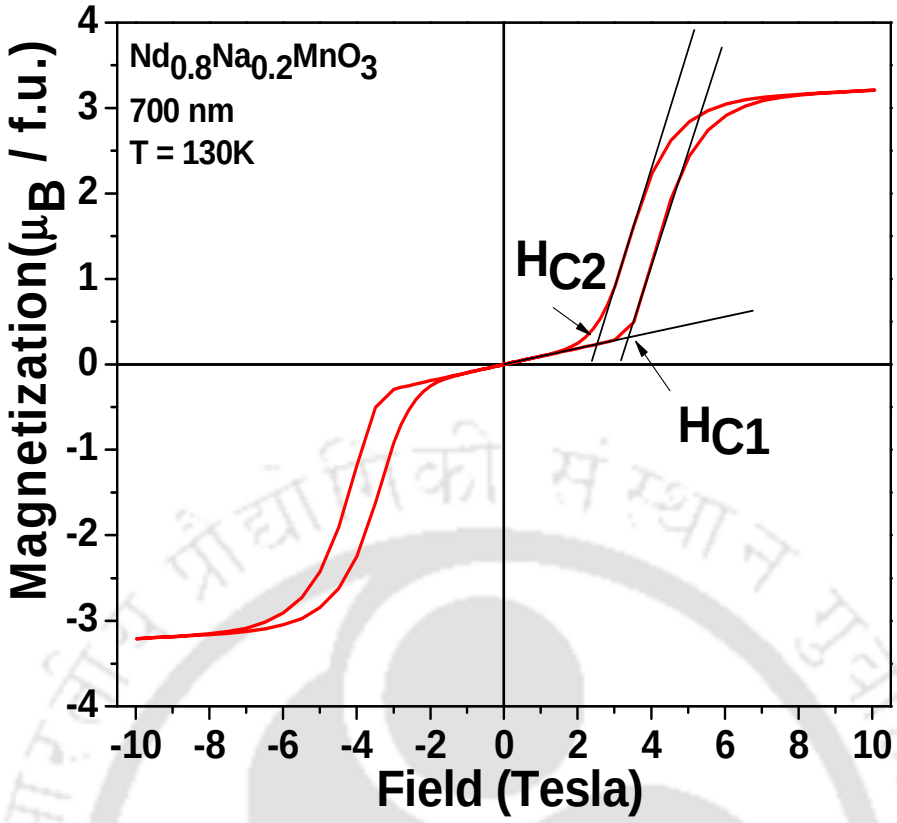

Figure 5.14: *M-H* curve of 700 nm sample of $Nd_{0.8}Na_{0.2}MnO_3$ compound at 130 K. Threshold magnetic fields for metamagnetic transition in increasing and decreasing process are marked as H_{C1} and H_{C2} respectively.

To draw the *T-H* phase diagram, we have measured the critical field H_{C1} required for CO-AFM to FM transition and the critical field H_{C2} at which the system returns back to AFM-CO state. The method of determination of H_{C1} and H_{C2} are depicted in figure 5.14. Similar technique was followed by Ouyang *et al.*[269]. The *T-H* phase diagram of D = 700 nm sample is shown in figure 5.15 (a). The open (closed) circles represent the H_{C1} (H_{C2}) values. The transition field decreases with decrease in temperature. The phase diagrams shows that $dH_{C1}/dT > 0$ in the temperature range $T_{CO} \geq T \geq 50$ K. In the temperature range 50 K $\geq T \geq$ 20 K, the phase boundary disappears due to dominant FM character for D = 700 nm sample. As explained in the previous section for $T < 20$ K, a new mechanism, namely field induced melting of RSG state occurs for $H > H_S$, and the shaded region ($T < 20$ K) is designated as RSG state. The boundary in the low temperature region can be assigned as spin frozen boundary. The phase diagram in *T-H* plane is also constructed for D = 250 nm and D = 140 nm as shown in figure 5.15 (b) and (c) respectively. For D = 250 nm sample, the phase separation boundary shifts towards the high temperature region and becomes comparatively narrow. The spin frozen state is shifted to further lower temperature. For D = 140 nm sample,

TH-1060_06612103

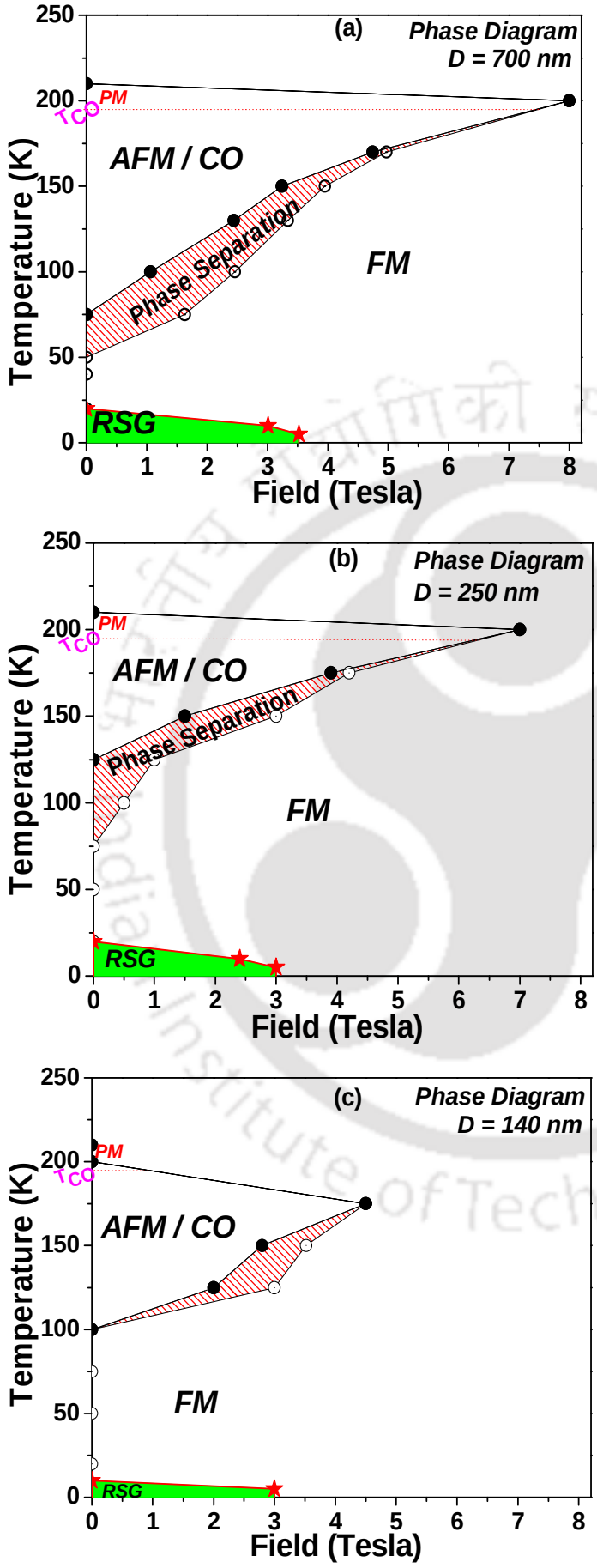

Figure 5.15: The phase diagrams of $Nd_{0.8}Na_{0.2}MnO_3$ for (a) D = 700 nm, (b) D = 250 nm and (c) D = 140 nm particle size samples obtained from magnetization measurements. Open and closed circles represent the threshold fields H_{C1} and H_{C2} respectively and stars represent H_S values.

TH-1060_06612103

the further shift in phase boundary is observed towards the higher temperature and lower field. At T ≥ 175 K the threshold fields H_{C1} and H_{C2} are found to merge for D = 140 nm sample. We have recorded the M vs H loops for D = 80 nm sample, but it was very difficult to deduce the threshold field values due to the considerable broadening of the transitions. The results for 80 nm sample depict the presence of weak charge-ordering. For the first time, we have observed the shifting of phase separation boundary between FM and AFM-CO state towards the higher temperature and lower field side and suppression of spin frozen boundary towards the low temperature by decreasing the particle size of the compound. So this suppression of CO state by reducing the average particle size of the $Nd_{0.8}Na_{0.2}MnO_3$ compound can be clearly seen by shifting of these phase boundaries.

5.5. Discussion

The suppression of CO state in the present $Nd_{0.8}Na_{0.2}MnO_3$ compound was studied by varying two parameters, namely the particle size and magnetic field. From the low field temperature variation of magnetization curves, it is clear that the present series of samples are in different magnetic ground states, namely PM, CO, FM, and RSG state in the temperature range T > 200 K, 130 < T < 200 K, 42 < T < 130 and T < 42 K respectively. The quenching of charge-ordering and enhancement of FM in nanoparticle materials have been studied by several authors especially in (La, Ca)-Mn-O [279-281, 291], (Pr, Ca)-Mn-O [281, 282, 284], and (Nd, Ca)-Mn-O [193, 285], compounds and different mechanisms were proposed to explain the suppression of the CO state in nanoparticle samples. The present results could be explained based on core-shell model reported by Bhowmik *et al.*[287], where a CO core is surrounded by spin canted shell. By reducing the particle size D, the uncompensated surface spins not only enhance the surface FM in spin canted shell but also disturbs the collinear AFM arrangement inside the core. This can be understood from the observed reduction in M_{SF} value with decrease in particle size. The percentage of increase in surface to volume (S/V) fraction was found to be 80 % with decrease in particle size from 700 nm to 250 nm, and it was calculated from the observed ΔM_C and ΔM_S values. By assuming that particles are in spherical shape, one can also estimate the S/V fraction. The percentage of increase in S/V for the variation of particle size from D = 700 nm to 250 nm is found to be 74% as per the later technique. This value is found to be comparable to that observed from magnetization analysis. According to the core-shell model [287], the total magnetization of the particle can be expressed as,

TH-1060_06612103

$M = \alpha M_{shell} \sum_{ij} cos\theta_{ij} + (1- \alpha) M_{core,}$ ---------- (5.1)

where α is the shell thickness, which increases with decrease in particle size. M_{shell} and M_{core} represent the magnetization of the shell and core respectively, and θ_{ij} with $0^{\circ} \leq \theta_{ij} \leq 180^{\circ}$ is the angle between neighboring spins. By reducing the particle size, the α value increases and the uncompensated magnetic spins in the shell contribute to the enhanced magnetization. As we have observed for $D \leq 140$ nm, α becomes so large that the uncompensated surface spins contribute to net FM component and are polarized with the application of magnetic field. Finally, after a critical value of α and θ_{ij}, the surface spins will be almost in random and disordered state and it leads to net decrease in magnetization. The other arguments such as enhancement of DE interaction due to itinerant charge carriers and the absence of super-cell modulation in nanoparticle materials were given by various authors. According to Chai *et al.*[284], the disturbance of local lattice structure and hence the local lattice potential in nanoparticles is expected to affect the balance state formed by Coulomb interaction and disfavors the CO arrangement inside the core. Suppression of charge-ordering and evolution of FM with reduction in grain size and low temperature spin glass like state was reported by Lu *et al.*[291] in electron doped $La_{0.4}Ca_{0.6}MnO_3$. The core-shell model was used in explaining the magnetic properties of $La_{0.67}Ca_{0.33}MnO_3$ and $La_{0.25}Ca_{0.75}MnO_3$ compounds [279, 292]. The lack of supercell modulation in nanoparticles of $La_{0.5}Ca_{0.5}MnO_3$ was explained as the reason for the suppression of charge-ordering [280]. Zhang *et al.*[283] have observed the complete collapse of CO in $Pr_{0.5}Ca_{0.5}MnO_3$ below 40 nm and explained that it was due to FM and canted AFM surface spins and their interaction with core spins. However, Chai *et al.*[284] have proposed a negligible inter particle interaction. By increase in inter particle distances, it not only modifies the electronic and magnetic transition but also shifts the CO transition to lower temperature.

In Nd-Mn-O system, the suppression of charge-ordering was not studied extensively. The surface disorder induced charge order suppression and exchange coupling between AFM core and FM shell are reported in (Nd, Ca)-Mn-O system [193, 285]. The shifting of phase boundary between AFM/CO and FM region in *T-H* plane by varying the doping concentration in (Pr, Ca) and (Nd, Ca) based CO manganites were reported by a few authors [70, 293]. We have mapped the phase diagram in *T-H* plane for different particle sizes in $Nd_{0.8}Na_{0.2}MnO_3$ compound. By decreasing the particle size, three major changes are observed in phase diagrams. The CO/AFM region in the temperature range 75 K $\leq T \leq$ 195 K for 700 nm sample and the respective phase separation boundary between AFM/CO and FM region shifts to higher temperature and lower field side by decreasing the particle size. The

TH-1060_06612103

FM region expands due to enhancement of surface FM. Finally the spin freezing boundary is found to be suppressed towards lower temperature. The observed phase separated boundaries between AFM/CO and FM region in figure 5.15 show that $dH_{C1}/dT > 0$. However, negative value of dH_{C1}/dT was reported in (Pr, Ca)-Mn-O [70, 269, 293], (Pr, Sr)-Mn-O [60] and (Nd, Ca)-Mn-O [70, 188] charge-ordered compounds, because these systems fall in narrow bandwidth category. In $Pr_{1-x}Ca_xMnO_3$ compounds, negative value of dH_{C1}/dT for x = 0.45 & 0.50 and positive value of dH_{C1}/dT for x = 0.4 were reported [70]. Millange *et al.*[188] have traced a phase diagram in *T-H* plane for $Nd_{0.5}Ca_{0.5}MnO_3$ compound and showed that charge and orbital ordering was present in the entire low temperature region with $dH_C/dT < 0$. However, the tilting of phase boundary towards $T = 0$ K has been also observed in $Nd_{0.6}Ca_{0.4}MnO_3$ compound, i.e., with $dH_C/dT > 0$. The observed phase separated boundary between AFM/CO and FM region in $Nd_{0.8}Na_{0.2}MnO_3$ compound is comparable to that of $Pr_{0.6}Ca_{0.4}MnO_3$ and $Nd_{0.6}Ca_{0.4}MnO_3$ compounds.

5.6. Conclusions

In summary, we have prepared single phase samples of charge ordered $Nd_{0.8}Na_{0.2}MnO_3$ with different particle sizes ranging from 700 nm to 30 nm. The effect of particle size and applied magnetic field on the magnetic properties of CO phase was studied extensively by measuring temperature and field variations of magnetization and their analysis. The bulk samples, i.e., with average particle size $D \geq 140$ nm, exhibit different magnetic ground states such as PM, CO, FM-cluster glass and AFM/RSG in different temperature regions. However, in nano-sized particles, with $D \leq 80$ nm suppression of CO and enhancement of FM-CG transition temperature (T_{CG}) were observed. *M-H* loops recorded at different temperatures show the field induced transition from CO-AFM to FM beyond a threshold field H_C. The threshold field is found to decrease with decrease in particle size at a given temperature. The observed *T-H* phase diagrams constructed from threshold field values show the narrowing of phase separation region and, the shifting of phase boundary between CO-AFM and FM towards higher temperature and lower field. The *M-H* loops recorded at 5 K, especially for samples with larger particle size $D \geq 140$ nm show a distinct field induced transition from AFM/RSG state to FM state beyond a characteristic field H_S and is quite different from the field induced CO-AFM to FM state observed at higher temperature. The above process is explained as a result of spin flipping of entire AFM/RSG core. The particle size dependence of saturation magnetization before and after the spin flip process exhibits an interesting feature and is

TH-1060_06612103

explained in terms of core-shell model. We have also estimated the surface to volume fraction from the measured magnetization loops and are comparable to the expected result as per the known particle size.

TH-1060_06612103

Chapter 6: Conclusions

To summarize, single phase samples of K-doped and Na-doped Nd-Mn-O series were prepared and, their crystal structure and magnetic properties were studied extensively. In addition to that, nanocrystalline samples of charge ordered $Nd_{0.8}Na_{0.2}MnO_3$ were prepared and the suppression of charge-ordering by tuning the particle size and external magnetic field has been studied. The important conclusions drawn in the above three series are summarized as follows.

The diffraction patterns of $Nd_{1-x}K_xMnO_3$ could be refined by using *Pnma* space group in orthorhombic crystal with typical lattice parameters a = 5.4868 Å, b = 7.7183 Å and c = 5.4450 Å. The lattice parameters were mostly found to increase with increase in doping concentration and it can be understood in terms of substitution of larger K^{1+} ions in place of smaller Nd^{3+} ions. The decrease in Mn-O bond lengths and increase in Mn-O-Mn bond angles were observed with increase in doping concentration. The diffraction patterns of Na-doped samples could be also refined by using *Pnma* space group with typical lattice parameters a = 5.4537 Å, b = 7.6805 Å and c = 5.4315 Å. The lattice parameters are found to be smaller than those of K-doped samples and it can be easily interpreted in terms of smaller ionic size of Na^{1+} compared to that of K^{1+}. The lattice parameters and unit cell volume of Na doped samples were found to decrease with increase in doping concentration. It is basically due to the comparable ionic size of Na^{1+} with Nd^{3+} ions and the generation of Mn^{4+} ions at the expense of Mn^{3+} ions.

The temperature variation of magnetization of the parent compound, $NdMnO_3$ exhibits a peak at around 75 K and it could be attributed to the AFM ordering of Mn ions. In addition to that, a secondary transition at 15 K with a sharp fall in magnetization to a negative value was observed. Such a negative magnetization value could be interpreted in terms of ferrimagnetic coupling between two magnetic sublattices, namely Mn and Nd ions. In *M-H* loop measurement, the magnetization could not be saturated even for a field of 10 T at 5 K and it indicates the presence of AFM. However, the observed remnant magnetization of 1.5 μ_B/f.u. suggests the coexistence of FM and AFM interactions. The estimated saturation magnetization (M_S) was found to be 2.62 ± 0.05 μ_B/f.u.

In K-doped samples, the FM T_C was found to increase from 116 K for x = 0.10 to 128K for x = 0.20 and, the T_C was found to decrease for further increase in doping concentration. Strong bifurcation between ZFC and FC magnetization was observed for $x \geq 0.20$ and it was mainly due to the presence of competing AFM in Mn^{4+}-O-Mn^{4+} networks.

TH-1060_06612103

The M_S value was found to increase with increase in doping concentration, i.e., 2.16 μ_B/f.u for x = 0.10 to 2.84 μ_B/f.u for x = 0.20. The field variation of magnetization could be fitted to Brillouin function model by considering the FM interaction and, the effective magnetic spin, S_{eff}, for FM contribution was estimated. They were found to increase with increase in doping concentration.

In order to investigate the spin glass like behavior, one of the K-doped samples, i.e., x = 0.15 sample was taken up for detailed measurements of frequency variation of fundamental susceptibility, temperature variation of third harmonic susceptibility and magnetic relaxation. The temperature variation of out of phase susceptibility, χ'' showed two peaks, one corresponding to FM T_C without any frequency dependence and another corresponding to spin glass freezing temperature, T_f with a strong frequency dependence. The estimated spin glass transition temperature T_g was found to be 97.6 ± 0.09 K. The presence of spin glass behavior was confirmed unambiguously from the observed critical behavior of third harmonic susceptibility. The estimated critical exponent γ' was found to be 3.09±0.05. The relaxation of thermoremanent magnetization was studied. The effective number of frustrated spins was found to decrease with increase in applied magnetic field and it was found to be in the order of 10^5. The large correlation length, ξ of the order of 100Å and spin flipping time, τ_0 of the order of 10^{-6} s suggest that the origin of spin glass behavior in the present sample was mainly due to the freezing of clusters rather than the magnetic frustration at atomic scale.

The critical exponent behavior was studied on two optimum K-doped samples, i.e., $Nd_{0.80}K_{0.20}MnO_3$ and $Nd_{0.70}K_{0.30}MnO_3$ by measuring the isothermal magnetization in the vicinity of T_C. The critical exponents β, γ and δ corresponding to the spontaneous magnetization, initial susceptibility and isothermal magnetization, respectively, were determined by analyzing the magnetization data in terms of modified Arrott plot method. The estimated values of critical exponents, i.e., β = 0.57±0.03, γ = 1.04±0.02, and δ = 2.82±0.03 for x = 0.20 and β = 0.53±0.02, γ = 1.07±0.04, and δ = 2.99±0.02 for x = 0.30 are found to be close to the mean-field model values. The observed long range FM interaction could be attributed to the formation of FM clusters just above T_C. The critical exponent values were found to be consistent with the Widom scaling relation and the universal scaling hypothesis.

The Na-doped samples (for x = 0.05 to 0.15) exhibit PM to FM transition with a maximum T_C of 113 K for x = 0.10 sample. They also show the evidence of presence of competing AFM and re-entrant spin glass like behavior below 40 K. However, x = 0.20

TH-1060_06612103

sample was found to exhibit a CO transition at 180K, followed by a weak ferromagnetic behavior below 100 K and spin glass like transition at around 40 K. The M_S values of x = 0.05, 0.10 and 0.15 samples, after subtracting the linear contribution were found to be 4.0, 4.3 and 3.3 μ_B/f.u. respectively at 5 K. The origin of such a large value of M_S was explained as a result of contribution from the polarized moment of 'Nd' ions.

One of the samples in Na-doped series, i.e., $Nd_{0.8}Na_{0.2}MnO_3$ was found to exhibit interesting magnetic dynamics. The applied magnetic field was found to enhance the low temperature FM phase with a large increase in the magnitude of magnetization along with shift in FM T_C towards higher temperature, i.e., 85 K for H = 1T to 166 K for H = 7 T. Moreover, the sharp fall in magnetization observed at low temperature due to the possible spin glass like transition was found to shift towards lower temperature and ultimately it disappeared for H = 7 T. Thus, the applied magnetic field tends to stabilize the FM phase at the expense of other competing magnetic interactions. On the other hand, the CO transition temperature observed at 180 K was found to be field independent and it could be seen prominently up to a magnetic field of 5 T and beyond that, it was found to merge with the enhanced FM signal. A reversible field induced metamagnetic transition from CO state to FM state was observed and it was found to be irreversible for T < 10 K.

NPD patterns for $Nd_{1-x}K_xMnO_3$ (x = 0.15 and 0.20) samples were recorded at different temperatures down to 22 K. The temperature variations of lattice parameters and Mn-O-Mn bond angles exhibit a clear transition in the vicinity of T_C. The stoichiometry ratio of the compounds as per the refinement of occupancy values for x = 0.15 and 0.20 samples are found to be $Nd_{0.80}K_{0.15}MnO_{2.97}$ and $Nd_{0.76}K_{0.20}MnO_{3.09}$ respectively. The increase in intensities of (101) and (121) fundamental reflections with decrease in temperature, especially below 125 K highlight the ferromagnetic ordering. The low temperature patterns for T < 125 K could be refined by taking into account the ferromagnetic phase in addition to the nuclear phase. The patterns at low temperature were refined by varying the magnetic moments of Mn ions. No ordering of Nd moments was observed in the measured temperature range. The best possible refinement was obtained for the Mn^{3+} magnetic moments oriented in the *ac*-plane of the unit cell. The maximum magnetic moment per Mn ion obtained from the above refinements for x = 0.15 and 0.20 samples were found to be 2.82(5) μ_B and 2.68(5) μ_B, respectively at 22K.

In Na doped series, NPD patterns were recorded for x = 0, 0.15 and 0.20 samples down to 5 K. The patterns could be refined by using *Pnma* space group. The patterns at low temperature could be refined by considering both nuclear and magnetic reflections based on

TH-1060_06612103

different magnetic structures. Decrease in Jahn-Teller distortion with increase in Na concentration was observed. The lattice parameters exhibit a clear fall in their magnitudes in the vicinity of Neel temperature, $T_N \approx 75$ K for the x = 0 sample. However, in x = 0.20 sample, the shrinkage of *b* parameter below 180 K and the moderate expansion of *a* and c parameters were seen and they reveal pseudo CE-type of AFM ordering. The magnetic structure of x = 0 sample could be refined by including *A*-type AFM ordering below 75 K with canted Mn moments away from the *ac*-plane. Therefore, two components of the moment were taken, namely *x*-component along *a*-axis and *y*-component along *b*-axis. The *x*-components were coupled ferromagnetically within the plane and antiferromagnetically between the planes along the *b*-axis. The *y*-components were coupled ferromagnetically both within the plane and between the planes. Secondly below 15 K, the Nd moment was found to be coupled ferrimagnetically to the *y*-component of the Mn moment. The magnitudes of moment due to Mn and Nd at 5 K were found to be 3 μ_B and 1.3 μ_B, respectively. On the other hand, for x = 0.15 sample, the increase in intensity of (101) and (121) peaks with decrease in temperature below 80 K demonstrates the ferromagnetic nature of the sample. The low temperature patterns below 80 K could be refined by taking into account the ferromagnetic phase in addition to the nuclear phase. The moments of the Mn ions were found to be ferromagnetically canted away from the *ac*-plane. However, three superlattice reflections of weak intensities were observed at 5 K and could be refined to the pseudo CE-type charge ordered phase. The refined magnetic moment components per Mn ion, corresponding to the FM structure at 5K were found to be M_x = -1.78(05) μ_B, M_y = 1.95(05) μ_B. The magnetic moments corresponding to Mn^{3+} and Mn^{4+} ions in pseudo CE-type AFM structure were found to be 1.11(07) μ_B, 0.94(09) μ_B respectively. For x = 0.20 sample, the three forbidden Bragg reflections (0 0 ½), (½ 0 ½) and (1 0 ½) at $2\theta = 6.57^\circ$, 9.30° and 14.73° respectively were observed especially $T < 125$ K. The intensity of these peaks was found to increase with decrease in temperature and they are attributed to the CO-AFM. These superlattice reflections were successfully indexed to a $2a \times b \times 2c$ cell, having a pseudo CE-type structure. The low temperature NPD data could be successfully refined by introducing pseudo CE-type AFM structure in the $P2_1/m$ space group. In this structure, two different Mn sublattices, i.e., Mn^{3+} and Mn^{4+} occupy two distinct sites. The Mn^{3+} sublattice was associated with the propagation vector k_1 = (0 0 ½) and that of Mn^{4+} was associated with k_2 = (½ 0 ½). The arrangement of the Mn ions in this superstructure is the direct evidence of the charge ordered state. The maximum refined moment for Mn^{3+} sublattice was found to be 3.20(05)

TH-1060_06612103

μ_B and that of Mn^{4+} sublattice was found to be 3.00(02) μ_B. Thus the analysis of NPD patterns in $Nd_{1-x}Na_xMnO_3$ shows A-type AFM ordering of x = 0 sample, FM ordering of x = 0.15 sample with the signature of pseudo CE type structure at 5 K and the robust pseudo CE type CO phase in x = 0.20 sample.

The charge-ordered (CO) state in $Nd_{0.8}Na_{0.2}MnO_3$ compound could be suppressed by varying the average particle size to nano metric scale and the applied magnetic field. The average particle size was varied from 700 nm to 30 nm. The CO peak observed at 195 K in 700 nm sample could be completely suppressed by reducing the average particle size to 50 nm. A clear shift in ferromagnetic cluster glass (FM-CG) transition towards higher temperature could be observed with decrease in particle size, i.e., 42 K for 700 nm to 84 K for 50 nm. The suppression of CO state with reduction in average particle size to nano-metric scale and the evolution of FM–CG phase could be explained in terms of evolution of spin configuration resulting from surface effect. The glassy behavior of the nanoparticles could be confirmed from the increase in the rate of magnetic relaxation with decrease in particle size. *M-H* loops recorded at different temperatures show the field induced transition from CO-AFM to FM state beyond a threshold field H_C. The threshold field was found to decrease with decrease in particle size at a given temperature. *T-H* phase diagrams were constructed from the observed threshold field values. They show the narrowing of phase separation region and the shifting of phase boundary between CO-AFM and FM phases towards higher temperature and lower field. The *M-H* loops recorded at 5 K, especially for samples with larger average particle size $D \geq 140$ nm were found to show a distinct field induced transition from AFM/RSG state to FM state, beyond a characteristic field H_S and is quite different from the field induced transition observed at higher temperature. The above process was explained as a result of spin flipping of entire AFM/RSG core. The particle size dependence of spontaneous magnetization before and after the spin flip process exhibits an interesting feature and was explained in terms of core-shell model. We estimated the surface to volume fraction from the measured magnetization loops and were comparable to the expected result as per the known particle size.

----------×----------

TH-1060_06612103

References:

[1] C. N. R. Rao and B. Raveau, Transition metal Oxides (2nd ed.), New York, Wiley-VCH, (1995)

[2] L. E. Cross, Ferroelectrics **76** (1987) 241.

[3] H. Schmid, Ferroelectrics **162** (1994) 317.

[4] C. N. R. Rao and B. Raveau, Colossal Magnetoresistance, Charge Ordering and Related Properties of Manganese Oxides, World Scientific, Singapore (1998)

[5] Y. Tokura, Colossal magneto-resistive Oxides, Gordon and Breach Science Publishers (2000)

[6] E. Dagotto, T. Hotta, and A. Moreo, Phys. Reports **344** (2001) 1.

[7] A. P. Ramirez, J. Phys.: Condens. Matter **9** (1997) 8171.

[8] J. M. D. Coey, M. Viret, and S. v. Molnar, Adv. Phys. **48** (1999) 167.

[9] M. B. Salamon and M. Jaime, Rev. Mod. Phys. **73** (2001) 583.

[10] J. G. Bednorz and K. F. Muller, Z. Phys. B **64** (1986) 189.

[11] C. W. Chu, P. H. Hor, L. Gao, Z. J. Huang, and Y. Q. Wang, Phys. Rev. Lett. **58** (1987) 405.

[12] S. N. Putlin, E. V. Antipov, O. Chmaissem, and M. Marezio, Nature **362** (1993) 226.

[13] M. Fiebig, J. Phys. D: Appl. Phys. **38** (2005) R123.

[14] S. W. Cheong and M. Mostovoy, Nat. Mater. **6** (2007) 13.

[15] R. Ramesh and N. A. Spaldin, Nat. Mater. **6** (2007) 21.

[16] R. V. Helmolt, J. Wecker, B. Holzapfel, L. Schultz, and K. Samwer, Phys. Rev. Lett. **71** (1993) 2331.

[17] E. O. Wollan and W. C. Koehler, Phys. Rev. **100** (1955) 545.

[18] J. B. Goodenough, Landolt-Bornstein Tabellen (II) (Springer-Verlag, Berlin, 1962), Part 9, pp. 2-208

[19] Q. Huang, A. Santoro, J. W. Lynn, R. W. Erwin, J. A. Borchers, J. L. Peng, and R. L. Greene, Phys. Rev. B **55** (1997) 14987.

[20] C. Zener, Phys. Rev. **81** (1951) 440.

[21] J. Goodenough, Phys. Rev. **100** (1955) 564.

[22] A. J. Millis, P. B. Littlewood, and B. I. Shraiman, Phys. Rev. Lett. **74** (1995) 5144.

[23] V. M. Goldschmidt, Geochemistry, Oxford University Press, London (1958) 730 pp.

[24] H. Y. Hwang, S.-W. Cheong, P. G. Radaelli, M. Marezio, and B. Batlogg, Phys. Rev. Lett. **75** (1995) 914.

TH-1060_06612103

[25] J. B. Goodenough, Magnetism and the Chemical Bond, (New York: Wiley–Inter science) (1966)

[26] Y. Guo, S. Roy, and N. Ali, J. Phys.: Condens. Matter **14** (2002) 181.

[27] B. Dabrowski, K. Rogacki, X. Xiong, P. W. Klamut, R. Dybzinski, J. Shaffer, and J. D. Jorgensen, Phys. Rev. B **58** (1998) 2716.

[28] G. H. Rao, J. R. Sun, K. Bärner, and N. Hamad, J. Phys.: Condens. Matter **11** (1999) 1523.

[29] T. Shimura, T. Hayashi, Y. Inaguma, and M. Itoh, J. Solid State Chem. **124** (1996) 250.

[30] M. Itoh, T. Shimura, J. D. Yu, T. Hayashi, and Y. Inaguma, Phys. Rev. B **52** (1995) 12522.

[31] S. Roy, Y. Q. Guo, S. Venkatesh, and N. Ali, J. Phys.: Condens. Matter **13** (2001) 9547.

[32] S. L. Ye, W. H. Song, J. M. Dai, S. G. Wang, K. Y. Wang, C. L. Yuan, and Y. P. Sun, J. Appl. Phys. **88** (2000) 5915.

[33] T. Tang, K. M. Gu, Q. Q. Cao, D. H. Wang, S. X. Zhang, and Y. W. Du., J. Magn. Magn. Mater. **222** (2000) 110.

[34] M. Kar and S. Ravi, Mater. Sci. & Eng. B **110** (2004) 46.

[35] S. Blundell, Magnetism in Condensed Matter, pp. 45, Chapter 3, Oxford University Press (2003)

[36] Y. Tokura and N. Nagaosa, Science **288** (2000) 462.

[37] P. W. Anderson and H. Hasegawa, Phys. Rev. **100** (1955) 675.

[38] C. Zener, Phys. Rev. **82** (1951) 403.

[39] P. G. d. Gennes, Phys.Rev. **118** (1960) 141.

[40] P. A. Algarabel, J. M. De Teresa, J. Blasco, M. R. Ibarra, C. Kapusta, M. Sikora, D. Zajac, P. C. Riedi, and C. Ritter, Phys. Rev. B **67** (2003) 134402.

[41] M. M. Savosta, V. I. Kamenev, V. A. Borodin, Nov, aacute, P. k, M. Maryscaronko, Hejtm, J. nek, ouml, K. rr, and M. Sahana, Phys. Rev. B **67** (2003) 094403.

[42] G. Papavassiliou, M. Fardis, M. Belesi, T. G. Maris, G. Kallias, M. Pissas, D. Niarchos, C. Dimitropoulos, and J. Dolinsek, Phys. Rev. Lett. **84** (2000) 761.

[43] G. Papavassiliou, M. Belesi, M. Fardis, and C. Dimitropoulos, Phys. Rev. Lett. **87** (2001) 177204.

[44] J. Kanamori, J. Phys. Chem. Solids **10** (1959) 87.

[45] J. F. Lawler, J. G. Lunney, and J. M. D. Coey, Appl. Phys. Lett. **65** (1994) 3017.

TH-1060_06612103

[46] M. Ohtaki, H. Koga, T. Tokunaga, K. Eguchi, and H. Arai, J. Solid State Chem. **120** (1995) 105.

[47] J. M. d. Teresa, M. Ibarra, P. A. Algarabel, C. Ritter, C. Marquina, J. Blasco, J. Garcia, A. d. Moral, and Z. Arnold, Nature **386** (1997) 256.

[48] T. T. M. Palstra, A. P. Ramirez, S. W. Cheong, B. Zegarski, P. Schiffer, and J. Zaanen, Phys. Rev. B **56** (1997) 5104.

[49] H. Roder, J. Zang, and A. R. Bishop, Phys. Rev. Lett. **76** (1996) 1356.

[50] J. Zang, A. R. Bishop, and H. Roder, Phys. Rev. B **53** (1996) R8840.

[51] P. G. Radaelli, M. Marezio, H. Y. Hwang, S. W. Cheong, and B. Batlogg, Phys. Rev. B **54** (1996) 8992.

[52] Z. Jirák, J. Hejtmánek, K. KnIzek, M. Marysko, E. Pollert, M. Dlouhá, S. Vratislav, R. Kuzel, and M. Hervieu, J. Magn. Magn. Mater. **250** (2002) 275.

[53] E. J. Vervey, Nature **144** (1939) 327.

[54] A. P. Ramirez, P. Schiffer, S.-W. Cheong, C. H. Chen, W. Bao, T. T. M. Palstra, P. L. Gammel, D. J. Bishop, and B. Zegarski, Phys. Rev. Lett. **76** (1996) 3188.

[55] C. H. Chen and S. W. Cheong, Phys. Rev. Lett. **76** (1996) 4042.

[56] Z. Jirák, S. Krupička, Z. Šimša, M. Dlouhá, and S. Vratislav, J. Magn. Magn. Mater. **53** (1985) 153.

[57] K. Knizek, Z. Jirák, E. Pollert, F. Zounová, and S. Vratislav, J. Solid State Chem. **100** (1992) 292.

[58] H. Kawano, R. Kajimoto, H. Yoshizawa, Y. Tomioka, H. Kuwahara, and Y. Tokura, Phys. Rev. Lett. **78** (1997) 4253.

[59] H. Kuwahara, Y. Tomioka, A. Asamitsu, Y. Moritomo, and Y. Tokura, Science **270** (1995) 961.

[60] Y. Tomioka, A. Asamitsu, Y. Moritomo, H. Kuwahara, and Y. Tokura, Phys. Rev. Lett. **74** (1995) 5108.

[61] G. Xiao, E. J. McNiff, Jr., G. Q. Gong, A. Gupta, C. L. Canedy, and J. Z. Sun, Phys. Rev. B **54** (1996) 6073.

[62] Q. Huang, J. W. Lynn, R. W. Erwin, A. Santoro, D. C. Dender, V. N. Smolyaninova, K. Ghosh, and R. L. Greene, Phys. Rev. B **61** (2000) 8895.

[63] Y. Moritomo, H. Kiwahara, Y. Tomioka, and Y. Tokura, Phys. Rev. B **55** (1997) 7549.

[64] V. Kiryukhin, D. Casa, J. P. Hill, B. Keimer, A. Vigliante, Y. Tomioka, and Y. Tokura, Nature **386** (1997) 813.

TH-1060_06612103

[65] S. Parashar, E. E. Ebenso, A. R. Raju, and C. N. R. Rao, Solid State Commun. **114** (2000) 295.

[66] K. Miyano, T. Tanaka, Y. Tomioka, and Y. Tokura, Phys. Rev. Lett. **78** (1997) 4257.

[67] Y. Tokura, H. Kuwahara, Y. Moritomo, Y. Tomioka, and A. Asamitsu, Phys. Rev. Lett. **76** (1996) 3184.

[68] C. N. R. Rao, A. Arulraj, A. K. Cheetham, and B. Raveau, J. Phys.: Condens. Matter **12** (2000) R83.

[69] Y. Okimoto, Y. Tomioka, Y. Onose, Y. Otsuka, and Y.Tokura, Phys. Rev. B **57** (1998) R9377.

[70] M. Tokunaga, N. Miura, Y. Tomioka, and Y. Tokura, Phys. Rev. B **57** (1998) 5259.

[71] H. T. Diep, Frustrated Spin System, Chapter1, World Scientific (2004)

[72] K. Binder and A. P. Young, Rev. Mod. Phys. **58** (1986) 801.

[73] C. Y. Huang, J. Magn. Magn. Mater. **51** (1985) 1.

[74] J. A. Mydosh, Spin glasses: an experimental introduction, Taylor & Francis Pub., London (1993)

[75] M. J. P. Gingras, Magnetic system with competing interaction, p. 238, ed. H. T. Diep, World Scientific pub. Singapore (1994)

[76] J. L. Tholence, Solid State Commun. **35** (1980) 113.

[77] S. Nagata, P. H. Keesom, and H. R. Harrison, Phys. Rev. B **19** (1979) 1633.

[78] C. A. M. Mulder, A. J. v. Duyneveldt, and J. A. Mydosh, Phys. Rev. B **23** (1981) 1384.

[79] S. Strickman and E. P. Wohlforth, Phys. Lett. **85A** (1981) 467.

[80] F. Mezei, J. Appl. Phys. **53** (1982) 7654.

[81] P. C. Hohenberg and B. I. Halperin, Rev. Mod. Phys. **49** (1977) 435.

[82] K. Gunnarsson, P. Svedlindh, P. Nordblad, L. Lundgren, H. Aruga, and A. Ito, Phys. Rev. B **43** (1991) 8199.

[83] J. Chalupa, Solid State Commun. **24** (1977) 429.

[84] M. Suzuki, Prog. Theor. Phys. **58** (1977) 1151.

[85] L. P. Levy, Phys. Rev. B **38** (1988) 4963.

[86] B. Ozcelik, K. Kiymac, J. C. Verstelle, A. J. v. Duyneveldt, and J. A. Mydosh, J. Phys.: Condens. Matter **4** (1992) 5801.

[87] A. Gencer, I. Ercan, and B. Özçelik, J. Phys.: Condens. Matter **10** (1998) 191.

[88] E. Vincent, J. P. Bouchaud, D. S. Dean, and J. Hammann, Phys. Rev. B **52** (1995) 1050.

TH-1060_06612103

[89] Y. G. Joh, R. Orbach, G. G. Wood, J. Hammann, and E. Vincent, Phys. Rev. Lett. **82** (1999) 438.

[90] D. Chu, G. G. Kenning, and R. Orbach, Philos. Mag. B **1** (1995) 479.

[91] G. G. Kenning, Y. G. Joh, D. Chu, and R. Orbach, Phys. Rev. B **52** (1995) 3479.

[92] F. Bert, V. Dupuis, E. Vincent, J. Hammann, and J.-P. Bouchaud, Phys. Rev. Lett. **92** (2004) 167203.

[93] H. Maletta and P. Convert, Phys. Rev. Lett. **42** (1979) 108.

[94] A. Chakravarti, R. Ranganathan, A. K. Raychaudhury, J. T. T. Kumaran, and C. Bansal, Solid State Commun. **77** (1991) 17.

[95] R. V. Helmolt, L. Haupt, K. Bärner, and U. Sondermann, Solid State Commun. **82** (1992) 693.

[96] C. Martin, A. Maignan, and B. Raveau, J. Material Chem. **6** (1996) 1245.

[97] A. Bajpai and A. Banerjee, J. Phys.: Condens. Matter **13** (2001) 637.

[98] J. Dho, W. S. Kim, and N. H. Hur, Phy. Rev. Lett. **89** (2002) 027202.

[99] S. K. Hasanain, W. H. Shah, A. Mumtaz, M. Nadeem, and M. J. Akhtar, J. Magn. Magn. Mater. **271** (2004) 79.

[100] P. Chaddah, K. Kumar, and A. Banerjee, Phys. Rev. B **77** (2008) R100402.

[101] R. Mathieu, A. Asamistu, Y. Kaneko, J. P. He, and Y. Tokura, Phys. Rev. B **72** (2005) 014436.

[102] S. Nair and A. K. Nigam, Phys. Rev. B **75** (2007) 214415.

[103] J. W. Cai, C. Wang, B. G. Shen, J. G. Zhao, and W. S. Zhan, Appl. Phys. Lett. **71** (1997) 1727.

[104] A. Chakravarti, R. Ranganathan, and S. Chatterjee, J. Magn. Magn. Mater. **138** (1994) 329.

[105] S. Mukherjee, R. Ranganathan, and S. B.Roy, Phys. Rev. B **50** (1994) 1084.

[106] L. D. Landau, Phys. Z. Sowjetunion **11** (1937) 26.

[107] A. Arrott, Phys. Rev. **108** (1957) 1394.

[108] S. K. Banerjee, Phys. Lett. **12** (1964) 16.

[109] H. E. Stanley, Introduction to Phase Transitions and Critical Phenomena, Oxford University Press, London (1971)

[110] A. Arrott and J. E. Noakes, Phys. Rev. Lett. **19** (1967) 786.

[111] R. V. Chamberlin, Nature **408** (2000) 337.

[112] B. Widom, J.Chem. Phys. **43** (1965) 3898.

TH-1060_06612103

[113] M. S. Green, M. Vicentini-Missoni, and J. M. H. L. Sengers, Phys. Rev. Lett. **18** (1967) 1113.

[114] P. Weiss and R. Forrer, Ann. Phys. (Paris) **5** (1926) 153.

[115] W. Archibald, J. S. Zhou, and J. B. Goodenough, Phys. Rev. B **53** (1996) 14445.

[116] H. S. Shin, J. E. Lee, Y. S. Nam, H. L. Ju, and C. W. Park, Solid State Commun. **118** (2001) 377.

[117] C. S. Hong, W. S. Kim, and N. H. Hur, Phys. Rev. B **63** (2001) 092504.

[118] S. E. Lofland, V. Ray, P. H. Kim, S. M. Bhagat, M. A. Manheimer, and S. D. Tyagi, Phys. Rev. B **55** (1997) 2749.

[119] K. Ghosh, C. J. Lobb, R. L. Greene, S. G. Karabashev, D. A. Shulyatev, A. A. Arsenov, and Y. Mukovskii, Phys. Rev. Lett. **81** (1998) 4740.

[120] C. V. Mohan, M. Seeger, H. Kronmüller, P. Murugaraj, and J. Maier, J. Magn. Magn. Mater. **183** (1998) 348.

[121] D. Kim, B. L. Zink, F. Hellman, and J. M. D. Coey, Phys. Rev. B **65** (2002) 214424.

[122] S. Nair, A. Banerjee, and A. V. Narlikar, Phys. Rev. B **68** (2003) 132404.

[123] W. Li, H. P. Kunkel, X. Z. Zhou, G. Williams, Y. Mukovskii, and D. Shulvatev, Phys.Rev. B **70** (2004) 214413.

[124] Y. Motome and N. Furukawa, Phys. Rev. B **68** (2003) 144432.

[125] A. Schwartz, M. Scheffler, and S. M. Anlage, Phys. Rev. B **61** (2000) R870.

[126] M. Kar, A. Perumal, and S. Ravi, Physica Status Solidi B **243** (2006) 1908.

[127] A. Olega, A. Salazar, D. Prabhakaran, and A. T. Boothroyd, Phys. Rev. B **70** (2004) 184402.

[128] R. Venkatesh, R. Nirmala, G. Rangarajan, S. K. Malik, and V. Sankaranarayanan, J. App. Phys. **99** (2006) 08Q311.

[129] J. M. D. Coey, M. Viret, L. Ranno, and K. Ounadjela, Phys. Rev. Lett. **75** (1995) 3910.

[130] M. Ziese and C. Srinitiwarawong, Phys. Rev. B **58** (1998) 11519.

[131] G. Jakob, W. Westerburg, F. Martin, and H. Adrian, Phys. Rev. B **58** (1998) 14966.

[132] N. F. Mott, Conduction in non-crystalline materials (2nd ed.) Oxford: Oxford University Press (1993)

[133] N. F. Mott, "Metal – Insulator Transitions" 2nd edition (London, Taylor & Francis) (1990)

[134] W. Thomson, Proc. Roy. Soc. London **8** (1857) 546.

[135] A. B. Pippard, Magnetoresistance (Cambridge:CambridgeUniversityPress) (1984)

TH-1060_06612103

[136] A. B. Pippard, Magnetoresistance in Metals (Cambridge:CambridgeUniversityPress) (1989)

[137] N. Ashcroft and B. Mermin, Solid State Physics (NewYork:HoltRinehartandWinston) (1976)

[138] S. Jin, T. H. Tiefel, M. McCormack, R. A. Fastnacht, R. Ramesh, and L. H. Chen, Science **264** (1994) 413.

[139] W. Prellier, P. Lecoeur, and B. Mercey, J. Phys.: Condens. Matter **13** (2001) R915.

[140] J. S. Moodera, J. Nowak, and R. J. M. van de Veerdonk, Phys. Rev. Lett. **80** (1998) 2941.

[141] T. Miyazaki and N. Tezuka, J. Magn. Magn. Mater. **139** (1995) L231.

[142] E. Y. Tsymbal, O. N. Mryasov, and P. R. LeClair, J. Phys. : Condens. Matter **15** (2003) R109.

[143] M. Jaime, M. B. Salamon, M. Rubinstein, R. E. Treece, J. S. Horwitz, and D. B. Chrisey, Phys. Rev. B **54** (1996) 11914.

[144] P. Schiffer, A. P. Ramirez, W. Bao, and S.-W. Cheong, Phys. Rev. Lett. **75** (1995) 3336.

[145] M. Jaime, P. Lin, M. B. Salamon, and P. D. Han, Phys. Rev. B **58** (1998) R5901.

[146] S. Angappane, K. Sethupathi, and G. Rangarajan, Pramana- J. of Phys. **58** (2002) 1079.

[147] I. Mannari, Prog. of Theo. Phys. **22** (1959) 335.

[148] X. Wang and X. G. Zhang, Phys. Rev. Lett. **82** (1999) 4276.

[149] N. Furukawa, J. Phys. Soc. Japan **69** (1954) 2000.

[150] H. Y. Hwang, S. W. Cheong, N. P. Ong, and B. Batlogg, Phys. Rev. Lett. **77** (1996) 2041.

[151] G. J. Snyder, R. Hiskes, S. DiCarolis, M. R. Beasley, and T. H. Geballe, Phys. Rev. B **53** (1996) 14434.

[152] K. Kubo and N. Ohata, J. Phys. Soc. Japan **33** (1972) 21.

[153] V. Ravindranath, M. S. R. Rao, G. Rangarajan, Y. Lu, J. Klein, R. Klingeler, S. Uhlenbruck, B. Buchner, and R. Gross, Phys. Rev. B **63** (2001) 184434.

[154] M. Jaime, H. T. Hardner, M. B. Salamon, M. Rubinstein, P. Dorsey, and D. Emin, Phys. Rev. Lett. **78** (1997) 951.

[155] A. L. Efros and B. I. Shklovskii, J. Physics C **8** (1975) L 49.

[156] G. Q. Gong, C. Canedy, G. Xiao, J. Z. Sun, A. Gupta, and W. J. Gallagher, Appl. Phys. Lett. **67** (1995) 1783.

TH-1060_06612103

[157] G. Q. Gong, A. Gupta, G. Xiao, P. Lecoeur, and T. R. McGuire, Phys. Rev. B **54** (1996) R3742.

[158] G. H. Rao, J. R. Sun, Y. Z. Sun, Y. L. Zhang, and J. K. Liang, J. Phys.: Condens. Matter **8** (1996) 5393.

[159] R. Mahesh, R. Mahendiran, A. K. Raychaudhuri, and C. N. R. Rao, Appl. Phys. Lett. **68** (1996) 2291.

[160] A. Urushibara, Y. Moritomo, T. Arima, A. Asamitsu, G. Kido, and Y. Tokura, Phys. Rev. B **51** (1995) 14103.

[161] H. L. Ju, J. Gopalakrishnan, J. L. Peng, Q. Li, G. C. Xiong, T. Venkatesan, and R. L. Greene, Phys. Rev. B **51** (1995) 6143.

[162] H. L. Ju and H. Sohn, Solid State Commun. **102** (1997) 463.

[163] S. S. Manoharan, N. Y. Vasanthacharya, M. S. Hegde, K. M. Satyalakshmi, V. Prasad, and S. V. Subramanyam, J. Appl. Phys. **76** (1994) 3923.

[164] R. Mahendiran, R. Mahesh, A. K. Raychaudhuri, and C. N. R. Rao, J. Phys. D: Appl. Phys. **28** (1995) 1743.

[165] G. Ji, X. J. Fan, J. H. Zhang, C. S. Xiong, and X.-G. Li, J. Phys. D: Appl. Phys. **31** (1998) 3036.

[166] Y. X. Jia, L. Lu, K. Khazeni, V. H. Crespi, A. Zettl, and M. L. Cohen, Phys. Rev. B **52** (1995) 9147.

[167] K. Dorr, K. H. Müller, E. S. Vlakhov, R. A. Chakalov, R. I. Chakalova, K. A. Nenkov, A. Handstein, B. Holzapfel, and L. Schultz, J. Appl. Phys. **83** (1998) 7089.

[168] A. Banerjee, S. Pal, E. Rozenberg, and B. K. Chaudhuri, J. Phys: Condens. Matter **13** (2001) 9489.

[169] G. Narsinga Rao, S. Roy, R. C. Yang, and J. W. Chen, J. Magn. Magn. Mater. **260** (2003) 375.

[170] T. Diehl, P. Chaudouët, J. C. Joubert, and J. Pierre, J. App. Phys. **81** (1997) 4970.

[171] X. L. Wang, S. J. Kennedy, P. Gehringer, W. Lang, H. K. Liu, and S. X. Dou, J. Appl. Phys. **83** (1998) 7177.

[172] C. Boudaya, L. Laroussi, E. Dhahri, J. C. Joubert, and A. Cheikh-Rouhou, J. Phys.: Condens. Matter **10** (1998) 7485.

[173] L. Pi, M. Hervieu, A. Maignan, C. Martin, and B. Raveau, Solid State Commun. **126** (2003) 229.

[174] M. Kar and S. Ravi, Mater. Sci. & Eng. B **107** (2004) 332.

[175] M. Kar and S. Ravi, Mod. Phys. Lett. B **19** (2005) 317.

TH-1060_06612103

[176] M. A. Gilleo, Acta Crystallogr **10** (1957) 161.

[177] A. Muñoz, J. A. Alonso, M. J. M. Lope, J. L. G. Muñoz, and M. T. Fernández-Díaz, J. Phys.: Condens. Matter **12** (2000) 1361.

[178] S. Y. Wu, C. M. Kuo, H. Y. Wang, W.-H. Li, K. C. Lee, J. W. Lynn, and R. S. Liu, J. Appl. Phys. **87** (2000) 5822.

[179] T. Chatterji, B. Ouladdiaf, and D. Bhattacharaya, J. Phys. : Condens. Matter **21** (2009) 306001.

[180] F. Bartolomé, J. Bartolomé, and J. Campo, Physica B **312** (2002) 769.

[181] F. Bartolome, J. Herrero-Albillos, L. M. Garcia, J. Bartolome, N. Jaouen, and A. Rogalev, J. Appl. Phys. **97** (2005) 10A503.

[182] I. O. Troyanchuk, V. A. Khomchenko, G. M. Chobot, A. I. Kurbakov, A. N. Vasil'ev, V. V. Eremenko, V. A. Sirenko, M. Y. Shvedun, H. Szymczak, and R. Szymczak, J. Phys. : Condens. Matter **15** (2003) 8865.

[183] T. Kimura, S. Ishihara, H. Shintani, T. Arima, K. T. Takahashi, K. Ishizaka, and Y. Tokura, Phys. Rev. B **68** (2003) 060403R.

[184] S. Landsgesell, A. Maljuk, T. C. Hansen, O. Prokhnenko, N. Aliouane, and D. N. Argyriou, Phys. Rev. B **80** (2009) 014412.

[185] V. Dyakonov, F. N. Bukhanko, V. I. Kamenev, E. E. Zubov, M. Arciszewska, W. Dobrowolski, V. Mikhaylov, R. Puzacuteniak, A. Wisacuteniewski, K. Piotrowski, V. Varyukhin, H. Szymczak, A. Szytulstroka, R. Duraj, St, uuml, N. sser, A. Arulraj, S. Baran, B. Penc, and T. Jaworska-Golstrokaogonb, Phys. Rev. B **77** (2008) 214428.

[186] I. O. Troyanchuk, D. A. Efimov, N. V. Samsonenko, E. F. Shapovalova, and H. Szymczak, J. Phys.: Condens. Matter **10** (1998) 7957.

[187] K. Liu, X. W. Wu, K. H. Ahn, T. Sulchek, C. L. Chien, and J. Q. Xiao, Phys. Rev. B **54** (1996) 3007.

[188] F. Millange, S. d. Brion, and G. Chouteau, Phys. Rev. B **62** (2000) 5619.

[189] J. P. Joshi, A. R. Bhagwat, S. Sarangi, A. Sharma, and S. V. Bhat, Physica B **349** (2004) 35.

[190] G. Cao, J. Zhang, S. Wang, J. Yu, Y. Xu, S. Cao, C. Jing, and X. Shen, J. Magn. Magn. Mater. **310** (2000) 777.

[191] V. A. Khomchenko, I. O. Troyanchuk, A. I. Kurbakov, H. Gamari-Seale, V. V. Eremenko, H. Szymczak, and R. Szymczak, J. Magn. Magn. Mater. **288** (2005) 224.

[192] T. Nagai, T. Kimura, A. Yamazaki, Y. Tomioka, K. Kimoto, Y. Tokura, and Y. Matsui, Phys. Rev. B **68** (2003) 092405.

TH-1060_06612103

[193] S. S. Rao, S. Tripathi, D. Pandey, and S. V. Bhat, Phys. Rev. B **74** (2006) 144416.

[194] V. Caignaert, A. Maignan, and B. Raveau, Solid State Commun. **95** (1995) 357.

[195] A. Poddar, P. Muruguraj, R. Fischer, E. Gmelin, K. Bärner, L. Haupt, P. Mandal, and G. H. Rao, Physica B: Condensed Matter **254** (1998) 21.

[196] M. Pattabiraman, G. Rangarajan, and P. Murugaraj, Solid State Commun. **132** (2004) 7.

[197] T. L. Phan, N. V. Khiem, N. X. Phuc, and S. C. Yu, J. Magn. Magn. Mater. **304** (2006) e334.

[198] S. Kundu and T. K. Nath, J. Magn. Magn. Mater. **322** (2010) 2408.

[199] K. Khazeni, Y. X. Jia, L. Lu, V. H. Crespi, M. L. Cohen, and A. Zettl, Phys. Rev. Lett. **76** (1996) 295.

[200] V. Caignaert, F. Millange, M. Hervieu, E. Suard, and B. Raveau, Solid State Commun. **99** (1996) 173.

[201] C. Ritter, R. Mahendiran, M. R. Ibarra, L. Morellon, A. Maignan, B. Raveau, and C. N. R. Rao, Phys. Rev. B **61** (2000) R9229.

[202] C. M. Srivastava, R. K. Dwivedi, S. Asthana, A. K. Nigam, and D. Bahadur, J. Magn. Magn. Mater. **284** (2004) 239.

[203] Z. Q. Li, H. Liu, Y. H. Cheng, W. B. Mi, A. Yu, H. L. Bai, and E. Y. Jiang, Physica B **353** (2004) 324.

[204] S. Angappane, M. Pattabiraman, G. Rangarajan, K. Sethupathi, and V. S. Sastry, Phys. Rev. B **69** (2004) 094437.

[205] J. H. Jung, H. J. Lee, T. W. Noh, E. J. Choi, Y. Moritomo, Y. J. Wang, and X. Wei, Phys. Rev. B **62** (2000) 481.

[206] H. Yoshizawa, H. Kawano, J. A. Fernandez-Baca, H. Kuwahara, and Y. Tokura, Phys. Rev. B **58** (1998) R571.

[207] H. Kuwahara, T. Okuda, Y. Tomioka, A. Asamitsu, and Y. Tokura, Phys. Rev. Lett. **82** (1999) 4316.

[208] T. Hayashi, N. Miura, K. Noda, H. Kuwahara, S. Okamoto, S. Ishihara, and S. Maekawa, Phys. Rev. B **65** (2001) 024408.

[209] Y. Moritomo, T. Akimoto, A. Nakamura, K. Ohoyama, and M. Ohashi, Phys. Rev. B **58** (1998) 5544.

[210] R. Kajimoto, H. Yoshizawa, H. Kawano, H. Kuwahara, Y. Tokura, K. Ohoyama, and M. Ohashi, Phys. Rev. B **60** (1999) 9506.

TH-1060_06612103

[211] U. Staub, M. García-Fernández, Y. Bodenthin, V. Scagnoli, R. A. De Souza, M. Garganourakis, E. Pomjakushina, and K. Conder, Phys. Rev. B **79** (2009) 224419.

[212] T. Kimura, K. Hatsuda, Y. Ueno, R. Kajimoto, H. Mochizuki, H. Yoshizawa, T. Nagai, Y. Matsui, A. Yamazaki, and Y. Tokura, Phys. Rev. B **65** (2001) 020407.

[213] T. Nagai, T. Kimura, T. Asaka, K. Kimoto, M. Takeguchi, and Y. Matsui, Phys. Rev. B **81** (2010) 060407.

[214] A. Biswas and I. Das, J. App. Phys. **102** (2007) 064303.

[215] L. Sudheendra, H. D. Chinh, A. R. Raju, A. K. Raychaudhuri, and C. N. R. Rao, Solid State Commun. **122** (2002) 53.

[216] I. O. Troyanchuk, I. M. Kolesova, H. Szymczak, and A. Nabialek, J. Magn. Magn. Mater. **176** (1997) 267.

[217] I. O. Troyanchuk, D. D. Khalyavin, S. V. Trukhanov, and H. Szymczak, J. Phys.: Condens. Matter **11** (1999) 8707.

[218] I. O. Troyanchuk, S. V. Trukhanov, D. D. Khalyavin, and H. Szymczak, J. Magn. Magn. Mater. **208** (2000) 217.

[219] V. A. Ryzhov, A. V. Lazuta, V. P. Khavronin, I. I. Larionov, I. O. Troaynchuk, and D. D. Khalyavin, Solid State Commun. **130** (2004) 803.

[220] A. V. Lazuta, V. A. Ryzhov, O. P. Smirnov, I. A. Kiselev, Y. P. Chernenkov, S. A. Borisov, I. O. Troaynchuk, and D. D. Khalyavin, J. Magn. Magn. Mater. **300** (2006) 44.

[221] G. Venkataiah and P. Venugopal Reddy, Solid State Commun. **136** (2005) 114.

[222] B. X. Gu, S. Y. Zhang, H. C. Zhang, and B. G. Shen, J. Magn. Magn. Mater. **204** (1999) 45.

[223] S. L. Young, Y. C. Chen, L. Horng, T. C. Wu, C. C. Chang, H. Z. Chen, and J. B. Shi, J. Magn. Magn. Mater. **239** (2002) 11.

[224] H. Jain, A. K. Raychaudhuri, N. Ghosh, and H. L. Bhat, Phys. Rev. B **76** (2007) 104408.

[225] N. Ghosh, S. Elizabeth, H. L. Bhat, G. N. Subanna, and M. Sahana, J. Magn. Magn. Mater. **256** (2003) 286.

[226] X. J. Liu, E. Y. Jiang, Z. Q. Li, B. L. Li, W. R. Li, A. Yu, and H. L. Bai, Physica B **348** (2004) 146.

[227] Z. Q. Li, H. Liu, X. J. Liu, X. D. Liu, H. L. Bai, C. Q. Sun, and E. Y. Jiang, J. Magn. Magn. Mater. **284** (2004) 133.

[228] T. Tang, C. Tien, and B. Y. Hou, J. of Alloys & Comp. **461** (2008) 42.

TH-1060_06612103

[229] Z. Q. Li, H. Liu, X. D. Liu, P. Wu, H. L. Bai, C. Q. Sun, and E. Y. Jiang, Physica B: Condensed Matter **351** (2004) 114.

[230] Z. Q. Li, X. H. Zhang, J. S. Yu, X. J. Liu, X. D. Liu, H. Liu, P. Wu, H. L. Bai, C. Q. Sun, J. J. Lin, and E. Y. Jiang, Physics Letters A **325** (2004) 430.

[231] S. K. Srivastava and S. Ravi, J. Phys.: Condens. Matter **20** (2008) 505212.

[232] T. Tang, C. Tien, and B. Y. Hou, Physica B: Condensed Matter **403** (2008) 2111.

[233] S. Zhang, S. Tan, W. Tong, and Y. Zhang, Phys.Rev. B **72** (2005) 014453.

[234] T. Yanagida, H. Tanaka, T. Kawai, E. Ikenaga, M. Kobata, J.-J. Kim, and K. Kobayashi, Phys. Rev. B **73** (2006) 132503.

[235] R. A. Young, "The Rietveld Method" International Union of Crystallography (New York, Oxford University Press) (1996)

[236] A. Taylor, X – ray Metallography (Wiley, New York,) (1961)

[237] O. Halpern and M. H. Johnson, Phys. Rev. **55** (1939) 898.

[238] S. K. Paranjpe and Y. D. Dande, Pramana- J. of Phys. **32** (1989) 793.

[239] G. L. Miller and J. Fischer, Nucl. Instrum. Methods **91** (1971) 389.

[240] G. H. Jeffery, J. Bassette, J. Mendham, and R. C. Denney, Vogal's Textbook of quantitative Chemical Analysis, 5th ed., Addison Wesley Longman Limited (1989)

[241] Z. Zeng, M. Greenblatt, and M. Croft, Phys. Rev. B **59** (1999) 8784.

[242] M. Ishizuka and Y. Tohi, Jpn. J. Appl. Phys. **19** (1980) 639.

[243] J. R. Owers-Bradley, W.-S. Zhou, and W. P. Halperin, Rev. Sci. Instr. **52** (1981) 1106.

[244] A. J. van Duyneveldt, J. App. Phys. **53** (1982) 8006.

[245] M. Ocio and J. Hammann, Rev. Sci. Instr. **56** (1985) 1367.

[246] A. F. Deutz, R. Hulstman, and F. J. Kranenburg, Rev. Sci. Instr. **60** (1989) 113.

[247] M. Couach and A. F. Khoder, Presented at the office of Navel Research Workshop on "Magnetic Susceptibility of Superconductor and Other Spin Systems", Berkeley, Springs, West Virgina (1991)

[248] R. B. Goldfarb, M. Lelental, and C. A. Thompson, Magnetic Susceptibility of superconductors and Other Spin Systems, ed. R. A. Hein, Plenum Press, New York, (1991), Page-49

[249] R. B. Goldfarb and J. V. Minervini, Rev. Sci. Instr. **55** (1984) 761.

[250] L. Sagnotti, P. Rochette, M. Jackson, F. Vadeboin, J. Dinarès-Turell, and A. Winkler, Physics of the Earth and Planetary Interiors **138** (2003) 25.

[251] S. Foner, Rev. Sci. Instr. **30** (1959) 548.

TH-1060_06612103

[252] S. Das and T. K. Dey, Solid State Commun. **134** (2005) 837.

[253] W. Zhong, W. Chen, W. P. Ding, N. Zhang, A. Hu, Y. W. Du, and Q. J. Yan, J. Magn. Magn. Mater. **195** (1999) 112.

[254] S. Das and T. K. Dey, J. of Alloy. & Comp. **440** (2007) 30.

[255] G. Huo, Z. Gu, S. Liu, Ye-Wang, and Y. Wang, J. of Alloy. & Comp. **433** (2007) 41.

[256] S. K. Srivastava, M. Kar, and S. Ravi, J. Phys.:Condens. Matter **20** (2008) 235201.

[257] T. Sudyoadsuk, R. Suryanarayanan, and P. Winotai, Solid State Commun. **131** (2004) 681.

[258] M. Viswanathan and P. S. A. Kumar, Phys. Rev. B **80** (2009) 012410.

[259] S. K. Srivastava, M. Kar, and S. Ravi, J. Magn. Magn. Mater. **307** (2006) 318.

[260] R. S. Freitas, L. Ghivelder, F. Damay, F. Dias, and L. F. Cohen, Phys. Rev. B **64** (2001) 144404.

[261] K. Huang, Statistical Mechanics (Wiley, New York), 2nd ed., Chap. 17.6, see and pp. 438 pp. 432 (1987)

[262] M. Sahana, U. K. Rössler, N. Ghosh, S. Elizabeth, H. L. Bhat, K. Dörr, D. Eckert, M. Wolf, and K. H. Müller, Phys. Rev. B **68** (2003) 144408.

[263] R. Venkatesh, M. Pattabiraman, S. Angappane, G. Rangarajan, K. Sethupathi, J. Karatha, M. Fecioru-Morariu, R. M. Ghadimi, and G. Guntherodt, Phys. Rev. **75** (2007) 224415.

[264] R. Venkatesh, M. Pattabiraman, K. Sethupathi, G. Rangarajan, S. Angappane, and J.-G. Park, J. Appl. Phys. **103** (2008) 07B319.

[265] B. Samantaray and S. Ravi, J. Magn. Magn. Mater. **321** (2009) 3671.

[266] X. X. Zhang, J. Tejada, Y. Xin, G. F. Sun, K. W. Wong, and X. Bohigas, Appl. Phys. Lett. **69** (1996) 3596.

[267] M. Viret, L. Ranno, and J. M. D. Coey, Phys. Rev. B **55** (1997) 8067.

[268] X. H. Zhang, Z. Q. Li, W. Song, X. W. Du, P. Wu, H. L. Bai, and H. Y. Jiang, Solid State Commun. **135** (2005) 356.

[269] Z. W. Ouyang, H. Nojiri, and S. Yoshii, Phys. Rev. B **78** (2008) 104404.

[270] D. Kim, B. Revaz, B. L. Zink, F. Hellman, J. J. Rhyne, and J. F. Mitchell, Phys. Rev. Lett. **89** (2002) 227202.

[271] I. Dhiman, A. Das, P. K. Mishra, and L. Panicker, Phys. Rev. B **77** (2008) 094440.

[272] A. Moreo, M. Mayr, A. Feiguin, S. Yunoki, and E. Dagotto, Phys. Rev. Lett. **84** (2000) 5568.

[273] S. Quezel-Ambrunaz, Bull. Soc. Fr. Mineral. Cristallogr. **91** (1968) 339.

TH-1060_06612103

[274] A. Kirste, M. Goiran, M. Respaud, J. Vanaken, J. M. Broto, H. Rakoto, M. v. Ortenberg, C. Frontera, and J. L. García-Muñoz, Phys. Rev. B **67** (2003) 134413.

[275] D. E. Cox, P. G. Radaelli, M. Marezio, and S. W. Cheong, Phys.Rev. B **57** (1998) 3305.

[276] J. L. Garcia-Munoz, C. Frontera, M. Respaud, M. Giot, C. Ritter, and X. G. Capdevila, Phys. Rev. B **72** (2005) 054432.

[277] Z. Q. Li, X. H. Zhang, W. R. Li, W. Song, J. Liu, P. Wu, H. L. Bai, and E. Y. Jiang, Physica B **371** (2006) 177.

[278] R. S. Freitas, L. Ghivelder, P. Levy, and F. Parisi, Phys. Rev. B **65** (2002) 104403.

[279] T. Zhang, T. F. Zhou, T. Qian, and X. G. Li, Phys. Rev. B **76** (2007) 174415.

[280] T. Sarkar, B. Ghosh, A. K.Raychaudhuri, and T. Chatterji, Phys. Rev. B **77** (2008) 235112.

[281] Z. Jirák, E. Hadová, O. Kaman, K. Knížek, M. Maryško, E. Pollert, M. Dlouhá, and S. Vratislav, Phys. Rev. B **81** (2010) 024403.

[282] T. Sarkar, P. K. Mukhopadhyay, A. K. Raychaudhuri, and S. Banerjee, J. Appl. Phys. **101** (2007) 124307.

[283] T. Zhang and M. Dressel, Phys. Rev. B. **80** (2009) 014435.

[284] P. Chai, X. Wang, S. Hu, X. Liu, Y. Liu, M. Lv, G. Li, and J. Meng, J. Phys. Chem. C **113** (2009) 15817.

[285] L. Liu, S. L. Yuan, Z. M. Tian, X. Liu, J. H. He, P. Li, C. H. wang, X. F. Zheng, and S. Y. Yin, J. Phys. D:Appl. Phys. **42** (2009) 045003.

[286] B. Samantaray and S. Ravi, J. Supercond. Nov. Magn. **DOI** 10.1007/s10948-010-1023-2

[287] R. N. Bhowmik, R. Nagarajan, and R. Ranganathan, Phys. Rev. B **69** (2004) 054430.

[288] I. G. Daec, S. V. Diaz, B. G. Kim, S.-W. Cheong, and P. Schiffer, Phys. Rev. B **65** (2002) 174426.

[289] B. Samantaray and S. Ravi, J. Magn. Magn. Mater. **322** (2010) 2038.

[290] D. S. Rana, D. G. Kuberkar, and S. K. Malik, Phys. Rev. B **73** (2006) 064407.

[291] C. L. Lu, S. Dong, K. F. Wang, F. Gao, P. L. Li, L. Y. Lv, and J.-M. Liu, Appl. Phys. Lett. **91** (2007) 032502.

[292] M. H. Zhu, Y. G. Zhao, W. Cai, X. S. Wu, S. N. Gao, K. Wang, L. B. Luo, H. S. Huang, and L. Lu, Phys. Rev. B **75** (2007) 134424.

[293] Y. Tomioka, A. Asamitsu, H. Kuwahara, Y. Moritomo, and Y. Tokura, Phys. Rev. B **53** (1996) R1689.

TH-1060_06612103

Publications in International Journals

From Thesis Work

1. Particle size effects on the suppression of charge-ordering in $Nd_{0.8}Na_{0.2}MnO_3$.

   B. Samantaray, S. K. Srivastava, and S. Ravi *Journal of Applied Physics* **111** (2012) 013919.

2. Magnetic structure and properties of $Nd_{1-x}Na_xMnO_3$ compounds.

   B. Samantaray, S. Ravi, A. Das, and S. K. Srivastava, *Journal of Applied Physics* **110**, (2011) 093906.

3. Magnetic dynamics of charge ordered $Nd_{0.80}Na_{0.20}MnO_3$ compound.

   B. Samantaray, S. K. Srivastava, and S. Ravi, *Journal of Magnetism and Magnetic Materials* **323** (2011) 2622.

4. Neutron powder diffraction studies and magnetic properties in $Nd_{1-x}K_xMnO_3$ (x=0.15 and 0.20) compounds.

   B. Samantaray, S. Ravi, A. Perumal, I. Dhiman, and A. Das, *Journal of Applied Physics* **109** (2011) 07E150.

5. Ferromagnetic and charge ordered phases in (Nd, Na)-Mn-O compounds.

   B. Samantaray, and S. Ravi, *Journal of Superconductivity and Novel Magnetism* **24** (2011) 809.

6. Critical behavior studies in ferromagnetic (Nd, K)-Mn-O compounds.

   B. Samantaray, S. Ravi, and A. Perumal, *Journal of Magnetism and Magnetic Materials* **322** (2010) 3391.

7. Reentrant spin glass behavior in $Nd_{0.84}K_{0.12}MnO_3$.

   B. Samantaray, and S. Ravi, *Journal of Magnetism and Magnetic Materials* **322** (2010) 2038.

8. Magnetic properties of $Nd_{1-x}K_xMnO_3$(x = 0.10-0.20) compounds.

   B. Samantaray, and S. Ravi, *Journal of Magnetism and Magnetic Materials* **321** (2009) 3671.

Other Related Work

9. Neutron powder diffraction study in $La_{0.85}Ag_{0.15}MnO_3$.

   B. Samantaray, S. K. Srivastava, S. Ravi, I. Dhiman, and A. Das, *Journal of Superconductivity and Novel Magnetism* **24** (2011) 1933.

TH-1060_06612103

10. Neutron powder diffraction study and magnetic properties in $LaMn_{1-x}Cu_xO_3$ (x=0.05, 0.10 and 0.15).

B. Samantaray, S. K. Srivastava, S. Mohanty, S. Ravi, I. Dhiman, and A. Das, *Journal of Applied Physics* **107** (2010) 09D719.

11. Ferromagnetism and bound magnetic Polaron behavior in $(In_{1-x}Co_x)_2O_3$.

Tribedi Bora, **B. Samantaray**, S. Mohanty, and S. Ravi, *IEEE Transactions on Magnetics* **47**, (2011) Issue No.10.

TH-1060_06612103

Papers Published in Refereed Conferences Proceeding and presented in National/ International Conferences:

1. Neutron powder diffraction studies in $Nd_{1-x}K_xMnO_3$(x=0.15 and 0.20) compounds.

   B. Samantaray, S. Ravi, A. Perumal, I. Dhiman, and A. Das, Presented in 55th Annual conference on Magnetism and Magnetic Materials, 14th-18th November, 2010, Atlanta, Georgia USA.

2. Ferromagnetism insulating state to charge ordered state in (Nd-Na)-Mn-O_3 series.

   B. Samantaray, and S. Ravi, Presented in International conference on superconductivity and magnetism, 25th-30th April, 2010, Antalya, Turkey.

3. Ferromagnetic insulating state to charge ordered state in (Nd,Na)-Mn-O series.

   B. Samantaray, and S. Ravi, Presented in National conference "Recent Advances in Correlated Electron Systems, 18th – 20th January, 2010, IIT Guwahati, India.

4. Neutron powder diffraction studies in $LaMn_{1-x}Cu_xO_3$ (x=0.05, 0.10 and 0.15).

   B. Samantaray, S. K. Srivastava, S. Mohanty, S. Ravi, I. Dhiman, and A. Das, Presented in 11th Joint MMM- Intermag conference, 18th -22nd January, 2010, Washington DC, USA.

5. Structural and Magnetic Properties of Alkali Doped Nd-Mn-O Series.

   B. Samantaray, and S. Ravi, Presented in National Conference in Platinum Jubilee of Sambalpur University 2009, Orissa, India.

6. Critical behavior studies in Nd-Mn-O based double exchange ferromagnetic compounds.

   B. Samantaray, S. Ravi and A. Perumal, Presented in Discussion meeting on Statistical and Condensed Matter Physics, 31st October 2009, IIT Guwahati, Guwahati, India.

7. Magnetic properties of $Nd_{1-x}K_xMnO_3$ compounds.

   B. Samantaray, and S. Ravi, Presented in National conference on Advance Materials 2009, PSN College of Engineering and Technology, Tamil Nadu, India.

8. Neutron Powder Diffraction Studies in $LaMn_{1-x}Cu_xO_3$ (x=0.15 and 0.20)

   B. Samantaray, S. Mohanty, S. Ravi, I. Dhiman, and A. Das, Presented in International Conference on Neutron Scattering and Mesoscopic Systems 2009, BARC, Mumbai, India.

9. Study of effective ferromagnetic spin contribution in Cr & Al doped $La_{0.85}Ag_{0.15}MnO_3$ compound.

TH-1060_06612103

S. K. Srivastav, **B. Samantaray**, and S. Ravi, Proc. DAE SSP, 53 (2008).

Presented in DAE Solid State Physics Symposium, December 2008, BARC Mumbai, India**.**

10. Asymptotic critical behavior studies in $Nd_{1-x}K_xMnO_3$ (x=0.10& 0.15) system.

B. Samantaray & S. Ravi, Proc. DAE SSP, 53 (2008).

Presented in DAE Solid State Physics Symposium, December 2008, BARC Mumbai, India**.**

11. Study of crystal structure and magnetic properties of $(Y_{1-x}Nb_x)_2Mn_2O_7$.

S. K. Srivastav, **B. Samantaray**, and S. Ravi, Presneted in Condensed matter Days (2007), NIT Rourkela, India**.**

------ ------ --- ---------- ------X--------- ---- -- ---------- ----------

TH-1060_06612103